Squeezed States for Advanced Gravitational Wave Detectors

by

Eric Oelker

B.A., University of California Berkeley (2009)

Submitted to the Department of Physics
in partial fulfillment of the requirements for the degree of

Doctor of Philosophy in Physics

at the

MASSACHUSETTS INSTITUTE OF TECHNOLOGY

September 2016

Author .....
Department of Physics
August 12, 2016

Certified by .....
Nergis Mavalvala
Professor of Physics
Thesis Supervisor

Accepted by .....
Nergis Mavalvala
Associate Department Head for Education

Squeezed States for Advanced Gravitational Wave Detectors

by

Eric Oelker

Submitted to the Department of Physics
on August 12, 2016, in partial fulfillment of the
requirements for the degree of
Doctor of Philosophy in Physics

Abstract

Quantum vacuum fluctuations impose strict limits on precision displacement measurements, those of interferometric gravitational-wave detectors among them. Introducing squeezed states into an interferometer's readout port can improve the sensitivity of the instrument, leading to richer astrophysical observations. In recent years, this technique has been used to improve the sensitivity of the GEO600 [101] and the Initial LIGO detector at Hanford, WA [102]. Squeezed states could be employed in advanced gravitational-wave detectors, such as Advanced LIGO, to further push the limits of the observable gravitational wave universe. To maximize the benefit from squeezing, environmentally induced disturbances such as back scattering and angular jitter need to be mitigated. Also, optomechanical interactions dictate that the quadrature of the squeezed vacuum state must rotate by 90° at around 50 Hz in order to achieve a broadband sensitivity improvement for Advanced LIGO.

In this thesis we describe a series of experiments that lead to a ultra-high vacuum (UHV) compatible, low phase noise, and frequency-dependent squeezed vacuum source required for Advanced LIGO and future gravitational-wave detectors. In order to develop the required technology, two proof-of-principal experiments were conducted. In the first experiment, we built a UHV compatible squeezed vacuum source and homodyne readout and operated them under high vacuum. We also commissioned a control scheme that achieved a record low $1.3^{+0.7}_{-0.5}$ mrad of phase noise. This is a nearly tenfold improvement over previously reported measurements with audio-band squeezed vacuum sources. In the second experiment we used a 2-m-long, high-finesse optical resonator to produce frequency-dependent squeezed quadrature rotation around 1.2 kHz. This demonstration of audio-band frequency-dependent squeezing uses technology and methods that are scalable to the required rotation frequency for Advance LIGO, firmly establishing the viability of this technique for application in current and future gravitational-wave detectors. We conclude with a discussion of the implications of these results for squeezing enhancement in Advanced LIGO and beyond.

Thesis Supervisor: Nergis Mavalvala

Title: Professor of Physics

Acknowledgments

During my time at MIT, I've had the great fortune to work with many talented students, staff scientists, and faculty. During the formative years of my PhD, I received countless hours of mentoring from Chris Wipf and Tim Bodyia. I also regularly sought advice from Nicolas Smith and Thomas Corbitt. I was extremely fortunate to arrive at our lab at a time when we were blessed with such a talented core of senior graduate students and postdocs. I hope that I have been able to live up to their example.

During the second half of my PhD, I was lucky to work on a project managed by Lisa Barsotti and John Miller. Their technical and organisational guidance always kept the project moving in the right direction. Down in the lab, I worked closely with Tomoki Isogai, Maggie Tse, Georgia Mansell, Fabrice Matichard, Alvaro Fernandez-Galiana, Haocun Yu, and Myron MacInnis. Matt Evans always had an open door whenever I reached an impasse or required a sounding board for a new idea. I'm proud of the progress we've made together over the last several years.

I'm particularly grateful to my advisor, Nergis Mavalvala. She has provided vital professional and scientific guidance and has always dealt with my ongoing health issues with compassion. I've tried to pay her back through hard work and productivity, but I suspect that I am still in her debt.

Most of all, I'd like to thank my family and friends for their unwavering support.

-Eric Oelker, July 19 2016.

Contents

List of Figures

List of Tables

%

Chapter 1

Quantum noise in Advanced LIGO

On September 14, 2015, the Advanced LIGO detectors ushered in the era of gravitational wave astronomy with their coincident detection of a gravitational wave from a binary black hole merger [29]. This detection, which came roughly 100 years after Einstein's original prediction of gravitational waves, represents the culmination of over four decades of research on interferometric gravitational wave detectors. The first detection is presented in Figure 1-1.

The current Advanced LIGO detectors feature an ultra-stable laser source, the worlds best seismic isolation system, and high quality mechanical test mass suspensions to reduce thermal noise. This low level of classical noise has allowed Advanced LIGO to reach an unprecedented level of strain sensitivity. As shown in Figure 1-2, the Advanced LIGO detectors will be limited by "quantum fluctuations" when they reach design sensitivity [103].

Quantum vacuum fluctuations permeate the entirety of space. Ordinarily benign, these jittering fields impose the strictest limit on the precision of microscopic measurements. In particular, quantum noise limits the performance of interferometric gravitational-wave detectors as they attempt to make observations of ripples in the very fabric of space-time [8, 34, 103].

Just as the ground state of the quantum harmonic oscillator has non-zero energy and an associated uncertainty principle, so too does that of the electromagnetic field. In the latter case, the ground state energy gives rise to so-called quantum vac-

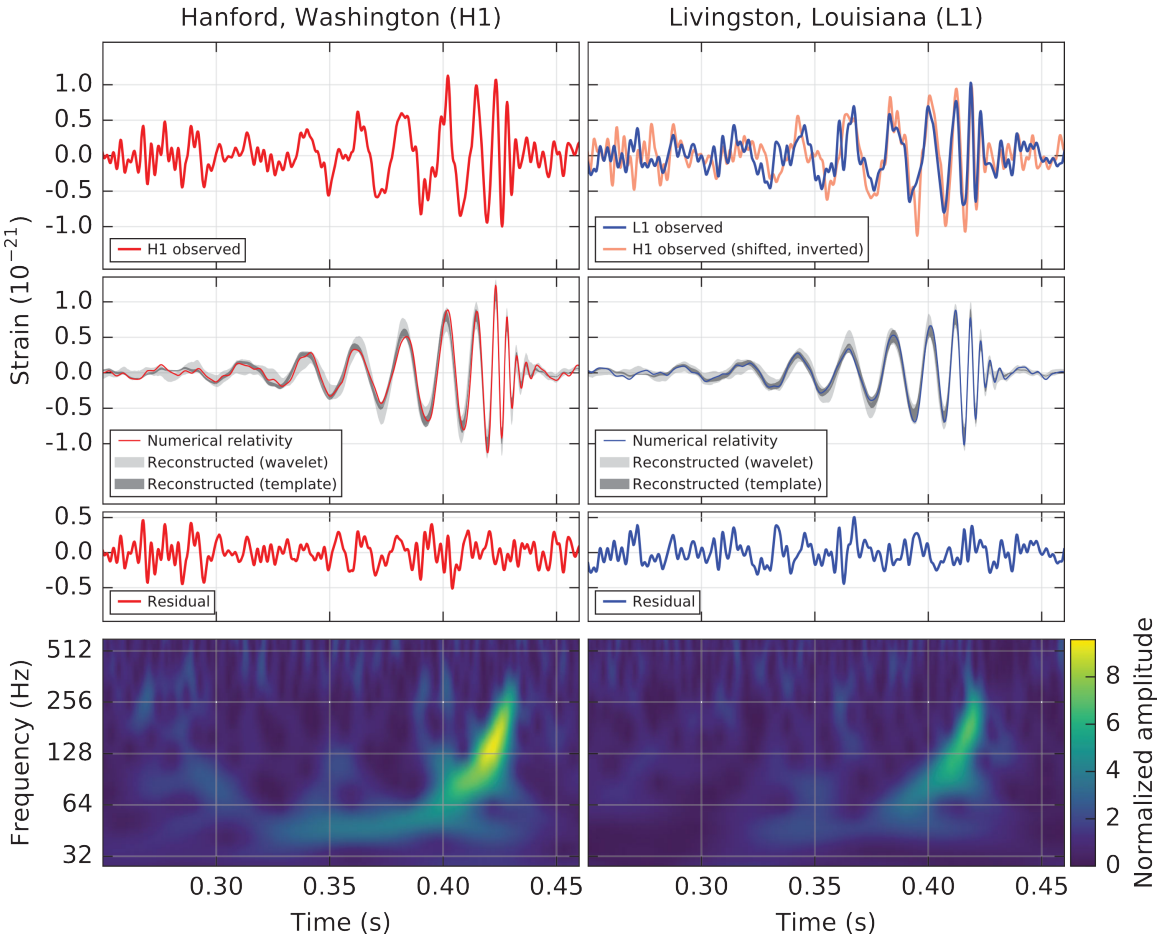

Figure 1-1: Advanced LIGO's first detection of a binary black hole merger shown for both the Hanford (Left) and Livingston (Right) detectors adapted from Reference [29]. Shown are plots of the band-passed strain spectrum, model fit from numerical relativity and a time-frequency plot showing the frequency chirp during the inspiral.

uum fluctuations in the field and the accompanying uncertainty principle relates the variances in its two orthogonal quadrature phases.

Although seemingly insignificant, quantum vacuum fluctuations impose the principal limit on the sensitivity of present-day gravitational wave interferometers. Both low-frequency radiation pressure noise and high-frequency shot noise arise due to the vacuum fluctuations which enter an interferometer's readout port [22].

What are these quantum noise fluctuations and how do we surpass this seemingly fundamental noise floor? This chapter will attempt to address this question.

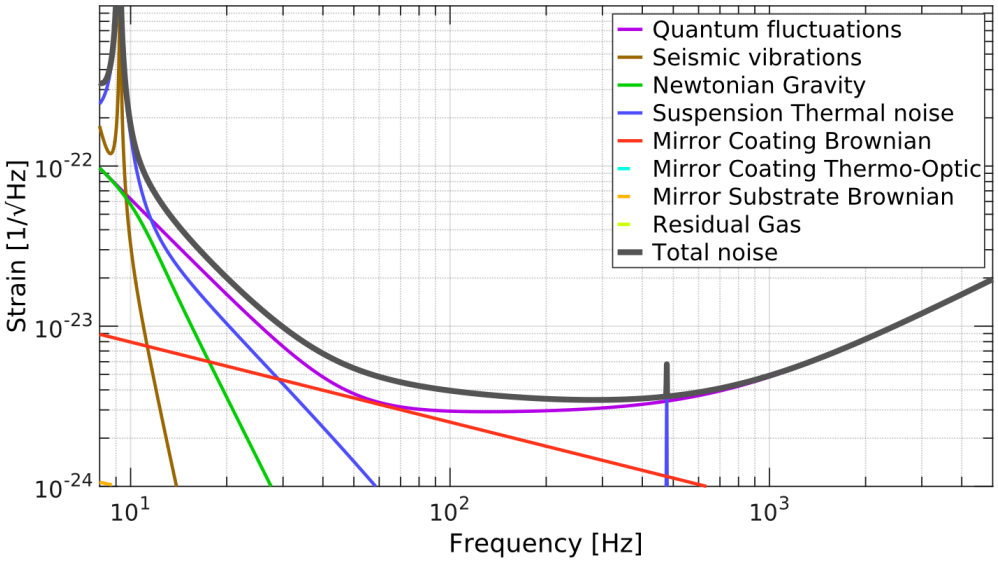

Figure 1-2: Noise Budget for Advanced LIGO generated using the LIGO simulation tool GWINC. The noise terms which are visible on the plot are quantum noise (purple), coating brownian thermal noise (red), gravity gradiant noise (green), suspension thermal noise (blue) and seismic noise (brown). The black curve shows a combination of all noise terms added in quadrature. At full design sensitivity, Advanced LIGO will be limited by quantum noise throughout its detection band.

1.1 The quantum nature of light

Prior to deriving the quantum limit for Advanced LIGO, we must walk through some of the background theory. In the following section, I describe the quantization of the electromagnetic field and the resulting quantum noise associated with these fields. It is assumed that this material is largely a review, so the results are presented relatively succinctly. The main purpose of going through this is to establish the conventions which will be used in the rest of this thesis.

I will mostly try to adhere to the conventions used in [63] (which uses the so-called 2-Photon Formalism established in [23]) since this paper is the foundation on which most other works on quantum filter cavities and quantum noise in Advanced LIGO are based.

1.1.1 Quantization of the electromagnetic field

We begin by expressing the electric field in the following form:

$$E(t) = E^{(+)}(t) + E^{(-)}(t) \tag{1.1}$$

where $E^{(+)}(t)$ and $E^{(-)}(t)$ correspond to the positive and negative frequency components of the electric field which are defined in terms of the following Fourier transforms:

$$E^{(+)}(t) = \int_0^\infty E(\omega) e^{-i\omega t} \frac{d\omega}{2\pi} \tag{1.2}$$

$$E^{(-)}(t) = \int_0^\infty E(-\omega) e^{i\omega t} \frac{d\omega}{2\pi} \tag{1.3}$$

where ω denotes the Fourier frequency in angular units and $E(\omega)$ is the (complex) Fourier component of $E(t)$ at frequency ω. Since E(t) is real, $E^{(-)}(t) = \left(E^{(+)}(t)\right)^*$ and $E(-\omega) = E(\omega)^*$. In this thesis, we will always choose to re-express ω in the above equations in terms of a fixed carrier frequency ω_0 and sideband frequencies Ω by making the following change of variables: $\omega = \omega_0 + \Omega$

$$E^{(+)}(t) = e^{-i\omega_0 t} \int_0^\infty \left(E(\Omega) e^{-i\Omega t} + E(-\Omega) e^{+i\Omega t}\right) \frac{d\Omega}{2\pi} \tag{1.4}$$

Here, and throughout this thesis, we will assume that $E(\Omega)$ is only appreciable at frequencies where $\Omega \ll \omega_0$. Therefore, I may formally extend the integrals from zero to infinity for ease of notation. We may rewrite 1.1 as:

$$E(t) = e^{-i\omega_0 t} \int_0^\infty \left(E(\Omega) e^{-i\Omega t} + E(-\Omega) e^{+i\Omega t}\right) \frac{d\Omega}{2\pi} + h.c. \tag{1.5}$$

We can express the amplitude coefficients in Equation 1.5 in terms of quantum photon annihilation operators by factoring out a term corresponding to the electric field

spectral density per photon

$$E(t) = e^{-i\omega_0 t} \int_0^\infty \left(\sqrt{\frac{2\pi\hbar(\omega_0 + \Omega)}{Ac}} a(\Omega) e^{-i\Omega t} + \sqrt{\frac{2\pi\hbar(\omega_0 - \Omega)}{Ac}} a(-\Omega) e^{+i\Omega t} \right) \frac{d\Omega}{2\pi} + h.c. \quad (1.6)$$

where A is the cross-sectional area of the mode. For the remainder of this thesis, I will always simplify expressions like this in the square root by neglecting the sideband frequency (since $\Omega \ll \omega_0$). For a more exact treatment containing all of these terms see the standard treatment of 2-photon quantum optics in Reference [23]. We then arrive at the formula for the quantized field:

$$E(t) = e^{-i\omega_0 t} \sqrt{\frac{2\pi\hbar\omega_0}{Ac}} \int_0^\infty \left(a(\Omega) e^{-i\Omega t} + a(-\Omega) e^{+i\Omega t} \right) \frac{d\Omega}{2\pi} + h.c. \quad (1.7)$$

This electric field operator is a Heisenberg picture operator which contains the full time evolution of the system. However, we note that $a(\Omega)$ is constant since we have chosen to factor out its explicit time dependence ($e^{-i\Omega t}$). We may also compute our field annihilation operators in the time domain via the following Fourier transform relations:

$$a(t) = \int_0^\infty \left(a(\Omega) e^{-i\Omega t} + a(-\Omega) e^{+i\Omega t} \right) \frac{d\Omega}{2\pi} = \int_{-\infty}^\infty a(\Omega) e^{-i\Omega t} \frac{d\Omega}{2\pi} \quad (1.8)$$

$$a(\Omega) = \int_{-\infty}^\infty a(t) e^{i\Omega t} dt \quad (1.9)$$

Comparing Equation 1.8 with Equation 1.4, we see that we may express $E^{(+)}(t)$ and $E^{(-)}(t)$ in Equation 1.1 in terms of $a(t)$:

$$E(t) = \sqrt{\frac{2\pi\hbar\omega_0}{Ac}} \left(a(t) e^{-i\omega_0 t} + a^\dagger(t) e^{i\omega_0 t} \right) \quad (1.10)$$

The time dependent annihilation and creation operators here are in the rotating frame at the optical frequency ω_0. In free space, or an empty cavity without losses, a would have no explicit time dependence. By allowing the annihilation and creation operators to have time dependence we can take into account interactions, and describe noise on the field.

Using the convention that $a^\dagger(t) = [a(t)]^\dagger$ (where $\dagger$ denotes taking the hermitian conjugate) we may also use Equations 1.8 and 1.9 to derive the following relation which will be useful in the next subsection:

$$[a(\Omega)]^\dagger = a^\dagger(-\Omega) \tag{1.11}$$

where the notation $a^\dagger(\Omega)$ corresponds to Fourier transform pair of $a^\dagger(t)$.

1.1.2 Quantized fields in the quadrature picture

When discussing uncertainty or noise associated with a quantized optical field, it is often useful to express the field in the quadrature picture. We may rewrite Equation 1.10 as follows:

$$E(t) = \sqrt{\frac{4\pi\hbar\omega_0}{Ac}}\left[a_1(t)\cos(\omega_0 t) + a_2(t)\sin(\omega_0 t)\right] \tag{1.12}$$

where we have defined the following quadrature operators:

$$\textbf{Amplitude Quadrature}: \; a_1(t) = \frac{a(t) + a^\dagger(t)}{\sqrt{2}} \tag{1.13}$$

$$\textbf{Phase Quadrature}: \; a_2(t) = \frac{a(t) - a^\dagger(t)}{i\sqrt{2}} \tag{1.14}$$

Using Equation 1.11, we may write the amplitude and phase quadrature operators in the frequency domain as: [1]

[1]The correct operators which actually correspond to the real and imaginary component of the electric field at each sideband frequency aren't actually a_1 and a_2 as defined. Instead, they are $\hat{\alpha}_1 = \sqrt{\frac{\Omega+\omega_0}{2\omega_0}}a_+ + \sqrt{\frac{\omega_0-\Omega}{2\omega_0}}a_-$, similar for $\hat{\alpha}_2$. A detailed argument about why this is necessary can

$$\textbf{Amplitude Quadrature}: \; a_1(\Omega) = \frac{a_+ + a_-^\dagger}{\sqrt{2}} \tag{1.15}$$

$$\textbf{Phase Quadrature}: \; a_2(\Omega) = \frac{a_+ - a_-^\dagger}{i\sqrt{2}} \tag{1.16}$$

where I have introduced an alternate expression for the annihilation operators in the frequency domain to simplify our notation:

$$a_+ = a(\Omega), \quad a_- = a(-\Omega) \tag{1.17}$$

More generally, we may define an operator for an arbitrary quadrature as follows:

$$a(\theta, \Omega) = a_1(\Omega)\cos(\theta) + a_2(\Omega)\sin(\theta) \tag{1.18}$$

$$= \frac{1}{\sqrt{2}}\left(a_+ e^{-i\theta} + a_-^\dagger e^{i\theta}\right) \tag{1.19}$$

In terms of these operators, Equation 1.7 may be rewritten to express the Electric field operator in terms of its in-phase (amplitude quadrature) and quadrature-phase (phase quadrature) components:

$$E(t) = \sqrt{\frac{4\pi\hbar\omega_0}{Ac}}\Bigg[\cos(\omega_0 t)\int_0^\infty (a_1(\Omega)e^{-i\Omega t} + a_1^\dagger(\Omega)e^{+i\Omega t})\frac{d\Omega}{2\pi} + \sin(\omega_0 t)\int_0^\infty (a_2(\Omega)e^{-i\Omega t} + a_2^\dagger(\Omega)e^{+i\Omega t})\frac{d\Omega}{2\pi}\Bigg] \tag{1.20}$$

1.1.3 Commutation relations and uncertainty principle

We will now address how this quantum mechanical description of light gives rise to quantum noise in the amplitude and phase quadratures. Fundamentally, this is due

be found in Section IV of ref [23]. Again, we sweep this detail under the rug for simplicity since $\Omega \ll \omega_0$

to the fact that the two quadrature operators do not commute, as we will derive presently. We start from the standard commutation relations for the photon creation and annihilation operators $\left[a, a^\dagger\right] = 1$. The commutation relation for the quadrature operators is then $[a_1, a_2] = i$. This gives rise to the uncertainty principle:

$$\Delta a_1^2 \Delta a_2^2 \geq |\frac{1}{2i}\langle [a_1, a_2]\rangle|^2 = 1/4 \tag{1.21}$$

The consequences of this result are significant. It implies that an electromagnetic field with zero mean amplitude will still have nonzero quadrature variances. Some residual noise must remain in both quadratures in order to satisfy Equation 1.21 even when the field is in its vacuum state. As we'll see, these vacuum fluctuations are what give rise to quantum noise in gravitational wave detectors.

Fourier transforming the time domain commutation relations, we arrive at the commutations for the annihilation and creation operators in the frequency domain. Here, the factor of 2π arises due to the fact that these commutation relations are expressed in angular frequency units.

$$\left[a_+, a_{+'}^\dagger\right] = 2\pi\delta(\Omega - \Omega'), \quad \left[a_-, a_{-'}^\dagger\right] = 2\pi\delta(\Omega - \Omega'), \tag{1.22}$$

All other commutators consisting of combinations of $a_+, a_-, a_+^\dagger$ and $a_-^\dagger$ are equal to zero. Inserting these relations into Equations 1.15 and 1.16 gives us the commutation relations for the quadrature operators.

$$\left[a_1, a_{2'}^\dagger\right] = -\left[a_2, a_{1'}^\dagger\right] = i2\pi\delta(\Omega - \Omega') \tag{1.23}$$

One can calculate the commutator between any arbitrary pair of orthogonal quadratures, $\left[a(\theta, \Omega), a(\theta + \pi/2, \Omega')^\dagger\right]$, by combining Equation 1.23 with Equation 1.18, though I won't write this out in detail. Finally, we can use this expression to derive the uncertainty relation for the variance of two orthogonal quadratures at a particular sideband frequency. We use an uncertainty relation for two non-hermitian operators which is painstakingly derived in an Appendix of [23]:

$$|\Delta a(\theta,\Omega)|^2|\Delta a(\theta+\pi/2,\Omega)|^2 \geq |\frac{1}{2i}\langle[a(\theta,\Omega),a^\dagger(\theta+\pi/2,\Omega)\rangle|^2 = \frac{1}{4} \tag{1.24}$$

1.1.4 Vacuum and coherent states of light

We can use the results of the preceding sections to evaluate the quantum mechanical properties of the most common states of light that one encounters in a laboratory: coherent states. Coherent states are defined as eigenstates of the single mode annihilation operator:

$$a\,|\alpha\rangle = \alpha\,|\alpha\rangle \tag{1.25}$$

I will summarize some of the standard properties of coherent states which can be found in any good textbook on quantum optics. We can expand the coherent state in the number state basis:

$$|\alpha\rangle = e^{-|\alpha|^2/2}\sum_{n=0}^{\infty}\frac{\alpha^n}{\sqrt{n!}}\,|n\rangle \tag{1.26}$$

The vacuum state is simply a coherent state for which $\alpha = 0$. For coherent states, both the mean $\langle\alpha|\hat{n}|\alpha\rangle$ and variance $\langle\alpha|(\Delta\hat{n})^2|\alpha\rangle$ of the number operator $\hat{n} = a^\dagger a$ are equal to $|\alpha|^2$. Photon number measurements of coherent states obey Poissonian measurement statistics:

$$P(n) = |\,\langle n|\alpha\rangle\,|^2 = e^{-\langle\hat{n}\rangle}\frac{\langle\hat{n}\rangle^n}{n!} \tag{1.27}$$

Coherent states can be "created" by applying the displacement operator $\hat{D}(\alpha)$ to the vacuum state:

$$\hat{D}(\alpha)\,|0\rangle = e^{(\alpha a^\dagger - \alpha^* a)}\,|0\rangle = |\alpha\rangle \tag{1.28}$$

The displacement operator gets its name from the fact that it corresponds to displacing the initial conditions of the harmonic oscillator in phase space from $0 \rightarrow \alpha = x+ip$.

Its action on the annihilation operator is given by $\hat{D}^{-1}(\alpha)a\hat{D}(\alpha) = a + \alpha$. We are particularly interested in the expectation values for the quadrature operator and its variance. We calculate these using Equations 1.15 and 1.16:

$$\langle\alpha|a_1(\Omega)|\alpha\rangle = \mathrm{Re}[\alpha]\ \delta(\Omega) \tag{1.29}$$

$$\langle\alpha|a_2(\Omega)|\alpha\rangle = \mathrm{Im}[\alpha]\ \delta(\Omega) \tag{1.30}$$

$$\langle\alpha||\Delta a_1(\Omega)|^2|\alpha\rangle = 1/2 \tag{1.31}$$

$$\langle\alpha||\Delta a_2(\Omega)|^2|\alpha\rangle = 1/2 \tag{1.32}$$

From these relations, we see that the expectation value for the quadrature operators is only non-zero at the carrier frequency (a "pure" coherent state as defined has no classical noise or modulation sidebands). The value of α gives us the complex amplitude of the phasor representing the carrier field. We also see that a coherent state is a minimum uncertainty state with equal uncertainty in both the amplitude and phase quadrature. One semi-classical interpretation of the quadrature variances is that the sidebands on a coherent state are populated with half a photon of energy, but that the phases of these sidebands are random and uncorrelated when measured at different times.

1.1.5 Squeezed states of light

The vacuum state naturally present in all modes of the electromagnetic field possesses equal uncertainty in each of its two quadratures. However, it is possible to redistribute the uncertainty, in accordance with the Heisenberg Uncertainty Principle, to produce a *squeezed* state, with reduced variance in one quadrature at the expense of increased variance in the orthogonal quadrature. Common techniques used include parametric down-conversion [48], four-wave mixing [66, 85, 94], the Kerr effect [45, 79] and nonlinearities in optomechanical systems [15, 88, 91]. The most advanced sources are currently optical parametric oscillators (OPOs) [28, 109]. The bandwidth of these de-

vices is 10 MHz, so that the redistribution of noise occurs essentially uniformly over the range of frequencies of interest for gravitational wave detectors.

For pedagogical reasons, I will give a brief description of squeezed states and their statistical properties, though a more detailed description of how squeezed light is generated will be deferred until Chapter 2. An ideal squeezed state may be produced by a system with the following Hamiltonian:

$$\hat{H} = \frac{i\hbar B}{2}\left(a^2 - a^{\dagger 2}\right) \tag{1.33}$$

where B is a constant which will be expressed in terms of physical parameters in the next chapter. If we allow this Hamiltonian to act on the system for a time Δt, an operator a evolves as follows:

$$a(\Delta t) = S(r)a(0)S^{\dagger}(r) \qquad S(r) = e^{\frac{-r}{2}(a^2 - a^{\dagger 2})} \tag{1.34}$$

where $S(r)$ is known as the squeezing operator and $r = B\Delta t$ is the squeezing factor. Applying this time evolution to the quadrature operators $a_{1,2}(t)$ yields:

$$a_1(\Delta t) = a_1 e^{r} \qquad a_2(\Delta t) = a_2 e^{-r} \tag{1.35}$$

This gives rise to the following quadrature variances for the vacuum state:

$$\langle 0|\Delta a_1(\Delta t)^2|0\rangle = \frac{e^{2r}}{2} \qquad \langle 0|\Delta a_2(\Delta t)^2|0\rangle = \frac{e^{-2r}}{2} \tag{1.36}$$

Comparing this to Equations 1.31 and 1.32 (with $\alpha = 0$ for the vacuum state), we see that the phase quadrature variance has been reduced below its nominal value by a factor of e^{-r}, while the amplitude quadrature has increased by a factor of e^{r}. We say that the phase quadrature has been "squeezed" while the amplitude quadrature has been "anti-squeezed". The resulting squeezed state is still a minimum uncertainty state, but the noise has been redistributed between the two quadratures. We may also act on $|0\rangle$ with $S(r)$ to compute the squeezed vacuum state:

$$S(r)\left|0\right\rangle = \frac{1}{\sqrt{\cosh(r)}} \sum_{n=0}^{\infty} \frac{\sqrt{(2n)!}}{2^n n!} (\tanh(r))^n \left|2n\right\rangle \tag{1.37}$$

Note that, despite the name "squeezed vacuum", this state has a nonzero probability amplitude to have an even number of photons. The fact that the number of photons created is always a multiple of 2 is significant. As we will learn in the next chapter, a squeezed vacuum source which realizes this Hamiltonian always generates pairs of correlated photons which give rise to squeezing.

Similarly, one can derive an expression for the squeezed coherent state wavefunction by acting on 1.37 with the displacement operator in Equation 1.28, though we leave this exercise to the reader.

1.2 Quantum noise in gravitational wave detectors

After four decades of research, interferometric gravitational wave detectors have achieved unprecedented levels of strain sensitivity. For the Advanced LIGO detectors [103], all sources of classical noise have been brought near or below quantum noise floor within the sensitivity band (10 Hz to 10 kHz). Shot noise dominates above 50 Hz, while quantum radiation pressure noise limits us at lower frequencies. It was shown by Caves [21, 22] that both of these quantum noise terms arise due to vacuum fluctuations entering from the anti-symmetric port of the interferometer.

In the subsections that follow, we derive the quantum limit for Advanced LIGO. This derivation will proceed in steps. We start by considering the simplest possible topology: the Michelson interferometer. Its poor quantum noise performance will help to motivate why Advanced LIGO requires a more complicated optical configuration to achieve its design sensitivity. Subsequently, we add arm cavities and finally dual recycling, to derive the quantum noise performance of Advanced LIGO.

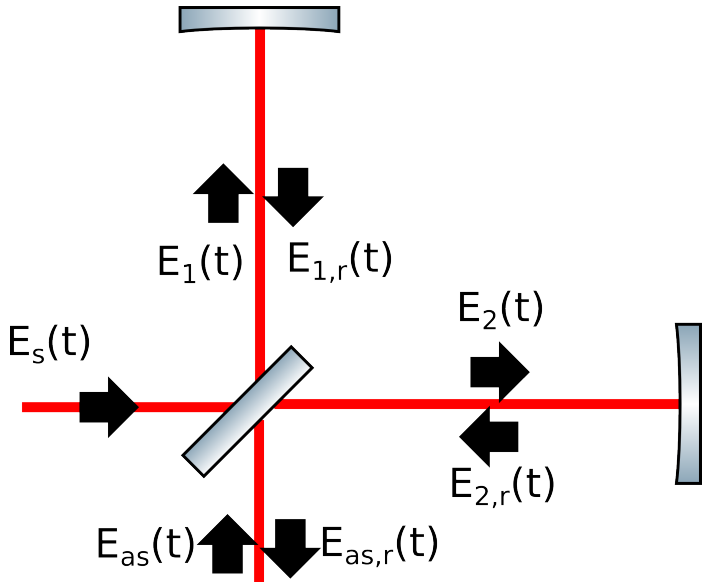

Figure 1-3: Schematic of a Michelson interferometer. A classical carrier field $E_s(t)$ enters from the interferometer symmetric port while a vacuum fluctuations represented by $E_{as}(t)$ enter from the anti-symmetric port. The quantum noise level at the readout is contained in the AC component of the field exiting the interferometer $E_{as,r}(t)$

1.2.1 Example: Michelson interferometer

We begin with the Michelson interferometer. The derivation will closely follow [32]. Figure 1-3 shows a schematic of the Michelson and all associated fields. We assume that the distance between the beamsplitter and the two end mirrors is exactly an integer number of wavelengths to simplify the notation. The main laser field enters the Michelson from the symmetric port:

$$E_s(t) = E_0 \cos(\omega_0 t) + \delta E_s(t) \tag{1.38}$$

Here, $E_0 = \sqrt{\frac{8\pi P}{Ac}}$, where A is the mode area and P is the laser power. The first term represents the classical field while the second term represents fluctuations of both classical and quantum origin. For this derivation and those that follow, we will assume that the Michelson is locked on a "dark fringe" so that the fluctuations interfere destructively at the anti-symmetric port. The field incident from the anti-symmetric port consists of vacuum fluctuations. Its electric field in terms of quadrature operators

is given by Equation 1.20 which we rewrite below for clarity:

$$E_{as}(t) = \sqrt{\frac{4\pi\hbar\omega_0}{Ac}}\Big[\cos(\omega_0 t)\int_0^\infty (a_1(\Omega)e^{-i\Omega t} + a_1^\dagger(\Omega)e^{+i\Omega t})\frac{d\Omega}{2\pi} + \sin(\omega_0 t)\int_0^\infty (a_2(\Omega)e^{-i\Omega t} + a_2^\dagger(\Omega)e^{+i\Omega t})\frac{d\Omega}{2\pi}\Big] \quad (1.39)$$

After the beamsplitter, which we assume is 50% transmissive, the fields incident on the two end mirrors are given by:

$$E_1(t) = \frac{1}{\sqrt{2}}[E_s(t) + E_{as}(t)] \quad (1.40)$$

$$E_2(t) = \frac{1}{\sqrt{2}}[E_s(t) - E_{as}(t)] \quad (1.41)$$

Here we have ignored the propagation time $\omega_0\delta t = \omega_0 L/c$ since we've assumed that it is an integer multiple of 2π and does not change the calculation. We are also implicitly neglecting the frequency dispersion of the Michelson by ignoring the small phase shift $\Omega L/c$. This is valid since the Michelson is short enough for this phase shift to remain small over the frequency band of interest. Any displacement of the end mirrors, $x_1(t)$ or $x_2(t)$, creates a phase shift on the reflected fields which we can express as

$$E_{1,r}(t) = \frac{1}{\sqrt{2}}[E_s(t - \frac{2x_1(t)}{c}) + E_{as}(t - \frac{2x_1(t)}{c})] \quad (1.42)$$

$$E_{2,r}(t) = \frac{1}{\sqrt{2}}[E_s(t - \frac{2x_2(t)}{c}) - E_{as}(t - \frac{2x_2(t)}{c})] \quad (1.43)$$

Assuming that the mirror displacements are small, we make a few simple approximations. First, we rewrite the cosine term in E_s using the identity $\cos(A-B) = \cos(A)\cos(B) + \sin(A)\sin(B)$, Taylor series expand the terms depending on $2\omega_0 x_1/c$,

and keep only the zeroth and first order terms. We also neglect the impact of the mirror on E_{as} since these correspond to second order terms (sidebands on the sidebands). We arrive at the following linearised expressions:

$$E_{1,r}(t) \approx \frac{1}{\sqrt{2}}[E_0 \cos(\omega_0 t) - E_0 \sin(\omega_0 t)\frac{2\omega_0 x_1(t)}{c} + E_{as}(t)] \tag{1.44}$$

$$E_{2,r}(t) \approx \frac{1}{\sqrt{2}}[E_0 \cos(\omega_0 t) - E_0 \sin(\omega_0 t)\frac{2\omega_0 x_2(t)}{c} - E_{as}(t)] \tag{1.45}$$

Calculating the field exiting at the anti-symmetric port, we find that it is equal to the field entering from that port with an additional term due to the differential displacement of the two mirrors.

$$E_{as,r}(t) = E_{as} + E_0 \frac{\omega_0[x_2(t) - x_1(t)]}{c} \sin(\omega_0 t) \tag{1.46}$$

This differential displacement $x_1(t) - x_2(t)$ can be broken into 3 terms:

$$x_1(t) - x_2(t) = x_{cl,1}(t) - x_{cl,2}(t) + \delta\hat{x}_1(t) - \delta\hat{x}_2(t) + Lh(t) \tag{1.47}$$

The first term corresponds to classical displacement noise (seismic, thermal, etc.), the second term corresponds to displacement noise due to quantum radiation pressure, and the final term corresponds to the strain induced by a passing gravitational wave. For the remainder of this chapter, I will omit the classical term for simplicity. The quantum radiation pressure noise term arises due to power fluctuations incident on the mirror caused by the interference between the carrier field and the vacuum fluctuations from the anti-symmetric port. For mirror 1, this is given by

$$\delta\hat{P}_1(t) = \frac{Ac}{4\pi}\overline{(E_s(t)E_{as}(t))} = \sqrt{P\hbar\omega_0}\int_0^\infty \left(a_1(\Omega)e^{-i\Omega t} + a_1^\dagger(\Omega)e^{i\Omega t}\right)\frac{d\Omega}{2\pi} \tag{1.48}$$

where we have averaged over the fast (ω_0) terms, but not the slower sideband terms in the integral. Fourier transforming the left hand side and equating terms under the

integral gives

$$\delta\hat{P}_1(\Omega) = \sqrt{P\hbar\omega_0}a_1 \tag{1.49}$$

The motion of the mirror due to radiation pressure is then

$$\delta\hat{x}_1(\Omega) = \chi(\Omega)\frac{2\delta\hat{P}_1(\Omega)}{c} = \frac{2\sqrt{P\hbar\omega_0}}{cM\Omega^2}a_1(\Omega) \tag{1.50}$$

Here $\chi(\Omega) = 1/(M\Omega^2)$ is the mechanical susceptibility of the test mass in the free mass limit and M is the mass of the mirror. Carrying out this analysis for the second mirror, derive the same force, but with the opposite sign due to the minus sign in Equation 1.46. Finally, we plug Equation 1.50 into Equation 1.46 to calculate the output field. Alternately one can express the outgoing field in terms of the outgoing quadrature operators $b_{1,2}$

$$E_{as,r}(t) = \sqrt{\frac{4\pi\hbar\omega_0}{Ac}}\Bigg[\cos(\omega_0 t)\int_0^\infty (b_1(\Omega)e^{-i\Omega t} + b_1^\dagger(\Omega)e^{+i\Omega t})\frac{d\Omega}{2\pi} + \sin(\omega_0 t)\int_0^\infty (b_2(\Omega)e^{-i\Omega t} + b_2^\dagger(\Omega)e^{+i\Omega t})\frac{d\Omega}{2\pi}\Bigg] \tag{1.51}$$

If we compare the above equation with Equation1.46 and equate terms, we can express the outgoing quadrature operators as

$$b_1(\Omega) = a_1(\Omega) \tag{1.52}$$

$$b_2(\Omega) = a_2(\Omega) - \mathcal{K}(\Omega)a_1(\Omega) - \sqrt{\frac{P\omega_0}{\hbar c^2}}Lh(\Omega) \tag{1.53}$$

where $\mathcal{K}(\Omega)$ is known as the radiation pressure coupling coefficient and is given by:

$$\mathcal{K}(\Omega) = \frac{4P\omega_0}{c^2M\Omega^2} \tag{1.54}$$

In order to detect gravitational waves, it is clear that we must measure the b_2 quadrature. When we take the variance of this quadrature, the a_1 term gives us shot noise while the $\mathcal{K}a_1$ is due to radiaion pressure noise. The strain amplitude spectral density of the quantum noise in the b_2 quadrature is

$$h_{QN}(\Omega) = \left(1/\mathcal{K}(\Omega) + \mathcal{K}(\Omega)\right) \frac{h_{SQL}}{2} \tag{1.55}$$

where

$$h_{SQL} = \sqrt{\frac{4\hbar}{M\Omega^2 L^2}} \tag{1.56}$$

is known as the "Free Mass Standard Quantum Limit", or SQL, for strain sensitivity. The SQL is a direct result of the Heisenberg uncertainty principle. As we measure the position of the mirror, the Heisenberg uncertainty principle (HUP) dictates that there must be a corresponding increase in the uncertainty in the mirrors momentum such that the overall uncertainty product still satisfies the HUP. This increase of uncertainty is often referred to as *quantum back-action*. This back-action adds noise to subsequent measurements of the mirror position. In Equation 1.55, the term proportional to $1/\mathcal{K}$ represents the initial uncertainty in the position and the term proportional to $\mathcal{K}$ represents the measurement back-action. The overall sensitivity is optimized when the two contributions are equal (ie when $\mathcal{K} = 1$). For a given operating power, this occurs at a measurement frequency given by

$$\Omega_{SQL}(P) = \sqrt{\frac{Mc^2}{4P\omega_0}} \tag{1.57}$$

In practice, it is not practical to reach SQL limited sensitivity in the detection band (10 Hz to 10 kHz) using a simple Michelson interferometer with gravitational wave detector-sized optics (10s of kg). For realistic levels of input power, the sensitivity of a Michelson is limited by a rather large level of shot noise. Resonant cavities are typically used to build up enough power to achieve the necessary reduction in shot noise required to measure gravitational waves. As we will see in the following sections,

Advanced LIGO uses a variety of optical cavities to achieve the desired sensitivity.

1.2.2 Example: Fabry-Perot Michelson interferometer

For the treatment of the Michelson interferometer in the previous subsection, we ignored the frequency dispersion of the interferometer by assuming that $c/L \gg \Omega$ over the frequency band of interest. For the Fabry-Perot Michelson, we will be assuming that the linewidth of the arm cavities are of order $\approx 100\,\mathrm{Hz}$, so we will no longer ignore the frequency dependence of the interferometer. For such an instrument, it is no longer convenient to propagate the entire fields $E_s(t)$ and $E_{as}(t)$ since they contain terms over a continuum of frequencies. Instead we will only propagate the quadrature operators at a single sideband frequency in Equation 1.39 for E_{as}. We neglect the fluctuations on E_s and only propagate the carrier term

$$E_s(t) = E_0 \cos(\omega_0 t) = \sqrt{\frac{4\pi\hbar\omega_0}{Ac}}\sqrt{2}D\cos(\omega_0 t) \tag{1.58}$$

where $D = \sqrt{\frac{I_0}{\hbar\omega_0}}$ is the carrier field amplitude in units of $\sqrt{Hz}$. We will now derive the input/output relations for the Fabry-Perot Michelson. This derivation is similar to that in Appendix B of [63], though we will neglect optical losses in the interferometer. The labelling convention for the fields is presented in Figure 1-4. At the input of each arm cavity the DC components of the fields are given by D and the AC components are given by

$$f_j^y = \frac{a_j}{\sqrt{2}}, \qquad f_j^x = \frac{-a_j}{\sqrt{2}} \tag{1.59}$$

where $j = 1, 2$ and we have dropped the explicit frequency dependence of the quadrature operators. We will continue using this shorthand notation for the remainder of this section for simplicity. Here, we assume that the cavity is lossless, other than the transmission of the input mirror, T. The derivation for the circulating fields is identical to that in [95], but with an additional AC source term due to the motion of the end mirror. The carrier field is just amplified by the standard resonance factor $2/\sqrt{T}$, becoming $\frac{2D}{\sqrt{T}}$ The quadrature operators obey the following interface relations

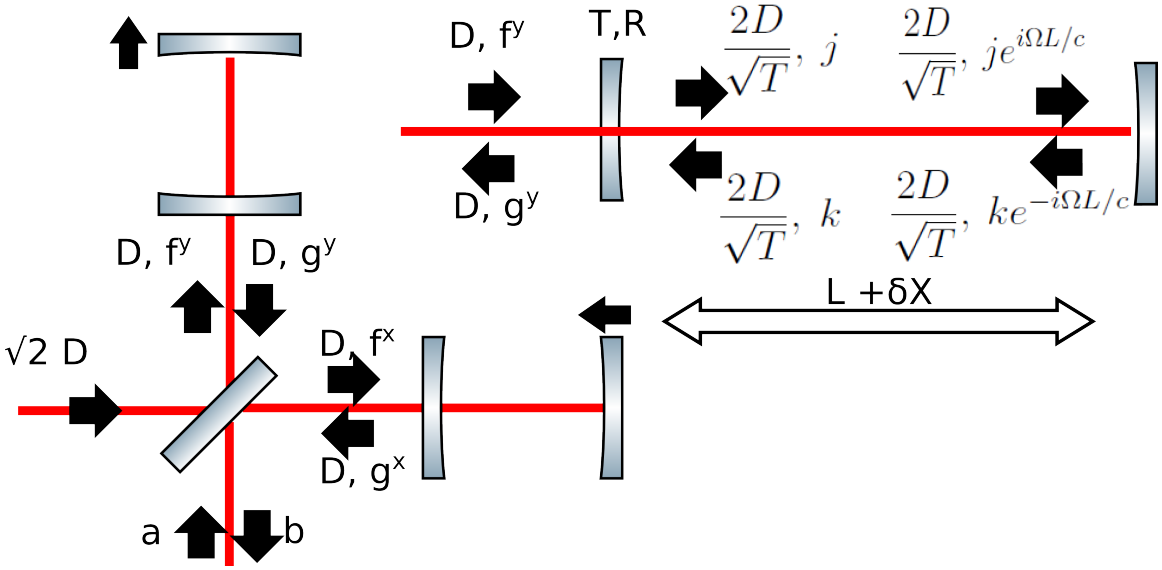

Figure 1-4: Fabry-Perot Michelson interferometer. Since the frequency dependence of the arm cavities cannot be ignored, the fields entering and exiting the interferometer at the anti-symmetric port have been written in terms of the field quadrature operators in the frequency domain ($a_j(\Omega)$ and $b_j(\Omega)$). The DC amplitude of the classical carrier field is represented by $\sqrt{2}D$. In the top right hand corner, the naming conventions for the intra-cavity fields are shown in detail.

at the input mirror

$$j_j = \sqrt{T} f_j + \sqrt{R} k_j, \qquad g_j = -\sqrt{R} f_j + \sqrt{T} k_j \tag{1.60}$$

The condition at the end mirror, which we assume is a perfect reflector, is given by

$$k_j e^{-i\Omega L/c} = j_j e^{i\Omega L/c} + \delta k_j \tag{1.61}$$

where δk_j arises due to the motion of the end mirror and, in analogy with1.44, can be expressed as

$$\delta k_1 = 0, \qquad \delta k_2 = \frac{2}{\sqrt{T}} D \frac{2\omega_0}{c} x \tag{1.62}$$

By combining the front and back mirror junction conditions, we can solve for the sideband amplitude in the cavity

$$j_j = \frac{\sqrt{T}f_j + \sqrt{R}e^{i\Omega L/c}\delta k_j}{1-\sqrt{R}e^{2i\Omega L/c}} \approx \frac{\sqrt{T}f_j + \delta k_j}{(2L/c)(\gamma - i\Omega)} = \frac{\mathcal{F}}{\pi}\frac{\sqrt{T}f_j + \delta k_j}{(1 - i\Omega/\gamma)} \tag{1.63}$$

Here, $\gamma = \frac{Tc}{4L} = 2\pi(\text{HWHM})$ is the cavity pole frequency in angular units and $\mathcal{F}$ is the cavity Finesse. We've made the approximations $\sqrt{R}e^{i\Omega L/c} \approx 1$ in the numerator and $1 - \sqrt{1-T}e^{i\Omega 2L/c} \approx 1 - (1 - T/2)(1 - i\Omega 2L/c) \approx (2L/c)(\gamma - i\Omega)$ in the denominator (assuming $T, \Omega L/c \ll 1$ and keeping only 1st order terms).

Lets take a minute to appreciate the consequences of Equation 1.63. The gravitational wave signal (which is contained in δk_2) is now resonantly enhanced by the arm cavities, but the interferometer now has finite bandwidth which is set by the cavity pole frequency. For $\Omega \gg \gamma$, the sensitivity falls off as $1/\Omega$.

The field at the output of the cavity is obtained by plugging Equation 1.61 and Equation 1.63 into Equation 1.60 which gives

$$g_j = \frac{e^{2i\Omega L/c} - \sqrt{R}}{1 - \sqrt{R}e^{2i\Omega L/c}}\, f_j \; + \frac{\sqrt{T}e^{i\Omega L/c}}{1 - \sqrt{R}e^{2i\Omega L/c}}\delta k_j \approx f_j e^{2i\beta} + \frac{\mathcal{F}}{\pi}\sqrt{\frac{T}{1 + (\Omega/\gamma)^2}}e^{i\beta}\delta k_j \tag{1.64}$$

where $\beta = \arctan(\Omega/\gamma)$ and where we've applied similar approximations to those used in Equation1.63. Finally, we arrive at the output fields

$$b_j = 1/\sqrt{2}(g_j^y - g_j^x) = a_j e^{2i\beta} + \frac{\mathcal{F}}{\pi}\sqrt{\frac{T}{1 + (\Omega/\gamma)^2}}e^{i\beta}\frac{\delta k^y - \delta k^x}{\sqrt{2}} \tag{1.65}$$

We now expand the second term by expressing it in terms of the displacement using Equation 1.62.

$$\frac{\delta k_2^y - \delta k_2^x}{\sqrt{2}} = 2\sqrt{\frac{2I_0}{\hbar\omega_0 T}}\frac{\omega_0 \delta x}{c} \tag{1.66}$$

As with the Michelson interferometer we can express δx as the sum of a strain and a radiation pressure term $\delta x(\Omega) = Lh(\Omega) + \delta\hat{x}(\Omega)$. The radiation pressure noise for a single arm of this interferometer has a form analogous to 1.50, except with the following substitutions

$$M \to M/2, \qquad P \to 4P/T, \qquad a_1 \to a_1 \frac{\sqrt{T}}{(2L/c)(\gamma - i\Omega)} \tag{1.67}$$

These substitutions correspond to replacing the end mirror mass by the reduced mass (both the input and end test masses experience a radiation pressure force) and accounting for the resonant enhancement of both the carrier and sideband fields. At the interferometer output, the radiation pressure noise term is then

$$\delta\hat{x} = \frac{4\sqrt{2P\hbar\omega_0}a_1}{m\Omega^2 L(\gamma - i\Omega)} = \sqrt{\mathcal{K}/2}Lh_{SQL}a_1 e^{i\beta} \tag{1.68}$$

where we have redefined the radiation pressure coupling constant and the free mass standard quantum limit as

$$\mathcal{K}(\Omega) = \frac{8\omega_0 P}{Mc^2\Omega^2}\frac{16}{T^2(1 + (\Omega/\gamma)^2)}, \qquad h_{SQL} = \sqrt{\frac{8\hbar}{M\Omega^2 L^2}} \tag{1.69}$$

Note that the radiation pressure coupling coefficient scales with the power gain of the cavity squared $(4/T)^2$. This is because both the incident fields which drive the mirror motion and the resulting modulation sidebands are resonantly enhanced. The following expression of $\mathcal{K}(\Omega)$ is also common and will prove useful in the following section

$$\mathcal{K}(\Omega) = \frac{8\omega_0 P_{circ}}{mLc}\frac{2\gamma}{\Omega^2(\Omega^2 + \gamma^2)} \tag{1.70}$$

Where $P_{circ} = 2P/T$ is the power circulating in the arm cavities. The standard quantum limit ($\mathcal{K}(\Omega) = 1$) is achieved at a single frequency for a given level of input power

$$\Omega^2_{SQL}(P) = \gamma^2 \frac{\sqrt{1 + 4(\Omega_c/\gamma)^2} - 1}{2} \tag{1.71}$$

where we've defined the following characteristic frequency $\Omega_c = \frac{8}{c}\sqrt{\frac{\omega_0 P_{circ}}{mT}}$. For input powers such that $\gamma \gg \Omega_c$, we find that $\Omega_{SQL} \approx \Omega_c$.

Plugging these expressions back into Equation 1.65 we arrive at the final form for

the output quadratures of a Fabry-Perot Michelson interferometer

$$b_1 = a_1 e^{2i\beta} \tag{1.72}$$

$$b_2 = (a_2 - \mathcal{K} a_1) e^{2i\beta} + \sqrt{2\kappa} \frac{h}{h_{SQL}} e^{i\beta} \tag{1.73}$$

1.2.3 Quantum noise in Advanced LIGO

Building on the previous section, we will now derive the quantum noise for Advanced LIGO. Advanced LIGO also employs power and signal recycling [72] in order to further enhance the quantum noise performance. Power recycling is achieved by adding an additional mirror at the symmetric port which forms an impedance matched cavity with the rest of the interferometer. This recirculates all optical power rather than directing it back towards the laser until it is eventually dissipated in the interferometer through losses. Power recycling effectively boosts the input power of the interferometer, but otherwise leaves the interferometers quantum noise input/output relations unchanged.

With Advanced LIGO, a type of signal recycling known as resonant sideband extraction is utilized. An additional signal recycling mirror (SRM) at the anti-symmetric output of the Michelson is used to effectively lower the arm cavity finesse for gravitational wave signals and thereby maintain a broad detector frequency response. A general discussion of the quantum noise performance of signal recycled interferometers can be found in a series of papers by Buonanno and Chen [17–20] (I recommend starting with [17] which is a synopsis of the other three papers). Here, we follow the derivation in [18], but will make several simplifications along the way to restrict ourselves the particular type of signal recycling used in Advanced LIGO.

The interferometer setup is shown in Fig. 1-5. As in the previous section, a and b are the input and output fields at the anti-symmetric port of the Michelson. Since the response of the rest of the instrument remains unchanged, their relation to one another is still given by 1.72 and 1.73. Four additional fields have been added at

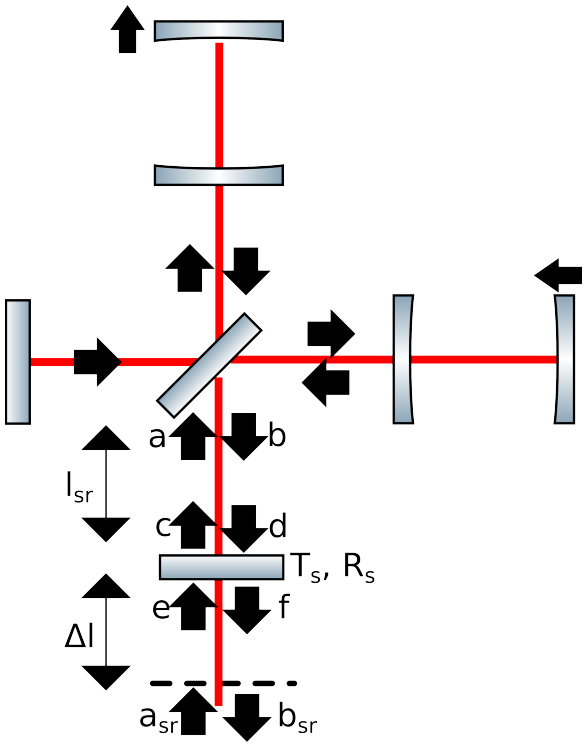

Figure 1-5: Dually recycled Fabrey-Perot Michelson interferometer (the topology used for Advanced LIGO). This is identical to the Fabry-Perot Michelson shown in Figure 1-4 with additional of signal and power recycling cavities. The relation between the fields a and b are identical to those derived in the previous section. The additonal fields on both sides of the signal recycling mirror are also shown. The input and output fields a_{sr} and b_{sr} are defined a distance Δl from the signal recycling mirror so that the output signal will still show up in the phase quadrature.

the interface created by the signal recycling mirror which has reflectivity R_s and transmission T_s. As in the previous section, we will ignore other sources of loss. For resonant sideband extraction, the length between the SRM and the beamsplitter is chosen such that $[\omega_0 l/c]_{Mod2\pi} = \pi/2$. This gives rise to the following relations when the fields are propagated across the signal recycling cavity length l

$$d_1 = -b_2, \;\; d_2 = b_1, \;\; c_1 = a_2, \;\; c_2 = -a_1 \tag{1.74}$$

where we have ignored the frequency dispersion of the signal recycling cavity for the sideband. The interface equations at the SRM are given by

$$c_1 = \sqrt{T_s}e_1 + \sqrt{R_s}d_1,\ c_2 = \sqrt{T_s}e_2 + \sqrt{R_s}d_2, \tag{1.75}$$

$$f_1 = \sqrt{T_s}d_1 + \sqrt{R_s}e_1,\ f_2 = \sqrt{T_s}d_2 + \sqrt{R_s}e_2 \tag{1.76}$$

In order to be consistent with the notation used later in this thesis, we define the input and output fields at a distance Δl away from the SRM such that $[\omega_0 \Delta l/c]_{mod2\pi} = \pi/2$ so that the signal will appear in the phase quadrature as before

$$e_1 = -a_{2,sr},\ \ e_2 = a_{1,sr},\ \ b_{1,sr} = f_2,\ \ b_{2,sr} = -f_1 \tag{1.77}$$

By combining these relations with Equations 1.72 and 1.73, we can solve this system of equations to derive the input/output relations for the whole interferometer. The math is quite tedious and provides limited physical insight, so I will just quote the result

$$\begin{pmatrix} b_{1,sr} \\ b_{2,sr} \end{pmatrix} = \frac{1}{M}\left[e^{2i\beta} \begin{pmatrix} C_{11} & C_{12} \\ C_{21} & C_{22} \end{pmatrix} \begin{pmatrix} a_{1,sr} \\ a_{2,sr} \end{pmatrix} + \sqrt{2\kappa T_s} e^{i\beta} \begin{pmatrix} D_1 \\ D_2 \end{pmatrix} \frac{h}{h_{SQL}} \right] \tag{1.78}$$

where

$$M = 1 + R_s e^{4i\beta} + 2\sqrt{R_s} e^{2i\beta} \tag{1.79}$$

$$C_{11} = C_{22} = 1 + R_s + 2\sqrt{R_s}\cos(2\beta) \tag{1.80}$$

$$C_{12} = 0, \qquad C_{21} = -T_s\kappa \tag{1.81}$$

$$D_1 = 0, \qquad D_2 = 1 + \sqrt{R_s} e^{2i\beta} \tag{1.82}$$

These are the correct input/output expressions[2]. However, at this point, one typically

[2]One should note that when the signal recycling cavity is detuned, the resulting optical spring gives rise to a parametric instability. This shows up in the more general form of Equation1.78 as roots of the equation M(Ω) = 0 which lie in the upper half complex plane. In this case, a renormalization of M is required. This is achieved by adding a suitable control system to counter these optomechanical instabilities. This is discussed in detail in Reference [19]. This is but one example of the interesting physics associated with detuned signal recycling cavities. However, there

expands the resulting expression in powers of T_s to express Equation 1.78 in a simpler form. To avoid going through this in detail, I will substitute M with the following magic value which converges to Equation 1.79 in the limit $T_s \ll 1$.

$$M \rightarrow \left(1 + R_s + 2\sqrt{R_s}\cos(2\beta)\right) e^{2i(\beta-\beta_{sr})} \tag{1.83}$$

This substitution [3], along with the handy identity $e^{2i\beta} = \frac{\gamma+i\Omega}{\gamma-i\Omega}$, allows us to put 1.78 into a form analogous to 1.72 and 1.73.

$$b_{1,sr} = a_{1,sr} e^{2i\beta_{sr}} \tag{1.84}$$

$$b_{2,sr} = (a_{2,sr} - \mathcal{K}_{sr} a_{1,sr}) e^{2i\beta_{sr}} + \sqrt{2\kappa_{sr}} \frac{h}{h_{SQL}} e^{i\beta_{sr}} \tag{1.85}$$

where we have defined

$$\beta_{sr} = \frac{\Omega}{\gamma_{sr}}, \;\; \gamma_{sr} = \frac{1+\sqrt{R_s}}{1-\sqrt{R_s}}\gamma, \;\; \mathcal{K}_{sr}(\Omega) = \frac{\mathcal{K}T_s}{1 + R_s + 2\sqrt{R_s}\cos(2\beta)} \tag{1.86}$$

It can be shown [20] that $\mathcal{K}_{sr}$ may also be expressed as

$$\mathcal{K}_{sr}(\Omega) = \frac{8\omega_0 P_{circ}}{mLc} \frac{2\gamma_{sr}}{\Omega^2(\Omega^2 + \gamma_{sr}^2)} \tag{1.87}$$

Note that this form is identical to that given in Equation 1.70 for a conventional Fabry-Perot Michelson interferometer, except that the addition of a signal extraction mirror effectively increases the linewidth of the arm cavities (though $P_{circ} = 2P/T$ still depends on the actual cavity linewidth). As always, the strain spectral density of the quantum noise is given by

is currently no plan to operate Advanced LIGO with detuned signal recycling, so we will not delve further into these details in this thesis.

[3] Two key differences from the derivation in [18] lead to the simplified form in 1.84 and 1.85. These differences are given in Eqns. 1.83 and 1.77. This simplified expression is given in Equation 30 of Reference [20]. The derivation there is more rigorous but is, in my opinion, far more esoteric.

$$h_q(\Omega) = \frac{h_{SQL}}{\sqrt{2}}\sqrt{\frac{1}{\mathcal{K}_{sr}} + \mathcal{K}_{sr}} \tag{1.88}$$

We may also derive an expression for Ω_{SQL} which is analogous to 1.71

$$\Omega^2_{SQL,sr}(P_{circ}) = \gamma^2 \frac{\sqrt{1 + 4(\Omega_{c,sr}/\gamma)^2} - 1}{2} \tag{1.89}$$

where $\Omega^2_{c,sr} = \frac{1-\sqrt{R_{sr}}}{1+\sqrt{R_{sr}}}\Omega^2_c$. As shown in Table 1.1, $\Omega_{SQL,sr} \ll \gamma_{sr}$ for Advanced LIGO. In this limit, $\Omega_{SQL,sr} \approx \Omega_{c,sr}$. In this limit one may also show that, for $\Omega \approx \Omega_{SQL,sr}$, $\mathcal{K}(\Omega) \approx \left(\frac{\Omega_{SQL,sr}}{\Omega}\right)^2$. As we will discuss in Chapter 3, these simplified expressions will allow us to implement frequency-dependent squeezing for Advanced LIGO using a single filter cavity.

1.2.4 Quantum noise convention for DC readout

Current gravitational wave detectors use a detection scheme known as DC readout [46] where a small differential detuning is introduced in the differential arm length degree-of-freedom (known as DARM) so that the interferometer is no longer locked on a dark fringe. This allows for a small amount of carrier light to exit the interferometer for use as a local oscillator field. A schematic showing the input and output fields for DC readout in Advanced LIGO is shown in Figure 1-6. We will represent the small DARM detuning by opposing phase shifts on the two arms of $e^{\pm i\phi(\Omega)}$ where $\phi(\Omega) \ll 1$. We can write the new output fields $b_{DC}(\Omega)$ and D_{DC} in terms of the un-detuned output b, incoming fluctuations from the symmetric port d, and a classical carrier term entering from the symmetric port with amplitude D_{LO}.

$$b_{DC,+} = b_+(\Omega)\frac{e^{i\phi} + e^{-i\phi}}{2} + a_+\frac{e^{i\phi} - e^{-i\phi}}{2} \approx b_+ \tag{1.90}$$

$$D_{DC} = D_{LO}\frac{e^{i\phi_0} - e^{-i\phi_0}}{2} = \sin\phi_0 e^{i\pi/2} D_{LO} \tag{1.91}$$

where $\phi_0 = \phi(\Omega = 0)$. Here, I neglect the fluctuations entering from the symmetric port for simplicity and I've used the fact that $i = e^{i\pi/2}$ to show that the output carrier

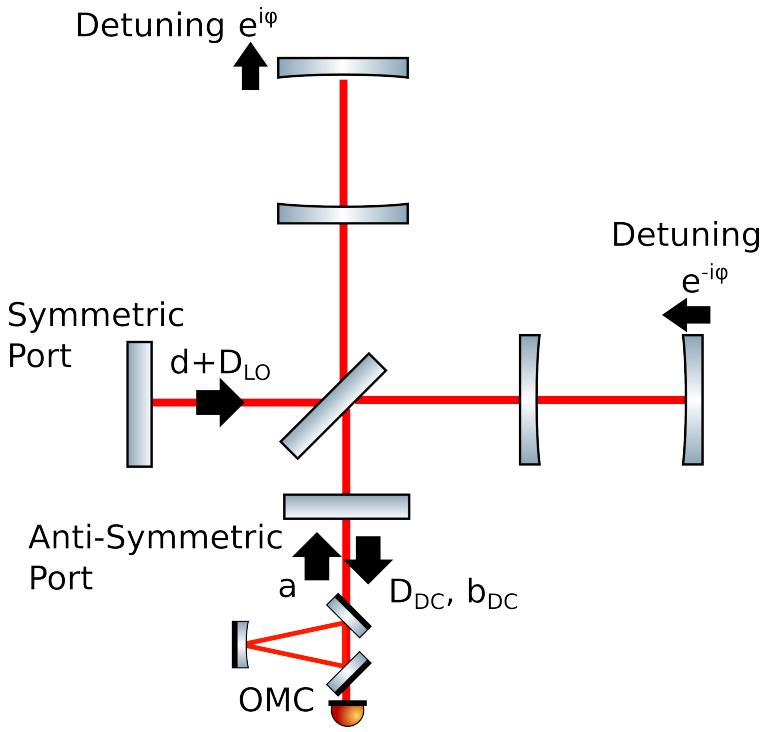

Figure 1-6: Input and Output fields for DC readout. The interferometer differential degree of freedom is detuned such that a fraction of DC carrier field at the input (D_{LO}) shows up in the output field (D_{dc}). An output mode cleaner (OMC) is used to spatially the output field.

field has picked up a 90^{deg} phase shift. The signal from the photodiode is proportional to

$$b_{DC,+}D^*_{DC} + D_{DC}b^\dagger_{DC-} = \sin\phi_0 D_{LO}(b_+ e^{-i\pi/2} + b^\dagger_- e^{i\pi/2}) = D_{LO}\sin\phi_0\, b_2 \qquad (1.92)$$

We see that this readout scheme still allows us to measure the signal quadrature b_2. However, because the portion of the carrier which doesn't cancel at the AS port has a phase shift of $\pi/2$, the b_2 field now shows up as amplitude fluctuations on the output carrier field. For this reason, when squeezing shot noise in an interferometer using DC readout, one is technically squeezing the amplitude quadrature of the output field even though the shot noise term in b_2 is due to a_2.[4]

[4]Strictly speaking, our designation of a_2 as the "phase quadrature" of the field entering from the AS port is physically meaningless when no carrier field is present. A squeezed vacuum state on its own does not have a well defined phase and therefore does not have well defined "in-phase"

I have always found this to be a bit counter-intuitive, since this convention means the radiation pressure noise gets worse when we squeeze the amplitude quadrature. This mystery is resolved when one notes that the carrier field in the arms of the interferometer does not have the $\pi/2$ phase shift acquired by the local oscillator field at the output. With respect to the arm cavity field, the quadrature field a_1 which gives rise to radiation pressure noise still corresponds to vacuum fluctuations in the amplitude quadrature as one would expect. Likewise, squeezing the shot noise still corresponds to squeezing the phase quadrature of the field in the interferometer arms. When we discuss frequency-dependent squeezed light later in this thesis, I will choose to define my quadratures in terms of the carrier field circulating in the Michelson and arm cavities rather than in terms of the output field. This is a bit unconventional within the gravitational wave community, but I find it to be more intuitive.

With this reasoning in mind, I will now specify the following value for the mean phase of the interferometer field at the antisymmetric port which will be used for the remainder of this thesis:

$$\theta_{ifo} = \pi/2 \tag{1.93}$$

1.3 Reducing quantum noise in Advanced LIGO

Given available technology and the various classical noise sources shown in Figure 1-2, one can choose an interferometer design to optimize the quantum noise performance as much as possible. Advanced LIGO is now reaching the limits of this classical optimization. At this point, the injection of squeezed vacuum into the interferometer output port becomes desirable to achieve a further reduction in quantum noise

1.3.1 Classical optimization

From Equations 1.87 and 1.88, we see that radiation pressure noise scales inversely with the test mirror mass and as the square root of the circulating power in the arm

quadrature.

Table 1.1: Symbols and values for aLIGO interferometer parameters.

Parameter	Symbol	Value
Frequency of the carrier field	ω_0	$2\pi\times$ 282 THz
Arm cavity length	L	3995 m
Signal recycling cavity length	$l_{\rm sr}$	55 m
Arm cavity half-width	γ	$2\pi \times 42$ Hz
Arm cavity input mirror power transmissivity	T	1.4 %
Signal recycling mirror power transmissivity	$T_{\rm s}$	35 %
Bandwidth	γ_{sr}	$2\pi \times 390$ Hz
SQL Frequency	Ω_{SQL}	$2\pi \times 70$ Hz
Intra-cavity power	$P_{\rm circ}$	800 kW
Mass of each of the test mass mirror	m	40 kg

cavities. Shot noise decreases as $1/P_{circ}$. The dominant source of classical noise below 100 Hz is thermal noise. With this in mind, one may do the following to optimise the sensitivity of the interferometer:

- Use as large of mirror mass as possible to suppress radiation pressure noise.
- Increase the circulating power until radiation pressure noise is roughly equal to thermal noise at low frequencies.
- Boost the circulating power using resonant arm cavities and power recycling.
- Use signal recycling to maintain a large detector bandwidth despite increasing the finesse of the arm cavities.

The instrument parameters Advanced LIGO are given in table 1.1. Currently, Advanced LIGO is using test masses within a factor of 2 of the largest which are commercially available. At full power, Advanced LIGO is anticipated to have roughly 800 kW circulating in the arm cavities and radiation pressure noise will be roughly equal to thermal noise below 50 Hz. However, reaching this level of circulating power will present significant technical challenges.

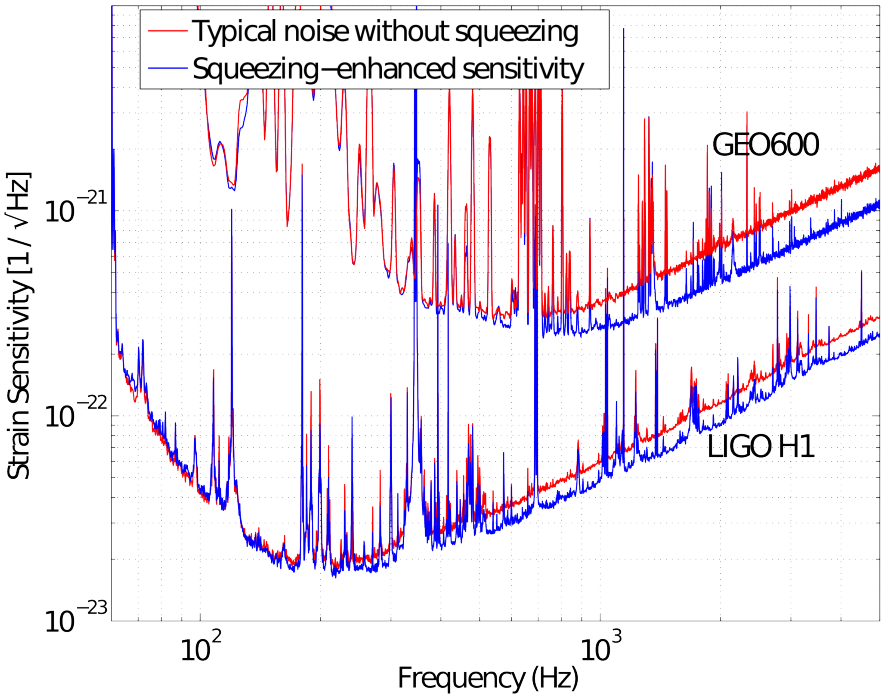

Figure 1-7: First demonstration of squeezing enhancement at GEO 600 [101] and LIGO Hanford Observatory [102]. Figure adapted from Reference [67]

1.3.2 Quantum enhancement

In 1981 Caves proposed the injection of squeezed vacuum, in place of coherent fluctuations, in order to reduce high-frequency shot noise in gravitational wave interferometers [22]. This idea came to fruition only in the current decade with successful demonstrations at the GEO600 and LIGO Hanford detectors [101, 102], proving that squeezed-light injection could be performed without degrading the exquisite low-frequency sensitivity of these instruments. The improved sensitivity of both detectors is shown in Figure 1-7.

Today, squeezed vacuum sources offer squeezing magnitudes of more than 10 dB (corresponding to approximately a 3-fold reduction in noise amplitude) and, critically, maintain this performance down to 10 Hz [73, 99]. Additionally, a squeezed vacuum source is permanently installed at GEO600, enabling investigations of long-term robustness [52] and the evaluation of different control schemes [35].

Building on this foundation, it is possible to utilize this technique to mitigate

quantum noise in current kilometer-scale gravitational wave interferometers such as Advanced LIGO. However, as we will discuss in Chapter 3, a simple frequency-independent squeezed vacuum source is not sufficient for the present generation of detectors [42]. To realize broadband noise reduction one must rotate the squeezed quadrature as a function of frequency in order to counter the rotation effected by the optomechanical coupling between the interferometer's 40 kg mirrors and the nearly 1 MW of circulating laser light [18]. The first demonstration of this frequency-dependent squeezing technique at frequencies relevant to gravitational wave detectors will be discussed extensively in Chapters 5 and 6.

1.4 Overview

For the remainder of this thesis, we detail how one can achieve a broadband reduction in quantum noise for Advanced LIGO using squeezed states of light. My thesis work has focused on producing a suitable squeezed light source to meet the needs of Advanced LIGO. In Chapter 2, we discuss some of the background theory concerning the generation and use of squeezed vacuum states. In Chapter 3, I'll outline the technical requirements for adding squeezing to Advanced LIGO and propose a suitable design. This design features two new components not present in the GEO and Initial LIGO squeezing demonstrations. First, we move a large portion into the Advanced LIGO vacuum envelope to address some technical deficiencies of previous designs. Secondly, we will use a technique known as *frequency-dependent squeezing* to simultaneously reduce radiation pressure noise and shot noise. Chapter 4 discusses the in-vacuum squeezed light source and its improved performance. Chapter 5 introduces our theoretical model for a realistic filter cavity which one could use to produce frequency-dependent squeezing for Advanced LIGO. Chapter 6 discusses our prototype frequency-dependent squeezed light source and the first demonstration of frequency-dependent squeezing in the audio band. Finally, I'll conclude with a discussion of the advanced LIGO squeezed light source design in Chapter 7, which incorporates lessons learned from the prototype experiments.

Chapter 2

Generating, measuring, and controlling squeezed vacuum States

2.1 Introduction

We now turn to a discussion of how to generate the squeezed vacuum states required to reduce quantum noise in Advanced LIGO. This chapter will work through the theory behind generating squeezed vacuum via parametric downconversion. With the addition of frequency-dependent squeezing for the Advanced LIGO, there is quite a bit of additional theory that must be discussed in this thesis. I will choose to present these new aspects in greater detail. The discussion on generating frequency *independent* squeezing in this chapter will be a bit more succinct to compensate for this. The reader who is looking for additional detail on the derivations is referred to previous theses on this topic [36, 50].

2.2 Second order nonlinear processes

There are numerous methods for generating squeezed states of light. In this thesis, we will limit the focus to generating squeezed vacuum via parametric down-conversion using a nonlinear crystal with a strong second order nonlinearity $\chi^{(2)}$. This is by far the most technologically mature method of squeezed light generation and is the

preferred means of producing squeezed vacuum in the GW band. Driving nonlinear materials induces the following time varying polarization

$$\vec{P} = \epsilon_0 \left(\chi^{(1)} \vec{E} + \chi^{(2)} \vec{E}^2 + ... \right) \tag{2.1}$$

In the classical picture, this produces an oscillating dipole which will re-radiate. Due to the quadratic dependence on $\vec{E}$, the resulting field can depend on an incident field with components at multiple frequencies. Here, we will denote the field at the fundamental (interferometer input laser) frequency by ω_0 (which is associated with an annihilation operator a) and the second harmonic frequency by $2\omega_0$ (annihilation operator b). To generate squeezed vacuum, we will utilize two nonlinear processes that rely on $\chi^{(2)}$. We use second harmonic generation to convert two photons at the fundamental frequency into a single photon at the second harmonic frequency. This field is then used to pump an optical parametric oscillator (OPO) cavity, where second harmonic photons are converted into two correlated squeezed vacuum photons at the fundamental frequency.

2.3 Ideal squeezed vacuum source

When optical losses are ignored, a degenerate OPO cavity is described by the following Hamiltonian [1].

$$H_{cav} = \hbar\omega_0 a^\dagger a + 2\hbar\omega_0 b^\dagger b + \frac{i\hbar}{2} \left(\epsilon a^{\dagger 2} b - \epsilon^* a^2 b^\dagger \right) \tag{2.2}$$

Here ϵ is a nonlinear coupling parameter that is purely real when the cavity is properly phase matched (a concept which will be defined shortly). Along with the free field terms, there is an interaction term which corresponds to nonlinear processes where photons are created or destroyed two at a time. In this thesis we will always assume

[1] Strictly speaking the OPO cavity does not create two photons at the same frequency but rather a pair at sideband frequencies of $\omega_0 \pm \Omega$. We will suppress this detail for now since this distinction will not be critical until the next section. For a rigorous treatment that includes all frequency dependencies see Chapter 2 of Reference [50]

that the pump field has a large and constant DC amplitude, which we will represent by substituting $b \rightarrow \beta \mathrm{e}^{i\theta_B}$. Also, for now we assume that we have perfect phase matching so that ϵ is purely real. We may then make the following simplification to the Hamiltonian:

$$H_{cav} = \hbar\omega_0 a^\dagger a + \frac{i\epsilon\hbar}{2}\left(\beta e^{i(\theta_B+2\omega_0 t)}a^{\dagger 2} - \beta e^{-i(\theta_B+2\omega_0 t)}a^2\right) \tag{2.3}$$

Moving into the interaction picture, where we remove the free field term and rewrite $a \rightarrow e^{i\omega_0 t}a$, we get the following time evolution operator:

$$\hat{U} = e^{-iH_{int}t/\hbar} = exp\left(\frac{\epsilon\beta\mathrm{e}^{i\theta_B}ta^{\dagger 2} - \epsilon\beta\mathrm{e}^{-i\theta_B}ta^2}{2}\right) \tag{2.4}$$

We see that $U(t)$ is just the squeezing operator given in Equation 1.34 where $r = \epsilon\beta t$ is the squeezing factor expressed in terms of the system parameters. Therefore, this lossless OPO will generate the squeezed states described in Section 1.3.5.

2.4 Equations of motion for a realistic OPO

The description of the lossless OPO given in the previous section leads to a tidy equation of motion. However, any description of a real OPO cavity must account for the effects of damping due to optical loss. Even if we assume that the process of generating squeezing is completely lossless, we at least need one of the mirrors to have finite transmission to get the squeezing out of the cavity!

There are several popular formalisms for dealing with damping in quantum systems. The most widely used formalism in the squeezed light community is Heisenberg-Langevin approach developed by Collet and Gardiner [31, 49]. We now derive the equations of motion for an OPO cavity. We will make some simplifying assumptions along the way, but keep the derivation general enough to allow us to use these expressions in Appendix A to describe the performance of the OPO in the presence of length, frequency, and temperature fluctuations. The derivation follows that given in [36].

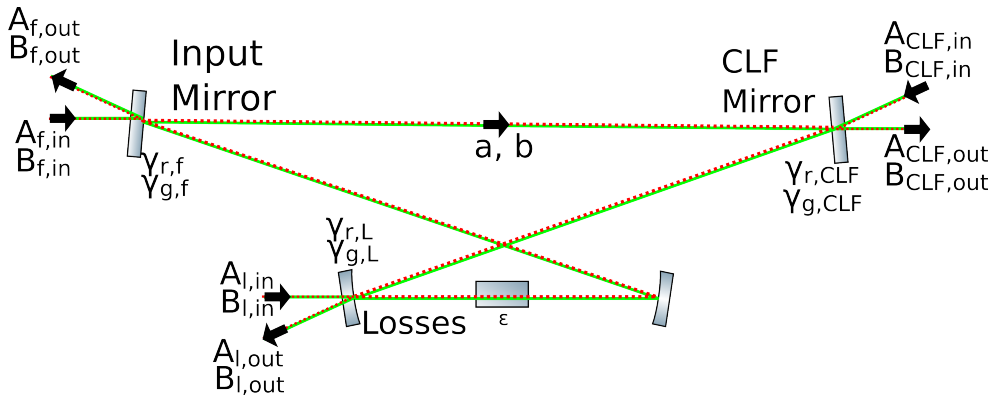

Figure 2-1: Model of an OPO cavity with loss. The input coupler (denoted by subscript f) and rear (subscript CLF) coupler are shown along with their incident and reflected fields and their loss rates due to transmission. The intra-cavity losses are represented by a third mirror (subscript l) whose effective transmission accounts for these losses. In this model, the fourth mirror and the nonlinear crystal are assumed to be lossless. The mirror loss rates γ are given for both the fundamental (subscript r) and second harmonic (subscript g) frequencies.

2.4.1 The Hamiltonian with losses

The total Hamiltonian for the OPO cavity depicted in Figure 2-1 is given by:

$$H = H_{cav} + \sum_j H^j_{bath} + \sum_j H^j_{int} \tag{2.5}$$

The sum in Equation 2.5 is taken over all of the mirrors in the cavity. The two flat mirrors represent the input coupler (whose transmission at the fundamental wavelength will be denoted by $T_{f,r}$) and the rear mirror ($T_{CLF,r}$) whose naming convention will become apparent when we introduce the control scheme for the squeezed light source later on. The two curved mirrors are two high-reflectivity (HR) mirrors, though one will have an effective transmission that is equal to the intra-cavity losses ($T_{l,r}$). H^j_{bath} is the Hamiltonian for all external modes which couple into the cavity through mirror j

$$H^j_{bath} = \int_{-\infty}^{\infty} \hbar\omega_0 A^\dagger_j(\Omega) A_j(\Omega) + 2\hbar\omega_0 B^\dagger_j(\Omega) B_j(\Omega) d\Omega \tag{2.6}$$

where A_j and B_j represent the fields associated with mirror j and are given in units

of $\sqrt{\text{photons/Hz}}$ at the fundamental and second harmonic frequencies respectively. H^j_{int} is given by

$$H^j_{int} = i\hbar \int_{-\infty}^{\infty} \sqrt{2\gamma^j_r}[A_j(\Omega)^\dagger a(\Omega) - a^\dagger(\Omega)A_j(\Omega)] + \sqrt{2\gamma^j_g}[B_j(\Omega)^\dagger b(\Omega) - b^\dagger(\Omega)B_j(\Omega)]d\Omega \tag{2.7}$$

where $\gamma^j_r = (1 - \sqrt{R_{r,j}})/\tau$ is the field decay rate due to the transmission of mirror j at the fundamental frequency (likewise for γ^j_b) and $\tau = L/c$ is the cavity round trip time. At this time I will also introduce the total cavity loss rates $\gamma^{tot}_{r,g} = \sum_j \gamma^j_{r,g}$ which correspond to the cavity HWHM frequencies in angular frequency units for the fundamental and pump fields, respectively.

2.4.2 The equations of motion

Using the Hamiltonian presented in the previous section, we may compute the Heisenberg equations of motion for the field operators

$$\dot{a}(t) = -\left(\gamma^{tot}_r + i\omega_r\right) a(t) + \epsilon a^\dagger(t)b(t) + \sum_j \sqrt{2\gamma^j_r} A_{in,j}(t) \tag{2.8}$$

$$\dot{b}(t) = -\left(\gamma^{tot}_g + i\omega_g\right) b(t) - \frac{\epsilon^*}{2}a(t)^2 + \sum_j \sqrt{2\gamma^j_g} B_{in,j}(t) \tag{2.9}$$

where we've introduced the cavity resonance frequencies $\omega_{r,g}$ which may differ slightly from the fundamental and pump frequencies. We then transform into the rotating frame and rewrite the above expressions in terms of the detuning from resonance ($\Delta_r = \omega_0 - \omega_r$ and $\Delta_g = 2\omega_0 - \omega_g$).

$$\dot{a}(t) = -\left(\gamma_r^{tot} - i\Delta_r\right) a(t) + \epsilon a^\dagger(t) b(t) + \sum_j \sqrt{2\gamma_r^j} A_{in,j}(t) \tag{2.10}$$

$$\dot{b}(t) = -\left(\gamma_g^{tot} - i\Delta_g\right) b(t) - \frac{\epsilon^*}{2} a(t)^2 + \sum_j \sqrt{2\gamma_g^j} B_{in,j}(t) \tag{2.11}$$

From the Hamiltonian one may also derive the following boundary conditions at each mirror known as the input/output relations [31]

$$\sqrt{2\gamma_r^j} a(t) = A_{j,out}(t) + A_{j,in}(t) \tag{2.12}$$

with similar equations for the second harmonic fields. At this point, it is useful to express all of the relevant fields in terms of some constant coherent amplitude plus a fluctuation term which can be either quantum or classical in origin

$$a(t) = \bar{a} + \delta a(t), \;\; b(t) = \bar{b} + \delta b(t), \;\; A_j(t) = \bar{A}_j + \delta A_j(t), \;\; B_j(t) = \bar{B}_j + \delta B_j(t) \tag{2.13}$$

Any field at the fundamental frequency with a nonzero DC component is typically referred to as a *seed* field. Here, we assume that all fields at the fundamental frequency have no DC amplitude $\bar{a} = \bar{A}_j = 0$ and that their fluctuating terms are purely quantum mechanical in origin.[2] This is always the case when generating squeezed *vacuum*, which is required for the application since a seed field can add technical noise in the GW band which can degrade the squeezing [71]. We also assume that the pump field is large and constant ($\delta b(t) = 0$), allowing us to set the left hand side of Equation 2.11 equal to zero. These assumptions also allow us to neglect terms like $a(t)^2$ and $\delta B_j(t)$. These assumptions are known as the parametric approximation or the un-depleted pump approximation. We can then solve Equation 2.11 for the circulating pump power.

[2] As we shall discuss in Chapter 4, $A_{CLF,in}(t)$ can have a nonzero DC amplitude and classical noise terms. This gives rise to additional noise couplings which can degrade the squeezing at low measurement frequencies if the seed field is large enough

$$\bar{b} = \frac{\sqrt{2\gamma_g^f}\bar{B}_{in,f}}{\gamma_r^{tot} - i\Delta_g} \tag{2.14}$$

For the remainder of this section, we will express Equation 2.14 as:

$$\bar{b} \to \frac{\beta e^{i\theta_B}}{1 - i\Delta_g/\gamma_g^{tot}} \tag{2.15}$$

We now Fourier transform Equation 2.10 and its complex conjugate to express the cavity equations in the sideband picture

$$i\Omega\delta\mathbf{a}(\Omega) = \gamma_r^{tot}\mathbf{M}\delta\mathbf{a}(\Omega) + \sqrt{2\gamma_r^l}\delta\mathbf{A}_{l,in}(\Omega) + \sqrt{2\gamma_r^f}\mathbf{A}_{f,in}(\Omega) + \sqrt{2\gamma_r^{CLF}}\mathbf{A}_{CLF,in}(\Omega) \tag{2.16}$$

where the matrix for a is given by

$$\delta\mathbf{a}(\Omega) = \begin{pmatrix} \delta a_+ \\ \delta a_-^\dagger \end{pmatrix} \tag{2.17}$$

with similar expressions for the incident field matrices. Here, we are using the sideband field naming convention introduced in Equation 1.17 as well as the convention for the Fourier transform $[a(t)]^\dagger \to a_-^\dagger$. The matrix M is given by

$$\mathbf{M} = \begin{pmatrix} -1 + i\frac{\Delta_r}{\gamma_r^{tot}} & \frac{\epsilon\beta e^{i\theta_B}}{\gamma_r^{tot}(1 - i\Delta_g/\gamma_g^{tot})} \\ \frac{\epsilon^*\beta e^{-i\theta_B}}{\gamma_r^{tot}(1 + i\Delta_g/\gamma_g^{tot})} & -1 - i\frac{\Delta_r}{\gamma_r^{tot}} \end{pmatrix} \tag{2.18}$$

The non-zero off diagonal elements create correlations between the upper and lower sideband operators and are responsible for generating squeezing. Using Equation 2.16 we can solve for the intra cavity field

$$\delta\mathbf{a}(\Omega) = \left(i\Omega\mathbf{I} - \gamma_r^{tot}\mathbf{M}\right)^{-1}\left[\sqrt{2\gamma_r^l}\delta\mathbf{A}_{l,in}(\Omega) + \sqrt{2\gamma_r^{CLF}}\delta\mathbf{A}_{CLF,in}(\Omega) + \sqrt{2\gamma_r^f}\delta\mathbf{A}_{f,in}(\Omega)\right] \quad (2.19)$$

and plug this expression into the input/output relation given in Equation 2.12 to solve for the exiting field

$$\begin{aligned}\delta\mathbf{A}_{f,out}(\Omega) &= \sqrt{2\gamma_r^f}\delta\mathbf{a}(\Omega) - \delta\mathbf{A}_{f,in}(\Omega)\\ &= \left(2\gamma_r^f(i\Omega\mathbf{I} - \gamma_r^{tot}\mathbf{M})^{-1} - \mathbf{I}\right)\delta\mathbf{A}_{f,in}(\Omega)\\ &+ 2\sqrt{\gamma_r^l\gamma_r^f}\left(i\Omega\mathbf{I} - \gamma_r^{tot}\mathbf{M}\right)^{-1}\delta\mathbf{A}_{l,in}(\Omega)\\ &+ 2\sqrt{\gamma_r^{CLF}\gamma_r^f}\left(i\Omega\mathbf{I} - \gamma_r^{tot}\mathbf{M}\right)^{-1}\delta\mathbf{A}_{CLF,in}(\Omega)\end{aligned} \quad (2.20)$$

2.4.3 Output quadrature fields and their variance

At last, we arrive at the equations for the output field in the quadrature picture:

$$\begin{aligned}\delta\mathbf{X}_{out}^f(\Omega) &= \left(2\gamma_r^f(i\Omega\mathbf{I} - \gamma_r^{tot}\Gamma\mathbf{M}\Gamma^{-1})^{-1} - \mathbf{I}\right)\delta\mathbf{X}_{in}^f(\Omega)\\ &+ 2\sqrt{\gamma_r^f\gamma_r^{CLF}}(i\Omega\mathbf{I} - \gamma_r^{tot}\Gamma\mathbf{M}\Gamma^{-1})^{-1}\delta\mathbf{X}_{in}^{CLF}(\Omega)\\ &+ 2\sqrt{\gamma_r^f\gamma_r^l}(i\Omega\mathbf{I} - \gamma_r^{tot}\Gamma\mathbf{M}\Gamma^{-1})^{-1}\delta\mathbf{X}_{in}^{l}(\Omega)\end{aligned} \quad (2.21)$$

where

$$\delta\mathbf{X}(\Omega) = \begin{pmatrix}\delta X_1(\Omega)\\ \delta X_2(\Omega)\end{pmatrix} = \sqrt{2}\begin{pmatrix}\delta A_1(\Omega)\\ \delta A_2(\Omega)\end{pmatrix} = \Gamma\delta\mathbf{A}(\Omega) = \begin{pmatrix}1 & 1\\ -i & i\end{pmatrix}\begin{pmatrix}\delta A_+\\ \delta A_-^\dagger\end{pmatrix} \quad (2.22)$$

is the vector of quadrature operators. Here I've scaled the quadrature operators defined in Equations 1.15 and 1.16 so that the quadrature variances for the unsqueezed field will equal 1[3]. I have also introduced the matrix Γ that converts the operators

[3]For some reason, all of the papers on filter cavities and quantum noise with gravitational wave

from the sideband (1-photon) picture to the quadrature (2-photon) picture.

Before expanding out Equation 2.21 and taking the variance, we make a few substitutions and simplifications. First of all we assume that both the fundamental field and pump field are undetuned ($\Delta_r = \Delta_g = 0$) and that the sideband frequencies of interest are small compared to the linewidth ($\Omega/\gamma_r^{tot} << 1$)[4]. Furthermore we will assume that the cavity is perfectly phase matched such that ϵ is real, we then get a simplified form for $\mathbf{M}$

$$\mathbf{M} = \begin{pmatrix} -1 & xe^{i\theta_B} \\ xe^{-i\theta_B} & -1 \end{pmatrix} \tag{2.23}$$

where we have defined the parameter $x = \frac{|\epsilon|\beta}{\gamma_r^{tot}}$ which is known as the normalized nonlinear interaction strength. This is the ratio of the rate at which photons at the fundamental frequency are being generated by the nonlinear process to the rate at which photons leave the cavity due to transmission or loss. If this ratio exceeds 1, a condition known as threshold, then we will build up a coherent amplitude amplitude. The input pump power at which $x = 1$ is achieved is known as the threshold power, and x may also be expressed as $x = \sqrt{\frac{P}{P_{\text{thresh}}}}$. We always operate the OPO below threshold.

Using these simplifications and the fact that the cross spectral density between any two different field operators is zero (ie $\langle 0|\delta X_n^i \delta X_m^{\dagger j}|0\rangle = \delta_{nm}\,\delta_{ij}$), the output quadrature variances are given by [50]

detectors use the normalization given in Chapter 1 which gives quadrature variances of 1/2. Papers on squeezing tend to normalize the quadrature operators as done in Equation 2.22. To get around this, I introduce a new set of operators, X, with $\sqrt{2}$ rescaling which I use for the remainder of the chapter

[4]This typically isn't the case when generating squeezing at RF sideband frequencies, but usually holds when discussing squeezing in the GW band

$$V_1(\Omega) = \left[\frac{2\sqrt{\gamma_r^f\gamma_r^l}}{\gamma_r^{tot}}\frac{1-x\cos(\theta_B)}{1-x^2}\right]^2 V_1^l(\Omega) + \left[\frac{2\sqrt{\gamma_r^f\gamma_r^l}}{\gamma_r^{tot}}\frac{x\sin(\theta_B)}{1-x^2}\right]^2 V_2^l(\Omega)$$
$$+ \left[\frac{2\sqrt{\gamma_r^f\gamma_r^{CLF}}}{\gamma_r^{tot}}\frac{1-x\cos(\theta_B)}{1-x^2}\right]^2 V_1^{CLF}(\Omega) + \left[\frac{2\sqrt{\gamma_r^f\gamma_r^{CLF}}}{\gamma_r^{tot}}\frac{x\sin(\theta_B)}{1-x^2}\right]^2 V_2^{CLF}(\Omega)$$
$$+ \left[\frac{2\gamma_r^f}{\gamma_r^{tot}}\frac{1-x\cos(\theta_B)}{1-x^2} - 1\right]^2 V_1^f(\Omega) + \left[\frac{2\gamma_r^f}{\gamma_r^{tot}}\frac{x\sin(\theta_B)}{1-x^2}\right]^2 V_2^f(\Omega) \tag{2.24}$$

$$V_2(\Omega) = \left[\frac{2\sqrt{\gamma_r^f\gamma_r^l}}{\gamma_r^{tot}}\frac{1+x\cos(\theta_B)}{1-x^2}\right]^2 V_2^l(\Omega) + \left[\frac{2\sqrt{\gamma_r^f\gamma_r^l}}{\gamma_r^{tot}}\frac{x\sin(\theta_B)}{1-x^2}\right]^2 V_1^l(\Omega)$$
$$+ \left[\frac{2\sqrt{\gamma_r^f\gamma_r^{CLF}}}{\gamma_r^{tot}}\frac{1+x\cos(\theta_B)}{1-x^2}\right]^2 V_2^{CLF}(\Omega) + \left[\frac{2\sqrt{\gamma_r^f\gamma_r^{CLF}}}{\gamma_r^{tot}}\frac{x\sin(\theta_B)}{1-x^2}\right]^2 V_1^{CLF}(\Omega)$$
$$+ \left[\frac{2\gamma_r^f}{\gamma_r^{tot}}\frac{1+x\cos(\theta_B)}{1-x^2} - 1\right]^2 V_2^f(\Omega) + \left[\frac{2\gamma_r^f}{\gamma_r^{tot}}\frac{x\sin(\theta_B)}{1-x^2}\right]^2 V_1^f(\Omega) \tag{2.25}$$

where we have defined $V_1^j = \langle 0||\delta X_1^{j,in}|^2|0\rangle$ as the variance of the appropriate input field quadrature operator. Since we have assumed that all incident fields consist of vacuum fluctuations only, we may set all $V_i^j = 1$. This allows us to simplify the expressions greatly

$$\mathbf{V}_{out}(\Omega,\theta_B) = \begin{pmatrix} V_1(\Omega) \\ V_2(\Omega) \end{pmatrix} = \begin{pmatrix} \cos^2(\theta_b/2) & \sin^2(\theta_b/2) \\ \sin^2(\theta_b/2) & \cos^2(\theta_b/2) \end{pmatrix} \begin{pmatrix} V_-(\Omega) \\ V_+(\Omega) \end{pmatrix} \tag{2.26}$$

where

$$V_-(\Omega) = 1 - 4\eta_{esc}\frac{x}{(1+x)^2} \tag{2.27}$$

$$V_+(\Omega) = 1 + 4\eta_{esc}\frac{x}{(1-x)^2} \tag{2.28}$$

are the squeezed and anti-squeezed quadrature variance and $\eta_{esc} = \frac{\gamma_r^f}{\gamma_r^{tot}}$ is known as the escape efficiency. With this convention, amplitude quadrature squeezing corresponds to $\theta_B/2 = 0$ and phase quadrature squeezing corresponds to $\theta_B/2 = \pi/2$. We see that we get the maximum amount of squeezing when the cavity losses are completely dominated by those of the input coupler γ_r^f.

2.4.4 The role of interference and the myth of "perfect squeezing"

Within the LIGO community, there seems to be some confusion concerning the concept of the escape efficiency. I've often heard people say that the intra-cavity field contains "perfect squeezing" (i.e. $V_- \to 0$ as $x \to 1$) and that the escape efficiency η_{esc} indicates the fraction of this perfect state that we're able to extract and use. This view is incorrect and a detailed explanation will provide us with some insight.

Let's begin by examining the quadrature variance of the intra-cavity field. By carrying out an analysis similar to that done for the output field in the previous section, one will arrive at the following equation for the quadrature variance.

$$\begin{pmatrix} V_{c,1}(\Omega) \\ V_{c,2}(\Omega) \end{pmatrix} = \frac{2}{\gamma_r^{tot}} \begin{pmatrix} \frac{1+x^2-2x\cos(\theta_B)}{(1-x)^2(1+x)^2} \\ \frac{1+x^2+2x\cos(\theta_B)}{(1-x)^2(1+x)^2} \end{pmatrix} \tag{2.29}$$

The level of squeezing is given by

$$\frac{V_{1,c}(x, \theta_B = 0)}{V_{1,c}(0, \theta_B = 0)} = \frac{1}{(1+x)^2} \tag{2.30}$$

implying that the maximum level of squeezing which we can attain ($x = 1$) is -3 dB or a 50% reduction in the variance compared to an unsqueezed state [93]. What is going on here? Recall the physical significance of x: it is the ratio of the rate at which squeezed photons are generated to the rate at which light leaves the cavity and is replaced by ordinary vacuum. As we approach threshold ($x \to 1$) these two rates become equal. It makes sense that the field is only half squeezed in this limit.

Since levels of squeezing up to -12.7 dB have been measured [40], clearly the naive

picture that we're extracting a "perfect squeezed state" from the OPO cavity isn't valid. How, then, does one obtain levels of squeezing greater than -3 dB? The answer is that the field leaving the OPO cavity interferes destructively with the promptly reflected vacuum field allowing for higher levels of squeezing. We can see this by examining the fifth term in Equation 2.24 which we rewrite below

$$V_1(\Omega) = ... + \left[\frac{2\gamma_r^f}{\gamma_r^{tot}}\frac{1 - x\cos(\theta_B)}{1 - x^2} - 1\right]^2 V_1^f(\Omega) + ... \tag{2.31}$$

The second term in the bracketed expression corresponds to the promptly reflected field. If we assume that $\eta_{esc} = 1$, all other terms in Equation 2.24 are zero and $\gamma_r^f = \gamma_r^{tot}$. For amplitude quadrature squeezing ($\theta_B = 0$), we see that $V_1 \to 0$ as $x \to 1$ meaning that we get complete destructive interference at the output of the OPO cavity.

The fact that $\langle 0|\delta X_n^i \delta X_m^{\dagger j}|0\rangle = \delta_{nm}\,\delta_{ij}$ implies that the vacuum fields entering the OPO from other open ports are incoherent with the promptly reflected field at the output and will not exhibit the same interference. Even though these fields are squeezed by the OPO, they are still a source of *decoherence* since they do not interfere coherently with the reflected field at the output. Consequently, when $\eta_{esc} < 1$ an infinitely squeezed state at the output is no longer possible.

2.5 Detection of squeezed vacuum states

Squeezed vacuum states offer us a means of enhancing the sensitivity of Advanced LIGO and other precision instruments. However, they are difficult to work with in practice since their carefully created quantum correlations are quite fragile. In the subsections that follow, we introduce the problem of measuring squeezed states. We begin by discussing how optical loss affects the level of measured squeezing. Then we discuss the detection schemes used to measure squeezing with a stand-alone squeezed vacuum source (balanced homodyne detection) and to measure the output of a squeezed light enhanced GW detector (self-homodyne detection or DC readout). In this section, I will drop the explicit time or frequency dependence of the

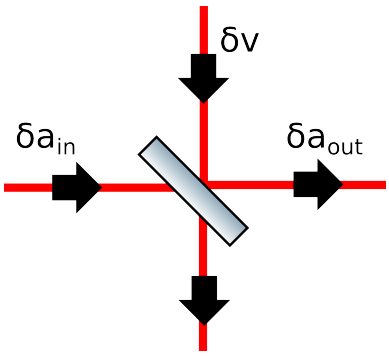

Figure 2-2: Beamsplitter model of loss. A propagation efficiency of η can be modelled as a beamsplitter with power reflectivity $(1-\eta)$ such that $\delta\mathbf{a}_{out} = \sqrt{\eta}\delta\mathbf{a}_{in} + \sqrt{1-\eta}\delta\mathbf{v}$ where $\delta\mathbf{v}$ represents unsqueezed vacuum fluctuations.

field operators and variances. The equations derived here hold for either the time or frequency domain.

2.5.1 Optical loss

Optical loss is the dominant source of decoherence in most squeezing experiments. Any level of loss L can be modeled as a beamsplitter with power reflectivity $\eta_{loss} = 1-L$. This is depicted in Fig. 2-2. From the other port in the beamsplitter, unsqueezed vacuum fluctuations enter to replace the lost portion of the squeezed field. The output field is given by

$$\delta\mathbf{a}_{out} = \sqrt{\eta_{loss}}\delta\mathbf{a}_{in} + \sqrt{1-\eta_{loss}}\delta\mathbf{v} \tag{2.32}$$

We may then calculate the resulting variance

$$\mathbf{V}_{out} = \eta_{loss}\mathbf{V}_{in} + (1-\eta_{loss})\mathbf{V}_{vac} \tag{2.33}$$

$$V_{out,\pm} = 1 \pm \frac{4\eta_{esc}\eta_{loss}x}{(1\mp x)^2} \tag{2.34}$$

In general, there will be multiple sources of loss during propagation and detection of the squeezed field. The total loss will be the product of the various η_{loss} terms.

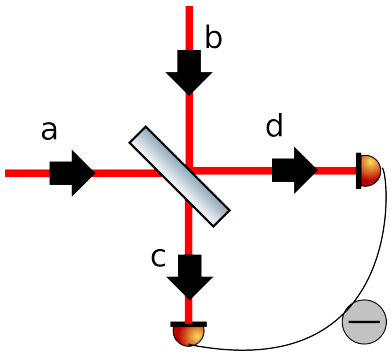

Figure 2-3: Balanced homodyne readout.

2.5.2 Balanced homodyne detection

How does one determine if a state is squeezed? A photodetector measures fluctuations in intensity rather than fluctuations in the quadrature fields. However, by interfering the squeezed field with a bright reference field of fixed phase, known as a local oscillator, we can convert the quadrature signals into intensity modulation which we can then measure. We will now examine the most popular method for measuring squeezed states: Balanced homodyne detection. A schematic of this is shown in Fig. 2-3. the squeezed field (a) and the local oscillator (b) are incident on a 50/50 beamsplitter. The detected fields are then given by:

$$\begin{pmatrix} c \\ d \end{pmatrix} = \frac{1}{\sqrt{2}} \begin{pmatrix} 1 & 1 \\ 1 & -1 \end{pmatrix} \begin{pmatrix} a \\ b \end{pmatrix} \tag{2.35}$$

The detected photocurrents are given by:

$$I_c = \frac{1}{2}\left(a^\dagger a + b^\dagger a + b a^\dagger + b^\dagger b\right) \tag{2.36}$$

$$I_d = \frac{1}{2}\left(a^\dagger a - b^\dagger a - b a^\dagger + b^\dagger b\right) \tag{2.37}$$

Subtracting the two photocurrents gives

$$I_{\text{diff}} = \left(b^\dagger a + a^\dagger b\right) \tag{2.38}$$

We will linearize the field operators as done when deriving the OPO equations of motion ($a \to \bar{a} + \delta a, b \to \bar{b} + \delta b$). Furthermore, we will assume that $\bar{a} = 0$ since we are measuring squeezed vacuum and that b has a variable phase θ_{LO} relative to a such that $b \to \left(\bar{b} + \delta b\right) e^{i\theta_{LO}}$. We will also drop all second order terms (terms proportional to $\delta a \delta b,\ \delta a^2,\ \delta b^2$). The difference current is then given by

$$I_{\text{diff}} = \bar{b}\left(\delta a e^{-i\theta_{LO}} + \delta a^\dagger e^{i\theta_{LO}}\right) = \bar{b}\left(\delta X_1 \cos\theta_{LO} + \delta X_2 \sin\theta_{LO}\right) \tag{2.39}$$

Notice how the above expression does not depend at all on δb. This is because the only term in Equations 2.36 and 2.37 which are first order in δb is $b^\dagger b$ which cancels out when we subtract the two signals. This feature is critical when measuring squeezing in the GW band, since otherwise the signal will be dominated by classical noise on the local oscillator field ($\bar{b}\delta b$ terms). Unbalanced homodyne detection requires that the local oscillator field be intensity stabilized such that it is shot noise limited in the band where we are measuring squeezing. Finally, we normalize Equation 2.39 by the local oscillator strength and compute the variance of the measured field

$$V_{\text{meas}} = V_1 \cos^2(\theta_{LO}) + V_2 \sin^2(\theta_{LO}) = V(\theta_{LO}) \tag{2.40}$$

We see that we may measure the variance of any quadrature operator simply by selecting the correct local oscillator phase. From the results of the previous section the squeezed quadrature (which I express as δX_{SQZ}) is rotated from the amplitude quadrature by $\theta_B/2$. So we may also express the measured quadrature as

$$\delta X_{\text{meas}} = \begin{pmatrix}\cos(\theta_{LO}) & \sin(\theta_{LO})\end{pmatrix} \begin{pmatrix}\cos(\theta_B/2) & \sin(\theta_B/2) \\ -\sin(\theta_B/2) & \cos(\theta_B/2)\end{pmatrix} \begin{pmatrix}\delta X_{SQZ} \\ \delta X_{ANTI}\end{pmatrix} \tag{2.41}$$

whose variance is given by

$$V_{meas} = \cos^2(\theta_{LO} - \theta_B/2)V_- + \sin^2(\theta_{LO} - \theta_B/2)V_+ \tag{2.42}$$

For the remainder of this thesis, I refer to $\theta_{LO} - \theta_B/2 \equiv \theta_{SQZ}$ as the *squeezing angle*. In a real experiment, θ_{SQZ} will fluctuate over time unless this degree of freedom is actively controlled. We will introduce a suitable control scheme in Section 2.7.

2.5.3 DC readout

Advanced LIGO uses an alternate technique known as self-homodyne detection. A small offset is added to the differential length degree of freedom such that a small amount of the interferometer carrier field exits at the dark port along with the injected squeezed field. The total field $\left[\bar{b}e^{i\theta_{ifo}} + \delta b\right]$ produces a photocurrent

$$I_{DC} = \bar{b}^2 + \bar{b}\left(\delta b e^{-i\theta_{ifo}} + \delta b^\dagger e^{i\theta_{ifo}}\right) = \bar{b}^2 + \bar{b}\delta X(\theta_{ifo}) \tag{2.43}$$

Due to the intensity stabilization of the interferometer laser and common mode rejection of the Michelson interferometer, we may ignore the classical fluctuations and assume that δb is purely quantum mechanical and due to the squeezed field entering from the anti-symmetric port. Proceeding as we did in the previous section, we get a normalized quadrature variance that is identical to Equation 2.42, with $\theta_{LO} \rightarrow \theta_{ifo}$.

Using the phase convention described in Section 1.2.4, $\theta_{ifo} = \pi/2$ and we would like to squeeze the amplitude quadrature ($\theta_{SQZ} = 0$) at the interferometer readout. Therefore, we must operate the squeezer with the pump phase set to $\theta_B = \pi/2$ in order to observe squeezed shot noise at the readout.

2.5.4 Detection Losses

The readout adds two additional sources of loss which will further reduce the level of measured squeezing. The first is mode mismatch between the squeezed and local oscillator fields. Its impact can be expressed in terms of the fringe visibility Vis as [16]

$$\eta_{HD} = \left(\frac{P_{max} - P_{min}}{P_{max} + P_{min}}\right)^2 = (Vis)^2 \tag{2.44}$$

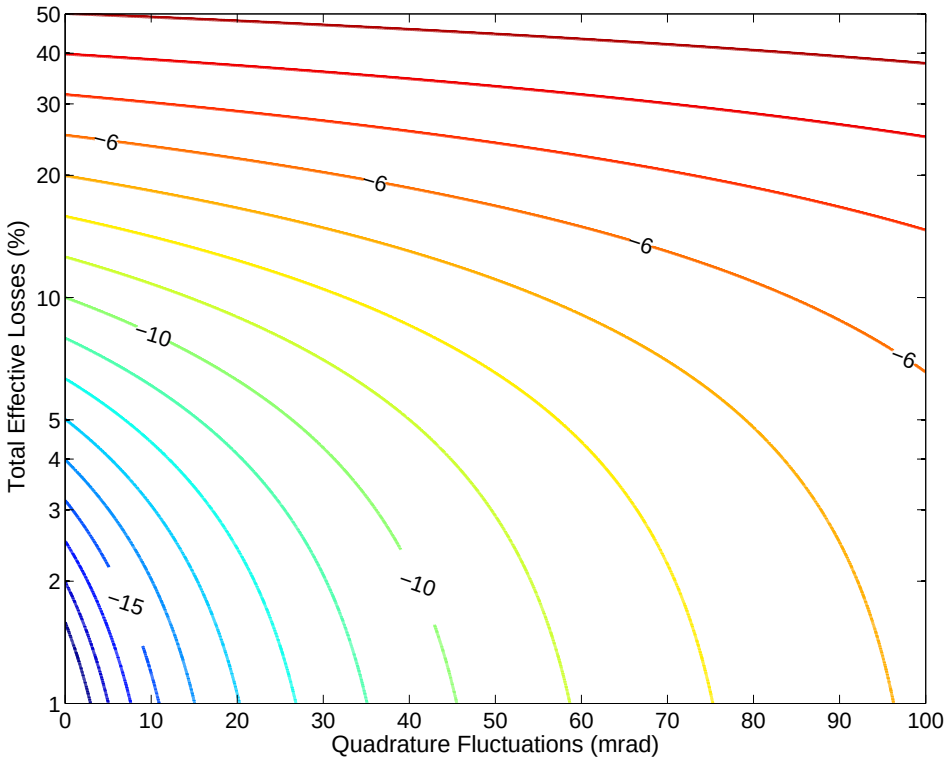

Figure 2-4: Maximum level of “effective" squeezing measurable in an optical system in the presence of optical losses and squeezed quadrature fluctuations, obtained by optimizing the amount of input squeezing [37]. Squeezing levels relative to shot noise are expressed in decibels.

Additionally, the photodiodes do not convert all incident photons into photocurrent. The quantum efficiency of the photodiodes η_{PD} is the fraction of the total energy conversion from photons to electrons and is defined by [50]

$$\eta_{PD} = \frac{hc}{\lambda e}\frac{I}{P} \tag{2.45}$$

where I is the photocurrent, e is the electron charge, and P is the incident laser power.

2.6 Phase noise

In addition to optical loss, relative fluctuations between the squeezed and measured quadrature angles further reduce the level of measured squeezing. If the period (τ) of these fluctuations is much longer than the measurement time (T_{meas}), they will cause

the level of squeezing to drift between measurements unless the measured quadrature angle is corrected. When fluctuations with $\tau \leq T_{meas}$ are present, the measured spectrum will be an average over a range of quadratures rather than the squeezed quadrature alone, resulting in a reduction in the maximum level of measurable squeezing. These fast fluctuations are commonly referred to as phase noise (or squeezed quadrature fluctuations) and are the primary focus of this section. The RMS level of phase noise $\tilde{\theta}_{RMS}$ is then given by

$$\tilde{\theta}_{RMS} = \left(\int_{1/T_{meas}}^{\infty} S_\theta(\Omega) d\Omega \right)^{1/2} \tag{2.46}$$

where S_θ is the power spectral density of phase noise. Lets assume that the mean squeezing angle is θ_{sqz} and there are gaussian fluctuations about this mean with standard deviation $\tilde{\theta}_{rms}$. These fluctuations impact the variance as follows [5, 36, 114]

$$\begin{aligned} V_{tot}(\theta_{sqz}, \tilde{\theta}_{rms}) &= \frac{1}{\tilde{\theta}_{rms}\sqrt{2\pi}} \int_{-\infty}^{\infty} dx e^{-x^2/2\tilde{\theta_{rms}}^2} \left(V_+ \sin^2(\theta_{sqz} + x) + V_- \cos^2(\theta_{sqz} + x) \right) \\ &\approx V(\theta_{sqz}) \cos^2 \tilde{\theta}_{rms} + V(\theta_{sqz} + \pi/2) \sin^2 \tilde{\theta}_{rms} \end{aligned} \tag{2.47}$$

which is valid assuming that $\tilde{\theta}_{rms} << 1$.

Setting $\theta_{sqz} = 0$ so that the mean quadrature is the squeezed quadrature, we see that the effect of phase noise is to contaminate the squeezed quadrature variance with with a projection from the orthogonal (anti-squeezed) quadrature. In fact, the more squeezed the state, the greater the contribution from the anti-squeezed quadrature as the quadrature angle fluctuates about its optimal mean value.

2.6.1 Optimizing the level of squeezing with phase noise

Since phase noise projects some of the anti-squeezed quadrature into the measurement, it is no longer true that increasing x necessarily leads to a higher level of

measured squeezing. As x gets larger, so does the level of antisqueezing. By setting $\theta_{sqz} = 0$ in Equation 2.47 and differentiating with respect to x we obtain

$$\frac{dV}{dx} = \frac{4\eta_{tot}}{(1-x)^3}\left((1+6x^2+x^4)\cos 2\tilde{\theta}_{rms} - 4x(1+x^2)\right) \tag{2.48}$$

For a given rms level of phase noise $\tilde{\theta}_{rms}$, we can calculate the optimal value for x by setting the above equation equal to zero and solving. To second order in $\tilde{\theta}_{rms}$, this yields [36]

$$x = 1 - 2\sqrt{\tilde{\theta}_{rms}} + 2\tilde{\theta}_{rms} - 2\tilde{\theta}_{rms}^{3/2} + 2\tilde{\theta}_{rms}^2 \tag{2.49}$$

In Figure 2-3, we plot the level of squeezing as a function of $\tilde{\theta}_{rms}$ and total loss. For each value of $\tilde{\theta}_{rms}$ the optimal value for x is used to compute the maximum possible level of squeezing. Typically, it is not practical to operate with $x > 0.9$. In Ref. [37] a similar plot is generated assuming that $x < 0.9$. The results are identical for $\tilde{\theta}_{rms} > 3\,\text{mrad}$.

2.6.2 Quadrature variance in decibels

After accounting for all sources of loss, phase noise, and any technical noise which couples into the measurement, the quadrature variance may be expressed as

$$V_{total}(\theta_{sqz}) = V_{tech}(\Omega) + V(\theta_{sqz})\cos^2(\tilde{\theta_{rms}}) + V(\theta_{sqz} + pi/2)\sin^2(\tilde{\theta_{rms}}) \tag{2.50}$$

$$V(\theta_{sqz}) = V_+\cos^2(\theta_{sqz}) + V_-\sin^2(\theta_{sqz}) \tag{2.51}$$

$$V_\pm = 1 \pm \frac{4x\eta_{tot}}{(1\mp x)^2} \tag{2.52}$$

where $\eta_{tot} = \eta_{esc}\eta_{loss}\eta_{HD}\eta PD$. One typically compares the total variance to that of shot noise ($V_{tech} = 0,\ x = 0$). This ratio is typically expressed in decibels (dB)

$$\text{dB} = 10\log_{10}\frac{V_{tot}}{V_{shot}} \tag{2.53}$$

Often we prefer to work in terms of amplitude spectral density (this is what we measure down in the lab with a spectrum analyzer). In this case

$$\mathrm{dB} = 20 \log_{10} \frac{V_{tot}^{1/2}}{V_{shot}^{1/2}} \tag{2.54}$$

2.7 Coherent control of squeezed vacuum states

When producing radio frequency (RF) squeezed vacuum sidebands, active stabilization of the measurement quadrature is not required to attain high levels of squeezing [40, 73] so long as the measurement times are kept relatively short (of order 0.1 seconds or less). Squeezing in the GW band does require active quadrature control since the longer measurement times involved result in an increased sensitivity to phase fluctuations at audio frequencies and below. Since squeezed vacuum has no coherent amplitude, there is no direct way to measure the relative phase between the squeezed and local oscillator (LO) fields which makes quadrature stabilization far more difficult.

The *coherent control* technique has emerged as the preferred means of stabilizing the measurement quadrature [24, 107]. This scheme uses a coherent field that is RF frequency shifted out of the squeezing band, hereafter referred to as the *coherent locking field* (CLF), whose phase is used as a surrogate for the squeezed quadrature angle. The incident field, which is a single (signal) sideband injected through the CLF mirror, is given by

$$\bar{\mathbf{A}}_{in,CLF} = \begin{pmatrix} A_s e^{i\phi_s} \\ 0 \end{pmatrix} \tag{2.55}$$

where the subscript s denotes the signal sideband. For now we will ignore the fluctuation term $\delta\mathbf{A}_{in,CLF}$ and consider only the DC fields. Noise propagation in coherent locking is discussed in detail in Appendix A. In general, calculating the resulting fields is quite complicated. For now we will simplify things by assuming that we have perfect phase matching, coresonance, and we shall neglect the detuning of the CLF

sidebands (assume $\Omega_{CLF} << \gamma_r^{tot}$)[5]. We shall deal with the more general case in Appendix A. We can then solve for the intra cavity CLF fields using the simplified expression for $\mathbf{M}$ given in Equation 2.23

$$\begin{pmatrix} \bar{a}_s \\ \bar{a}_i^\dagger \end{pmatrix} = \frac{\sqrt{2\gamma_r^{CLF}}}{\gamma_r^{tot}} \mathbf{M}^{-1} \bar{\mathbf{A}}_{in} = \frac{\sqrt{2\gamma_r^{CLF}} A_s}{(1-x^2)\gamma_r^{tot}} \begin{pmatrix} e^{i\phi_s} \\ xe^{-i(\theta_B - \phi_s)} \end{pmatrix} \tag{2.56}$$

We see that an idler sideband (denoted with a subscript i) has been generated with detuning $-\Omega_{CLF}$ and with a phase of $\phi_i = \theta_B - \phi_s$. This is an example of a nonlinear process known as *difference frequency generation*. Note that the generated idler field depends on the phase of the pump field. We will use this to generate an error signal which depends on the relative phase between the pump and CLF fields. The goal here is to stabilize the squeezing angle $\theta_{sqz} = \theta_{LO} - \theta_B/2$. We will do this by phase locking the CLF field to the pump and then phase locking the LO to the CLF. By transitivity this will stabilize θ_B with respect to θ_{LO}

Using the input-output relations given in Equation 2.12, we then solve for the reflected field from the CLF mirror.

$$\bar{\mathbf{A}}_{out,CLF} = \sqrt{2\gamma_r^{CLF}}\bar{\mathbf{a}} - \bar{\mathbf{A}}_{in,CLF} = \frac{2\gamma_r^{CLF} A_s}{(1-x^2)\gamma_r^{tot}} \begin{pmatrix} e^{i\phi_s} \\ xe^{-i(\theta_B - \phi_s)} \end{pmatrix} - \begin{pmatrix} A_s e^{i\phi_s} \\ 0 \end{pmatrix} \tag{2.57}$$

If we measure the interference between the upper and lower sideband in reflection and demodulate at $2\Omega_{CLF}$ we get an error signal which we can use to phase lock the CLF to the pump field[6]

$$\mathrm{E}_{2\Omega_{CLF}} = \frac{4A_s^2 x \gamma_r^{CLF} \cos(\theta_B - 2\phi_s - \psi_{2\Omega_{CLF}})}{(1-x^2)\gamma_r^{tot}} \tag{2.58}$$

where $\psi_{2\Omega}$ is the demodulation phase. In transmission, the fields are given by

[5]This last assumption, in particular, is not true in most instances. In Appendix A, we'll see how the finite detuning of the CLF can have a significant impact on the phase noise performance of the squeezer.

[6]To get this simple form for Equation 2.58, I neglected the portion of the signal field in Equation 2.57 that escapes from the cavity. I only include the promptly reflected term. This approximation is valid so long as $\gamma_r^{CLF}/\gamma_r^{tot} << 1$.

$$\bar{\mathbf{A}}_{out,f} = \sqrt{2\gamma_r^f}\begin{pmatrix}\bar{a}_s\\ \bar{a}_i^\dagger\end{pmatrix} = \frac{2\sqrt{\gamma_r^{CLF}\gamma_r^f}A_s}{(1-x^2)\gamma_r^{tot}}\begin{pmatrix}e^{i\phi_s}\\ xe^{-i(\theta_B-\phi_s)}\end{pmatrix} \tag{2.59}$$

At the homodyne detector, we measure the interference of this field with a local oscillator $A_{lo}e^{i\theta_{LO}}$ and demodulate at Ω_{CLF}

$$\mathrm{E}_{1\Omega_{CLF}} = \frac{4A_{LO}A_s\sqrt{\gamma_r^{CLF}\gamma_r^f}}{(1-x^2)\gamma_r^{tot}}\left(x\cos(\theta_B-\theta_{LO}-\phi_s+\psi_{1\Omega_{CLF}})+\cos(\theta_{LO}-\phi_s-\psi_{1\Omega_{CLF}})\right) \tag{2.60}$$

where $\psi_{1\Omega}$ is the demodulation phase. With the $2\Omega_{CLF}$ loop engaged and the appropriate demodulation phase chosen, we can set $\phi_s = \theta_B/2$ and the expression simplifies to[7]

$$\mathrm{E}_{1\Omega_{CLF}} = \frac{4A_{LO}A_s\sqrt{\gamma_r^{CLF}\gamma_r^f}}{(1-x^2)\gamma_r^{tot}}(1+x)\cos(\theta_{sqz}-\psi_{1\Omega}) \tag{2.61}$$

By engaging this servo, we fix θ_{sqz} and we can measure any quadrature by changing the demodulation phase.

[7]In practice, it isn't necessary to set the demodulation phase for the $2\Omega_{CLF}$ loop to any particular value. In fact, one can also rotate the $2\Omega_{CLF}$ demod phase to adjust the squeezing angle. This is done here only for the purpose of simplifying the equations.

Chapter 3

Design requirements for the Advanced LIGO squeezed vacuum source

3.1 Overview

The advanced generation of gravitational wave detectors imposes stricter constraints on the squeezed light source than its predecessors. The purpose of this chapter is to establish the requirements for an advanced squeezed light source, compare these requirements to what has been achieved to date and to propose a design that closes the gap between the two. Our proposed design aims to maximize the benefit from squeezing by minimizing the impact of known noise sources, such as optical losses, phase noise and back scattered noise [27, 37]. Additionally, our design will achieve a simultaneous reduction in both shot noise and radiation pressure noise as required to achieve a broadband sensitivity improvement.

This solution meets the requirements for advanced detectors, and it is suitable for the third generation of detectors envisioned for the next decade [3, 39, 86]. Realizing greater levels of squeezing at any frequency allows gravitational wave detectors to probe an observation volume that increases as the cube of the sensitivity improvement [30]. Moreover, pushing the squeezing enhancement to lower frequencies is critical for early detection of coalescing compact binaries and parameter estimation [69, 75].

3.2 Limits to effective squeezing

As discussed in chapter 2 and written in Eqn 2.50, the amount of effective squeezing that can be measured in any optical system limited by quantum noise is determined by how much squeezing is injected into the apparatus (which depends on the nonlinear interaction strength x), by the losses in the apparatus (η_{tot}), and by the rms level of phase noise ($\tilde{\theta}_{rms}$). Losses reduce the level of measured squeezing by mixing in ordinary vacuum with the squeezed field. Phase noise arises from relative fluctuations between the squeezed quadrature and the measured quadrature. These fluctuations project noise from the anti-squeezed quadrature into the measurement. Moreover, scattered light can add noise to the squeezed field, reducing the level of measured squeezing.

Figure 2-4 shows how squeezed quadrature fluctuations and optical losses determine the maximum amount of effective squeezing. For optical losses of 30% or more, squeezed quadrature fluctuations could be as high as tens of mrad without significantly reducing the maximum squeezing. However, the sensitivity to squeezed quadrature fluctuations increases as the optical losses are reduced. For instance, 10% to 15 % losses allow for -8 to -10 dB of squeezing provided that squeezed quadrature fluctuations are reduced to a few milliradians.

We give a detailed description of the elements and operation of a squeezed vacuum source in Chapter 4. For now, a simplified schematic of squeezed light injection in a first generation gravitational wave detector is shown in the top panel of Figure 3-1. The squeezed light source is located outside the interferometer's vacuum envelope. A sub-threshold optical parametric oscillator (OPO) is pumped with light at 532 nm to produce squeezed vacuum at 1064 nm via parametric downconversion in a second-order nonlinear PPKTP crystal. Squeezed vacuum is injected into the interferometer through the output Faraday isolator. It is then reflected back toward the output mode cleaner (OMC), and together with the interferometer beam reaches the "output photodiode" which measures the gravitational wave signal through homodyne detection [46].

Specific details of the squeezed light sources employed so far in gravitational wave detectors can be found in [101, 102]. The relative phase between the interferometer and squeezed fields is stabilized using the *coherent control* technique introduced in section 2.7. A single RF "control" sideband $\omega_0 - \Omega_{CLF}$, with detuning Ω_{CLF} with respect to the "pump laser" frequency ω_0, is injected into the OPO. In the presence of an intense pump field at twice the laser frequency $2\omega_0$, this sideband undergoes difference frequency generation which produces a second sideband with the opposite detuning, $\omega_0 + \Omega_{CLF}$. Both the squeezed field and the control sidebands are injected into the interferometer and return along with the interferometer field. Along the readout path, a small sample of the light is picked-off to measure the interference between interferometer and control fields. Demodulation of this interference signal at Ω_{CLF} allows us to lock the relative phase (*squeezing angle*) between the squeezed field and the interferometer field by actuating on the pump laser frequency.

Connecting a squeezed vacuum source to the output port of a gravitational wave interferometer opens another port that may introduce scattered light [27]. Light exiting the interferometer from the Output Faraday Isolator toward the squeezer can scatter off of moving surfaces in the squeezing injection path and propagate to the interferometer readout photodetector, degrading the detector sensitivity in the audio frequency band. One additional Faraday Isolator (Squeezing Injection Faraday Isolator, see top panel of figure 3-1) is placed in between the squeezer source and the interferometer to mitigate the impact of back scattered light noise. Although both the GEO600 and LIGO squeezing demonstrations were able to mitigate backscatter well enough to demonstrate squeezing without degrading the detector's strain spectrum, the total noise of these first generation interferometers was at least a factor of 50 above quantum noise below 50 Hz [101, 102], while in advanced detectors quantum noise will be a dominant noise source in the entire detection band down to 10 Hz [103].

In the sections that follow we describe these noise sources in detail, and explain how they can be overcome to maximize squeezing enhancement in future gravitational wave detectors. Specifically, we discuss *losses* arising from the optical train and from

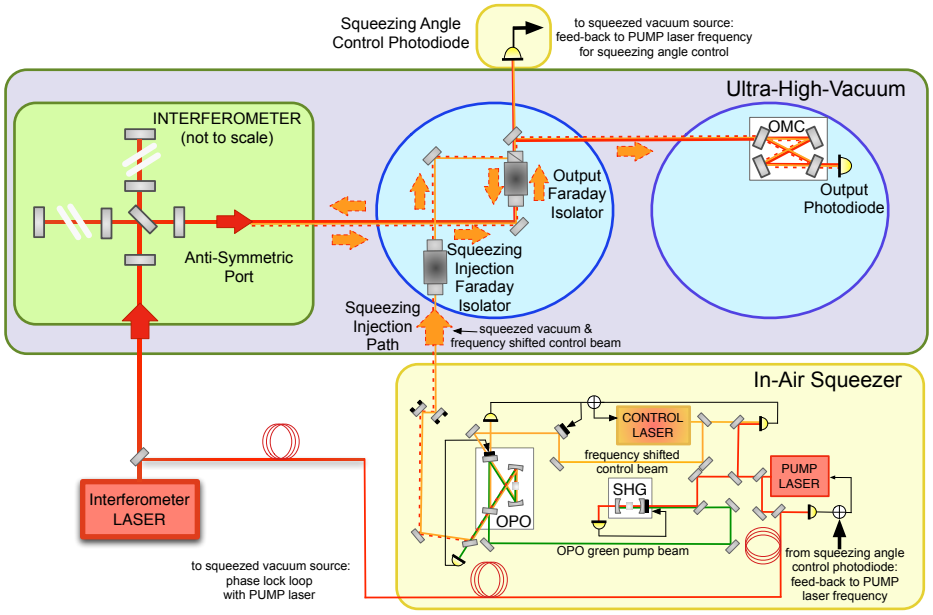

(a) **Top**

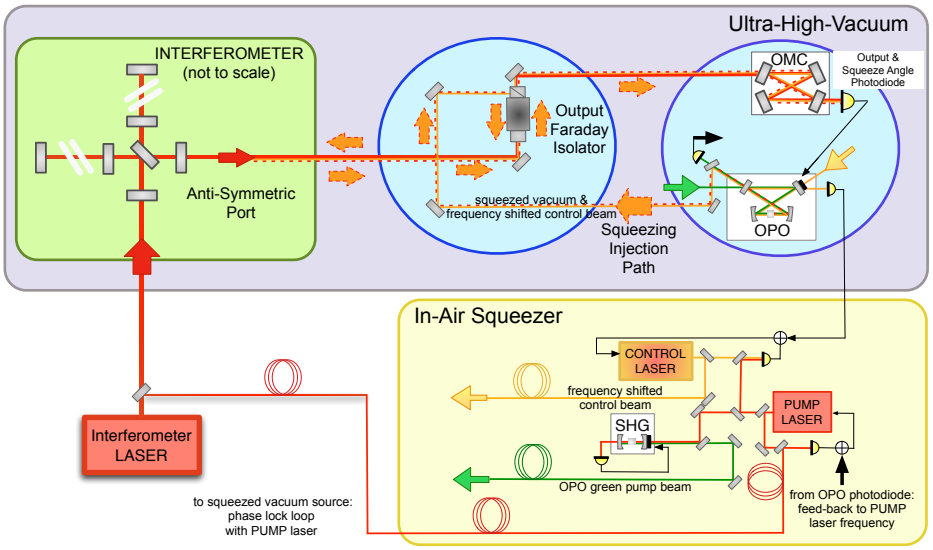

(b) **Bottom**

Figure 3-1: Figure adapted from Reference [82]. **Top:** A typical set-up for squeezing injection with a first generation gravitational wave detector using DC readout [46]. The shaded gray region corresponds to the detector vacuum chamber. The squeezed light source is housed outside of vacuum. The OPO cavity is locked to the green pump light. The squeezed (dashed red) and control (orange) fields enter vacuum through a viewport and are injected into the interferometer through the Output Faraday Isolator. A Squeezing Injection Faraday Isolator is inserted between the squeezed light source and the Output Faraday to provide additional attenuation of backscattered light [27, 101]. A small pickoff beam is sampled prior to the output mode cleaner (OMC) to control the squeezed quadrature angle. The squeezed and interferometer fields are measured in transmission through the OMC to obtain the gravitational wave signal. Details of the control topologies adopted in first generation detectors can be found in [101,102]. **Bottom:** Proposed design for future detectors. This design features an in-vacuum OPO. The remainder of the squeezed light source remains outside of vacuum. The coherent control error signal is now derived in transmission through the OMC [52]. Details of this new control topology can be found in section 3.7.

misaligned optical fields in Section 3.3. In Section 3.4 we address *quadrature angle fluctuations* arising from fluctuations in the OPO length and alignment jitter. In Section 3.5 we will discuss how to control *scattered light*. In Section 3.6 we discuss how the emergence of quantum radiation pressure noise in Advanced detectors require the use of quantum filter cavities to suppress quantum noise at all frequencies. In Section 3.7 we evaluate the impact of these noise sources on Advanced LIGO and *show a design* for a squeezed light source that can satisfy the stringent requirements of advanced detectors.

3.3 Losses

Quantum states are fragile and, therefore, easily degraded by losses in the optical system. We consider two mechanisms that give rise to substantial losses.

3.3.1 Optical losses

The squeezed beam experiences losses in the optical path from the squeezing source to the interferometer readout photodetector (see Figure 3-1). These losses are typically determined by imperfections in optical surfaces and polarizing optics (such as Faraday isolators), and by imperfect spatial overlap (*mode matching*) when coupling the beam to resonant cavities such as the OMC. In table top squeezing experiments, total losses of 5% or less have been realized, yielding squeezing enhancement of more than 10 dB [40, 73, 99].

However, in large scale interferometers there are additional optical components and resonant cavities in between the squeezed light source and the interferometer readout, and the losses are typically much higher. In the GEO600 and LIGO H1 squeezing demonstrations [101, 102], optical losses of 38% and 56% respectively were measured, limiting the squeezing enhancement to 3.5 dB and 2.1 dB. Some of the losses were due to particular limitations of the experimental set-ups; total losses of 20% to 30% should be readily achievable in advanced detectors, allowing for 6 dB of noise reduction using squeezing. Reducing the losses down to the 10% level will

require additional effort to limit the loss from each source, and will allow for 10 dB of noise reduction due to squeezing, as will be detailed in section 3.7.

3.3.2 Losses induced by alignment fluctuations

Alignment fluctuations of the squeezed field also introduce losses by reducing the coupling through the OMC or arm cavities. A misalignment or displacement of the squeezed beam on a steering optic in between the OPO and the asymmetric port of the interferometer reduces the power in the TEM_{00} mode [4] and it is equivalent to a loss L

$$L = \left(\frac{\tilde{\theta_x}\omega_0\pi}{\lambda}\right)^2 + \left(\frac{\tilde{\Delta x}}{\omega_0}\right)^2 \tag{3.1}$$

where ω_0 is the beam waist (radius) and $\tilde{\theta_x}$ and $\tilde{\Delta}_x$ are the RMS values for the fluctuations in beam angle and displacement respectively. The beam waist will vary from approximately $\omega_0 = 100$ μm in the OPO to $\omega_0 = 1$ mm at the asymmetric port of the interferometer where the beam is injected. Equation 3.1 can be written as

$$L = 0.01 \times \left[\left(\frac{0.3\tilde{\theta_x}}{100\ \mu\text{rad}}\right)^2 + \left(\frac{\tilde{\Delta x}}{10\ \mu\text{m}}\right)^2\right] \quad \text{for } \omega_0 = 100\ \mu\text{m} \tag{3.2}$$

$$L = 0.01 \times \left[\left(\frac{0.3\ \tilde{\theta_x}}{10\ \mu\text{rad}}\right)^2 + \left(\frac{\tilde{\Delta x}}{100\ \mu\text{m}}\right)^2\right] \quad \text{for } \omega_0 = 1\ \text{mm} \tag{3.3}$$

To keep the losses below 1% ($L < 0.01$) the displacement of the squeezed beam on the steering optics need to be reduced to less than 10 μm RMS where the beam is small, and angular jitter needs to be reduced to less than 30 μrad RMS where the beam is large. Meeting these requirements on an in air table without seismic and acoustic isolation can be challenging. [1] Because previous squeezing demonstrations in gravitational wave detectors were dominated by optical losses (see 3.3.1), losses

[1] Recently, GEO 600 implemented active alignment control [92] with an in-air squeezer. Their spectra appear to have a low enough RMS below 10 Hz, though their total RMS was likely higher since acoustic noise will add fluctuations in the audio band. Their sensor noise level appears to be too high to say anything definitive about their alignment noise above 6 Hz. One could reasonably conclude, however, that the GEO control scheme combined with an isolated in-vacuum squeezer would meet this requirement.

induced by alignment fluctuations were negligible. However, they must be taken into account when aiming to reduce the total losses down to 10%.

3.4 Phase noise

Many mechanisms have been identified which cause phase noise [37]. We will introduce a few of them in this chapter to motivate our proposed design for Advanced LIGO, but detailed derivations and a discussion of other sources of phase noise will be postponed until Chapter A. The LIGO H1 control scheme was designed to suppress quadrature fluctuations by relying on high bandwidth feedback from the squeezeing angle control photodiode to the frequency of the pump laser (see figure 3-1). However, this control scheme is not optimal.

For an interferometer with Fabry-Perot arm cavities, the bandwidth of the squeezing angle control loop is limited by the arm cavity free-spectral-range. The 4 km long arm cavities of LIGO have a free spectral range of 37.5 kHz. They are operated on resonance for the interferometer carrier field while the detuning of the squeezing control field, Ω_{CLF}, is tuned to be anti-resonant in the arm cavities. Quadrature fluctuations will impress audio sidebands on the control field with detuning $\Omega_{CLF} + \Omega$. When $\Omega_{CLF} + \Omega$ is an integer multiple of $2\pi \times 37.5\,\mathrm{kHz}$ these sidebands become resonant in the arm cavities which will shift their phase relative to the control field. These phase shifted sidebands can cause instabilities in the squeezing angle control loop if they are within the servo bandwidth. This effect was indeed observed during the LIGO H1 squeezing experiment, limiting the squeeze angle control bandwidth to 10 kHz [36].

As we will discuss in detail in Chapter A, the coherent control technique is also susceptible to lock point errors which can limit its ability to suppress phase noise. Fluctuations in the OPO cavity length and drift in the relative alignment between the interferometer and squeezed fields generate lock point errors, as will be detailed in the sections that follow. These allow for significant squeezed quadrature fluctuations even within the control bandwidth.

3.4.1 Quadrature fluctuations due to OPO length noise

In an OPO cavity, fluctuations in the cavity length lead to phase noise on the squeezed field exiting the cavity. These phase fluctuations will result in fluctuations of the measured quadrature phase at the interferometer readout.

Both implementations of squeezed enhancement in gravitational wave detectors [101, 102] used OPO cavities which were exposed to air currents and the ambient acoustic environment of the laboratory. With little isolation, environmental vibrations led to fluctuations in the length of the OPO cavity, and consequently to quadrature fluctuations.

For an OPO cavity where the pump field is used for Pound-Drever-Hall locking, a closed-form expression for the contribution of the OPO length noise to the total quadrature fluctuations is [37]:

$$\frac{d\theta_{sqz}}{d\delta L} = \frac{\omega_0}{\bar{L}} \left(\frac{1}{\gamma_b^{tot}} + \frac{1}{\gamma_a^{tot}(1+x^2)} \right) . \tag{3.4}$$

Here, ω_0 is the frequency of the squeezed field, $\bar{L}$ is the OPO cavity length at zero detuning. One may obtain an estimate for the squeezed quadrature fluctuations by multiplying equation 3.4 by a calibrated length spectrum and correcting for the noise suppression provided within the bandwidth of the squeezed quadrature control loop.

The coherent control error signal measures phase of the control sidebands relative to the interferometer field, and works on the assumption that the control field responds in the same way to disturbances as the audio frequency sidebands that make up the squeezed field. However, because coherent sidebands are typically detuned from the OPO resonance by more than 10 MHz, they respond differently than the squeezed field does to changes in the cavity length [37]. In the LIGO squeezing experiment, this meant that the coherent control scheme only corrected for half of the quadrature fluctuations due to cavity length fluctuations. While the control field detuning could be lowered to improve the accuracy of the error signal, it must remain large enough to avoid contaminating the squeezed field. The most effective way to reduce these quadrature fluctuations is to reduce the cavity length fluctuations themselves.

Quadrature fluctuations due to OPO length noise in the LIGO squeezing demonstration were measured to be 25 mrad RMS [37], however smaller total phase noise (on the order of 10 mrad) has been measured with OPOs outside of vacuum [26, 61, 73].

3.4.2 Quadrature fluctuations due to alignment jitter

The approach used in [101, 102] to lock the squeezing angle was to pick off a sample of the interferometer output field using a beamsplitter inserted before the OMC and measure its interference with the control field (see Figure 3-1). At the squeezing angle control photodetector both fields contain higher order modes TEM_{ij} that have phase offsets relative to the TEM_{00} mode which we will denote as ϕ_{ij}^{ifo} and ϕ_{ij}^{clf} for the interferometer and coherent locking control fields, respectively. When there is a relative misalignment between the interferometer and control beams, the difference between these two phase shifts $\phi_{ij} = \phi_{ij}^{ifo} - \phi_{ij}^{clf}$ can be non-zero. This relative phase shift gives rise to an offset in the lock point for the squeezing angle [36]:

$$\Delta\theta_{alignment} = \frac{\sum_{ij} \rho_{ij}^{clf} \rho_{ij}^{ifo} sin\phi_{ij}}{1 + \sum_{ij} \rho_{ij}^{clf} \rho_{ij}^{ifo} cos\phi_{ij}} \approx \sum_{ij} \rho_{ij}^{clf} \rho_{ij}^{ifo} sin\phi_{ij} \,. \tag{3.5}$$

$\rho_{ij}^{ifo}, \rho_{ij}^{clf}$ are the ratio of the amplitudes of the TEM_{ij} to TEM_{00} spatial modes for the two fields. Here, we have assumed that both fields are dominated by the TEM_{00} mode, so that the summation in the denominator may be neglected. When both fields are very well aligned, the lock point error is small and any coupling of alignment jitter to the measured quadrature phase is second order. However, when a static misalignment is present in one of the fields, the coupling is linear and the resulting quadrature fluctuations can be significant. Assuming that the control field is misaligned, we may linearise the above equation and express the quadrature fluctuations as:

$$\delta\theta_{sqz}(t) \approx \sum_{ij} \bar{\rho}_{ij}^{clf} \delta\rho_{ij}^{ifo} (1 + \bar{\phi}_{ij}) \delta\phi_{ij}(t) \tag{3.6}$$

Here $\bar{\rho}_{ij}^{clf}$ and $\bar{\phi}_{ij}$ result from a static misalignment of the control field and $\delta\rho_{ij}^{ifo}$ and $\delta\phi_{ij}^{ifo}$ arise due to jitter in the alignment of the interferometer beam. Alignment jitter

can be a crippling source of quadrature fluctuations, and was measured to contribute 35 to 100 mrad depending on the alignment in the H1 experiment [37].

3.5 Backscattered light noise

When integrating a squeezed vacuum source into a gravitational wave detector, the OPO becomes a source of scattered light. Imperfections in the output Faraday isolator allow a small fraction of the light exiting the interferometer to travel towards the squeezed vacuum source, and a part of it is scattered back towards the interferometer. Relative motion between the scattering surface and the suspended interferometer optics generates phase fluctuations on the backscattered light which will interfere with the signal field and add noise to the gravitational wave spectrum [27].

For an OPO motion δz_{sc} which is small compared to the wavelength λ, the relative intensity noise (RIN) due to scattered light at the interferometer output (RIN_{sc}) relative to quantum noise (RIN_{qn}) scales linearly with δz_{sc} [36]:

$$\frac{RIN_{sc}}{RIN_{qn}}(f) = 4\pi\delta z_{sc}(f)\sqrt{\frac{\eta_{PD}P_{sc}}{\lambda hc}} \tag{3.7}$$

where λ is the laser light wavelength, η_{PD} is the quantum efficiency of the read-out photodiode, h and c are the Planck constant and speed of light, and P_{sc} is the backscattered power that reaches the output photodetector. P_{sc} can be explicitly written as:

$$P_{sc} = P_{sc,inc}R_{OPO}\eta_{loss} \tag{3.8}$$

where $P_{sc,inc}$ is the carrier power from the anti-symmetric port which is incident on the OPO, η_{loss} accounts for propagation losses between the OPO and the readout photo-detector, and R_{OPO} is the reflection coefficient of the OPO which is given by [27]

$$R_{OPO} = \text{BSDF} \times \frac{16\Omega_{1/e}}{(1-R_{in})^2}\left(\frac{1-2x\cos(\theta_{sc})+x^2}{(1-x^2)^2}\right) \tag{3.9}$$

where the bidirectional scatter distribution function (BSDF) is a measure that characterizes the backscattering impact for a transmissive optic, such as in the case of the nonlinear crystal of the OPO (BSDF $= (9 \pm 3) \times 10^{-5}\text{str}^{-1}$), θ_{sc} is the phase of the backscattered field relative to the pump field ($2\theta_{bs} - \theta_B$), Rin is the reflectivity of the OPO input coupler and $\Omega_{1/e} = \lambda^2/(\pi W_0^2)$ is the solid angle subtended by the crystal at the beam waist.

Backscattered light from the OPO can also degrade the interferometer sensitivity through non-linear couplings which up-convert low frequency noise into the gravitational wave band. These processes are non stationary and can prevent gravitational wave detectors in reaching shot noise limited performance in their most sensitive band around 150 Hz. They will be even more harmful in advanced detectors where quantum noise limits the sensitivity down to 10 Hz (see [27] and references therein). We therefore require scattered light noise to be at least a factor of 10 below quantum noise over the entire aLIGO detection band, down to 10 Hz, to have enough margin to account for non stationarity. With squeezing enhancement, quantum noise will be reduced by a factor of $10^{s/20}$, where s is the level of noise reduction due to squeezing in decibels (dB). Thus, we impose:

$$\frac{RIN_{sc}}{RIN_{qn}}(f) = 4\pi\delta z_{sc}(f)\sqrt{\frac{\eta_{PD}P_{sc}}{\lambda hc}} \leq \frac{10^{s/20}}{10}\,. \tag{3.10}$$

Here we make the optimistic assumption that squeezing enhancement will be obtained over the entire frequency band. More realistically, the quantum noise reduction below 50 Hz will be significantly less than at higher frequencies [42, 65].

From Equations (3.8) and (3.10), it is clear that there are three ways of minimizing the impact of scattered light: minimizing the OPO reflection coefficient R_{OPO}, decreasing the amount of light incident on the OPO cavity $P_{sc,inc}$, and reducing the motion of the OPO δz_{sc}. In first generation detectors, the LIGO H1 squeezing experiment employed a travelling wave OPO cavity design to obtain 50 dB of intrinsic power isolation, $R_{OPO} = 10^{-5}$ [28]. A Faraday isolator between the squeezed light source and the interferometer (see Figure 3-1, top panel) further reduces the amount

of spurious light reaching the squeezer source. As shown in [27], even with this amount of optical isolation, the squeezing set-up employed during the LIGO H1 experiment would not meet the noise requirements for Advanced LIGO. GEO600 adopted a linear OPO cavity, relying exclusively on Faraday isolators for spurious light attenuation. In principle, a cascade of Faraday isolators could be inserted in Advanced LIGO between the output Faraday isolator and the OPO to reduce $P_{sc,inc}$. However, this approach has the downside of introducing additional losses in the squeezing injection path, and potentially introduces back scattered light noise from the Faraday isolators themselves.

3.6 Radiation pressure noise

At full design sensitivity, Advanced LIGO will be limited by quantum radiation pressure noise below 50 Hz and shot noise at higher frequencies [103]. Both noise sources arise due to vacuum fluctuations entering the interferometer from the anti-symmetric port. From Equation 1.85, we see that radiation pressure noise is driven by vacuum fluctuations in the amplitude quadrature while shot noise is driven by noise in the phase quadrature. During the LIGO and GEO 600 squeezing experiments, they set $\theta_{sqz} = \pi/2$ in order to squeeze shot noise at high frequencies. This alters the strain spectral density of quantum noise from Equation 1.88 as follows

$$h_{qn}(\Omega) = \frac{h_{SQL}}{\sqrt{2}}\sqrt{\frac{1}{\mathcal{K}_{sr}e^{2r}} + \mathcal{K}_{sr}e^{2r}} \tag{3.11}$$

where the first and second term under the radical correspond to shot noise and radiation pressure noise respectively. We see that the LIGO and GEO 600 squeezing experiments used squeezed light to reduce shot noise at the expense of increased radiation pressure noise due to the injected antisqueezing in the amplitude quadrature. This was not a limitation for these experiments since they were not radiation pressure noise limited. A simultaneous reduction in radiation pressure noise and shot noise, as required for the current generation of advanced detectors, can be achieved by combining a traditional squeezed vacuum source with a quantum filter cavity to rotate

the squeezed quadrature as a function of frequency [63].

3.6.1 The interferometer as a ponderomotive squeezer

In order to gain some more intuition about radiation pressure noise in Advanced LIGO it is useful to rewrite the input-output relations for the interferometer's quadrature operator in an alternate form.

As shown in Equations 1.84 and 1.85, the action of the interferometer on our field entering from the antisymmetric port is given by

$$\begin{pmatrix} b_1 \\ b_2 \end{pmatrix} = e^{2i\beta} \begin{pmatrix} 1 & 0 \\ -\mathcal{K} & 1 \end{pmatrix} \begin{pmatrix} a_1 \\ a_2 \end{pmatrix} \tag{3.12}$$

It turns out that the above input-output matrix is equivalent to a rotation in the a_1, a_2 plane followed by a squeezing operator [63, 65].

$$\mathbf{b} = \mathbf{S}(\sigma_{\text{ifo}}, \phi_{\text{ifo}})\mathbf{R}(\theta_{\text{ifo}})\mathbf{a} \tag{3.13}$$

where

$$\begin{aligned} \sigma_{\text{ifo}} &= -\operatorname{arcsinh}(\mathcal{K}/2), \\ \phi_{\text{ifo}} &= \tfrac{1}{2}\operatorname{arccot}(\mathcal{K}/2), \\ \theta_{\text{ifo}} &= -\arctan(\mathcal{K}/2). \end{aligned}$$

and

$$\begin{aligned} \mathbf{S}(r,\phi) &= \mathbf{R}(\phi)\mathbf{S}(r,0)\mathbf{R}(-\phi) = \mathbf{R}_\phi \mathbf{S}_\sigma \mathbf{R}_\phi^\dagger \\ &= \begin{pmatrix} \cos\phi & -\sin\phi \\ \sin\phi & \cos\phi \end{pmatrix} \begin{pmatrix} \mathrm{e}^{r} & 0 \\ 0 & \mathrm{e}^{-r} \end{pmatrix} \begin{pmatrix} \cos\phi & \sin\phi \\ -\sin\phi & \cos\phi \end{pmatrix}, \end{aligned} \tag{3.14}$$

which describes squeezing by e^{-r} at angle ϕ and anti-squeezing by e^{r} at $\phi + \pi/2$.

Physically, due to the optomechanical nature of our interferometer, we are generating what is known as optomechanical or ponderomotive squeezing. One may think of radiation pressure noise as a projection of ponderomotive antisqueezing into our measurement quadrature.

The problem of achieving a broadband reduction in quantum noise can be solved by rotating the squeeze angle of the input field as a function of frequency such that it is always aligned with the signal quadrature at the output of the interferometer. Here we are compensating for the rotation by θ_{ifo} and the effective rotation from the squeezing operation given by ϕ_{ifo}.

Intuitively, if we wish to reduce radiation pressure noise and shot noise, we need to rotate θ_{sqz} by 90° so that we are squeezing the amplitude quadrature at low frequencies where radiation pressure noise dominates and the phase quadrature where we are shot noise limited. More precisely, the strain spectral density as a function of squeeze angle and sideband frequency is given by [63]

$$h_{qn}^2(\Omega, \theta_{sqz}) = \frac{h_{SQL}^2}{2}\left(\frac{1}{\mathcal{K}(\Omega)} + \mathcal{K}(\Omega)\right)\left(\cosh 2r - \cos[2(\theta_{sqz} + \operatorname{arccot}\mathcal{K}(\Omega))]\sinh 2r\right) \tag{3.15}$$

which is minimized by making the last term equal to $\cosh 2r - \sinh 2r$. This is achieved with the following frequency-dependent squeezing angle[2]

$$\theta_{sqz}(\Omega) = -\operatorname{arccot}\mathcal{K}(\Omega) \tag{3.16}$$

[2]There are several other quantum nondemolition measurement techniques which one may use instead of frequency-dependent squeezing to achieve a broadband sensitivity improvement. The two most established ideas are speedmeter interferometers [87] and variational readout [63]. Both schemes are examples of "back-action evasion" which can, in principle, remove the radiation pressure noise entirely. However, the efficacy of both are limited by optical losses and require complicated changes to the interferometer topology. For these reasons, they are not yet considered to be practical alternatives to frequency-dependent squeezing for advanced gravitational wave detectors.

3.6.2 Quantum noise filter cavities

The canonical paper on frequency-dependent squeezing, Kimble et al [63] (which we will subsequently refer to as KLMTV), proposed using quantum noise filter cavities to achieve the desired squeeze angle rotation. As we will discuss in more detail in Chapter 5, the filter cavities are operated detuned so that the upper and lower squeezing sidebands experience a different phase shift, thus rotating their quadrature as a function of frequency. To achieve the optimal squeeze angle frequency dependence given in Equation 3.16, two filter cavities are required to compensate for the effects of the interferometer on the squeezed field.

In order to achieve the necessary relative phase shift between upper and lower sidebands an extremely long cavity storage time is required. In fact the linewidth of the two filter cavities must be of the same order as those of the Advanced LIGO arm cavities ($\approx 100\,\mathrm{Hz}$ FWHM). KLMTV proposed using two 4km filter cavities running parallel to the existing arm cavities in order to achieve the desired storage time while keeping the additional optical losses as low as possible. While such a scheme would provide optimal performance, it would be a costly and involved undertaking. A more practical design is required to make frequency-dependent squeezing a viable upgrade for Advanced LIGO.

3.7 Squeezing injection for Advanced LIGO

The maximum benefit from squeezing in future detectors can be achieved by minimizing the impact of all the noise sources described above. The Advanced LIGO case will be addressed here, but the analysis that follows can be extended to other advanced detectors. With the currently envisioned commissioning timeline, it is likely that *frequency-independent* squeezing will be implemented first (as shown in the bottom panel of Figure 3-1) and that a filter cavity will be added later to suppress radiation pressure noise once R&D efforts on the Advanced LIGO filter cavity have been completed.

3.7.1 Lowering optical losses

Table 3.1 summarizes the “expected" optical losses that the squeezed beam would experience in Advanced LIGO, given the interferometer optical components currently being installed. The total losses will realistically be between 20% and 30%, limiting the maximum amount of effective squeezing to 6 dB. However, several techniques to reduce optical losses are currently under investigation. The light coupling through the OMC can be improved by actively controlling the mode matching [14, 60, 68], and a similar approach can be used to mode match the squeezed beam to the interferometer. Moreover, studies of losses in fused silica optics and resonant cavities can be used to maximize the throughput of the Faradays isolators and the OMC [10,11,59,77]. These techniques have the potential to reduce the total optical losses down to 10% - 15%.

Loss Source	**Estimated**	**Projected**
OPO	2%	2%
Squeezing injection optics	1%	1%
Squeezing injection Faraday	3% - 5%	0% - 2%
Output Faraday in Reverse	3% - 5%	1% - 2%
Mode matching (squeezed beam to interferometer)	4% - 6%	1% - 2%
Alignment fluctuations (squeezed beam to interferometer)	0% - 1%	0% - 1%
Total injection losses	10% - 18%	5 % - 9%
Output Faraday	3% - 5%	1% - 2%
OMC transmission	3% - 6%	1% - 2%
Mode matching (interferometer to OMC)	4% - 6%	2% - 3%
Photo-detector	2%	2%
Total readout losses	10% to 17%	5% - 9%
Total losses	**20% - 32%**	**9% - 17%**

Table 3.1: *Expected* sources of loss for squeezing injection in advanced detectors (left), compared to *projected* losses achievable in the near future.

3.7.2 Housing the OPO in the interferometer vacuum enclosure

Optical losses as low as 10% open up the possibility of achieving up to 10 dB of squeezing enhancement provided that quadrature fluctuations, backscattered light

noise, and losses induced by misalignments are also reduced. We propose building a monolithic OPO cavity and housing it on a seismically isolated platform in vacuum in order to address these issues.

In Advanced LIGO, the interferometer readout path (which includes the output Faraday isolator and OMC) is placed on seismically isolated platforms within the main vacuum envelope. These platforms are large enough to accommodate the OPO and the entire squeezing injection path as well. This allows for a compact design which limits the number of optical components (each being a potential scatterer or source of loss) needed to route the squeezed beam to the interferometer output Faraday isolator.

A monolithic OPO that is seismically and acoustically isolated will have very little length noise. The noise performance should be comparable to the OMC cavities used in Advanced LIGO, which are designed to have less than $1 \times 10^{-15} m/\sqrt{Hz}$ of length noise at 100 Hz and above [6]. Below 100 Hz, the length noise of monolithic cavities typically scales as $1/\sqrt{f}$ [80]. Therefore, we expect an RMS length noise of 10^{-12}m. Assuming that the optical parameters are identical to those used during the LIGO squeezing experiment, the OPO will generate 90 mrad of quadrature fluctuations per nanometer of RMS length noise [37], and thus will contribute less than 0.1 mrad RMS of phase noise. Squeezed quadrature fluctuations due to OPO length noise become negligible, and the resulting lock point errors in the coherent control scheme described in 3.4.1 become unimportant.

With a length noise of $1 \times 10^{-15}\,\mathrm{m}/\sqrt{\mathrm{Hz}}$ @ 100 Hz, an in vacuum OPO becomes a good frequency reference. For an OPO cavity length $l = 20$ cm, the frequency noise $\delta\nu$ for $\lambda = 1.064\ \mu m$ laser light ($v = c/\lambda = 2.8 \times 10^{14}$) is:

$$\delta\nu = \frac{\nu}{l}\delta l \sim 1\ \frac{\mathrm{Hz}}{\sqrt{\mathrm{Hz}}}\ @\ 100\ Hz \tag{3.17}$$

This performance is comparable to a typical reference cavity. As a result, the error signal used to lock the OPO will be more sensitive to phase noise on the incoming pump field. The control topology of the OPO length servo can be modified by adding

high bandwidth feedback to the pump laser frequency to suppress this noise. Although the pump laser itself is already stabilized by phase locking it to the interferometer laser (as depicted in Figure 3-1), additional sources of phase noise exist on the pump path, such as length noise on the SHG cavity. Suppressing this noise is desirable, as it too will couple to the squeezed quadrature angle.

Additionally, housing the OPO and all of the injection optics in an acoustically and seismically isolated environment will reduce alignment jitter on the injected squeezed field. Typical mechanical resonances of seismically isolated optics are below 10 Hz, within the bandwidth of an automatic alignment system [92].

A simplified schematic of the proposed implementation of frequency independent squeezing in Advanced LIGO with the OPO in vacuum is shown in the bottom panel of Figure 3-1.

3.7.3 Squeezing angle sensing in transmission through the OMC

GEO600 recently employed a new control scheme where the squeezing angle error signal is derived in transmission through the OMC [35,52]. In addition to providing an improved error signal to shot noise ratio, we explicitly show here how the attenuation of higher order mode content by the OMC reduces the quadrature fluctuations and lock point errors due to misalignment (see Appendix A.3 for a detailed derivation). Equations 3.5 and 3.6 may be rewritten in transmission through the OMC as:

$$\Delta\theta^{trans}_{alignment} \approx \sum_{ij} A_{ij}\rho^{clf}_{ij}\rho^{ifo}_{ij} sin\phi_{ij} \tag{3.18}$$

$$\delta\theta^{trans}_{sqz}(t) \approx \sum_{ij} A_{ij}\bar{\rho}^{clf}_{ij}\delta\rho^{ifo}_{ij}(1+\bar{\phi}_{ij})\delta\phi_{ij}(t) \tag{3.19}$$

These equations are identical to Equations (3.5) and (3.6) with an additional factor, A_{ij} which accounts for the attenuation of higher order modes by the OMC.

The filtering of higher order modes by the Advanced LIGO OMC provides a 100-fold reduction in the coupling of alignment jitter to the squeezed quadrature angle

(see Table A.1 in Appendix A.3), making this noise source negligible.

3.7.4 Back scattering noise mitigation

In order to minimize backscatter, we propose maintaining the bow-tie geometry for the OPO cavity which provides 50 dB isolation from light exiting the squeezing injection port [28]. Moreover, placing this cavity on a seismically isolated platform will greatly reduce the OPO motion. In Advanced LIGO, isolated platforms provide a factor of 100 isolation from ground motion above 1 Hz. Figure 3-2 shows plausible projections for back scattered light noise in a squeezing enhanced Advanced LIGO detector, calculated using equations (3.7) and (3.8). Here we assume 100 mW interferometer light reaching the anti-symmetric port and 80 dB isolation in the path from the anti-symmetric port to the squeezer source and back to the interferometer (30 dB isolation from the output Faraday isolator toward the squeezing injection path, and 50 dB isolation from the OPO itself).

We analyze three cases:

- OPO placed on a optics table with no seismic isolation, with a Squeezing Injection Faraday Isolator placed between the interferometer Output Faraday Isolator and the squeezing source (providing an additional 30 dB isolation);
- OPO placed on a seismically isolated platform, with a Squeezing Injection Faraday Isolator placed between the interferometer Output Faraday Isolator and the squeezing source (providing an additional 30 dB isolation);
- OPO *suspended* on a seismically isolated platform, without a Squeezing Injection Faraday isolator.

The curves in Figure 3-2 confirm that placing the OPO on an optics table without seismic isolation would not meet the Advanced LIGO requirements below 200 Hz without inserting additional Faraday isolators which would in turn increase the optical losses. Moving the OPO onto a seismic isolated platform will meet the back scattered light noise requirements above 30 Hz, and it might be acceptable at low

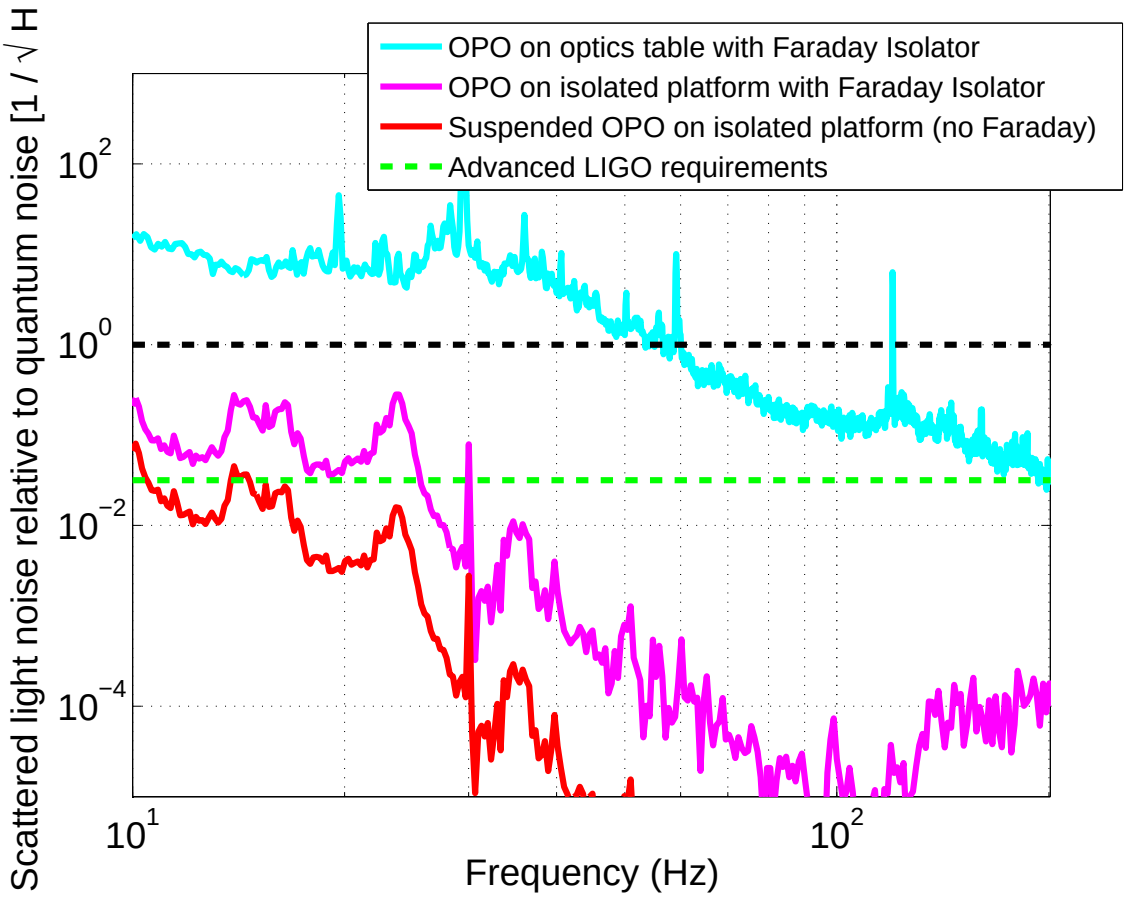

Figure 3-2: Figure adapted from Reference [82]. Backscattered light noise projections for three different scenarios: OPO placed on an optics table on the ground, without seismic isolation, OPO placed on an isolated platform enclosed in the main LIGO vacuum envelope; OPO *suspended* on an isolated platform enclosed in the main LIGO vacuum envelope. In the first two cases, 30 dB of isolation from spurious light reaching the OPO is also assumed. The requirement curve optimistically targets 10 dB of broadband squeezing.

frequencies depending on the actual OPO seismic motion and the amount of squeezing measured at low frequency with realistic filter cavities [42]. Suspending the OPO by a single stage suspension (1 Hz pendulum) would reduce the back scattered noise below requirements without the need of a Squeezing Injection Faraday Isolator. All the steering optics in the squeezing injection path would need a similar attenuation.

3.7.5 16 meter filter cavity

In order to achieve a broadband reduction in quantum noise, we propose implementing frequency-dependent squeezing. Using two kilometer-scale filter cavities as recommended in KLMTV to achieve the desired quadrature rotation angle with minimal added loss would require prohibitively expensive modifications to the existing LIGO observatories. However, one could conceivably add a single 16 meter filter cavity within the existing Advanced LIGO vacuum envelope between HAM 4 and HAM 5 as illustrated in Figure 3-3. While two filter cavities are required to achieve the correct frequency dependence with conventional interferometers where $\gamma \approx \Omega_{SQL}$ (the case discussed in KLMTV) or when the signal recycling cavity is detuned [53], one can show that for a broadband signal recycled interferometer like Advanced LIGO, where the approximation $\mathcal{K}(\Omega) \approx (\Omega_{SQL}/\Omega)^2$ holds for sideband frequencies $\Omega \approx \Omega_{SQL}$(See Equation 1.89 and the discussion that follows) one can achieve a nearly optimal quadrature angle rotation with a single filter cavity. The quadrature rotation using a single detuned filter cavity is given by [65]

$$\alpha_p(\Omega) \simeq \arctan\left(\frac{(2-\epsilon)\gamma_{\rm fc}\ \Delta\omega_{\rm fc}}{(1-\epsilon){\gamma_{\rm fc}}^2 - {\Delta\omega_{\rm fc}}^2 + \Omega^2}\right) \tag{3.20}$$

where $\gamma_{\rm fc}$ is the filter cavity linewidth and $\Delta\omega_{\rm fc}$ is the filter cavity detuning, both expressed in radial frequency units. And ϵ is given by

$$\epsilon = \frac{f_{FSR}}{\gamma_{\rm fc}} t_{rt}^2 \tag{3.21}$$

where t_{rt}^2 is the round-trip power loss of the filter cavity (not including the input mirror transmission). From Equation 3.16, the desired quadrature rotation requires that

$$\alpha_p(\Omega) = \arctan\big([\Omega_{SQL}/\Omega]^2\big) \tag{3.22}$$

Which can be achieved by setting [65]

$$\Delta\omega_{\rm fc} = \sqrt{1-\epsilon}\gamma_{\rm fc}, \qquad \gamma_{\rm fc} = \sqrt{\frac{2}{(2-\epsilon)\sqrt{1-\epsilon}}}\frac{\Omega_{SQL}}{\sqrt{2}} \tag{3.23}$$

Using Equations 3.23 and 3.21, we may solve for epsilon:

$$\epsilon = \frac{4}{2+\sqrt{2+2\sqrt{1+\left(\frac{2\Omega_{sql}}{f_{FSR}t_{\rm rt}^2}\right)}}} \tag{3.24}$$

after which $\Delta\omega_{\rm fc}$ and $\gamma_{\rm fc}$ follow immediately. Of course, with a shorter filter cavity, a relatively high finesse (≈70000) is required to achieve the required cavity linewidth $\gamma_{\rm fc} \approx 2\pi \times 60\,{\rm Hz}$ [65]. Since the squeezing sidebands must propagate a certain distance inside the cavity to achieve the desired phase shift, the important figure of merit for the filter cavity is the *loss per unit length* which is give by t_{rt}^2/L. Recent measurements have shown that a 16 meter filter cavity with losses of order 1 ppm/meter or lower are readily achievable [59]. Such a filter cavity can produce frequency-dependent squeezed light with roughly 2 dB of low frequency squeezing for radiation pressure noise reduction [65]. In Chapter 5 we will present a rigorous model of a realistic filter cavity with losses and discuss the expected performance of an Advanced LIGO filter cavity in far more detail.

A schematic of the combined system is shown in Figure 3-3. As shown, a separate laser table and SHG are used to produce a field for stabilizing the length of the filter cavity using its lower finesse (≈ 2000) cavity at the second harmonic wavelength (532 nm). This auxiliary laser is also phase locked to the main interferometer laser. This control scheme is currently the baseline design for Advanced LIGO, though we will propose a simpler control scheme in Chapter 7.

3.8 Outlook

We have identified some of the most significant barriers to achieving high levels of squeezing in Advanced GW detectors, and have proposed solutions to overcome them. Specifically, we show how that there are four major deterrents: losses arising from op-

tical components, from mode matching, and from misaligned optical beams; quadrature fluctuations due to length noise in the OPO and alignment jitter; noise arising from backscattered light; radiation pressure noise due to vacuum fluctuation in the orthogonal quadrature. We quantified the contributions from each of these imperfections to the overall performance of a gravitational wave detector like Advanced LIGO, and we show how an in-vacuum OPO, together with an improved control scheme can minimize the impact of all of these noise sources. These proposed solutions, when coupled with a quantum noise filter cavity [42] promise to deliver up to 6 dB of squeezing enhancement across a broad range of frequencies for Advanced LIGO.

In the chapters that follow we discuss the R&D experiments that I performed during my thesis research to develop the two new required technologies. In Chapter 4, we discuss the development of a low phase noise frequency independent squeezed light source operated in vacuum. In Chapters 5 and 6 we discuss our R& D efforts towards producing frequency-dependent squeezed light in the GW frequency band. Finally, we conclude by discussing the mechanical design and control scheme for the Advanced LIGO frequency-dependent squeezed light source based on lessons learned from our prototype experiments.

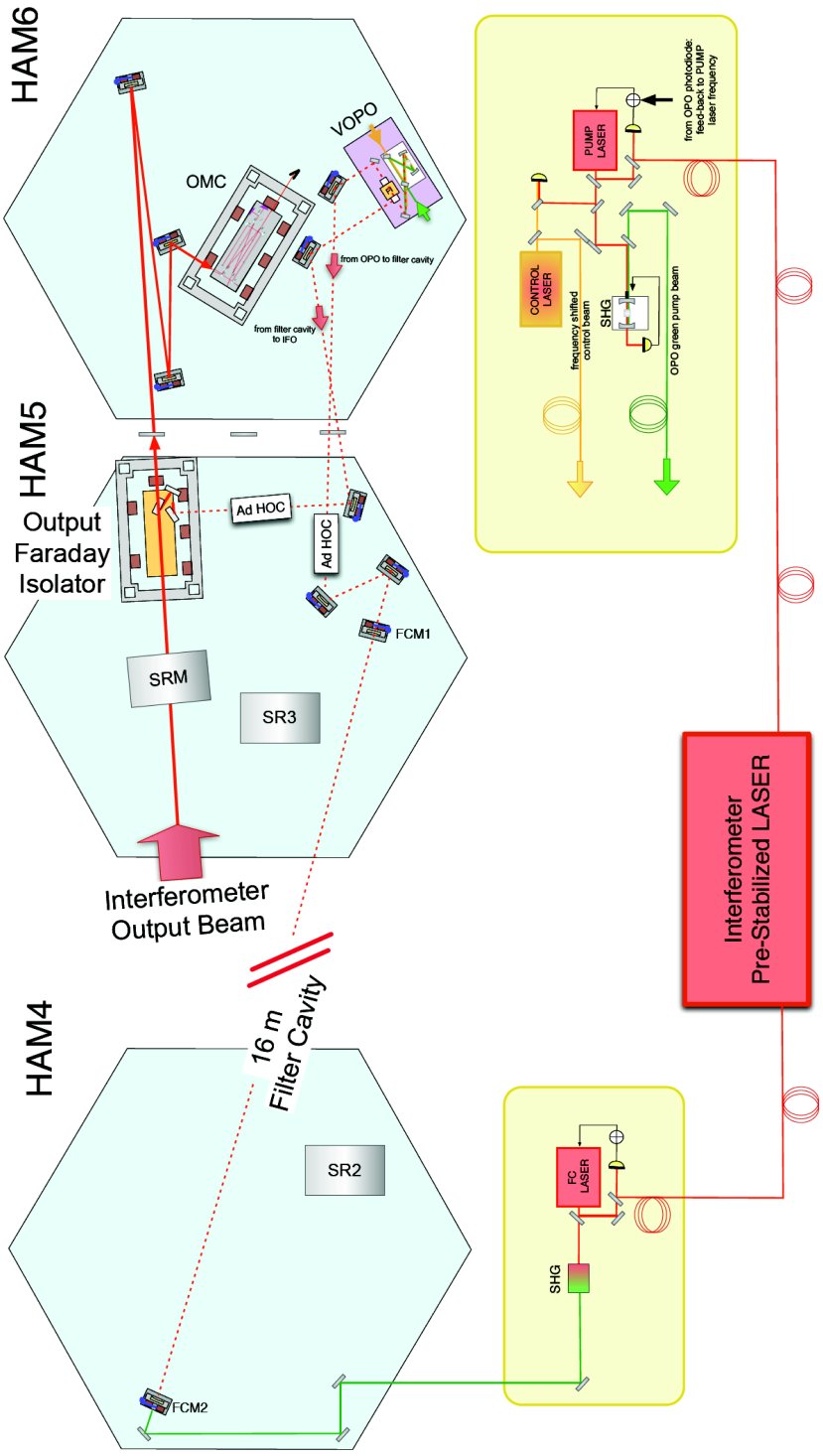

Figure 3-3: Full aLIGO squeezer layout with filter cavity (adapted from [42]). The filter cavity is expected to be added later on on once development has concluded. This figure depicts operating the filter cavity with a separate laser and SHG which are also phase locked to the main interferometer laser. This is our baseline design. A simplified control scheme will be presented in Chapter 7.

Chapter 4

In-vacuum squeezed light source

As discussed in Chapter 3, in order to realize the full potential of squeezed vacuum injection, the OPO cavity must be moved inside of the aLIGO vacuum enclosure to reduce technical noise from backscattered light. Additionally, future squeezed light sources must have a significant reduction in phase noise in order to achieve squeezing levels of 10 dB or higher with achievable levels of loss.

In this chapter, we will discuss the in-vacuum squeezed light source built at MIT over the last year which aims to address both of these technical requirements. Though this experiment took place after the audio-band frequency-dependent squeezing experiment discussed in Chapter 6, we will discuss this experiment first in order to introduce the various components of a frequency *independent* squeezed vacuum source before discussing the more complicated frequency-dependent squeezer. In-vacuum operation of an OPO cavity was demonstrated previously by the McClelland group at ANU [112].

The experiment incorporated the ANU design for the in-vacuum OPO (VOPO) cavity and added some additional in-vacuum subsystems which we wanted to prototype before incorporating them into the final design for Advanced LIGO. First, we wanted to fiber couple the pump and CLF fields into vacuum rather than sending them in through viewports. When the final VOPO cavity is seismically isolated and suspended in the Advanced LIGO, the incident pump and CLF fields would require active alignment control. Fiber coupling the input fields onto the suspended plat-

form housing the VOPO cavity would eliminate the need for these additional servos. Secondly, we wanted to add in-vacuum Homodyne readout as this may be desirable for advanced LIGO and will be a critical technology when implementing quantum non-demolition readout techniques in future GW detectors [47]. The previous experiment at ANU was unable to achieve low phase noise performance despite using an intrinsically low length noise OPO cavity. Another primary goal of this experiment was to design and implement an improved control scheme to achieve a substantial improvement in phase noise performance.

In this chapter we will describe these efforts. The fiber coupling and in-Vacuum homodyne readout have been successfully demonstrated, though further work is needed to address certain technical issues and to increase reliability and demonstrate long-term stable operation. The outcome of the work on prototyping a suitable control scheme was much more definitive: we were able to achieve the lowest level of phase noise ever measured, smaller than the previous best audio band squeezed vacuum source [35, 61] by nearly an order of magnitude.

4.1 Overview of squeezed light source

A detailed layout of the squeezed light source is shown in Figure 4-1. The squeezer consists of an In-air table where the pump, local oscillator (LO), coherent locking field (CLF) and a diagnostic seed field are prepared. These fields are fiber coupled into the vacuum chamber through custom UHV compatible fiber feedthroughs. Once in vacuum the pump and CLF fields are mode matched into the front and rear inputs of the VOPO cavity to generate and control the squeezed vacuum state. The OPO cavity is locked on resonance for 532 nm using the Pound-Drever-Hall technique. The 2Ω error signal for coherent control, previously described in Section 2.7, is measured in reflection from the rear of the VOPO cavity. Both RFPDs for these two servo loops are located on a separate table outside of vacuum and the reflected pump and CLF fields are directed out of vacuum through viewports.

The VOPO cavity, Described in Section 4.1.4, is operated sub-threshold to produce

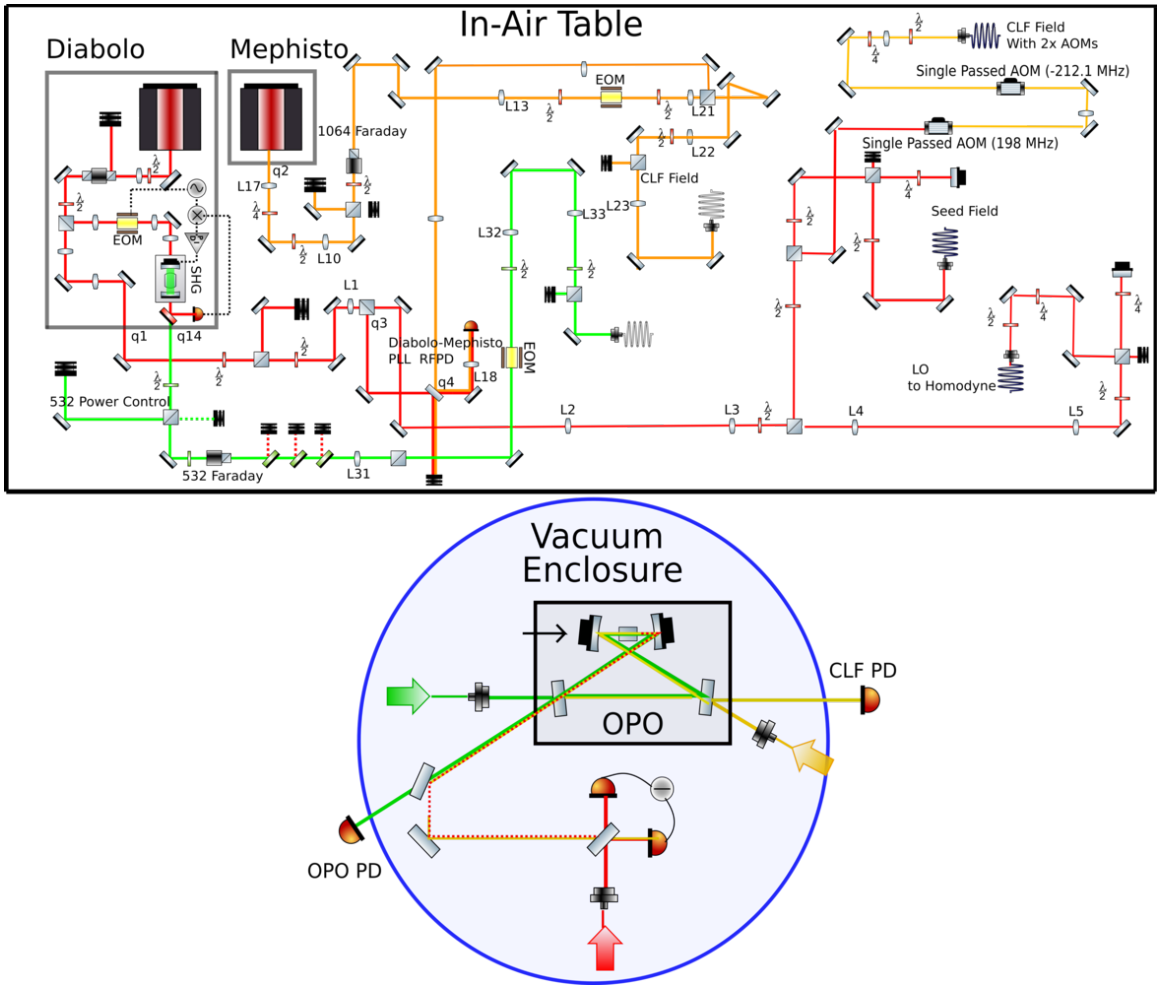

Figure 4-1: Layout of squeezed vacuum source. The pump, CLF, LO, and seed fields are prepared on an in-air table and fiber coupled into vacuum where squeezing is produced and measured using an in-vacuum OPO and homodyne. In this setup, we can generate the CLF using either an auxiliary laser (Innolight Mephisto) which is phase locked to the main laser or a double AOM setup (see Section 4.1.2).

a squeezed vacuum state. The output field, which contains both the squeezed state and the CLF, is characterized using a custom UHV compatible homodyne detector. A picture of the in-vacuum squeezed light source is shown in Figure 4-2

4.1.1 Second harmonic generator

In this experiment, the pump field was generated with a second harmonic generator which is internal to the laser source (Innolight Diabolo). Nonetheless we will walk through a brief description of how a second harmonic generator works. In analogy

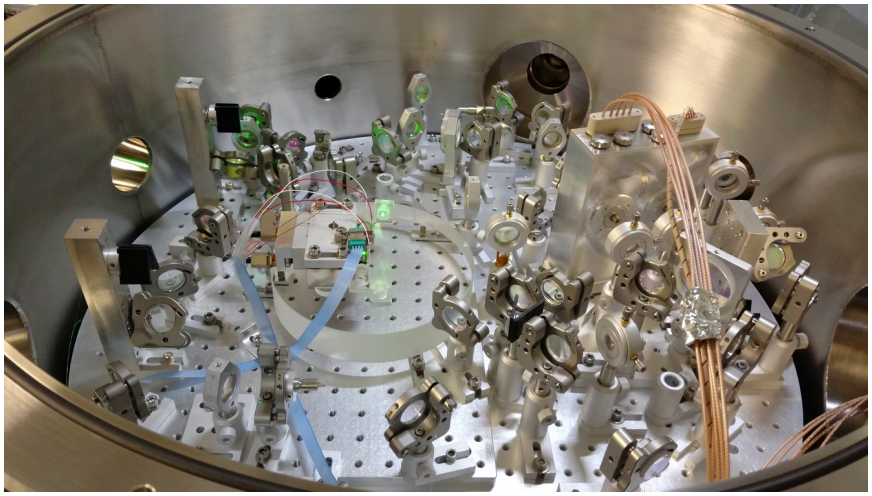

Figure 4-2: Inside the Vacuum enclosure

with Section 2.4.2, we can write the equations of motion for an SHG cavity as [36]:

$$\dot{a} = -\left(\gamma^{tot}_{r,SHG} + i\Delta_r\right) a + \epsilon a^\dagger b + \sqrt{2\gamma^f_{r,SHG}} A_{in,f} \tag{4.1}$$

$$\dot{b} = -\left(\gamma^{tot}_{g,SHG} + i\Delta_g\right) b - \frac{\epsilon^*}{2} a^2 \tag{4.2}$$

We will assume that the detunings are both equal to zero, that we have perfect phase matching (ϵ is real) and that the SHG is resonant for the fundamental field alone so $\gamma^{tot}_{g,SHG} = 1/\tau_{shg} = 2L/c$. We are interested in the steady-state solution, which is given by the solution to

$$0 = -\gamma^{tot}_{r,SHG} \bar{a} + \epsilon \bar{a}^\dagger \bar{b} + \sqrt{2\gamma^f_{r,SHG}} \bar{A}_{in,f} \tag{4.3}$$

$$0 = -\frac{1}{\tau_{SHG}} \bar{b} - \frac{\epsilon}{2} \bar{a}^2 \tag{4.4}$$

Using the input-output relations, given in Equation 2.12, we may solve for the the circulating and exiting fields:

$$\bar{b} = \frac{-\epsilon \bar{a}^2 \tau_{shg}}{2} \tag{4.5}$$

$$\bar{B}_{f,out} = -\epsilon \bar{a}^2 \sqrt{\frac{\tau_{shg}}{2}} \tag{4.6}$$

$$\bar{a} = \frac{\sqrt{2\gamma^f_{r,SHG}}\bar{A}_{f,in}}{\left(\gamma^{tot}_{r,SHG} + \frac{\epsilon^2 \tau_{SHG}|\bar{a}|^2}{2}\right)} \tag{4.7}$$

Note that the equation for $\bar{a}$ is nonlinear and can only be solved numerically. The overall conversion efficiency is given by

$$\eta_{SHG} = \frac{P_{532}}{P_{1064}} = \frac{2|\bar{B}_{f,out}|^2}{|\bar{A}_{f,in}|^2} = \frac{2\gamma^{in}_{r,SHG}\tau_{shg}\epsilon^2|\bar{a}|^2}{\left(\gamma^{tot}_{r,SHG} + \frac{\tau_{shg}\epsilon^2|\bar{a}|^2}{2}\right)^2} \tag{4.8}$$

Note that the conversion efficiency scales with the circulating power ($\propto |\bar{a}|^2$). For the stand-alone SHG discussed in Chapter 6, we typically operated with roughly 300 mW of 1064 nm of fundamental power and achieved conversion efficiencies around 50%.

4.1.2 Generation of the CLF

In the earliest audio-band squeezed vacuum sources using coherent control, the CLF was generated using a single acousto-optic modulator (AOM) [106, 107] to frequency shift a beam at the carrier frequency ω_0 to the desired CLF frequency $\omega_0+\Omega$. However, an AOM will not convert 100% of the incident carrier light to the desired frequency. A portion of the light will remain at the fundamental frequency, while another portion will be shifted into higher order beams with detunings of $n\Omega$ where n is an integer. By momentum conservation, the shifted fields will leave the AOM at an angle proportional to their frequency shift. However, imperfections in the AOM crystal can result in some of the unshifted field scattering into the CLF beam. As will be discussed in detail in Section 4.2.3, the presence of a seed field can result in added technical noise which can degrade the level of squeezing, especially at frequencies in the GW band.

To mitigate this effect, the squeezed light source presented in [106, 107] used a low CLF power and a large CLF frequency (40 MHz) which allowed CLF beam to diverge significantly from all other beam orders so that the 0th order (unshifted)

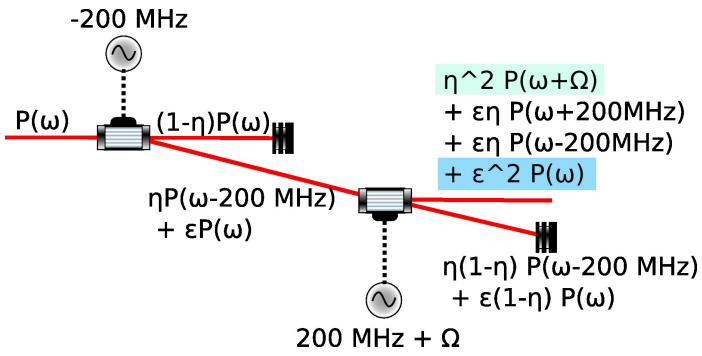

Figure 4-3: Double AOM Setup. After the light is passed through two AOMs, the level of remaining seed light has been attenuated by ϵ^2 where $\epsilon << 1$. This can result in a negligible level of seeding provided that RF crosstalk between the two AOMs is kept to a minimum.

field could be safely dumped[1]. Though they succeeded at producing squeezing at low measurement frequencies, this single AOM design was abandoned for the GEO 600 squeezer. Instead, their CLF is obtained from an auxiliary laser source which is phase locked to the main laser with a frequency offset equal to Ω. This same approach was also used by audio-band squeezers at MIT and ANU.

As depicted in Figure 4-1, the squeezer is capable of generating its CLF using an auxiliary laser phase locked to the main Diabolo laser. However, all squeezing spectra presented in this thesis were actually obtained while we were generating the CLF using a double AOM set-up. Both AOMs have large shift frequencies ($\approx$ 200MHz) to allow for easy isolation of the first order field and the two drive frequencies are offset to produce a CLF with $\Omega = 14.1$MHz. As shown in Figure 4-3, using multiple AOMs can dramatically reduce the level of seed field contamination. If the level of contamination from unshifted light is given by ϵ, then the level of unshifted light after two AOMs can be as low as ϵ^2. In practice, crosstalk between the two RF signals driving the AOMs can result.

This double AOM technique simplifies the control scheme by eliminating the need for an additional phase lock servo. Also, dispensing with an auxiliary laser also eliminates the dominant source of relative frequency noise between the pump and CLF fields, a significant source of phase noise if not properly suppressed.

[1]These choices results in a relatively poor signal-to-noise ratio for the 2Ω servo which can be a limiting source of phase noise.

Table 4.1: Seeding produced by various 200 MHz AOMs. The bottom half correspond to the double AOM set-up with various types of RF cabling

AOM	**Aperture Size**	**Seed contamination (ppm)**
Gooch and Housego AOMO-3200-1113	0.1 mm	3×10^{-1}
AA OptoElectronics MT200	0.5 mm	5×10^{-3}
IntraAction ATM-200-2DA6	2 mm	7×10^{-4}
RF Cable (isolation)	**Seed Contamination (ppm)**	
RG-58 (60 dB)	2×10^{-1}	
RG-142B (90 dB)	2×10^{-4}	
CommScope Heliax (120 dB)	1.3×10^{-7}	

Measurements of seed contamination for various AOMs are shown in Table 4.1. The double AOM setup includes one AA OptoElectronics MT200 and one IntraAction ATM-2002DA6. We found that the contamination was lowest when larger beam diameters were used (which required a larger AOM aperture). Due to RF crosstalk we also found that the performance of the double AOM setup depended strongly on the quality of RF cabling used.

Currently the two AOMs are right next to one another on the optical table. We believe that we are still limited by RF crosstalk and that the performance can be improved significantly by spatially separating the two AOMs. However, we have not observed any degradation in squeezing due to seeding since replacing the original RG-58 cables. With 3 mW of CLF power, the current level of seed contamination is only 0.38 fW. This is nearly four orders of magnitude less than the best measured value for a single AOM. However, based on the single AOM measurements, we should be able to reduce this by another 5 orders of magnitude if RF crosstalk is eliminated completely.

4.1.3 Fiber coupling

As discussed previously, fiber coupling the input fields for the VOPO will be necessary to eliminate the need for active alignment control of the Pump and CLF when the squeezer is interfaced to Advanced LIGO. Incorporating optical fibers into a set-up like ours poses several technical challenges which we will now discuss.

First of all, optical fibers are susceptible to acoustic noise. This can impose both phase and polarization fluctuations on the field propagating through the fiber. For

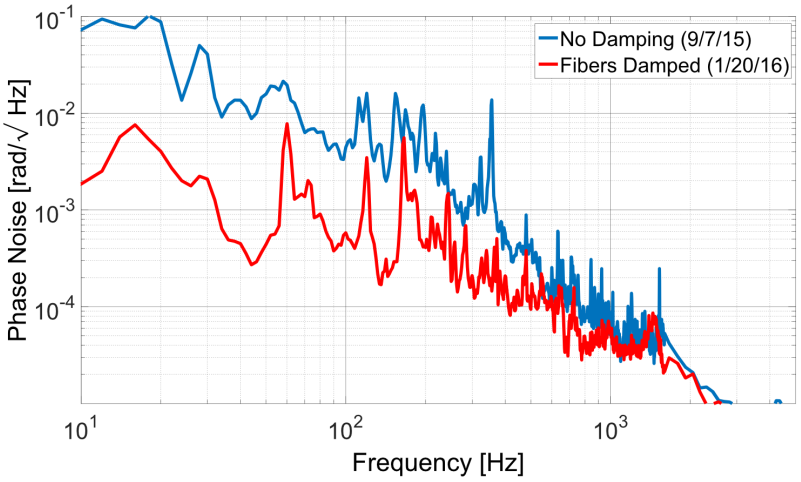

Figure 4-4: Improvement in LO loop free-running phase noise after damping optical fibers. Below 1 kHz we achieved a roughly one order of magnitude reduction in fiber phase noise. Above 1 kHz the phase noise spectrum was dominated by a contribution from SHG length noise.

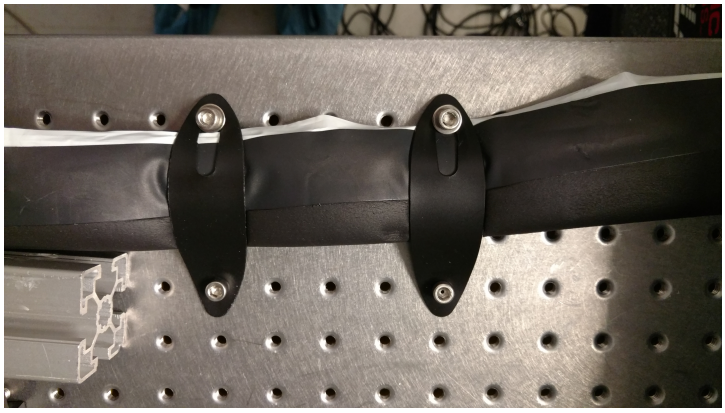

Figure 4-5: Damping of pump fiber with foam tubing.

this reason, we had to carefully isolate the optical fibers from acoustic noise and vibrating surfaces. Figure 4-4 shows the significant drop in the free-running phase noise of the LO servo that we observed after damping the optical fibers. A picture of the damping material is shown in Figure 4-5. This was not carefully optimized and there is most likely plenty of room for improvement.

Secondly, single mode fibers can handle only limited levels of optical power. The level of incident power that an optical fiber can withstand depends on the cross-sectional area of its core. 532 nm fibers require a small core diameter to achieve single mode performance. This is unfortunate given that we require a significant level of 532

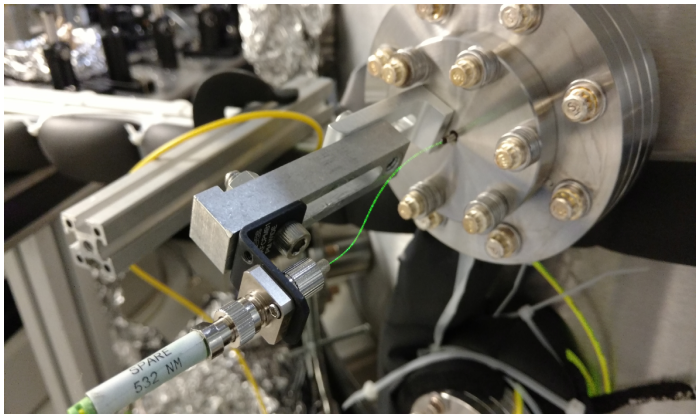

Figure 4-6: Custom 532 nm single mode UHV fiber feedthrough made using UHV compatible epoxy and polyimide coated optical fiber.

nm power to pump the OPO cavity. When coupling into a fiber in free-space, we've found that we can routinely couple up to 300 mW without damaging the input. This is more than enough to meet the needs. However, we've experienced more problems when connecting two fibers with a mating sleeve. Even when taking precautions to keep all fiber surfaces well polished and clean, we periodically damage fibers with 100 mW or less of 532 nm power. Currently, the OPO cavity has a threshold power around 90 mW and we typically operate with between 40-50 mW of pump power. To give us additional headroom, we are planning on increasing the OPO finesse for the Advanced LIGO VOPO.

Thirdly, good quality single-mode UHV fiber feedthoughs and UHV compatible optical fibers are not readily available. This problem is made worse by the uniquely demanding vacuum cleanliness requirements mandated by the LIGO collaboration. We were able to procure suitable polyimide coated single mode fibers from Nufern[2] as well as commercial fiber feedthroughs for the 1064 nm CLF and LO fields. However, due to the power handling requirements, we've needed to develop the own custom fiber feed-through. The current prototype is pictured in4-6

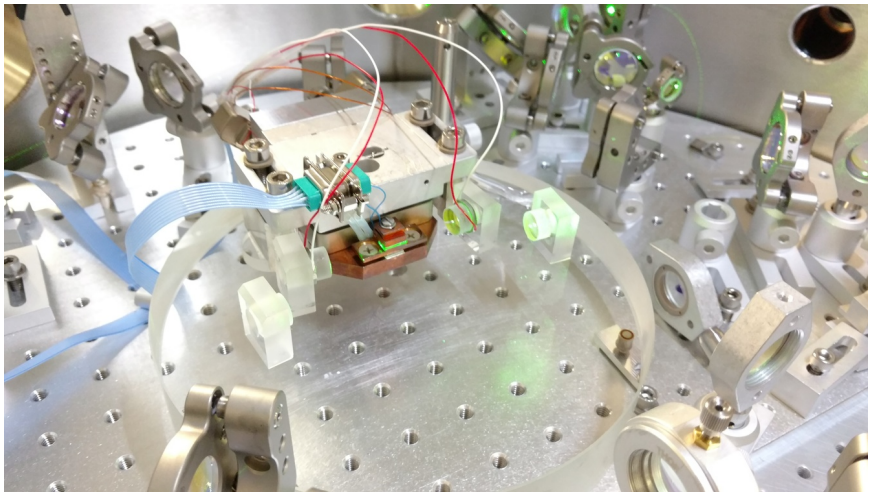

Figure 4-7: The nearly monolithic in-vacuum OPO Cavity

4.1.4 Nearly monolithic in-vacuum OPO cavity

The OPO cavity, depicted in Figure 4-7, is based on the ANU VOPO design used in [112] described in detail in [113], though a motorized translation stage for the OPO crystal was added to allow for crystal translation under vacuum. It was built with help from Georgia Mansell of ANU who visited the lab for 9 months during 2015. The cavity is dually resonant, allowing us to lock the cavity using the pump field without the need for the frequency-shifted subcarrier field used with the GEO squeezer [108]. The dually resonant cavity also acts as a spacial mode cleaner for the pump field and as a filter for the SHG and OPO control sidebands, allowing us to do without the extra mode cleaner cavity required for singly-resonant OPO cavities. As described in the previous chapter, it also features a travelling wave (bow-tie) design to attenuate backscattered light [28]. The optical parameters of the cavity are given in Table 4.2.

The cavity design was inspired by the Advanced LIGO Output Mode Cleaner (OMC). The cavity is monolithic (except for the crystal translation stage) with all four cavity optics glued to super-polished tombstones which are optically contacted to a breadboard made of Corning Ultra-low Expansion (ULE) glass.

As discussed in the previous chapter, length noise on the OPO cavity can be a crippling source of phase noise. It contributed 21 mrad of phase noise with the

[2]Nufern FUD-4194 for 532 nm and Nufern 1060-OCT-P for 1064 nm.

Table 4.2: Cavity parameters for the VOPO

Cavity Parameter	Symbol	Value
Cavity round trip length	L	0.345 m
Free Spectral Range	FSR	849
Finesse (1064 nm)	$\mathcal{F}_{1064}$	37
Finesse (532 nm)	$\mathcal{F}_{532}$	18
Curved mirror ROC	ROC	-50 mm
Cavity Linewidth fundamental (pump)	$\Delta\nu_{1064}(\Delta\nu_{532})$	23 MHz (48 MHz)
Wast size within the crystal (1064)	$\omega_{0(1064)}$	$\approx 30\mu$m
Wast size within the crystal (532)	$\omega_{0(532)}$	$\approx 30\mu$m
Input Coupler reflectivity fundamental (pump)	R_f	0.845 (0.70)
CLF Coupler reflectivity fundamental	R_{CLF}	0.9996
Other intra-cavity losses fundamental	T^l_{1064}	0.11%
Escape efficiency	η_{esc}	$99.1 \pm 0.1\%$
Crystal Interaction length	L_c	10mm
Crystal wedge angle	θ_w	1.15mm
Cavity angle	θ_c	12°
Flat mirror separation	d_f	110 mm
Curved mirror separation	d_c	60.42 mm
Threshold Power	P_{Thresh}	90.5 ± 1.2 mW

previous LIGO Squeezer, which had 0.5 nm RMS of length noise. The primary motivation for the monolithic design of the VOPO was to reduce length noise. A rough measurement of the VOPO length noise was made in-air using frequency stabilized light which was fiber coupled from the LASTI PSL table. The VOPO was locked to this reference laser with a UGF of 200 Hz using an SR560. As shown in figure 4-8, the RMS level of length noise is 2 orders of magnitude lower than before.

Its worth noting that this measurement gives us an answer which is almost certainly a pessimistic overestimate. First of all, the measurement was made in-air. The actual aLIGO VOPO will be suspended in-vacuum on top of a HAM-ISI table, greatly reducing the vibrations which create length noise. Also, the spectrum is sensor noise limited above 5kHz and at lower frequencies is potentially limited by acoustic noise pick-up from the 100 m fiber used to transfer light from the PSL to the squeezer. Finally, we used a modest 200 Hz UGF servo with no boosts. The H1 Squeezer servo had a 2 kHz UGF and a 4/400 Hz boost filter [3]. Most likely, this cavity is over-designed in terms of length noise.

[3]It is the residual length noise after feedback which matters, not the free-running length noise.

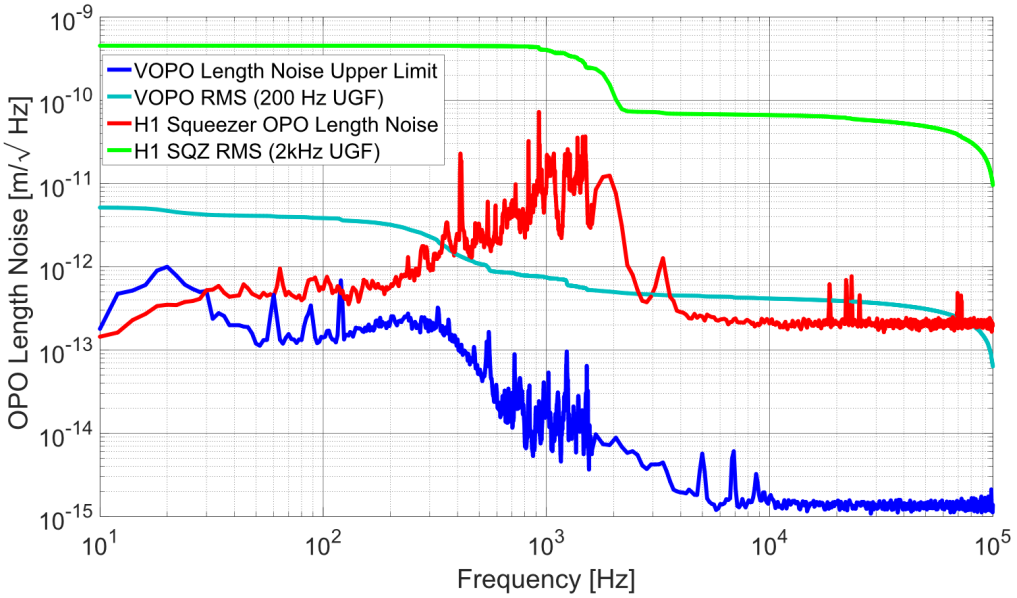

Figure 4-8: Upper limit for the VOPO length noise (closed loop performance). The length noise for the H1 squeezer OPO is also plotted for reference. The new VOPO design achieves a two order of magnitude reduction in RMS length noise.

The the H1 Squeezer OPO design was particularly prone to length noise because it was built using off-the-shelf newport mirror mounts. There's probably a happy medium between this floppy design and the nearly monolithic design used for the current VOPO. We believe that we could get away with a simpler non-monolithic design without seeing a noticeable degradation in phase noise performance. This option will be explored in more detail in Chapter 7 when we propose a design for the Advanced LIGO squeezed vacuum source.

4.1.5 Phase matching

In order to achieve a strong nonlinear interaction in the OPO cavity, the phase relationship between the pump and fundamental fields needs to remain fixed. If this condition is not met, the generated squeezed field will become out of phase with the circulating field generated at earlier times leading to destructive interference. This is depicted by the phasor diagram in panel a) of Figure 4-9. In practice, achieving phase matching is non-trivial since the nonlinear crystal is dispersive ($n(\omega) \neq n(\omega')$).

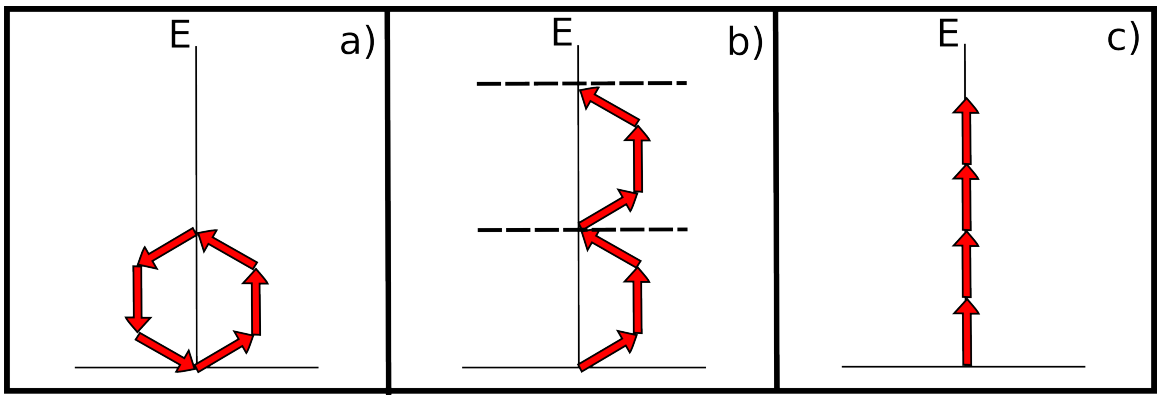

Figure 4-9: Phasor diagrams showing generated fundamental field in an OPA in the phase mismatched, a), quasi-phase matched, b), and phase matched cases.

From the description of parametric down-conversion in Chapter 2 we know that this process must conserve energy ($\omega_g = 2\omega_r$). We have not yet discussed *conservation of momentum*. The condition for phase matching can be formulated in terms of momentum conservation between the annihilated and created photons

$$\hbar\Delta k = \hbar\left(\frac{\omega_g n(\omega_g)}{c} - 2\frac{\omega_r n(\omega_r)}{c}\right) = 0 \tag{4.9}$$

From energy conservation, $\omega_g = 2\omega_r$ and the phase matching condition reduces to $n(\omega_g) = n(\omega_r)$. Typically one measures the strength of the nonlinear interaction by injecting a small seed field into the cavity and operating it as an OPA. Assuming that the seed field remains small so that the second harmonic field experiences no appreciable depletion, the generated seed power as a function of the phase mismatch is given by [13]

$$I(\Delta k L_c) = I_0\left(\frac{\sin \Delta k L_c/2}{\Delta k L_c/2}\right)^2 \tag{4.10}$$

where I_0 is the level of seed power with perfect phase matching and L_c is the interaction length in the nonlinear crystal. In the OPO, we use a technique known as quasi-phase matching where the direction of one crystal axis is switched throughout the interaction length of the crystal to introduce a phase shift of π on the generated field. If this poling is spaced correctly, as depicted in Figure 4-9 b), we may still produce a large nonlinear gain. Comparing Figure 4-9 b) and c), it appears that

Table 4.3: Parameters of KTP [41]

α_{KTP}	$(6.7 \pm 0.7) \times 10^{-6}[1/^{\circ}C]$
$\frac{dn(\omega_r)}{dT}(T = 25^{\circ}C)$	$1.4774 \times 10^{-5}[1/^{\circ}C]$
$\frac{dn(\omega_g)}{dT}(T = 25^{\circ}C)$	$2.4188 \times 10^{-5}[1/^{\circ}C]$
$n(\omega_r)(T = 25^{\circ}C)$	1.830
$n(\omega_g)(T = 25^{\circ}C)$	1.889

quasi-phase matching is intrinsically weaker than ideal phase matching. While this is technically true, in practice quasi-phase matching allows one to use stronger nonlinearities that are not well suited to other phase maching techniques, such as the d_{33} nonlinearity in KTiOPO_4 (KTP). The ideal poling period for quasi-phase matching is given by Λ_{opt}

$$\Lambda_{opt} = \frac{2\pi}{\Delta k} = \frac{\lambda_r}{2(n(\omega_g) - n(\omega_r))} \tag{4.11}$$

In practice the interaction length, the indices of refraction, and the polling period Λ all vary with temperature. The phase mismatch may be expressed as a function of temperature as follows

$$L_c \Delta k = 2\pi L_c(T) \left(\frac{2}{\lambda_r}[n(\omega_g, T) - n(\omega_r, T)] - \frac{1}{\Lambda(T)} \right) \tag{4.12}$$

In order to optimize the phase matching, one must set the crystal temperature equal to the *phase matching temperature* T_0. By expanding Equation 4.12 around T_0 we get [36, 44]

$$L_c \Delta k = 2k_r L_{c,0} \left(\alpha_{KTP}[n(\omega_g) - n(\omega_r)] + \frac{dn(\omega_g)}{dT} + \frac{dn(\omega_g)}{dT} \right) (T - T_0) \tag{4.13}$$

Here, α_{KTP} is the linear coefficient of thermal expansion for KTP and all temperature dependent parameters have been evaluated at room temperature ($25^{\circ}C$) since these values are readily available (see Table 4.3).

4.1.6 Dispersion compensation for co-resonance

With the dully-resonant cavity design, we stabilize the length of the cavity using a PDH servo with the pump field. This keeps the pump field on resonance, but this does not guarantee that the fundamental field will also be resonant because the nonlinear crystal is dispersive. In order to maintain a high and constant level of squeezing we must ensure that the fundamental field remains resonant. The condition for co-resonance is that the round trip phase for both the pump and fundamental fields be a multiple of 2π. When the dual resonance condition is met, the round trip phase shifts are given by

$$\phi_r = k_r[Ln_{cav}(\omega_r, P) + (n(\omega_r) - 1)L_{c,tot}] + \phi_{r,m} = 2\pi m_r \tag{4.14}$$

$$\phi_g = k_g[Ln_{cav}(\omega_g, P) + (n(\omega_g) - 1)L_{c,tot}] + \phi_{g,m} = 2\pi m_g \tag{4.15}$$

where L is the total round trip cavity length, $L_{c,tot}$ is the total crystal length, $\phi_{r,m}$, $\phi_{g,m}$ account for the phase shifts due to reflections off of the cavity mirrors, n_{cav} is the index of refraction outside of the crystal (which depends on the pressure in the vacuum chamber), and m_r, m_g are integers. The PDH lock holds the cavity at a fixed length which one may calculate by solving Equation 4.15 for L. At this length Equation 4.14 will not, in general, be satisfied. The strategy for achieving co-resonance is to vary the crystal length in order to allow both Equations 4.14 and 4.15 to be realized simultaneously. In principle, one may adjust the length by changing the crystal temperature. The temperature dependence of the dispersion mismatch is given by [36]

$$\frac{d\Delta\phi_r}{dT} = k_r L_{c,tot}\left(\alpha_{KTP}[n(\omega_r) - n(\omega_g)] + \frac{dn(\omega_r)}{dT} - \frac{dn(\omega_g}{dT}\right) = \frac{-L_{c,tot}}{2L_c}\frac{d\Delta kL_c}{dT} \tag{4.16}$$

We see that the temperature dependence of the dispersion mismatch is nearly the same as that of the phase mismatch given in Equation 4.13. This makes it difficult to satisfy both conditions simultaneously just by adjusting the temperature alone. For

this reason, the crystal contains a small non poled region in addition to the interaction length L_c. This section is wedged such that the total crystal length may be varied by translating the crystal perpendicular to the beam path. With this additional degree-of-freedom one can show [36] that the phase dispersion mismatch is given by

$$\Delta\phi_r \approx k_r L_c \left(\alpha_{KTP}[n(\omega_r) - n(\omega_g)] + \frac{dn(\omega_r)}{dT} - \frac{dn(\omega_g)}{dT} \right) (T - T_0) + k_r \sin\theta_w [n(\omega_r) - n(\omega_g)](y - y_0) + k_r L[n_{cav}(\omega_r, P) - n_{cav}(\omega_g, P)] \quad (4.17)$$

where T_0 is the phase matching temperature and y_0 is the crystal position where the cavity is co-resonant at the phase matching temperature and when the cavity is under vacuum ($n_{cav} = 1$). From this expression, we note that the required cavity dispersion compensation is pressure dependent (ie the optimal value of y is different from y_0 when the vacuum chamber is vented). For this reason, we required a motorized translation stage for the crystal which could be adjusted after pumpdown. With a 5 mm wide crystal and a wedge angle $\theta_w = 1.15°$, there are approximately 10 locations across the crystal where co-resonance is possible, though in practice only a few are far enough from the edges of the crystal to avoid clipping the beam.

4.1.7 Optimizing the parametric gain

We now examine the parametric gain in the presence of imperfect phase matching and deviation from co-resonance caused by an offset from the ideal temperature (ΔT) or crystal position (Δy). The impact of a phase mismatch is to alter the normalized nonlinear interaction strength [51]

$$x'(\Delta T) = x e^{i\Delta k L_c/2} \mathrm{sinc}(\Delta k L_c/2) \quad (4.18)$$

If co-resonance is not satisfied, then a detuning Δ_r is introduced for the fundamental field.

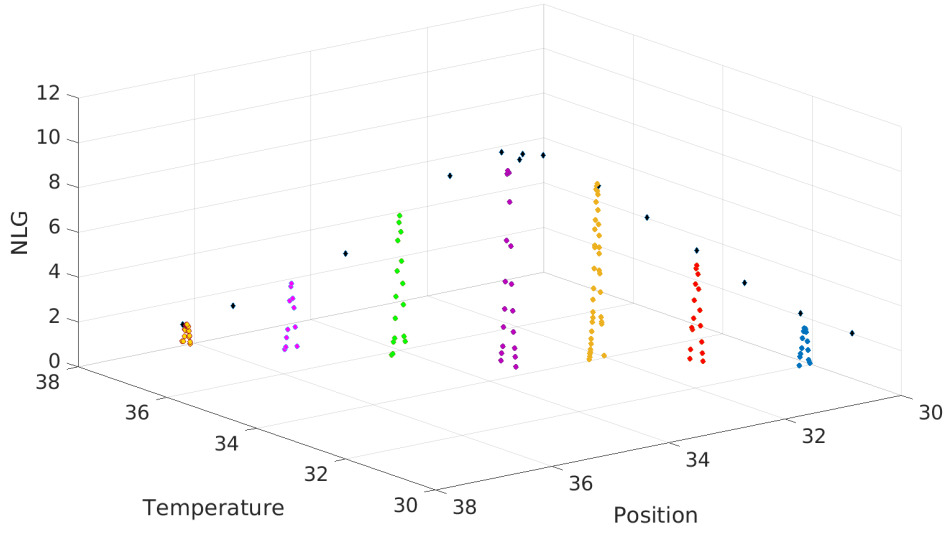

Figure 4-10: Measured nonlinear gain as a function of temperature and crystal position [104]. At each crystal position, the temperature was varied to trace out the dependence of the nonlinear gain on the co-resonance condition. The peak of each measurement corresponds to co-resonance at that particular crystal position. After measuring at various positions, the optimal temperature and crystal position can be determined by fitting the data to Equation 4.21.

$$\Delta_a(\Delta T, \Delta y) = \frac{\Delta\phi_r}{\tau} \tag{4.19}$$

Typically, we determine the parametric gain of the OPO by injecting a small seed field through the CLF mirror and measuring the amplification of the transmitted seed field. The resulting parametric gain is given by [36]

$$G = \frac{1 + (\Delta_r/\gamma_r^{tot})^2}{(1 + (\Delta_r/\gamma_r^{tot})^2 - |x'|^2)^2} |1 + i\frac{\Delta_r}{\gamma_r^{tot}} + |x|^2 e^{i(\theta_b + \Delta k L_c/2)}|^2 \tag{4.20}$$

Choosing θ_b to optimize G yields

$$G_{max}(x, \Delta T) = \left(1 - \frac{x\ \mathrm{sinc}(\Delta k L_c/2)}{\sqrt{1 + (\Delta_r/\gamma_r^{tot})^2}}\right)^{-2} \tag{4.21}$$

which reduces to a value g, which we will refer to as the nonlinear gain, when the cavity is co-resonant and perfectly phase matched

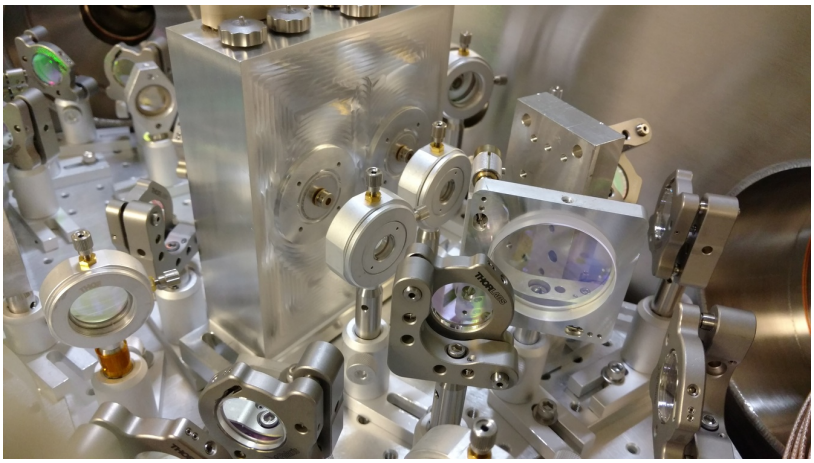

Figure 4-11: Picture of the in-vacuum homodyne detector. The circuit is enclosed in a hermetically sealed aluminium box from SRI Hermetics.

$$G_{max}(x) = \frac{1}{(1-x)^2} \equiv g \tag{4.22}$$

For KTP, the HWHM of the sinc function describing the phase matching as a function of ΔT is around 2°C. The dependence of Δ_r/γ_r^{tot} on ΔT is much larger and leads to a HWHM for G_{max} of ≈ 0.1 degrees for the cavity. This means that **the level of squeezing produced by the OPO is far more sensitive to temperature fluctuations than that of a cavity which is resonant for the fundamental field alone**. This is the main technical drawback for using a doubly-resonant design.

In practice, one must measure the parametric gain as a function of temperature and crystal position to find the optimal operating point. The standard procedure for doing this is described in [98]. The measurement is shown in Figure 4-10 which determined the phase matching temperature to be $33.58°C$ in-air [104] and $33.36°C$ when under vacuum [105] [4].

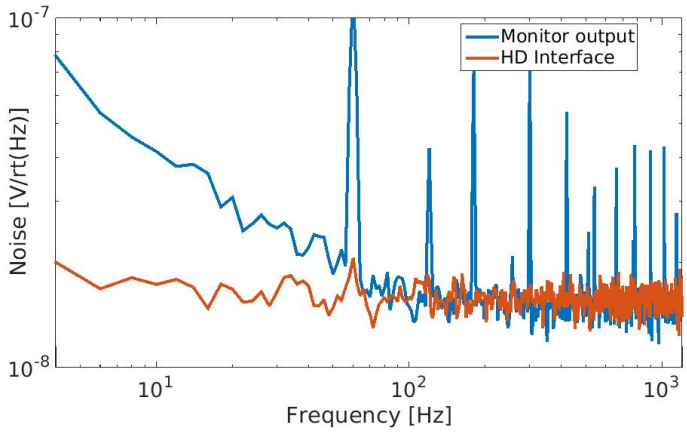

Figure 4-12: Homodyne Low frequency noise performance. The interface board noise spectrum has been divided by the relative gain between the two outputs for clarity.

4.1.8 In-vacuum homodyne readout

The homodyne detector, which is described in detail in several LIGO technical documents [56, 57], is designed to have a dark noise level 20 dB below shot noise for 1 mW of LO Power. It has comparable noise performance to the AEI homodyne used during the H1 Squeezing experiment and features a few minor improvements. The detector has higher bandwidth on the DC path (800 kHz instead of 100 kHz), it uses a series resonant circuit design for the RF path for better noise performance and isolation from the DC path, and has additional low bandwidth single PD readouts for convenience. This circuit was enclosed inside of a hermetically sealed and UHV compatible box and installed in the vacuum chamber. It is pictured in Figure 4-11.

It is reasonably well described in [57]. A homodyne interface box was later designed which, among other functions, adds some additional pre-amplification which makes it easier to achieve good low frequency noise performance. Figure 4-12 shows a comparison in noise performance between the monitor output on the homodyne and the pre-amplified output from the interface board. As shown here, the former can sometimes deteriorate when plugged into test equipment.

[4]These values should be the same, in principle, but are slightly offset due to sensor error. The thermistor doesn't measure the crystal temperature but that of a metal block in thermal contact with the crystal. The thermistor value for the phase matching temperature ends up depending on both the circulating pump power and the pressure in the chamber

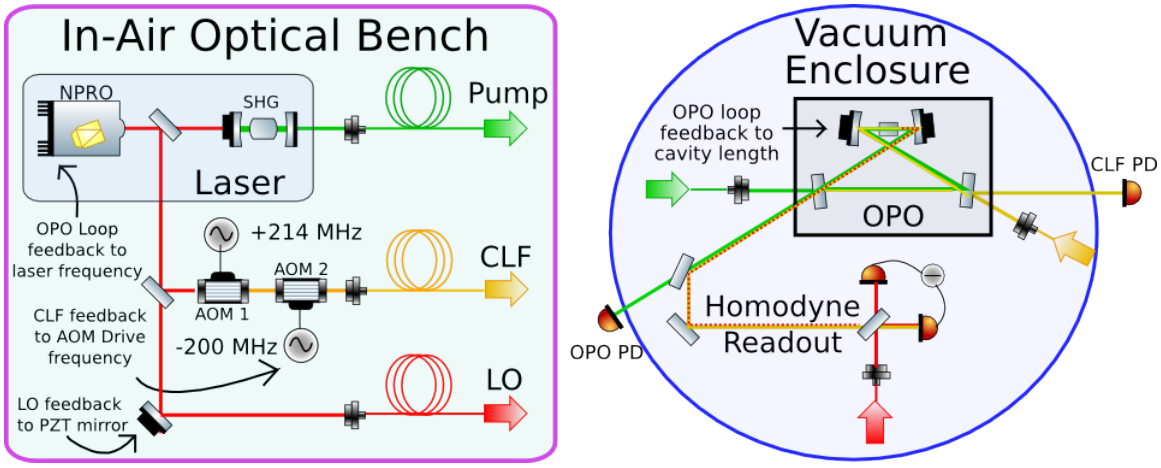

Figure 4-13: Simple schematic of VOPO experiment control scheme. The OPO servo employs feedback to both the cavity length and pump laser frequency. The CLF servo feeds back to a VCO driving of one of the AOMs. The LO servo feeds back to a piezo which actuates on the LO field phase.

4.2 Control scheme performance and technical noise

Due to the double AOM technique, the control system for this experiment was actually quite simple. A depiction of the control scheme is given in Figure 4-13. We will briefly describe the three servos and their noise performance.

4.2.1 OPO length servo

As discussed in Chapter 3, OPO length noise limited the phase noise performance of the previous LIGO squeezer. In principle, any fluctuations in detuning can result in phase noise and should be suppressed. The OPO servo typically used a bandwidth of between 10-20 kHz with feedback to both the OPO length and pump laser frequency (crossover frequency of 250 Hz). An open-loop transfer function is shown in Figure 4-14. Figure 4-15 shows a typical calibrated error signal spectrum for the current operating conditions (UGF 10 kHz with a roughly 1/f loop shape), which is shot noise limited at all frequencies. The shot noise level is relatively high since the modulation depth was kept modest to avoid adding additional RF phase noise. In hindsight, it appears that a slightly lower UGF around 5kHz would have been optimal.

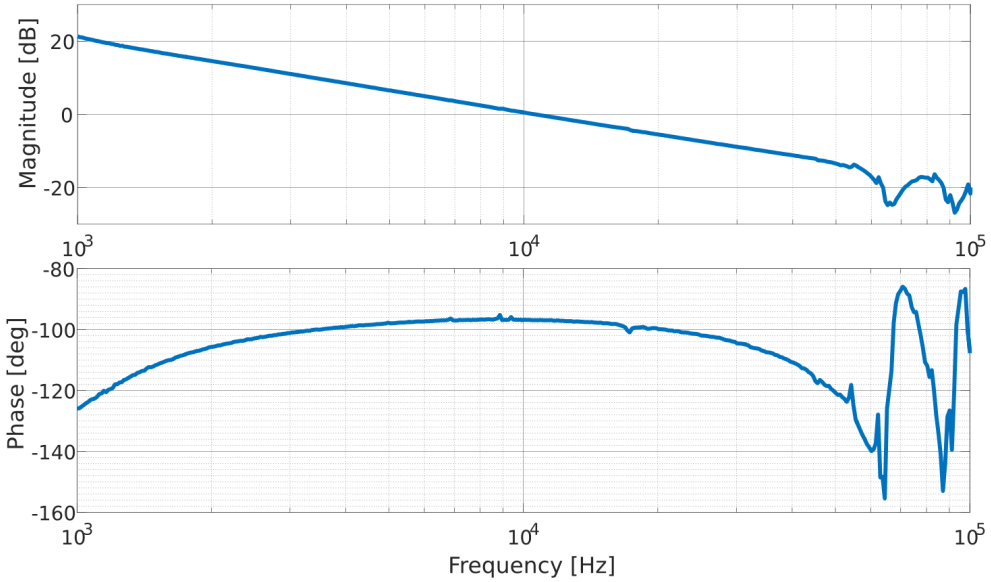

Figure 4-14: A transfer function for the OPO servo. With a single 10 Hz/1 kHz boost enabled, the loop has a roughly 1/f response with a 10 kHz UGF and around 80 degrees of phase margin. This servo achieves shot noise limit performance at all frequencies. Figure 4-15 shows an error signal spectrum with the current operating parameters.

4.2.2 Coherent locking

As described in Section 2.7, two servos are required to stabilize the squeezing angle: one to stabilize the CLF phase relative to the pump phase (CLF loop) and another to stabilize the LO phase relative to the CLF phase (LO loop).

For the CLF loop, we fed back to a VCO (Marconi 2026) providing the RF drive for one of the AOMs. A typical open-loop transfer function is shown in Figure 4-16. This servo was typically operated with a unity gain frequency of 20 kHz. Higher bandwidths would only be beneficial if the shot noise level were reduced. A typical error signal spectrum is shown in Figure 4-17.

The LO servo used a Noliac 2123 ring PZT actuator which had a fundamental resonance around 90 kHz. Initially, we operated this loop with a UGF around 10 kHz, but over time the piezo assembly developed a feature around 20 kHz which limited the bandwidth to 5 kHz. Higher unity gain frequencies would have been beneficial. Though, in Advanced LIGO, the unity gain must be kept low enough to keep the control sidebands resonating in the arm cavities (which have a free spectral range

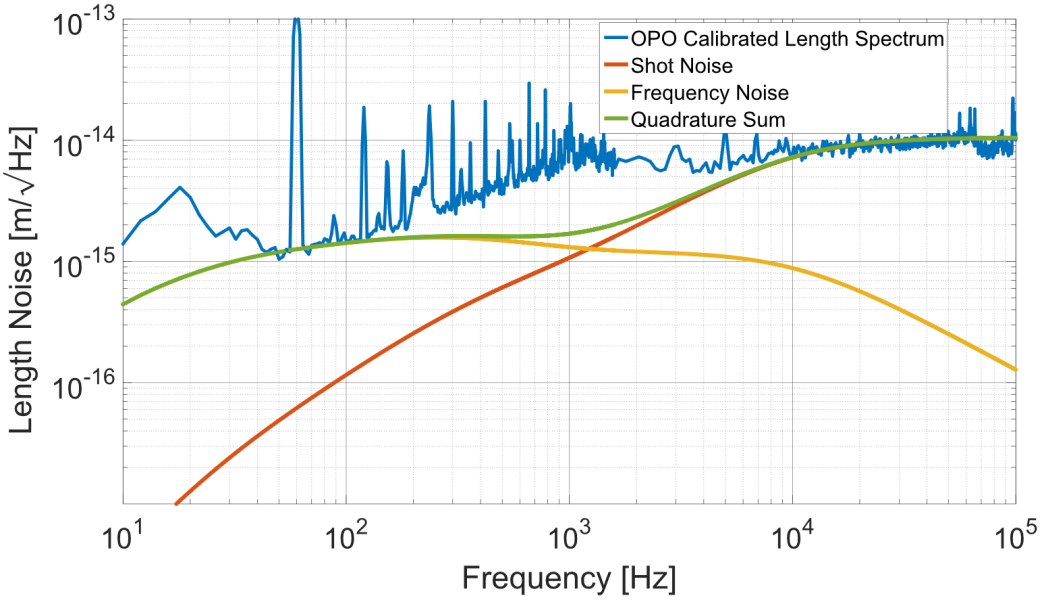

Figure 4-15: Calibrated error signal for OPO Servo showing contributions from shot noise and frequency noise. The servo is completely shot noise limited.

of $\approx 37.5\,\mathrm{kHz}$). A typical transfer function is shown in Figure 4-18 and a typical calibrated error signal is shown in Figure 4-19.

4.2.3 Technical noise from the seed field

When a small seed field is present on the CLF, classical noise on the seed field can degrade the squeezing at low frequencies. Additionally, classical noise on the pump field can be transferred to the seed field via the nonlinear interaction in the OPO cavity[5]. This becomes an issue if the contribution to the total variance of the output field due to classical noise is comparable to or larger than the contribution from quantum noise. To calculate the impact of classical noise, we will use the model developed in [51]. Further discussions of this model may be found in several theses [50, 70, 98].

In order to account for classical noise couplings between the seed and pump field we must expand the formalism presented in Section 2.4.2 to include the required cross-coupling terms. One can derive the equations that follow by starting from Eqn. 2.13

[5]When the seed amplitude is zero, this coupling becomes second order. For an OPO which is truly vacuum seeded, classical noise on the pump field is not an issue

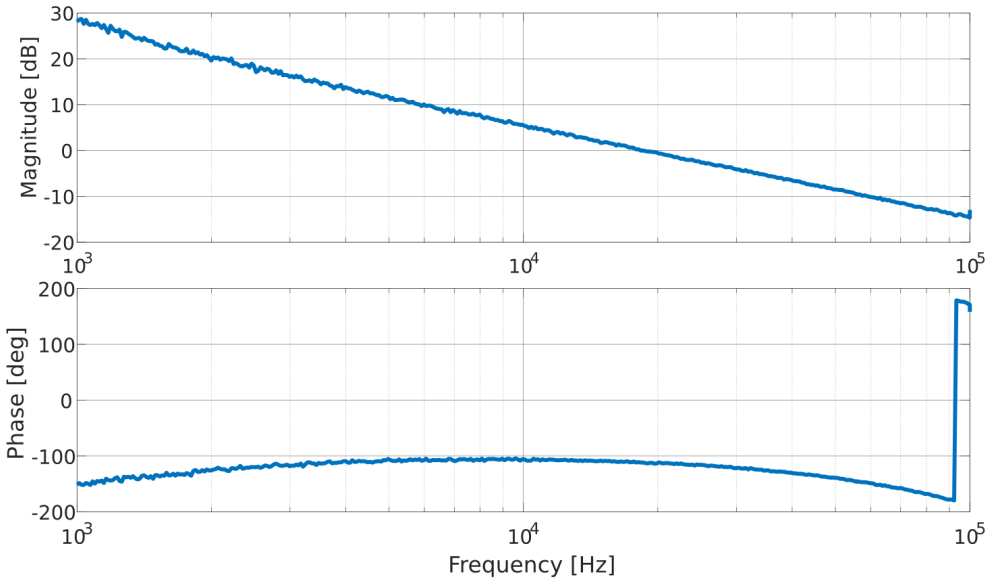

Figure 4-16: Typical transfer function for the CLF servo. UGF of 20 kHz and 70 degrees of phase margin. At high frequencies, we see considerable phase loss due to the sound wave propagation time across the crystal. High bandwidth operation would require an AOM with a smaller crystal.

and no longer assuming that $\bar{a}$ and δb are zero. As shown in Chapter 5 of [70], Equation 2.20 becomes:

$$\delta \mathbf{X}^f_{out}(\Omega) = \Theta_f \delta \mathbf{X}^f_{in} + \Theta_{clf} \delta \mathbf{X}^{clf}_{in} + \Theta_l \delta \mathbf{X}^l_{in} + \Theta_\Delta \tag{4.23}$$

Where the definitions for δX^i_{in} are generalizations of those given in Eqn. 2.22:

$$\delta X = \sqrt{2} \begin{pmatrix} \delta A_1 \\ \delta A_2 \\ \delta B_1 \\ \delta B_2 \end{pmatrix} \equiv \begin{pmatrix} \delta X_1 \\ \delta X_2 \\ \delta Y_1 \\ \delta Y_2 \end{pmatrix} \tag{4.24}$$

And the noise transfer functions are defined as

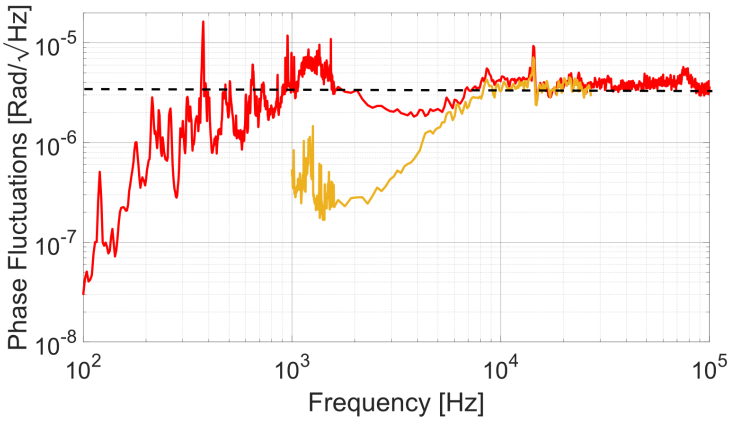

Figure 4-17: Calibrated error signal for CLF Servo showing contributions from shot noise (dashed black line) and SHG Length noise (Orange Trace)

$$\Theta_f = \Gamma[\mathbf{M}_f(i\Omega - \mathbf{M})^{-1}\mathbf{M}_f - \mathbf{I}]\Gamma^{-1} \tag{4.25}$$

$$\Theta_{clf} = \Gamma\mathbf{M}_f(i\Omega - \mathbf{M})^{-1}\mathbf{M}_{clf}\Gamma^{-1} \tag{4.26}$$

$$\Theta_l = \Gamma\mathbf{M}_f(i\Omega - \mathbf{M})^{-1}\mathbf{M}_l\Gamma^{-1} \tag{4.27}$$

$$\Theta_\Delta = \Gamma\mathbf{M}_f(i\Omega - \mathbf{M})^{-1}\chi_\Delta \tag{4.28}$$

where Γ, defined previously in Equation 2.22, is the operator for transforming from the sideband picture to the two-photon picture. Here we've generalized Eqn. 2.18 to include additional cross coupling terms between the seed and pump field.

$$\mathbf{M} = \begin{pmatrix} -\gamma_r^{tot} & \epsilon\beta e^{i\theta_B} & \epsilon\alpha e^{-i\theta_A} & 0 \\ \epsilon^*\beta e^{-i\theta_B} & -\gamma_r^{tot} & 0 & \epsilon^*\alpha e^{i\theta_A} \\ -\epsilon^*\alpha e^{i\theta_A} & 0 & -\gamma_g^{tot} & 0 \\ 0 & -\epsilon\alpha e^{-i\theta_A} & 0 & -\gamma_g^{tot} \end{pmatrix} \tag{4.29}$$

where we have assumed that we are perfectly co-resonant ($\Delta_a = \Delta_b = 0$) and have expressed the DC circulating field at the fundamental frequency as $\bar{a} = \alpha e^{i\theta_A}$ and M_i

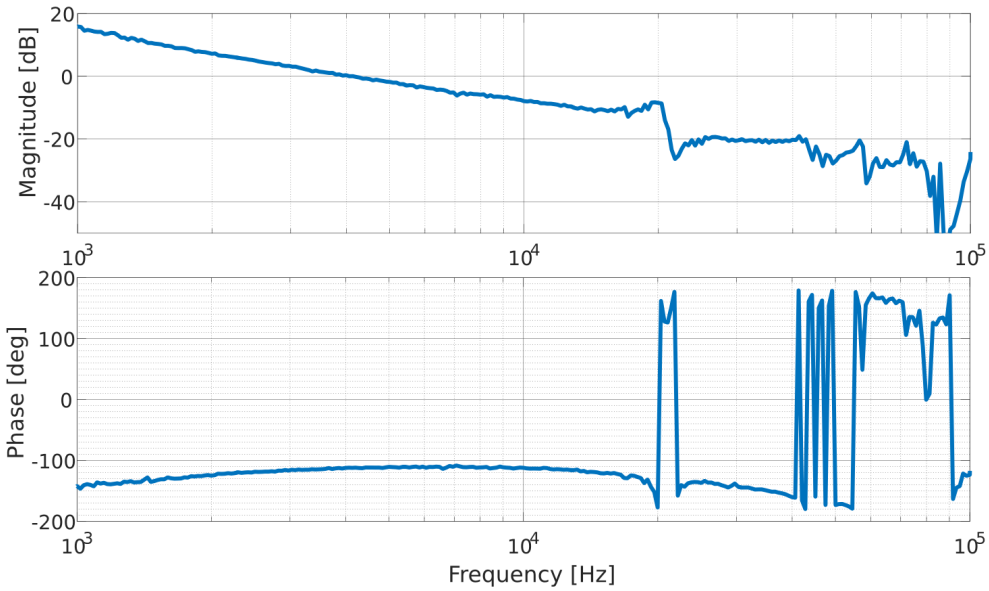

Figure 4-18: Open Loop transfer function for LO servo.

is defined as

$$\mathbf{M}_i = \begin{pmatrix} \sqrt{2\gamma_r^i} & 0 & 0 & 0 \\ 0 & \sqrt{2\gamma_r^i} & 0 & 0 \\ 0 & 0 & \sqrt{2\gamma_g^i} & 0 \\ 0 & 0 & 0 & \sqrt{2\gamma_g^i} \end{pmatrix} \tag{4.30}$$

and χ_Δ represents the coupling of detuning fluctuations ($\delta\Delta_{a,b}$) to the output fields and is given by

$$\chi_\Delta = \begin{pmatrix} -i\alpha e^{i\theta_A}\delta\Delta_a \\ i\alpha e^{-i\theta_A}\delta\Delta_a \\ -i\beta e^{i\theta_B}\delta\Delta_b \\ i\alpha e^{-i\theta_B}\delta\Delta_b \end{pmatrix} \tag{4.31}$$

Using these expressions we may calculate the variance of the output field. Before computing this expression, it is useful to make a few simplifying assumptions. First we will assume that $\theta_B/2 = \pi/2$, as required for Advanced LIGO. Second, we are only looking at squeezing sidebands in the audio band, so we may neglect Ω. Third, we assume that the phase matching is perfect such that $\epsilon^* = \epsilon$. Also, we can set all

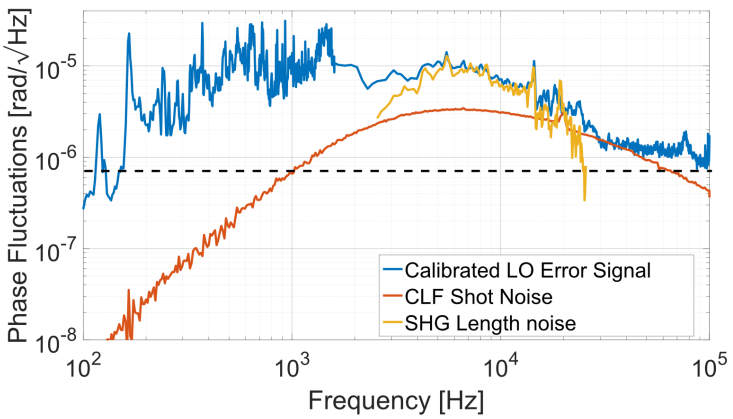

Figure 4-19: Calibrated error signal for LO Servo showing contributions from SHG length noise, shot noise, and CLF loop shot noise.

variances due to entering vacuum fluctuations equal to unity. Finally, I'll choose to neglect the detuning noise term, Θ_Δ. Applying these assumptions to Eqn. 4.23 and computing the variance yields:

$$V_1^{out} = |\Theta_f^{(1,1)}|^2 + |\Theta_l^{(1,1)}|^2 + |\Theta_{clf}^{(1,1)}|^2 V_1^{clf,in} + |\Theta_f^{(1,3)}|^2 V_1^{pump,in} + |\Theta_l^{(1,3)}|^2 + |\Theta_{clf}^{(1,3)}|^2 + |\Theta_f^{(1,4)}|^2 V_2^{pump,in} + |\Theta_l^{(1,4)}|^2 + |\Theta_{clf}^{(1,4)}|^2 + |\Theta_\Delta^{(1)}|^2 \tag{4.32}$$

$$V_2^{out} = |\Theta_f^{(2,2)}|^2 + |\Theta_l^{(2,2)}|^2 + |\Theta_{clf}^{(2,2)}|^2 V_2^{clf,in} + |\Theta_f^{(2,3)}|^2 V_1^{pump,in} + |\Theta_l^{(2,3)}|^2 + |\Theta_{clf}^{(2,3)}|^2 + |\Theta_f^{(2,4)}|^2 V_2^{pump,in} + |\Theta_l^{(2,4)}|^2 + |\Theta_{clf}^{(2,4)}|^2 + |\Theta_\Delta^{(2)}|^2 \tag{4.33}$$

Where, to first order in α the above coefficients are given by

$$\Theta_f^{(1,1)} = \frac{2\gamma_r^f}{\gamma_r^{tot}(1+x)} - 1, \quad \Theta_l^{(1,1)} = \frac{2\sqrt{\gamma_r^f \gamma_r^l}}{\gamma_r^{tot}(1+x)}, \quad \Theta_{clf}^{(1,1)} = \frac{2\sqrt{\gamma_r^f \gamma_r^{clf}}}{\gamma_r^{tot}(1+x)} \tag{4.34}$$

$$\Theta_f^{(2,2)} = \frac{2\gamma_r^f}{\gamma_r^{tot}(1-x)} - 1, \quad \Theta_l^{(2,2)} = \frac{2\sqrt{\gamma_r^f \gamma_r^l}}{\gamma_r^{tot}(1-x)}, \quad \Theta_{clf}^{(2,2)} = \frac{2\sqrt{\gamma_r^f \gamma_r^{clf}}}{\gamma_r^{tot}(1-x)} \tag{4.35}$$

$$\Theta_f^{(1,3)} = \frac{2\alpha\epsilon\cos\theta_A\sqrt{\gamma_g^f \gamma_r^f}}{\gamma_r^{tot}\gamma_g^{tot}(1+x)}, \quad \Theta_l^{(1,3)} = \frac{2\alpha\epsilon\cos\theta_A\sqrt{\gamma_g^l \gamma_r^f}}{\gamma_r^{tot}\gamma_g^{tot}(1+x)}, \quad \Theta_{clf}^{(1,3)} = \frac{2\alpha\epsilon\cos\theta_A\sqrt{\gamma_g^{clf} \gamma_r^f}}{\gamma_r^{tot}\gamma_g^{tot}(1+x)} \tag{4.36}$$

$$\Theta_f^{(1,4)} = -\frac{2\alpha\epsilon\sin\theta_A\sqrt{\gamma_g^f\gamma_r^f}}{\gamma_r^{tot}\gamma_g^{tot}(1+x)},\ \ \Theta_l^{(1,4)} = -\frac{2\alpha\epsilon\sin\theta_A\sqrt{\gamma_g^l\gamma_r^f}}{\gamma_r^{tot}\gamma_g^{tot}(1+x)},\ \ \Theta_{clf}^{(1,4)} = -\frac{2\alpha\epsilon\sin\theta_A\sqrt{\gamma_g^{clf}\gamma_r^f}}{\gamma_r^{tot}\gamma_g^{tot}(1+x)} \tag{4.37}$$

$$\Theta_f^{(2,3)} = \frac{2\alpha\epsilon\sin\theta_A\sqrt{\gamma_g^f\gamma_r^f}}{\gamma_r^{tot}\gamma_g^{tot}(1-x)},\ \ \Theta_l^{(2,3)} = \frac{2\alpha\epsilon\sin\theta_A\sqrt{\gamma_g^l\gamma_r^f}}{\gamma_r^{tot}\gamma_g^{tot}(1-x)},\ \ \Theta_{clf}^{(2,3)} = \frac{2\alpha\epsilon\sin\theta_A\sqrt{\gamma_g^{clf}\gamma_r^f}}{\gamma_r^{tot}\gamma_g^{tot}(1-x)} \tag{4.38}$$

$$\Theta_f^{(2,4)} = \frac{2\alpha\epsilon\cos\theta_A\sqrt{\gamma_g^f\gamma_r^f}}{\gamma_r^{tot}\gamma_g^{tot}(1-x)},\ \ \Theta_l^{(2,4)} = \frac{2\alpha\epsilon\cos\theta_A\sqrt{\gamma_g^l\gamma_r^f}}{\gamma_r^{tot}\gamma_g^{tot}(1-x)},\ \ \Theta_{clf}^{(2,4)} = \frac{2\alpha\epsilon\cos\theta_A\sqrt{\gamma_g^{clf}\gamma_r^f}}{\gamma_r^{tot}\gamma_g^{tot}(1-x)} \tag{4.39}$$

and the terms due to detuning fluctuations are given by

$$\Theta_\Delta^{(1)} = 0, \quad \Theta_\Delta^{(2)} = \frac{2\alpha e^{i\theta_A}(\delta\Delta_a - \frac{\epsilon\beta}{\gamma_g^{tot}}\delta\Delta_b)\sqrt{2\gamma_r^f}}{\gamma_r^{tot}(1+x^2)} \tag{4.40}$$

We may recover the variances V_+ and V_- from Eqns. 2.27 and 2.28 by setting the seed field amplitude equal to zero in Eqns. 4.32 and 4.33. To avoid degrading the interferometer spectrum with technical noise, we require that the contribution due to classical noise be at least a factor of ten below the quantum noise level[6]. The ratio of classical noise to quantum noise in each quadrature may be computed as follows:

$$\frac{V_{1,classical}}{V_+} = \frac{V_1^{out} - V_+}{V_+} \leq 0.1,\ \ \frac{V_{2,classical}}{V_-} = \frac{V_2^{out} - V_-}{V_-} \leq 0.1 \tag{4.41}$$

From Eqns. 4.32 and 4.33, we see that the only information we need to determine everything is the quadrature variances of the input fields normalized to their respective shot noise levels. As an example, we calculate $V_2^{clf,in}$ from a phase noise amplitude spectral density $s_\phi(\Omega)$ (in radians/rt(Hz)) by dividing by the shot noise amplitude spectral density in the phase quadrature:

[6]In principle, it is only the noise in the squeezed quadrature that effects the strain sensitivity, provided that we've included an appropriate filter cavity. In practice, however, we'd like to be able to characterize the quantum noise in all quadratures for diagnostic purposes prior to injecting into the interferometer. Also, the requirement for the squeezed quadrature can be relaxed somewhat when allowing for realistic levels of optical loss between the squeezer and the interferometer readout.

$$V_2^{clf,in} = \left(\frac{s_\phi(\Omega)}{\sqrt{2\hbar\omega_r / P_{seed}}} \right)^2 \tag{4.42}$$

where P_{seed} for the case of the experiment was 0.38 fW. With this seed power level, we can place some constraints on the required noise performance of the pump and seed field. The pump field must have a relative intensity noise (RIN) of $\leq 4 \times 10^{-3}\, 1/\sqrt{\text{Hz}}$ and a relative phase noise with respect to the local oscillator field of $\leq 3 \times 10^{-3}\, \text{rad}/\sqrt{\text{Hz}}$ at all measurement frequencies within the detection band (10 Hz - 10 kHz). Likewise the seed field must have a RIN$\leq 0.25\, 1/\sqrt{\text{Hz}}$ and a relative phase noise with respect to the local oscillator field of $\leq 3 \times 10^{-3}\, \text{rad}/\sqrt{\text{Hz}}$. We see that these requirements are quite reasonable. As a result we did not have any issues with technical noise from the seed field with the double AOM setup once we reduced RF crosstalk between the two AOMs.

4.2.4 Comparison with technical noise from backscattered light

We note that the noise coupling due to path length fluctuations between the readout and squeezed light source discussed in 3.5 in the context of the backscattered light field can, in principle, add technical noise to the seed field as well. This is discussed in Chapter 6 of Sheila Dwyer's thesis [36]. However, with only 0.38 fW of seed field incident on the OPO, this is not expected to be a limiting noise source. By comparison, the backscatter calculation for a suspended VOPO with no added Faraday Isolator presented in Figure 3-2 correspond to a seed power level of roughly 1 nW incident on the input coupler of the VOPO. For this reason, all noise couplings presented in the previous subsection which are proportional to α, such as down-conversion of classical noise on the pump field, will be more of an issue for the backscattered field than they will be for the seed field. We will discuss these noise couplings in detail in Chapter 7.

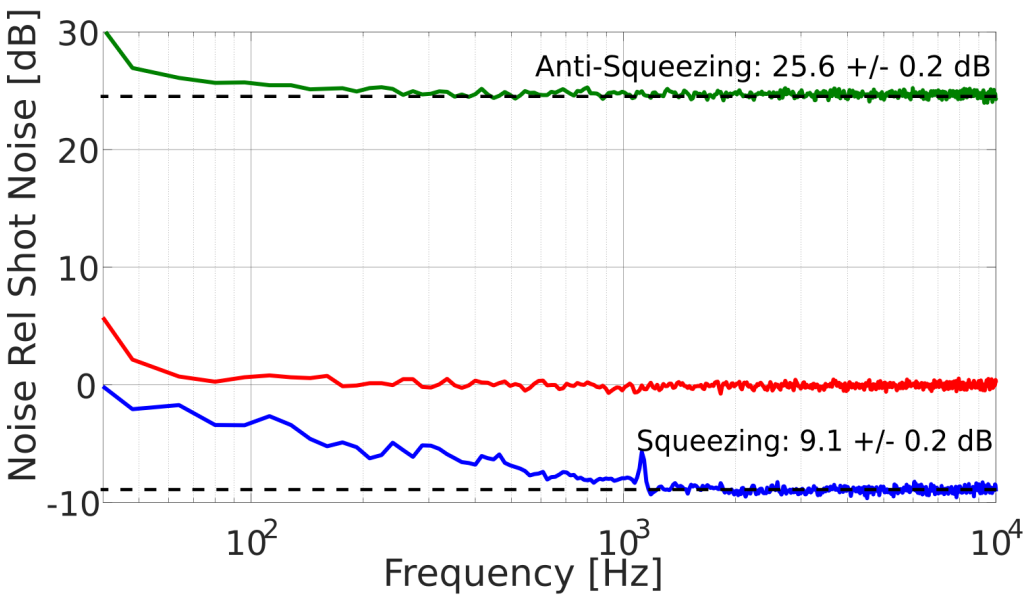

Figure 4-20: Highest level of measured squeezing (in-air). This spectrum was taken prior to optimizing the readout for low backscatter performance.

4.3 Squeezed light source performance

To date, the level of squeezing measured with the set-up has been modest. We are primarily limited by readout losses due to the photodiode quantum efficiency (95%) and homodyne visibility.

The highest level of squeezing to date was -9 dB observed above 1 kHz on 11/03/2015, as shown in Figure 4-20. At this point we had a homodyne visibility of $\approx 97.5\%$, but we were still limited by technical noise due to backscatter at lower frequencies. In the process of tracking down this excess technical noise, the lenses on the squeezing path were cocked slightly to eliminate potential spurious interferometers. Since then, a homodyne visibility of $\approx 95\%$ has been more typical.

The best in-vacuum spectrum to date is shown in Figure 4-21. This spectrum deteriorates at low frequencies due to excess intensity noise caused by polarization fluctuations on the light exiting the LO fiber. We were able to reduce this effect by isolating the fiber from vibrating surfaces.

After venting and fixing the polarization fluctuation issue, we were able to obtain nearly flat squeezing down to below 1 Hz, as shown in Figure 4-22. An improved

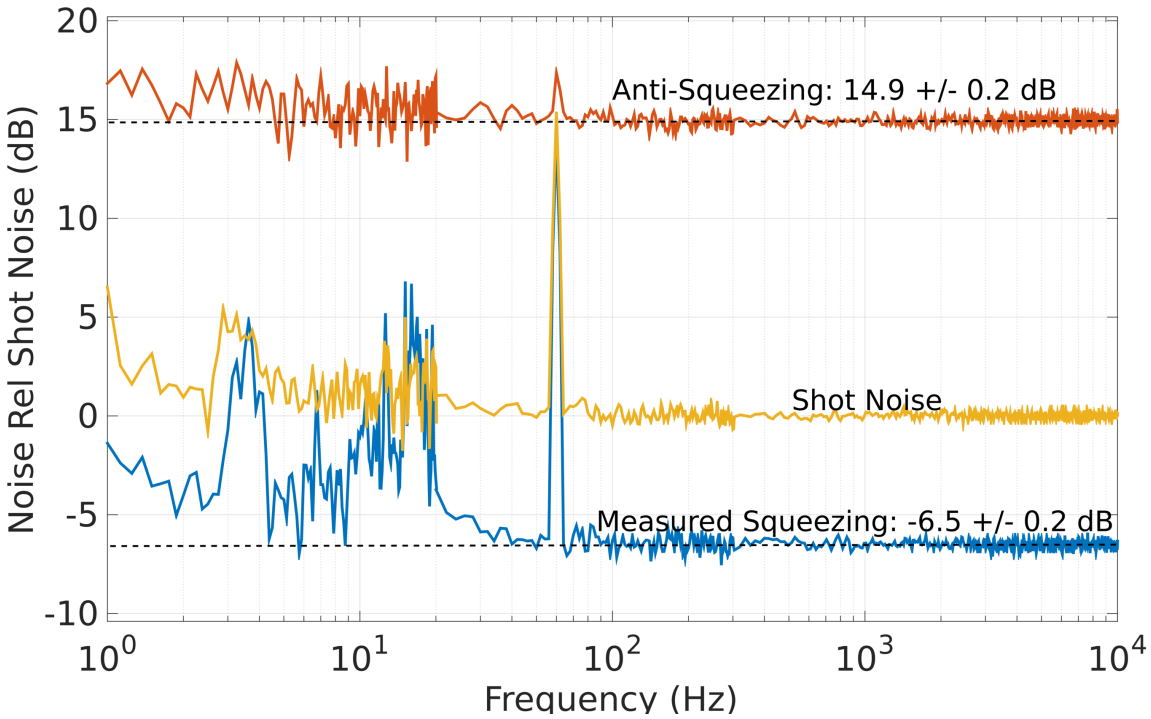

Figure 4-21: Best in-vacuum spectrum

in-vacuum spectrum is expected in the near future.

4.3.1 Phase noise performance

One major goal for the Advanced LIGO squeezed vacuum source is to achieve a significant reduction in the phase noise level intrinsic to the squeezer itself. Using a rigid OPO cavity design and high bandwidth feedback, we were able to attain a level of phase noise almost an order of magnitude lower than the previous best audio-band squeezer [61].

The coherent control technique described in Section 2.7 uses two servos to stabilize the squeezed quadrature angle. The first servo, the coherent locking field (CLF) loop, phase locks the CLF to the pump field. Since the phase of the pump field determines the orientation of the squeezing ellipse, this effectively stabilizes the phase of the CLF relative to the squeezed field. The second servo, which we will refer to as the LO loop, phase locks the LO field to the CLF. The aggregate effect of these two loops is to stabilize the phase of the LO relative to that of the squeezed field. Therefore one

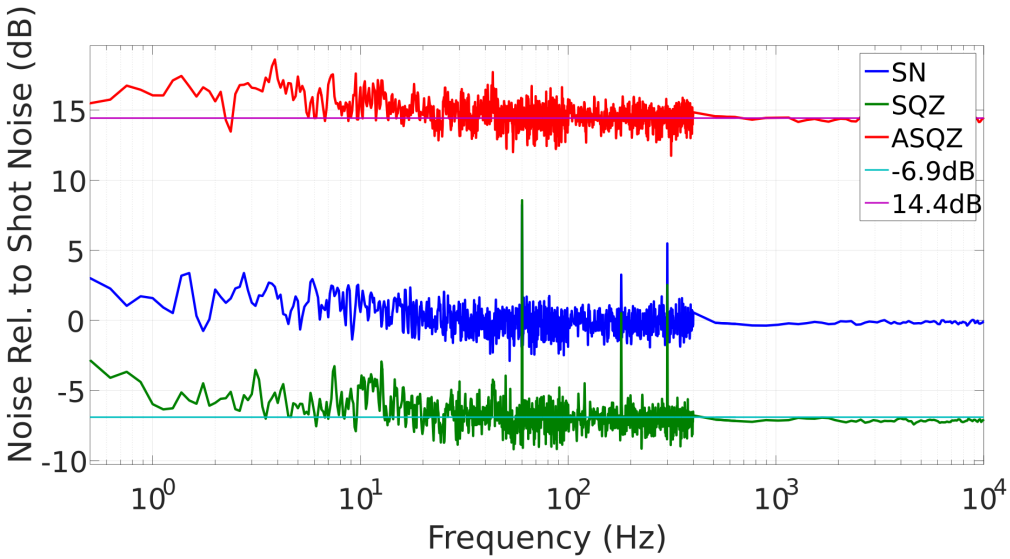

Figure 4-22: An in-air spectrum showing nearly flat squeezing down to $< 1\,\mathrm{Hz}$

may use the quadrature sum of the two calibrated error signals as an estimate of the phase noise.

In practice, using the CLF and LO error signals to determine the phase noise can be difficult. The coherent control technique is susceptible to lock-point errors. When lock-point errors are present, the coherent control error signals are no longer a reliable measure of the total phase noise. Both the LIGO and GEO 600 squeezing experiments suffered from lock-point errors, and their quadrature control error signals vastly underestimated the level of phase noise as a result [35, 37].

Consequently, we chose to infer the phase noise level using a more direct method. By measuring the level of squeezing and anti-squeezing at a variety of non-linear gain values, one can determine the level of phase noise by fitting the data to Equation 2.47 in order to determine η_{tot} and θ_{RMS}. The measurement is shown in Figure 4-23. We see that the phase noise level is given by $\theta_{RMS} = 1.3^{+0.7}_{-0.5}$ mrad.

Due to the extensive efforts to minimize OPO Detuning noise, we believe that the apparatus is not significantly impacted by lock-point errors. To verify this we compared the direct measurement of the phase noise with the total predicted by the quadrature control error signals and found the two to be in agreement.

Calibrated error signals are shown in Figures 4-17 and 4-19. We see that the CLF

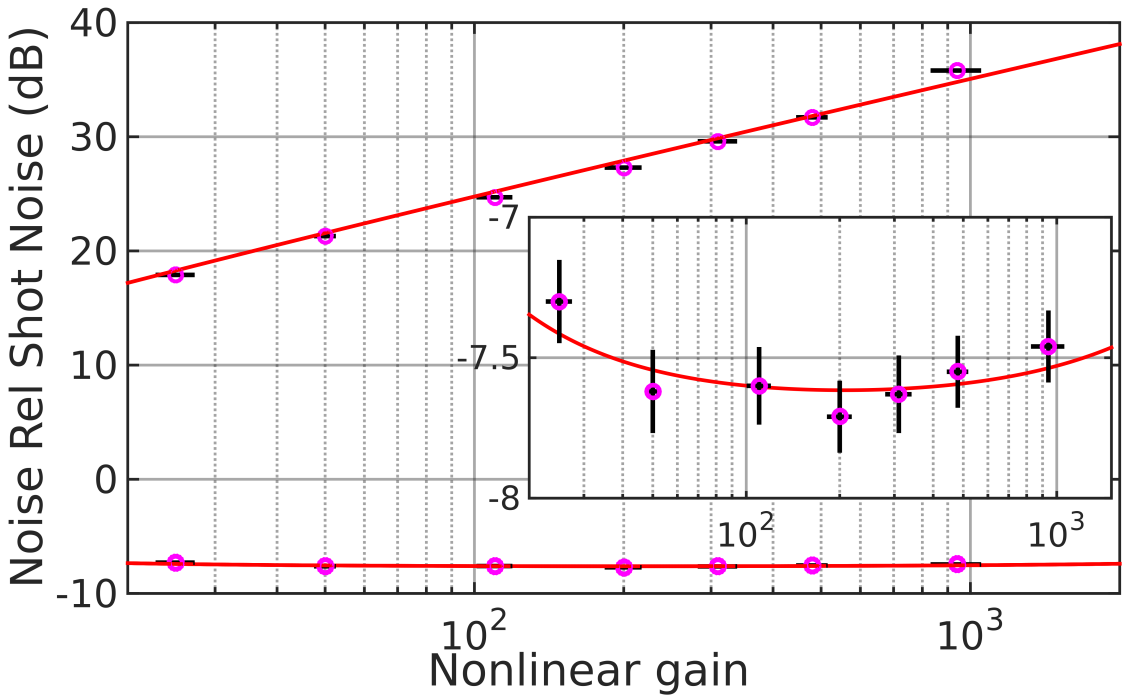

Figure 4-23: Data and fit for the phase noise characterization measurement. The red traces correspond to the theoretical values for squeezing and anti-squeezing as a function of non-linear gain for $\eta = 0.829$ and $\theta_{rms} = 1.3$ mrad. The sub-figure shows a close-up of the fit for the squeezing data.

loop has achieved broadband shot noise limited performance. As shown in Figure 4-19, the shot noise fluctuations imposed on the CLF by the CLF servo show up in the LO loop error signal, though this contribution is well suppressed within the control bandwidth. The bulk of the RMS for the LO loop is caused by length noise on the SHG cavity. The SHG length noise contribution to both error signals was estimated by multiplying the error signal spectrum for the SHG length servo by a transfer function from the error point on the SHG servo to the error points on both quadrature control loops. This estimate is only plotted in regions where the transfer function had good coherence. The total phase noise due to SHG length noise (1 ± 0.3 mrad) and CLF shot noise (0.9 ± 0.3 mrad) listed in Table 4.4 represent the quadrature sum of their contributions to both error signals.

Some additional phase fluctuations in the LO loop are present below 2 kHz, but they do not significantly alter the estimate of the total phase noise. These fluctuations have not been rigorously characterized, though we did observe a significant decrease

Table 4.4: **Loss and phase noise budget**

Source of Loss	Value (%)
OPO Escape Efficiency	2 ± 1
Propagation Losses	1 ± 0.2
95% Homodyne Visibility	10 ± 0.5
Photodiode quantum efficiency	5 ± 3
Total Efficiency	$\eta = 0.83 \pm 0.03$
Source of Phase noise	Value (mrad)
OPO Detuning Noise	0.35 ± 0.1
OPO Control Sidebands	0.35 ± 0.1
SHG length noise	1 ± 0.3
CLF shot noise	0.9 ± 0.3
Total Phase Noise	$\theta_{rms} = 1.4 \pm 0.5$

in noise at these frequencies when we acoustically isolated the optical fibers.

The remaining detuning noise on the OPO cavity also contributes some phase fluctuations. Since OPO detuning noise gives rise to lock-point errors, this term cannot be reliably inferred from the quadrature control error signals. Instead, we measured a calibrated error signal for the OPO length servo and computed the resulting squeezing angle fluctuations using Equation 3.4 as done in [**?**]. Due to the intrinsically low cavity length noise and high servo bandwidth, this error signal is completely shot noise limited. Using this method, we calculated a contribution of 0.35 ± 0.1mrad due to OPO detuning noise.

Additionally, a small portion of the 86 MHz control sidebands on the pump field used to lock the OPO cavity are converted into phase fluctuations on the squeezed field via parametric down-conversion. Based on a measurement of the modulation depth of these control sidebands, their contribution to the total phase noise is 0.35 ± 0.1mrad.

All major sources of phase noise are listed in Table 4.4. The quoted uncertainties for the OPO Detuning noise, SHG Length noise, and CLF shot noise contributions represent the uncertainties in calibrating the relevant error signals in each case. The total phase noise level listed at the bottom of the table is computed by taking the quadrature sum of all of the individual noise terms.

Chapter 5

Theoretical model of a realistic filter cavity

In this chapter we will introduce a formalism for modelling the various technical defects of quantum noise filter cavities. This chapter is loosely based on a paper authored by the MIT LIGO group a few years ago [65]. Though I was not an author on this paper, I lead the experimental effort to validate its predictions using the 2 meter filter cavity prototype which will be discussed in Chapter 6. Therefore, I will still present this background theory in detail.

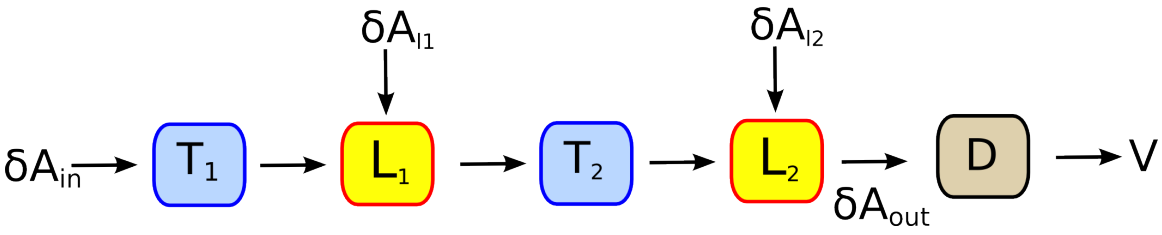

Figure 5-1: A quantum noise model of an optical system. This consists of transition matrices T_i representing components of the optical setup, loss terms L_i which degrade the squeezed field and add incoherent vacuum fluctuations and a detector which computes the variance.

5.1 Formalism

As depicted in Figure 5-1, we will build a model of the quantum noise in the system using four basic components: Input fields $\delta\mathbf{A}_i$ representing vacuum fluctuations, 2×2 matrix operators $\mathbf{T}_i$ representing various components of the system, Loss operators $\mathbf{L}_i$ which account for the attenuation due to losses and the additional vacuum fluctuations which enter the system, and a detector which computes the variance based on the transfer matrices for the various vacuum fluctuation fields.

All operators will be expressed using the two photon formalism. The input vacuum fluctuation fields are written as a vector of quadrature operators:

$$\delta\mathbf{A}_i(\Omega) = \begin{pmatrix} \delta A_{i,1}(\Omega) \\ \delta A_{i,2}(\Omega) \end{pmatrix} \tag{5.1}$$

The component matrices map incoming 2-photon states $\delta\mathbf{A}_{in}(\Omega)$ to outgoing 2-photon states $\delta\mathbf{A}_{out}(\Omega)$. Sometimes these will be most naturally expressed in terms of their 1-photon matrices:

$$\mathbf{T} = \Gamma\mathbf{T}_{1p}\Gamma^{-1} \tag{5.2}$$

where Γ is the 1-photon to 2-photon conversion matrix defined previously in Equation 2.22. As shown in Figure 5-2 we will treat our optical loss elements as a two port system using the "Beamsplitter Model" introduced in Section 2.5.1. For each

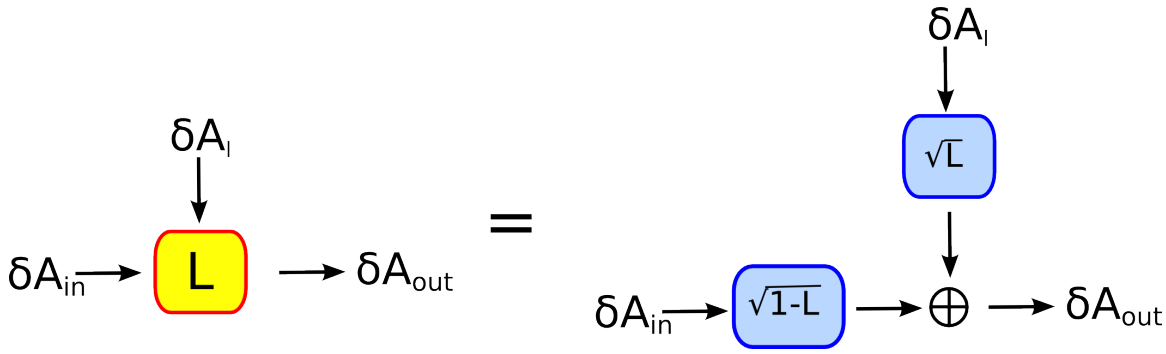

Figure 5-2: Modelling optical loss as a two port system. The squeezed field $\delta\mathbf{A}_{in}(\Omega)$ is attenuated and incoherent vacuum fluctuations $\delta\mathbf{A}_l(\Omega)$ are added in. This is equivalent to the beamsplitter model of optical loss discussed in Chapter 2.

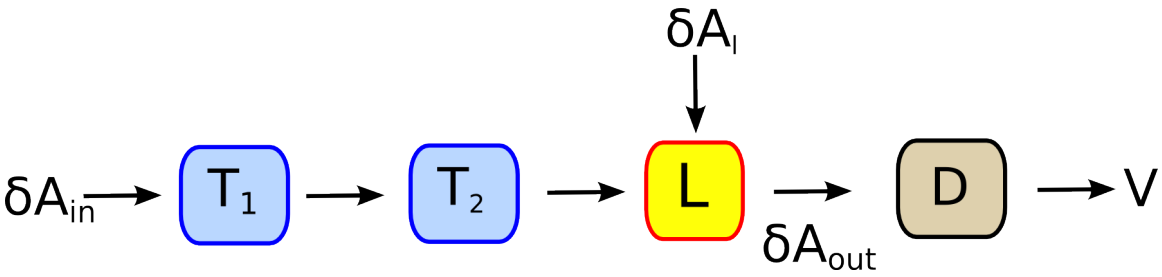

Figure 5-3: A simplified version of Figure 5-1 where the two loss terms have been combined. Losses may be combined when $\mathbf{T}_2$ is diagonal. When off-diagonal matrix elements are present, $\mathbf{T}_2$ will correlate the two quadratures of δA_{l1} and the two entering vacuum fluctuation fields may no longer be combined into a single term.

loss term, an additional vacuum fluctuation field is summed into the system.

We note that, when the matrix $\mathbf{T}_2$ in Figure 5-1 is diagonal, then we may gather the two loss terms L_1 and L_2 into a single loss term L[1] with a single vacuum input field $\delta\mathbf{A}_l(\Omega)$ as shown in Figure 5-3. If the off-diagonal elements of $\mathbf{T}_2$ are non-zero, then $\mathbf{T}_2$ will introduce correlations between the two quadratures of $\delta\mathbf{A}_{l1}(\Omega)$ and this grouping of loss terms is no longer valid. Assuming that $\mathbf{T}_2$ is diagonal, the output field $\delta\mathbf{A}_{out}(\Omega)$ is given by:

$$\delta\mathbf{A}_{out}(\Omega) = \mathbf{T}_{in}\delta\mathbf{A}_{in}(\Omega) + \mathbf{T}_l\delta\mathbf{A}_l(\Omega) \tag{5.3}$$

$$\mathbf{T}_{in} = \sqrt{1-L}\,\mathbf{T}_2\mathbf{T}_1 \tag{5.4}$$

$$\mathbf{T}_l = \sqrt{L} \tag{5.5}$$

The detector D then computes the output variance based on the tranfer matrices for the various vacuum fields entering the system:[2]

$$V(\phi_{LO},\Omega) = \sum_n \frac{1}{2} d^T_{\phi LO}\left(\mathbf{T}_n\mathbf{T}_n^\dagger + [\mathbf{T}_n\mathbf{T}_n^\dagger]^*\right) d_{\phi LO} \tag{5.6}$$

where T indicates transpose, * indicates conjugate, and † indicates conjugate trans-

[1] we define L such that $1-L = (1-L_1)(1-L_2)$ or, in terms of the notation used in Chapter 2, $\eta = \eta_1\eta_2$

[2] I won't derive this formula rigorously here. A detailed proof can be found in Chapter 4 of Tomoki Isogai's thesis [58]

pose. Here, we've defined

$$d_{\phi LO} = \begin{pmatrix} \cos\phi_{LO} \\ \sin\phi_{LO} \end{pmatrix} \tag{5.7}$$

where ϕ_{LO} is the measurement quadrature angle.

5.1.1 Formalism for Advanced LIGO

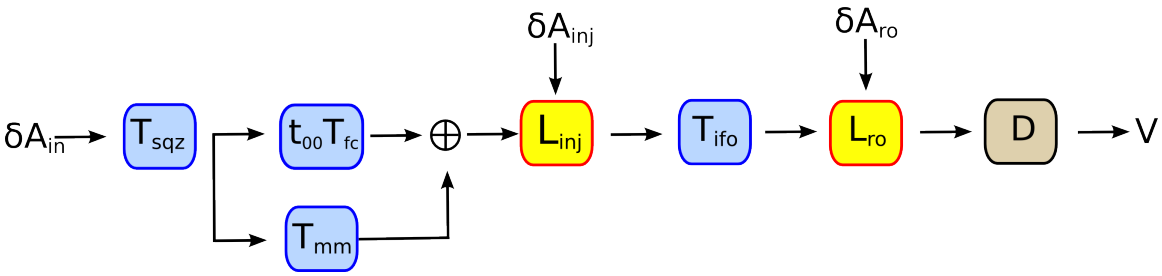

Figure 5-4: A model of Advanced LIGO using the formalism. This model contains a squeezer ($\mathbf{T}_{sqz}$), a filter cavity with mode mismatch ($t_{00}\mathbf{T}_{fc}$ and $\mathbf{T}_{mm}$), and an interferometer ($\mathbf{T}_{ifo}$). The loss terms must be separated into injection and readout losses (L_{inj} and L_{ro}) because optomechanical effects in the interferometer introduce an off-diagonal matrix element in $\mathbf{T}_{ifo}$. The individual transition matrices are derived in the main text.

Using the formalism we've developed, we may build a model of Advanced LIGO with frequency-dependent squeezed vacuum injection. A schematic of the model is shown in Figure 5-4. The model consists of five basic components. First, the input vacuum fluctuations pass through a frequency independent squeezed vacuum source with transfer matrix $\mathbf{T}_{sqz}$. Next the squeezed state passes through a filter cavity represented by $\mathbf{T}_{fc}$, though any portion of the field which is not correctly mode-matched will bypass the filter cavity. Finally, the frequency-dependent squeezed state is injected into the interferometer ($\mathbf{T}_{ifo}$) before being detected at the output port. We must treat the losses along the injection path (L_{inj}) and the readout path (L_{ro}) separately since $\mathbf{T}_{ifo}$ has non-zero off-diagonal values which introduce correlations between the two quadratures of $\delta\mathbf{A}_{inj}$.

5.2 Components of the model

We will derive matrices for the various components of the model for Advanced LIGO.

5.2.1 Squeezed vacuum source

For the purposes of this model, the squeezed vacuum source may be treated as an ideal squeezed light source (as presented in Section 2.3) followed by a loss representing the escape efficiency of the OPO cavity. This loss term will be grouped with the rest of the injection losses in L_{inj}. We compute $\mathbf{T}_{sqz}$ by expressing Equation 2.4 as a two-photon operator in matrix form:

$$\begin{aligned}\mathbf{T}_{sqz}(r,\theta) &= \mathbf{R}(\theta_B/2)\mathbf{S}(r,0)\mathbf{R}(-\theta_B/2) = \mathbf{R}_{\theta B/2}\mathbf{S}_r\mathbf{R}^{\dagger}_{\theta B/2} \\ &= \begin{pmatrix} \cos\theta_B/2 & -\sin\theta_B/2 \\ \sin\theta_B/2 & \cos\theta_B/2 \end{pmatrix} \begin{pmatrix} \mathrm{e}^{r} & 0 \\ 0 & \mathrm{e}^{-r} \end{pmatrix} \begin{pmatrix} \cos\theta_B/2 & \sin\theta_B/2 \\ -\sin\theta_B/2 & \cos\theta_B/2 \end{pmatrix}, \end{aligned} \tag{5.8}$$

5.2.2 Filter cavity

The portion of the field incident on the filter cavity which overlaps with the TEM00 mode of the cavity, denoted by t_{00} will experience a frequency-dependent quadrature rotation. The impact of the filter cavity on the squeezing sidebands depends on its complex amplitude reflection coefficients:

$$r_{\mathrm{fc}}(\Omega) = r_{\mathrm{in}} - \frac{t_{\mathrm{in}}^2}{r_{\mathrm{in}}} \frac{r_{\mathrm{rt}}\mathrm{e}^{-\mathrm{i}\Phi(\Omega)}}{1 - r_{\mathrm{rt}}\mathrm{e}^{-\mathrm{i}\Phi(\Omega)}}\ , \tag{5.9}$$

where r_{in} is the amplitude reflectivity of the input mirror and r_{rt} is the cavity's round-trip amplitude reflectivity. For a linear cavity of length L_{fc} and resonant frequency ω_{fc}, the round-trip phase $\Phi(\Omega)$ is defined as

$$\Phi(\Omega) = (\Omega - \Delta\omega_{\mathrm{fc}})\,\frac{2L_{\mathrm{fc}}}{c}, \tag{5.10}$$

where $\Delta\omega_{\mathrm{fc}} = \omega_{\mathrm{fc}} - \omega_0$ is the cavity detuning with respect to the carrier frequency.

For a high-finesse cavity near to resonance, we can make the approximations

$$\mathrm{e}^{-\mathrm{i}\Phi(\Omega)} \simeq 1 - \mathrm{i}\Phi(\Omega) \tag{5.11}$$

$$\text{and} \quad r_{\mathrm{rt}} \simeq r_{\mathrm{in}} \simeq \sqrt{1 - t_{\mathrm{in}}^2 - t_{loss}^2}$$

$$\simeq 1 - (t_{\mathrm{in}}^2 + t_{loss}^2)/2, \tag{5.12}$$

where t_{loss}^2 accounts for the power lost during one round-trip in the cavity (not including input mirror transmission).

Under these approximations, and neglecting higher order terms in t_{loss}^2, t_{in}^2 and $\Phi(\Omega)$, 5.9 can be rewritten as

$$r_{\mathrm{fc}}(\Omega) = 1 - \frac{2-\epsilon}{1+i\xi(\Omega)} = \frac{\epsilon - 1 + i\xi(\Omega)}{1+i\xi(\Omega)} \tag{5.13}$$

where

$$\epsilon = \frac{2t_{loss}^2}{t_{\mathrm{in}}^2 + t_{loss}^2} = \frac{c\, t_{loss}^2}{2L_{\mathrm{fc}}\gamma_{\mathrm{fc}}} = \frac{f_{\mathrm{FSR}}}{\gamma_{\mathrm{fc}}}\, t_{loss}^2, \tag{5.14}$$

$$\xi(\Omega) = \frac{2\Phi(\Omega)}{t_{\mathrm{in}}^2 + t_{loss}^2} = \frac{\Omega - \Delta\omega_{\mathrm{fc}}}{\gamma_{\mathrm{fc}}} \tag{5.15}$$

and the cavity linewidth (HWHM) is defined as

$$\gamma_{\mathrm{fc}} = \frac{1 - r_{\mathrm{rt}}^2}{2}\frac{c}{2L_{\mathrm{fc}}} = \frac{t_{\mathrm{in}}^2 + t_{loss}^2}{2}\frac{c}{2L_{\mathrm{fc}}}. \tag{5.16}$$

We note that γ_{fc} depends inversely on the cavity length and it is therefore the *loss per unit length* $t_{loss}^2/L_{\mathrm{fc}}$ which determines the filter cavity performance. The matrix T_{fc} can be written in terms of a 1-photon matrix with diagonal matrix elements given by Equation 5.9 evaluated for the upper and lower quantum noise sidebands:

$$\mathbf{T_{fc}} = \Gamma \begin{pmatrix} r_+ & 0 \\ 0 & r_-^* \end{pmatrix} \Gamma^{-1} \tag{5.17}$$

where $r_\pm = r_{\mathrm{fc}}(\pm\Omega)$. At this point, it is convenient express $r_\pm$ as a phasor:

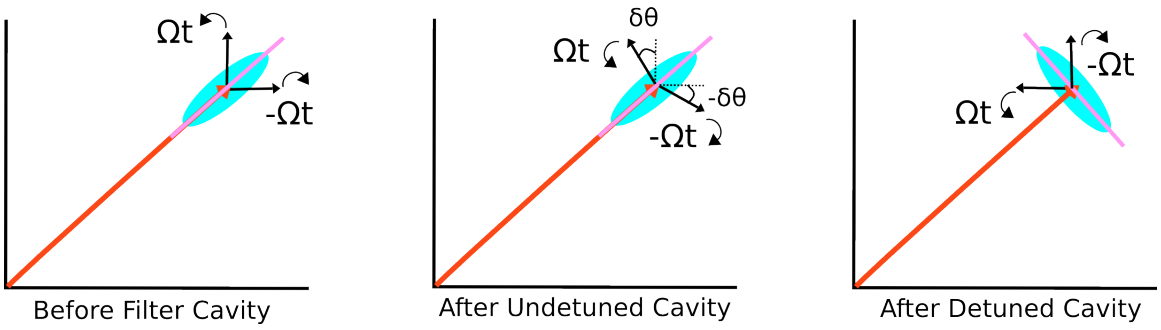

Figure 5-5: Schematic showing the impact of the detuning on the observed quadrature rotation. A carrier field has been added for clarity. Here the pink line represents the sum of the two sidebands as they evolve in time and indicates which quadrature is being modulated. For an undetuned filter cavity, we only get a differential phase shift between the two sidebands. This does not actually rotate the modulation quadrature. When the filter cavity is detuned, we get a common phase shift which does result in a quadrature rotation.

$$r_{\pm} = \rho_{\pm} e^{\alpha_{\pm}} \tag{5.18}$$

and to define the common and differential quantities[3]:

$$\alpha^{p}_{m} = \frac{\alpha_{+} \pm \alpha_{-}}{2} \quad \text{and} \quad \rho^{p}_{m} = \frac{\rho_{+} \pm \rho_{-}}{2} \tag{5.19}$$

In terms of these quantities, we may rewrite $\mathbf{T}_{fc}$ in the following form for additional insight:

$$\mathbf{T_{fc}} = \underbrace{e^{i\alpha_m}\mathbf{R}_{\alpha_p}}_{\text{lossless}} \underbrace{\left(\rho_p\ \mathbf{I} - i\rho_m\ \mathbf{R}_{\pi/2}\right)}_{\text{lossy}}, \tag{5.20}$$

The first term consists of an overall phase shift and a quadrature rotation operation. This term represents the action of a lossless filter cavity. Note that it is the **common** phase shift between the upper and lower squeezing sideband, dentoted by α_p, which gives rise to the quadrature rotation while the **differential** phase shift α_m just applies a term which is equivalent to a time evolution of both sidebands. This explains why the filter cavity must be *detuned*, since $\alpha_p = 0$ for an undetuned filter

[3]This is the same α_p which appears in Equation 3.20. We derive the closed form given in Equation 3.20 using Equation 5.13.

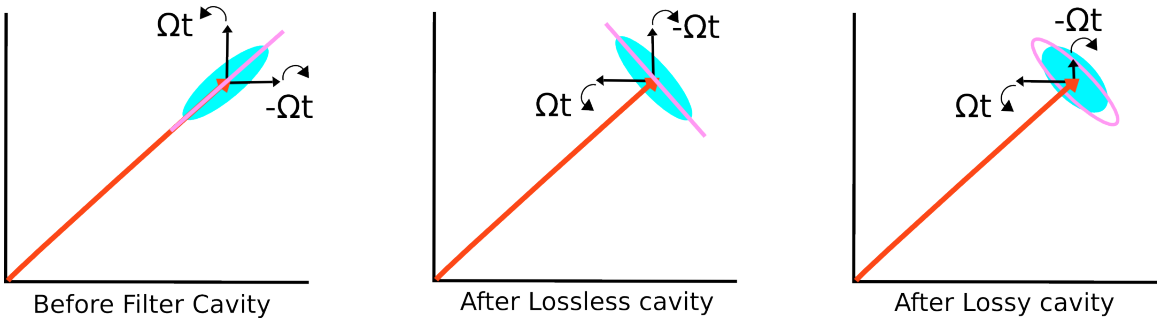

Figure 5-6: Schematic showing the impact of coherent dephasing on the anti-squeezing sidebands. A carrier field has been added for clarity. Here the pink curve represents the sum of the two sidebands as they evolve in time and indicates which quadrature is being modulated. In the presence of loss, the sidebands become unbalanced. As a result a small portion of the anti-squeezing contaminates the measurement quadrature. Since the pink modulation curve is now elliptical instead of linear we cannot simply rotate the sidebands to get rid of this contamination.

cavity. The impact of common and differential phase shifts are depicted in Figure 5-5.

The second term in Equation 5.20 represents the impact of optical loss on the action of the filter cavity. Note that this term does not correspond to decoherence (i.e. the replacement of squeezed photons with unsqueezed vacuum), which is accounted for by the injection loss term in the model. Instead it is a consequence of the fact that one of the sidebands is closer to the cavity resonance and therefore experiences a higher level of loss. As depicted in Figure 5-6, this causes the two sidebands to become *unbalanced* ($\rho_m \neq 0$) and results in a small amount of the anti-squeezed quadrature contaminating the measurement quadrature. This effect is known as *coherent dephasing* and cannot be undone by applying another rotation to the sidebands.

In some sense, coherent dephasing is similar to phase noise in that it limits how high we can increase the normalized non-linear interaction strength x. Eventually the increase in anti-squeezing will begin to dominate the squeezed quadrature variance. Unlike phase noise, however, this technical effect is highly frequency-dependent. We will discuss the implications of coherent dephasing for Advanced LIGO in Section 5.3.

5.2.3 Mode mismatch

As shown in Figure 5-4, only the portion of the squeezed field which is properly mode matched will enter the interferometer. Likewise, the mode matching between the squeezed field and the local oscillator (interferometer field in the case of DC readout) will also impact the measured variance. In order to compute the impact of mode matching, it is useful to expand the squeezed and LO fields in the basis of the Hermite-Gaussian modes of the filter cavity, denoted by U_n

$$U_{\rm sqz} = \sum_{n=0}^{\infty} a_n U_n, \quad \text{with} \quad a_0 = \sqrt{1 - \sum_{n=1}^{\infty} |a_n|^2} \tag{5.21}$$

$$U_{\rm lo} = \sum_{n=0}^{\infty} b_n U_n, \quad \text{with} \quad b_0 = \sqrt{1 - \sum_{n=1}^{\infty} |b_n|^2} \tag{5.22}$$

where a_n and b_n are complex coefficients and U_0 is the filter cavity fundamental mode. Since the filter cavity is held near the resonance of the fundamental mode, we assume that all other modes (U_n with $n > 0$) are far from resonance. They are reflected by the input coupler, but are otherwise unmodified by the cavity. Thus, the squeezed beam after reflection from the filter cavity is given by

$$U_{\rm rfc} = r_{\rm fc}(\Omega) \cdot U_{\rm sqz} = r_{\rm fc}(\Omega)\ a_0\ U_0 + \sum_{n=1}^{\infty} a_n U_n\ . \tag{5.23}$$

We will express the spatial overlap integral of the reflected field and the LO field as

$$\langle U_{\rm lo} | U_{\rm rfc} \rangle = t_{00}\ r_{\rm fc}(\Omega) + t_{\rm mm} \tag{5.24}$$

where $t_{00} = a_0 b_0^*$ and $t_{\rm mm} = \sum_{n=1}^{\infty} a_n b_n^*$. From Equation 5.24 and it's adjoint, we can derive the two photon transition matrix shown in Figure 5-4 which take us from the input field to the portion of the output field which overlaps with the local oscillator[4]

[4]The the remainder of the reflected field which is not mode matched to the LO is effectively lost as it cannot be measured. As a result we must account for this the injection loss term.

$$t_{00}\mathbf{T}_{fc} + \mathbf{T}_{mm} \tag{5.25}$$

where $\mathbf{T}_{mm}$ is defined as:

$$\mathbf{T_{mm}} = \Gamma \cdot \begin{pmatrix} t_{\mathrm{mm}} & \\ & t^*_{\mathrm{mm}} \end{pmatrix} \cdot \Gamma^{-1} = |t_{\mathrm{mm}}|\ \mathbf{R}\big(\arg(t_{\mathrm{mm}})\big)\ . \tag{5.26}$$

The addition of this coupling path results in a frequency dependent rotation error with respect to the rotation expected from a perfectly mode matched filter cavity. If the mode mismatch is small (less than 10%), this error can be corrected by a small change in the filter cavity detuning. In general, the phase $\arg(t_{mm})$ is unconstrained. As we shall see, this leads to some uncertainty in the level of anti-squeezing that is inadvertently rotated into the measurement quadrature which in turn creates uncertainty in the level of measured squeezing at low frequencies.

5.2.4 Interferometer

The transition matrix for the interferometer can be obtained by writing the quantum noise terms from Equations 1.84 and 1.85 in matrix form

$$\mathbf{T}_{ifo} = \begin{pmatrix} 1 & 0 \\ -\kappa & 1 \end{pmatrix} \tag{5.27}$$

where we have omitted the uninteresting phase shift term $\mathrm{e}^{-2i\beta}$. For the purpose of this calculation, we will assume that the interferometer is lossless and note that a formalism for including the effects of loss is given in [18]. The parameters for Advanced LIGO were presented previously in Table 1.1.

5.2.5 Propagation and loss terms

We may now compute the total transition matrices needed to express the measured variance in terms of the input vacuum fluctuation fields. The transition matrix for the squeezed field (which originates from $\delta\mathbf{A}_{in}$) is given by

$$\mathbf{T}_{in} = \sqrt{1 - L_{ro}}\sqrt{1 - L_{inj}(\Omega)}\mathbf{T}_{ifo}\left(t_{00}\mathbf{T}_{fc} + \mathbf{T}_{mm}\right)\mathbf{T}_{sqz} \tag{5.28}$$

Here, we have defined L_{ro} as the total losses between the interferometer and the readout, and a frequency-dependent injection loss term $L_{inj}(\Omega)$. Prior to specifying L_{inj} it is useful to define the audio-sideband transmission coefficient from the squeezer to the interferometer:

$$\tau_{inj}(\Omega) = \left(t_{00}r_{fc}(\Omega) + t_{mm}\right)\sqrt{\eta_{esc}}\sqrt{\eta_{prop}} \tag{5.29}$$

where η_{esc} and η_{prop} are the OPO escape efficiency and propagation efficiency along the injection path respectively. We may then define the two photon injection loss as an average of that for the upper and lower sidebands:

$$L_{inj}(\Omega) = 1 - \left(|\tau_{inj}(+\Omega)|^2 + |\tau_{inj}(-\Omega)|^2\right)/2 \tag{5.30}$$

Using these expressions we can compute the transfer matrices for the injection and readout loss fields $\delta\mathbf{A}_{inj}$ and $\delta\mathbf{A}_{ro}$.

$$\mathbf{T}_{inj} = \sqrt{1 - L_{ro}}\sqrt{L_{inj}(\Omega)}\mathbf{T}_{ifo} \tag{5.31}$$

$$\mathbf{T}_{ro} = \sqrt{L_{ro}}\mathbf{I} \tag{5.32}$$

5.2.6 Phase noise

As with the losses, phase noise can be broken into two categories: frequency independent phase noise which impacts the level of squeezing at all measurement frequencies and frequency *dependent* phase noise which disproportionately impacts the squeezing sidebands that are within the filter cavity linewidth. The only source of frequency-dependent phase noise treated in [65] comes from detuning noise on the filter cavity. Calculating a closed-form expression for this term is difficult and it is typically computed numerically. Once computed, the measured variance is given by:

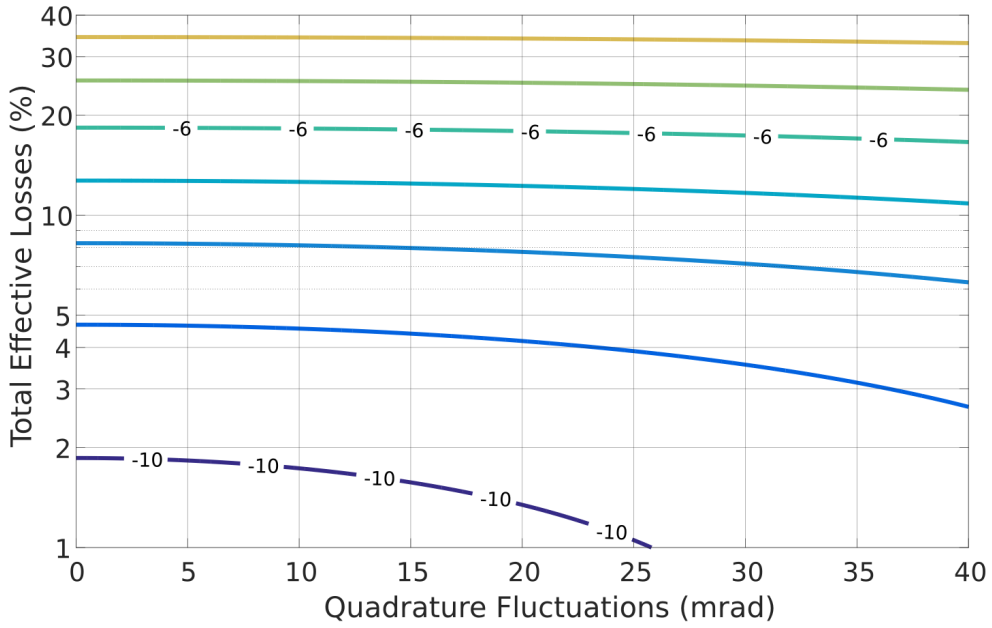

Figure 5-7: Maximum level of squeezing as a function of loss and phase noise with $g \leq 5$ (maximum of 10 dB of injected anti-squeezing). We see that phase noise has a limited impact for realistic levels of optical loss.

$$V'(\phi_{LO}, \Omega) = V(\phi_{LO}, \Omega) \cos^2 [\theta_{rms}(\Omega)] + V_(\phi_{LO} + \pi/2, \Omega) \sin^2 [\theta_{rms}(\Omega)] \tag{5.33}$$

Where $V(\phi_{LO}, \Omega)$ is computed using Equation 5.6 and $\theta_{rms}(\Omega)$ is the RMS level of phase noise experienced at sideband frequency Ω.

5.3 The impact of coherent cephasing and frequency-dependent phase noise

The phase sensitivity (in rad/m) of a Fabry-Perot cavity scales linearly with the Finesse and the Finesse required for the filter cavity scales inversely with L_{fc}. As a result, relatively modest levels of length noise can add significant levels of phase noise for shorter filter cavities. Available suspension and seismic isolation technology can suppress the length noise to a level where it becomes inconsequential, though such

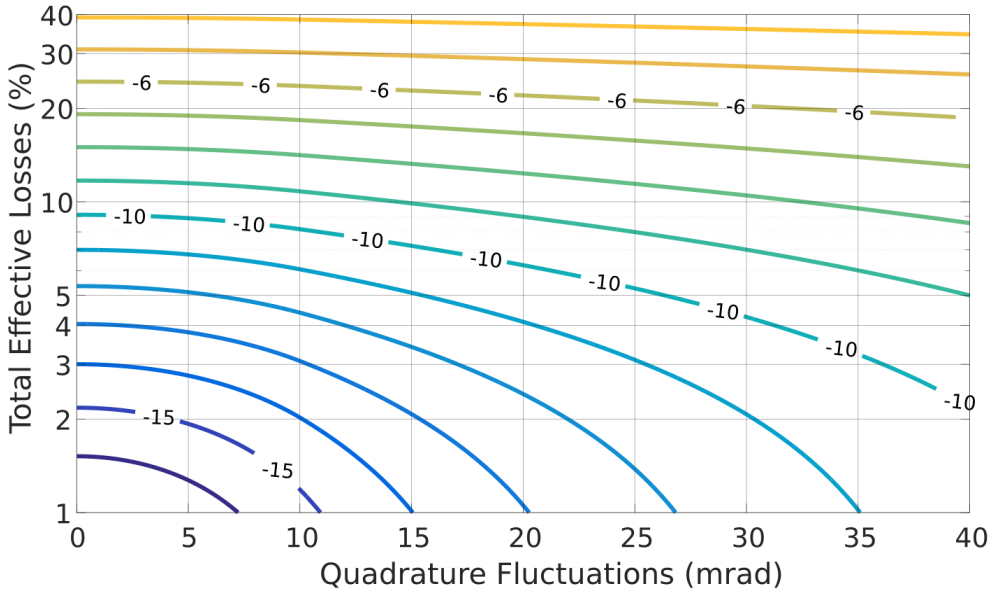

Figure 5-8: Maximum level of squeezing as a function of loss and phase noise for a frequency-dependent squeezed light source with a kilometer-scale filter cavity. This allows for a nonlinear gain $g \leq 30$ (Maximum of 19 dB of injected anti-squeezing). For phase noise levels ≥ 10 mrad, we recover the performance shown in Figure 2-4.

hardware can increase the cost significantly.

As discussed previously, coherent dephasing results in an unavoidable addition of anti-squeezing into the measurement quadrature. Unlike frequency-dependent phase noise, this effect cannot be further mitigated with current technology without increasing the filter cavity length.

In principle, these effects only degrade the squeezing at frequencies that are of order γ_{fc} or smaller. However, recent analysis has shown that the sensitivity improvement from low frequency squeezing is critical for maximizing the detection range for compact binary inspirals [75]. Therefore, it is likely that Advanced LIGO will elect to reduce the level of injected anti-squeezing by turning down the nonlinear gain in order to minimize the degradation at low frequencies due to coherent dephasing and frequency-dependent phase noise [5].

[5] mode mismatch can also have an impact, since the portion of the squeezed field which bypasses the filter cavity can project anti-squeezing into the measurement quadrature at low frequencies. However, the strong dependence of filter cavity performance on cavity length in [75], suggest that this did not pose a major limitation.

Unfortunately, this will result in a decrease in the level of high frequency squeezing. According to the analysis in [75], a nonlinear gain of $g = 5$ (or roughly 10 dB of injected anti-squeezing) is optimal for a 16 meter filter cavity with losses of order 8 ppm/m. In analogy with Figure 2-4 we plot the optimal level of measured squeezing as a function of total loss and phase noise for $g \leq 5$ in Figure 5-7. In this scenario, we would measure roughly a dB less of squeezing with 25% total loss than would be possible with a more reasonable nonlinear gain. One should also note that having low frequency independent[6] phase noise performance will avail us little in this scenario due to the restriction on the nonlinear gain. With a 16 m filter cavity, low phase noise would only be useful in specialized circumstances when it is advantageous to turn up the nonlinear gain to optimize the high frequency sensitivity[7].

By comparison, a km-scale filter cavity considered in [75] would perform optimally with a nonlinear gain of $g = 30$ (or roughly 19 dB of injected anti-squeezing). As shown in Figure 5-8 the performance shown in Figure 2-4 is mostly recovered for achievable levels of total loss and phase noise.

5.4 Expected performance of the Advanced LIGO 16 m filter cavity

Table 5.1 lists the parameters for Advanced LIGO used in [65]. The Filter cavity and detuning and linewidth were determined by plugging t_{rt}^2 into Equations 3.23 and 3.21 and computing the desired parameters. Here we are assuming a slightly lower value for the frequency independent losses ($\approx 15\%$) than what we initially anticipate for Advanced LIGO (See the first column of Table 3.1). This value was chosen to allow for 6 dB of squeezing using a low nonlinear gain as discussed in Section 5.3. From Figure 5-7, we see that with more realistic levels of loss ($\approx 25\%$) one would get roughly 5 dB of squeezing at high frequencies.

[6] The CLF will not enter the filter cavity. Therefore the frequency-dependent phase noise caused by filter cavity detuning noise will not be suppressed by coherent control.

[7] or in the event that we are unable to achieve radiation pressure limited performance for whatever reason

Table 5.1: Parameters used in in the application of this model to Advanced LIGO. Reproduced from [65]

Parameter	Symbol	Value
Filter cavity length	L_{fc}	16 m
Filter cavity half-bandwidth	γ_{fc}	$2\pi \times 61.4$ Hz
Filter cavity detuning	$\Delta\omega_{\mathrm{fc}}$	$2\pi \times 48$ Hz
Filter cavity input mirror transmissivity	t^2_{in}	66.3 ppm
Filter cavity losses	t^2_{rt}	16 ppm
Escape Efficiency	η_{esc}	2%
Propagation Efficiency	$\eta_{\mathrm{propdesign}}$	3%
Readout losses	L_{ro}	5%
Mode-mismatch losses (squeezer-filter cavity)	t^2_{mmFC}	2%
Mode-mismatch losses (squeezer-local oscillator)	t^2_{mmLO}	5%
Frequency independent phase noise (RMS)	$\delta\zeta$	30 mrad
Filter cavity length noise (RMS)	δL_{fc}	0.3 pm
Injected squeezing	σ_{dB}	9.1 dB

Figure 5-9 shows the expected reduction in quantum noise for Advanced LIGO. We see that the low frequency level of squeezing is primarily degraded by the intra-cavity loss. Also note that, due to the extremely high cavity finesse ($\approx$ 70000), the level of degradation caused by detuning noise (frequency-dependent phase noise) is significant despite the modest RMS value of 0.3 pm for the filter cavity length noise. Though the level of squeezing at low frequencies is modest, a realistic 16 meter filter cavity still offers considerable performance gains and remains a worthwhile upgrade.

One should note the uncertainty introduced by the mode mismatch. As discussed in Section 5.2.3, because the phase of t_{mm} is unconstrained, this creates some uncertainty in the quadrature angle of the field which bypasses the filter cavity due to mode mismatch. The cyan curves in Figure 5-9 represent the expected degradation as $\arg(t_{mm})$ is allowed to vary.Consequently, this results in some uncertainty in the level of squeezing measured at low frequencies. If either the mode-matching between the squeezed field and the LO or between the squeezed field and the filter cavity are perfect, $t_{mm} = 0$ and this uncertainty disappears. The sole impact of any remaining

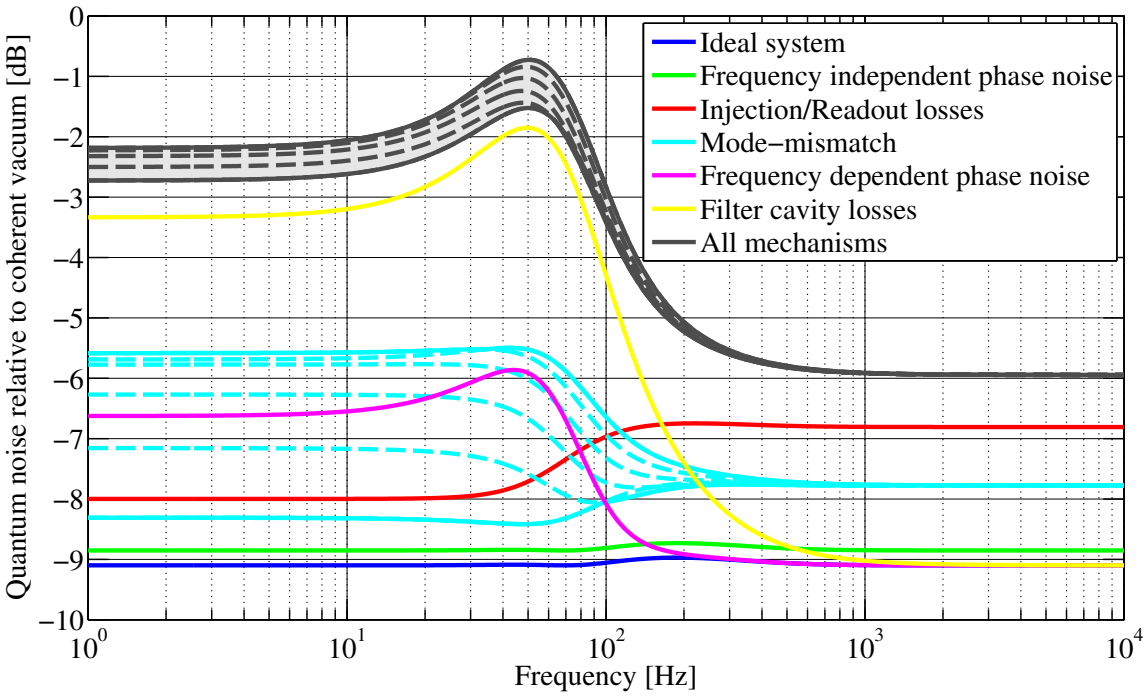

Figure 5-9: Quantum noise reduction for Advanced LIGO using a 16 m filter cavity (adapted from Ref. [65]). The predominant source of degradation at low frequencies is optical loss inside the filter cavity.

mode-mismatch is to add an additional frequency independent loss.

Chapter 6

Audio-band frequency-dependent squeezing experiment

By squeezing the vacuum fluctuations entering an interferometer's readout port, the sensitivity of the instrument can be significantly improved [22, 100–102], leading to richer astrophysical observations. However, optomechanical interactions dictate that the vacuum's squeezed quadrature must rotate by 90 degrees around 50 Hz [9, 63, 65]. In this chapter I describe an experiment where we store spectral components of a squeezed state for 128 µs in a 2-m-long, high-finesse optical resonator to produce frequency-dependent squeezed vacuum.

To implement frequency-dependent squeezing in Advanced LIGO [103] a 3 ms storage time is required; comparable to the longest ever recorded [110]. As optical losses severely limit the finesse and storage time achievable for a given cavity length [59], experimental realization of such cavities is extremely challenging, with the only prior demonstration of quadrature rotation in this way having targeted MHz frequencies [25]. Nevertheless, filter cavities represent the best prospect for developing an audio-band frequency-dependent squeezed vacuum source in the near future, with other techniques restricted by thermal noise [89], the level of squeezing produced at low frequencies [33] or loss-induced decoherence [55].

By injecting light from a squeezed vacuum source into a filter cavity and measuring the spectrum of noise in the reflected field as a function of quadrature phase, we

Table 6.1: Parameters of our two meter filter cavity. The range in the values indicated with a * will be discussed in Section 6.1.3

Parameter	**Value**
Cavity length	1.938 m
Free Spectral Range	77.33 MHz
Input Mirror Transmission (1064 nm)	192.2 ± 1.3 ppm
End Mirror Transmission (1064 nm)	1.55 ± 0.14 ppm
*Intra-cavity loss (1064 nm)	4.5-16.5 ppm
*Finesse (1064 nm)	29900-31700
*Linewidth (1064 nm)	2.44-2.56 kHz
Input Mirror Transmission (532 nm)	$\approx 1\%$
End Mirror Transmission (532 nm)	$\approx 3\%$
Finesse (532 nm)	≈ 150
Linewidth (532 nm)	≈ 500 kHz

demonstrate 90° quadrature rotation of a squeezed vacuum state at 1.2 kHz. This is the first demonstration of the desired 90° rotation required for advanced LIGO. This first demonstration of frequency-dependent squeezing in the audio-band uses technology and methods that are scalable to the required rotation frequency, heralding application of the technique in all future gravitational-wave detectors [75, 83].

6.1 Experimental overview

In the following subsections we will present the experimental apparatus in detail.

6.1.1 2 meter filter cavity

The only previous demonstration of frequency-dependent squeezed light generation [25] was done at frequencies of order 15 MHz, where the requirements for the filter cavity are relatively lax. To achieve the desired frequency-dependent quadrature rotation of our squeezing ellipse at audio-band frequencies, a long storage time optical resonator is required. In order to keep the filter cavity length at a practical scale for a table-top experiment, we chose a ≈ 2 m cavity length with a finesse of ≈ 30000, resulting in the desired linewidth of ≈ 2.5 kHz. The filter cavity mirrors are dichroic and also form a low finesse (≈ 150) cavity at 532 nm. A complete list of the filter

cavity parameters is given in Table 6.1.

6.1.2 Filter cavity control and diagnostics

The layout of our filter cavity table is shown in Figure 6-1. The output of a 500 mW, 1064 nm Nd:YAG solid state laser (filter cavity laser) was split into two portions. The first was frequency doubled using a single pass SHG and used to lock the laser to the filter cavity with a bandwidth of 30 kHz with a Pound-Drever-Hall servo in reflection from the end mirror of the filter cavity. The lower finesse 532 nm cavity is used to avoid the added difficulty in acquiring and maintaining lock with the 1064 nm cavity directly. As we will discuss in Section 6.1.3, a robust length servo is required to keep the level of frequency-dependent phase noise added by detuning noise at a reasonable level.

The remainder of the was double-passed through an AOM (200 MHz Crystal Technologies AOMO 3200-1113) which shifts the field frequency by the required detuning $\Delta\omega_{fc}$ (see Equation 3.23) plus an integer number multiple of the filter cavity free spectral range. A fraction of this frequency shifted light is then fiber coupled over to our squeezed light source (see Section 6.1.4) and is used to phase lock the pump laser to the filter cavity laser[1]. The result of this phase lock is that the frequency offset of the pump laser, and therefore the squeezed vacuum, from resonance in the filter cavity was stabilised and could be controlled by varying the AOM's drive frequency in order to produce the desired 90° quadrature rotation.

The remainder of this frequency shifted field is split into two diagnostic paths which we shall refer to as the *cavity beam* and the *diagnostic beam*. In order to set the detuning, we injected the cavity beam through the end mirror and measured the power in transmission (using PD_{rt}) and changed the detuning AOM drive frequency accordingly. We also made a mode measurement of the cavity beam in transmission through the filter cavity and used to optimize the mode matching of the squeezed

[1]This light is first passed through an AOM which shifts its frequency up by 80 MHz, the pump laser is then phase locked with a -80 MHz offset resulting in no relative frequency shift. This frequency offsetting is required to avoid using a DC phase lock which suffer from undesirable intensity noise couplings.

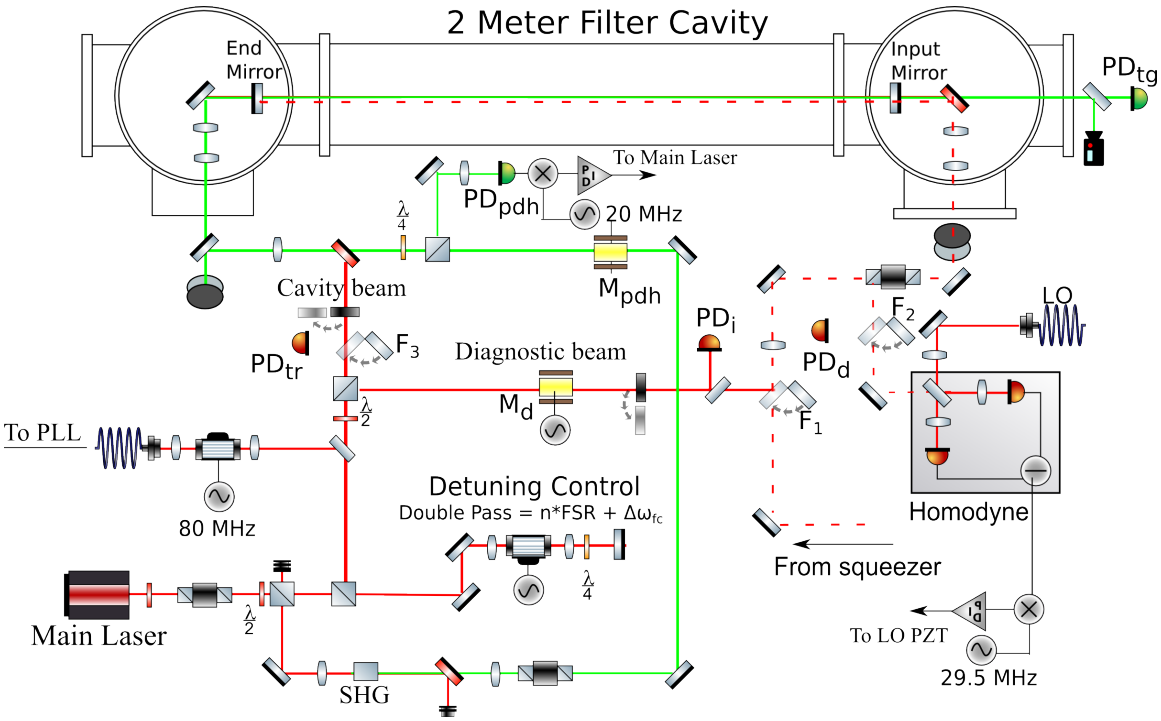

Figure 6-1: Filter cavity table schematic. The output of a 700 mW 1064 nm NPRO is split between two paths. The first path contains a single-pass SHG. The generated 532 nm field is used to lock the laser to the filter cavity 532 nm resonance. The remaining light is double passed through an AOM which frequency shifts the field by an integer number of FSR plus $\Delta\omega_{fc}$ which is tuned to 1.2 kHz as required to achieve a 90 degree squeezed quadrature rotation. Some of this light is fiber coupled to the squeezer table and is used to phase lock the pump laser to the filter cavity laser in fix the squeezed field detuning at $\Delta\omega_{fc}$. The phase lock field is first shifted up in frequency by 80 MHz and the phase lock beat note is demodulated at -80 MHz to avoid running the phase lock loop at DC where intensity noise can couple into the measurement. The remainder of the frequency shifted light is split into two diagnostic paths referred to as the "cavity beam" and "diagnosic beam". One must toggle the position of several flipper mirrors and beam blocks in order to use these paths. Their function is described in the main text. The squeezed field generated by our frequency independent squeezed vacuum source is injected into one end of the filter cavity and characterized with a balanced homodyne readout.

field into the filter cavity. With this technique, we were able to quickly achieve 99% mode matching. Finally one may also use the cavity beam to measure the relative overlap between the cavity field and the local oscillator. As discussed in Section 5.2.3, mode mismatch can significantly degrade the performance of a frequency-dependent squeezed vacuum source, particularly at measurement frequencies $\leq \gamma_{\mathrm{fc}}$.

The diagnostic beam was primarily used to characterize the loss and length noise performance of the cavity. By adjusting three flipper mounts (F1, F2, and F3) one can inject the diagnostic beam into the front of the cavity and measure the incident field, the field in transmission, and the field in reflection with PD_i, PD_{tr}, and PD_d respectively as required for our loss measurement techniques [59]. The diagnostic beam was also used on occasion to lock the laser to the 1064 nm cavity directly using a reflection Pound-Drever-Hall servo. The same PDH setup was also used as an out-of-loop sensor of the detuning noise performance of the filter cavity when the laser was locked to the 532 nm cavity. The calibrated detuning noise spectrum shown in Figure 6-3 was measured using this out-of-loop sensor.

6.1.3 Filter cavity characterization measurements

As discussed in Chapter 5, intra-cavity loss and detuning noise can significantly degrade the performance of quantum filter cavities. The impact of both of these technical effects is more acute for shorter filter cavities which require a very high finesse to reach the desired linewidth. A shorter filter cavity will have a larger loss level per meter resulting in a larger degradation in squeezing [42]. A cavity with a higher finesse is also a more potent detuning noise to phase noise transducer, necessitating a much better suppression of detuning noise. For this reason, we undertook an extensive effort to minimize the level of optical loss in our filter cavity. We also designed a suitable control scheme to suppress detuning noise.

A detailed study of optical loss from our filter cavity mirrors was carried out both at MIT [59] and at Caltech [78, 111]. Figure 6-2 shows the results the MIT study of cavity loss as a function of spot size and spot position[2]. The spot size was varied by

[2]Additional details about these loss measurements can be found in Tomoki Isogai's thesis [58]

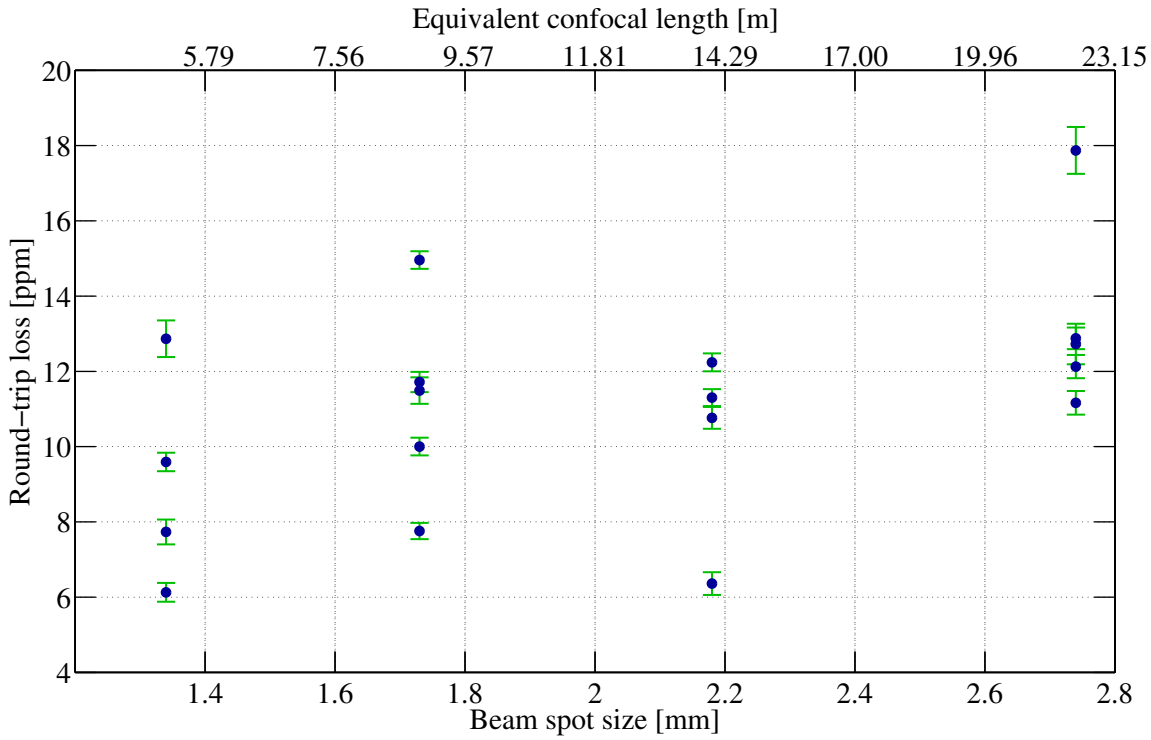

Figure 6-2: A summary of the loss measurements made with our 2 meter filter cavity (adapted from Ref [59]). Here the plotted loss value represents the sum of the intra-cavity loss and end mirror transmission ($\approx 1.5\,\mathrm{ppm}$). The losses were measured as a function of beam spot size and spot position on the optic.

adjusting the length our nearly concentric cavity. No significant dependence on beam spot size was observed, but the loss varied significantly for different spot positions on the optics. By carefully selecting a low loss position on the optics, intra-cavity loss levels as low as $\approx 2.5\,\mathrm{ppm}$ per optic were achieved. One should note that the range in the values for the intra-cavity loss, finesse, and linewidth in Table 6.1 account for the various data points in Figure 6-2. The loss values obtained here suggest that we can easily meet our target of $\leq 1\,\mathrm{ppm/m}$ for the Advanced LIGO filter cavity (16 m Confocal cavity).

A calibrated displacement spectrum for the filter cavity length servo is shown in Figure 6-3. The bulk of the RMS comes from unsuppressed frequency noise above a few kHz. This is above the cavity pole ($\approx 1.2\,\mathrm{kHz}$) so its impact on the phase of the reflected squeezed field is significantly reduced.

Figure 6-4 shows the level of frequency-dependent phase noise as a function of

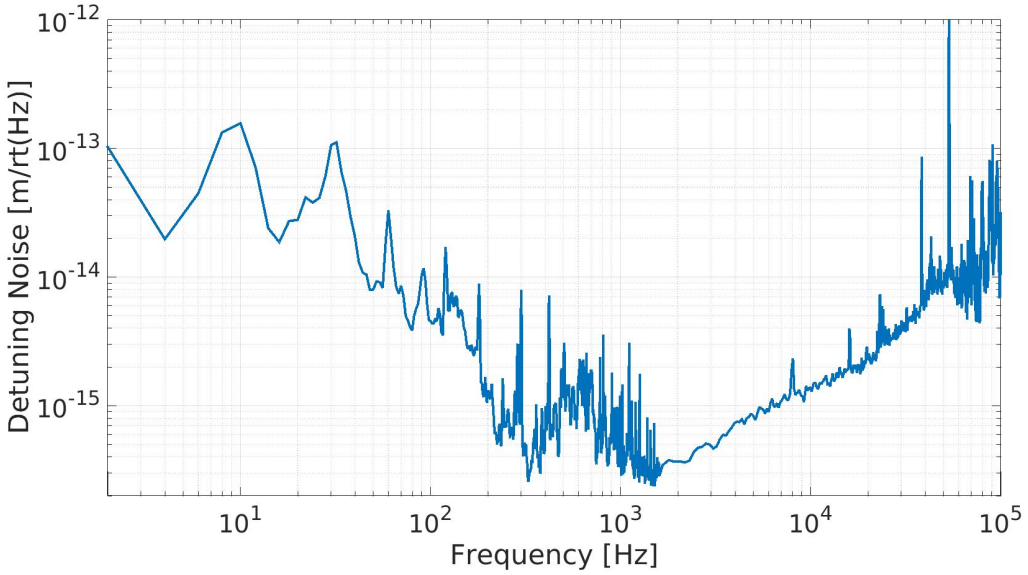

Figure 6-3: Calibrated displacement spectrum of Filter cavity length servo error signal. The filter cavity length servo was typically operated with a bandwidth of 30 kHz

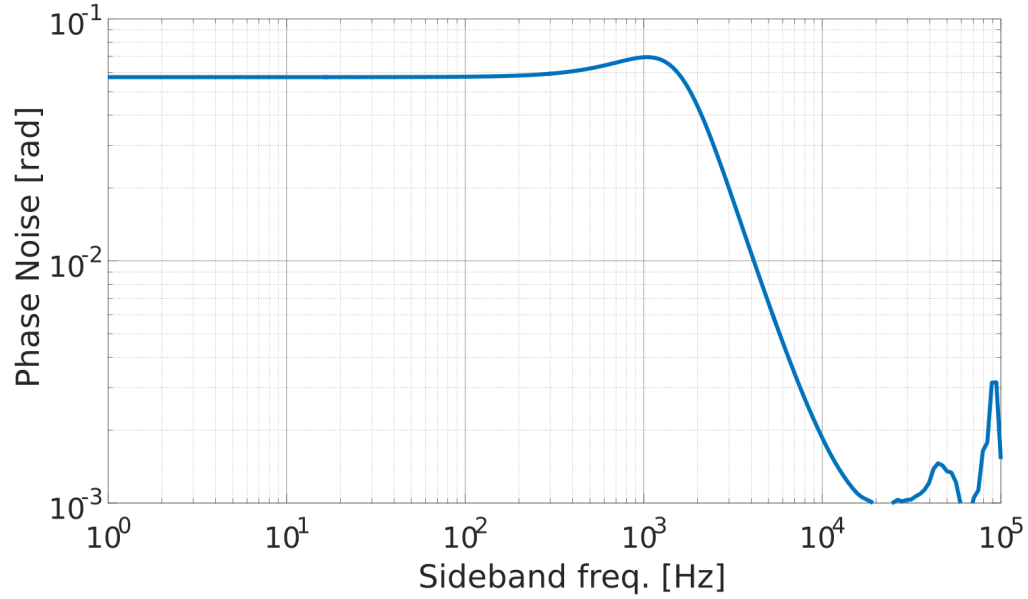

Figure 6-4: frequency-dependent phase noise due to Filter Cavity detuning noise. Based on a length noise measurement from 8-24-14 shown in Figure 6-3. 60 Hz harmonic line noise was not subtracted from the displacement noise spectrum, as had been done with previous detuning noise estimates.

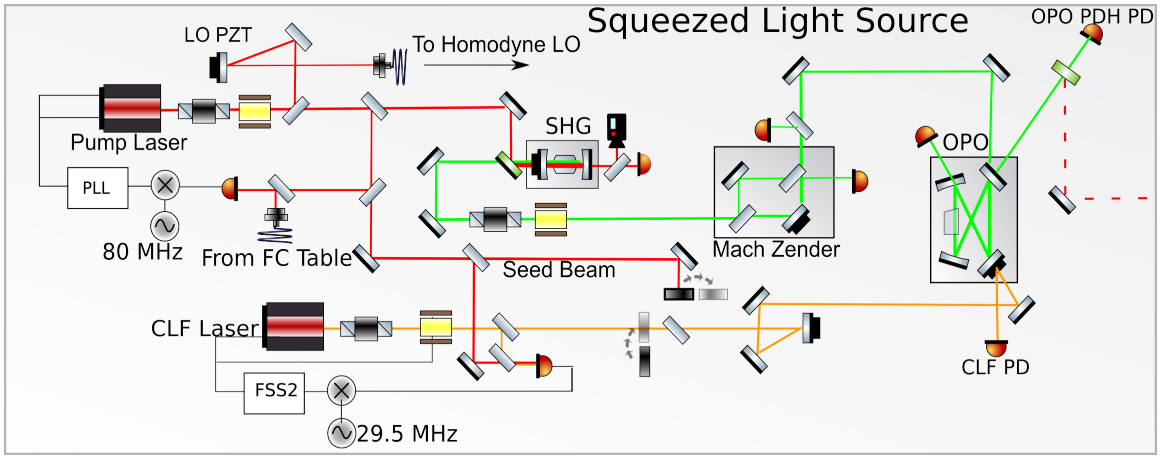

Figure 6-5: Schematic of the squeezed vacuum source used in this experiment. This instrument was used for the H1 squeezing experiment [102] and is described in detail in several theses [26, 36, 98]. It is functionally identical to the instrument presented in Chapter 4, though there several differences in implementation. In this case, the CLF is generated using a second laser phase locked to the pump laser, the SHG cavity is external to the pump laser source, and the OPO cavity is operated in-air. The pump laser is phase locked to the filter cavity laser in order to stabilize the squeezed field detuning from the filter cavity resonance.

squeezing sideband frequency. For sideband frequencies $\leq \gamma_{\mathrm{fc}}$, detuning noise adds approximately 60 mrad of frequency-dependent phase noise, with the contribution falling off rapidly at higher frequencies. The impact of this detuning noise on our squeezing sidebands is significant, but not completely debilitating, as will be discussed in Section 6.2.1.

6.1.4 Squeezed vacuum source

The squeezed vacuum source, depicted in Figure 6-5, was the same instrument which was used during the LIGO Squeezing experiment in 2011 [102]. It was shipped back to MIT after the conclusion of the H1 squeezing test and was recommissioned for squeezed vacuum injection into the 2 meter filter cavity. A detailed description of this squeezed vacuum source can be found in several theses [26, 36, 98] and relevant characterization measurements can be found in [37, 43]. Unlike the squeezed vacuum source presented in Chapter 4, all components are operated in-air. The OPO used in this experiment is based on a design developed by the McClelland Group at ANU.

The control scheme for this squeezed vacuum source is largely the same as that presented in Chapter 4 for the in-vacuum squeezer with a few modifications. This squeezed light source used a second laser phase locked to the pump laser with a frequency offset to generate the CLF. This additional high bandwidth (400 kHz) servo made this squeezed vacuum source somewhat more cumbersome to work with. Additionally, an external Second Harmonic Generator (SHG) cavity was used rather than a Diabolo laser. A theoretical overview of second harmonic generation was presented in Section 4.1.1. An additional phase lock between the pump and filter cavity lasers (denoted PLL in Figure 6-5) was used to stabilize the detuning of the squeezed field relative to the filter cavity, as discussed in the previous section. This second phase lock used a more modest bandwidth of ≈ 30 kHz.

During the LIGO squeezing experiment, the pump laser was phase locked to the interferometer laser instead to ensure that the injected squeezing was at the correct frequency. This servo had high bandwidth (≈ 250 kHz) to suppress the relative phase noise between the pump and interferometer lasers as much as possible. In this experiment, the goal of the PLL is to suppress frequency-dependent phase noise caused by the relative detuning noise between the squeezed field and filter cavity. Since the filter cavity laser servo also had modest bandwidth, a high bandwidth phase lock would only succeed in suppressing the relative frequency noise between the two lasers at higher frequencies. Therefore an increase in phase lock bandwidth without a similar overhaul for the filter cavity servo would have been of limited value. Consequently, we decided to forego the additional bandwidth for the sake of simplicity.

In addition to the various servos required to measure squeezing spectra, we also implemented a simple servo for amplifying and stabilizing the intensity of the diagnostic seed field. This was extremely helpful for characterizing the alignment of the squeezed field to the Filter Cavity, since a relatively bright seed field is required to get a decent signal in transmission through the filter cavity. The set-up is depicted in Figure 6-6. The seed field injected through the rear of the OPO cavity will experience a phase dependent amplification due to the non-linear interaction:

$$P_{out} = \frac{4P_{seed}\gamma_r^{clf}\gamma_r^{in}\left(1 + x^2 + 2x\cos(\theta_B - 2\phi_{seed})\right)}{[(1-x^2)\gamma_r^{tot}]^2} \tag{6.1}$$

where P_{seed} and ϕ_{seed} are the incident seed field power and phase respectively and P_{out} is the transmitted seed field power. We see that this gives us an error signal for phase locking the seed to the pump field, which in turn stabilizes the transmitted seed power. Using a thin pellicle mirror we picked off a small amount of the transmitted seed power and fed back this error signal to the CLF path PZT to lock the seed phase to the pump field. This servo was kept locked while aligning to the filter cavity and when optimizing the visibility at the homodyne readout.

6.2 Production of frequency-dependent squeezing

We achieve the appropriate quadrature rotation by reflecting a standard frequency-independent squeezed vacuum state off the Filter cavity [54, 62, 63, 65]. As with other resonances, that of the filter cavity is dispersive. Spectral components of the squeezed vacuum that lie within the linewidth of the cavity experience a change in their phase upon reflection; those outside the linewidth do not. By operating the filter cavity in a detuned configuration, differential phase can be imparted upon the upper and lower squeezed vacuum sidebands, leading to frequency dependent quadrature rotation.

The combined experimental setup is depicted in Fig. 6-7. The apparatus consists of the broadband squeezed vacuum source described in Section 6.1.4, a detuned filter

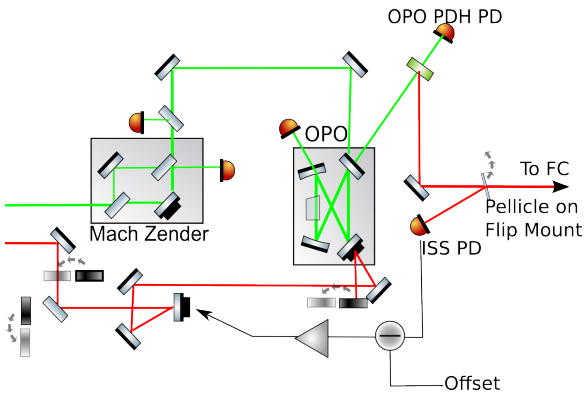

Figure 6-6: Set-up of the seed stabilization servo.

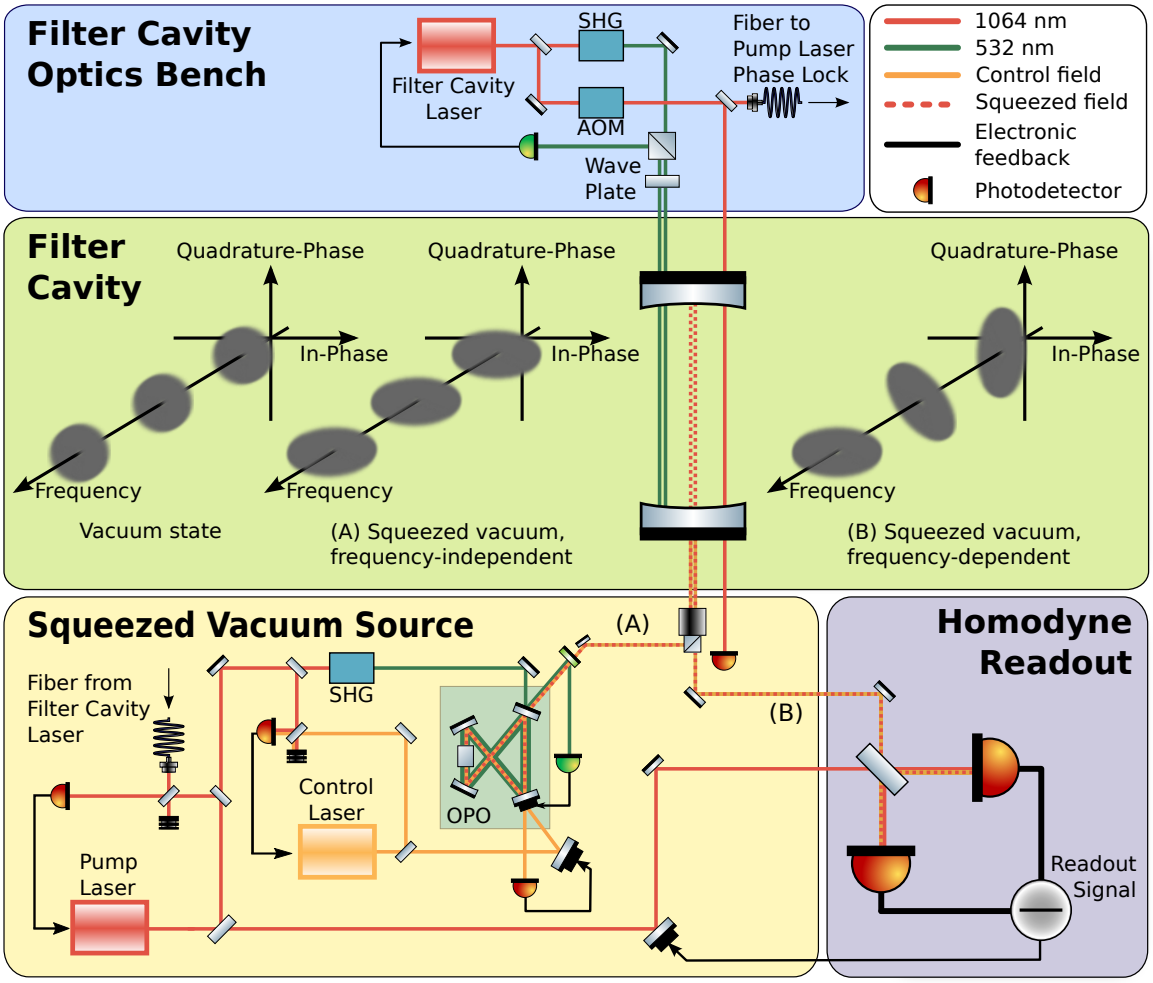

Figure 6-7: Audio-band frequency-dependent squeezed vacuum source. Frequency-independent squeezed vacuum is produced using a dually-resonant sub-threshold OPO operated in a traveling-wave configuration. The OPO is pumped with light provided by a Second Harmonic Generator (SHG). The generated squeezed state is subsequently injected into a dichroic (1064/532 nm) filter cavity along path (A) where it undergoes frequency-dependent quadrature rotation. A Faraday isolator redirects the returning squeezed field along path (B) towards a homodyne readout system where frequency-dependent squeezing is measured. The control laser is phase locked to the pump field with a detuning of 29.5 MHz and is injected through the rear of the OPO cavity. This field co-propagates with the squeezed field to the homodyne readout and is used to lock the local oscillator phase using the coherent control technique. The detuning of the filter cavity is set using an acousto-optic modulator (AOM).

Table 6.2: Parameters of the frequency-dependent squeezed vacuum source. Entries marked by an asterisk were determined most accurately through fitting to recorded data. In all cases fitting produced values in keeping with independent measurements and their uncertainties.

Parameter	Value
Filter cavity length	1.938 408(6) m
Filter cavity storage time	127.5(25) µs
Filter cavity decoherence time	1.8(4) ms
OPO nonlinear gain*	12.7(4)
OPO escape efficiency	95.9(10) %
Propagation loss*	11.9(9) %
Homodyne visibility	96.6(10) %
Photodiode quantum efficiency	93(1) %
Filter cavity round-trip loss*	7.0(16) ppm
Freq. indep. phase noise (RMS)*	31(7) mrad
Filter cavity length noise (RMS)*	$(7.8 \pm 0.2) \times 10^{-13}$ m
Filter cavity-squeezed vacuum mode coupling	97(2) %

cavity described in Section 6.1.1 which produces the desired frequency-dependent rotation of the squeezed quadrature, ancillary systems which set the detuning of the filter cavity as described in Section 6.1.2, and a balanced homodyne detection system for measuring the squeezed state. Key parameters of the system are listed in Table. 6.2.

The squeezed vacuum source is built around a traveling-wave OPO cavity [28, 99] resonant for both the 532 nm pump light and the 1064 nm squeezed vacuum field it generates. The OPO outputs 11.8(5) dB of squeezing via parametric down-conversion in a non-linear periodically-poled KTP crystal. After leaving the OPO, the squeezed field is reflected off the filter cavity, inducing rotation of the squeezed quadrature for spectral components that lie within the cavity linewidth.

The filter cavity is a symmetric, near-concentric, 2 m long Fabry-Perot cavity. It has a storage time of 128 µs and a finesse of ∼30000 for 1064 nm light. The inferred cavity round-trip loss, excluding input coupler transmissivity, is $L_{\mathrm{rt}} = 7$ ppm [59],

corresponding to a decoherence time, defined by

$$\tau_{\text{decoherence}} = \frac{-2L_{\text{fc}}}{c\ln(1-L_{\text{rt}})}, \tag{6.2}$$

of 1.8 ms. The cavity also features a low-finesse (∼150) 532 nm resonance which is used to stabilize the detuning of the squeezed field relative to the filter cavity.

Finally, balanced homodyne detection [47, 99] is used to measure the squeezed state after reflection from the filter cavity. The output of the homodyne detector is used to fix the quadrature of the squeezed state relative to the local oscillator field using the coherent control technique [24].

Measured quantum noise spectra are presented in Fig. 6-8. The data are normalized with respect to the value detected with unsqueezed vacuum fluctuations such that the reported values describe the deviation from shot noise due to the addition of squeezing.

Rotation of the squeezed quadrature occurs near 1 kHz. Squeezing levels of 5.4(3) dB and 2.6(1) dB are observed at high and low frequency, respectively. Weaker squeezing at low frequencies is due to the spectral selectivity and internal losses of the filter cavity, which result in some decoherence of the squeezed state. To achieve the desired quadrature rotation, the central frequency of the squeezed vacuum field is held close to filter cavity resonance; low-frequency squeezing sidebands thus interact with the filter cavity whereas high-frequency sidebands are reflected and incur very little loss.

6.2.1 Realistic model of the filter cavity

A quantum noise model of the form presented in Chapter 5 that includes realistic frequency-dependent decoherence and degradation mechanisms was used to evaluate the results [65]. The model, depicted in Figure 6-9, is similar to the model for Advanced LIGO presented in Section 5.4 and depicted in Figure 5-4 except that the interferometer has been removed.

While all aspects of the system were meticulously characterized, certain parameters were most accurately quantified through fitting this model to the measured data

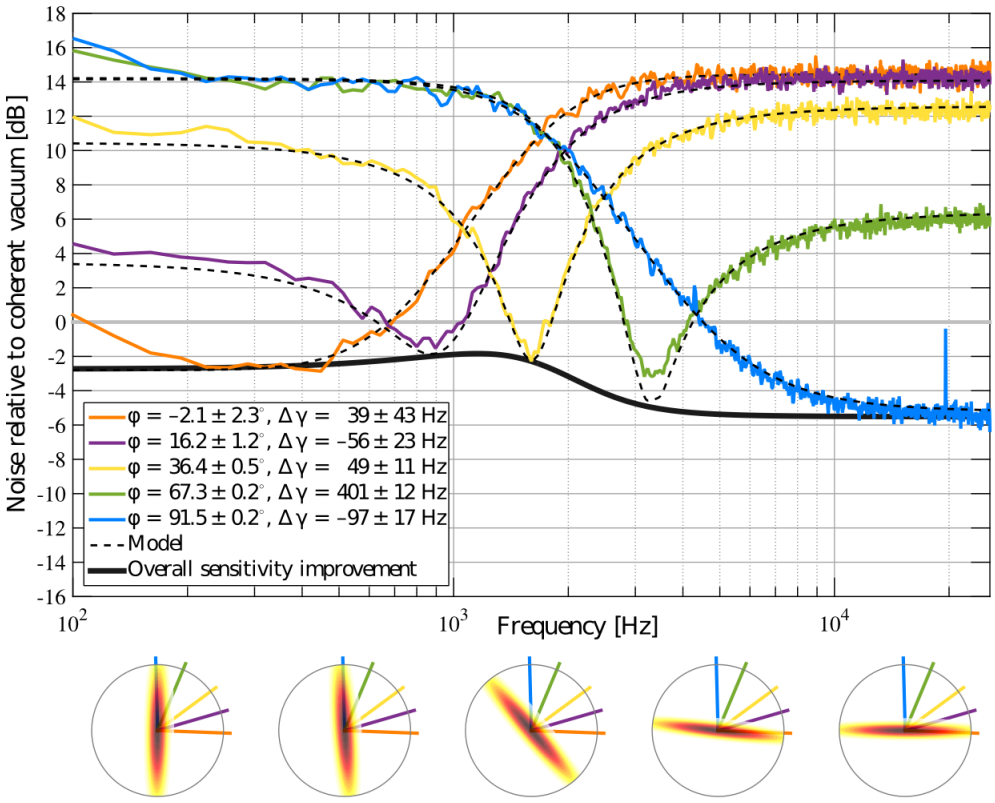

Figure 6-8: Demonstration of frequency-dependent squeezing. Measured noise relative to that due to the naturally occurring vacuum state (shot noise) as a function of sideband frequency and readout quadrature ϕ. The difference between the experimental filter cavity detuning (offset from resonance) and the desired value of 1248 Hz is denoted by $\Delta\gamma$. Dashed curves represent the output of the model described in [65] using the parameters given in the legend and Table. 6.2. The deviation of the recorded data from prediction below ∼300Hz is due to unmodeled environmental disturbances rather than a fundamental limitation of the technique. Data in this band were excluded from the analyses. The solid black curve provides an estimate of the overall improvement achievable if this frequency-dependent squeezed vacuum source were applied to the appropriate interferometer. Ellipses illustrate the modeled squeezing magnitude and angle (Wigner function) at the frequency at which they are located. The measured noise is given by the projection of the ellipse onto the appropriately coloured readout vector.

(see Table 6.2). With the exception of filter cavity detuning and readout quadrature angle, which are different for each of the five measurements reported, a single value for each system parameter was determined using all available data sets. In all cases, fitted values were consistent with direct measurements, given their uncertainties. Furthermore, the close agreement between the measured data and the quantum

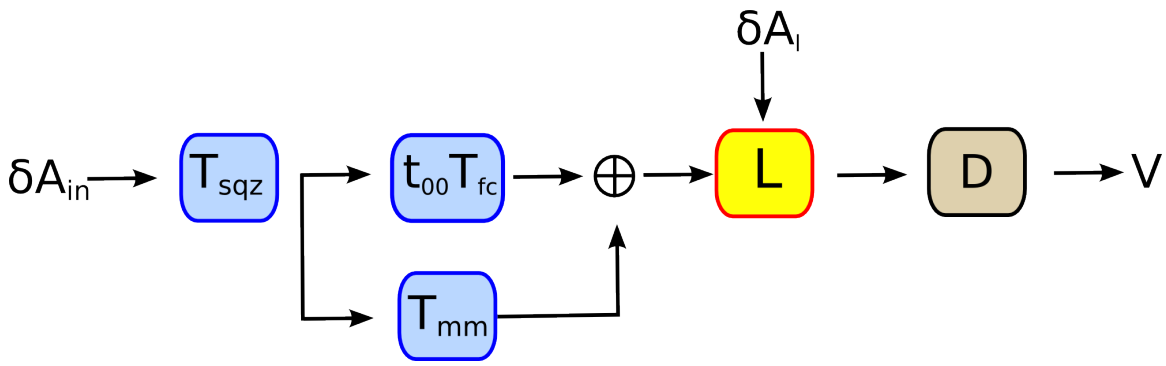

Figure 6-9: A diagram for the noise model of the 2 meter filter cavity. Except for the omission of the interferometer (T_{IFO}), this model is similar to the model for Advanced LIGO discussed in Section 5.4 and depicted in Figure 5-4

noise model, presented in Fig. 6-8, indicates that all significant sources of squeezed state decoherence and degradation are well modeled.

Optical loss, mode mismatch, and squeezed quadrature fluctuations (or phase noise) cause decoherence and a reduction in measurable squeezing [37, 65]. For instance, an ideal squeezed vacuum source with the operating parameters should produce 15.6 dB of squeezing, yet, as expected when the deterioration due to the above listed effects is taken into account, the level we measured was below 6 dB.

Each source of loss leads to decoherence of the entangled photons which make up a squeezed vacuum state. Losses outside the filter cavity affect all frequencies equally and arise due to imperfect optics (propagation loss, OPO escape efficiency), non-unity photodiode quantum efficiency, and imperfect mode overlap between signal and local oscillator beams at the homodyne detector (visibility). One may combine all of these factors in to a single *detection loss*, which was 29 % in the system. Detection loss can be reduced, though at significant cost, through use of improved polarization optics [96], superior photodetectors and active mode matching [76].

The treatment of filter cavity losses is more complicated due to their frequency dependence (see Chapter 5). As an indication, the total loss of the cavity was approximately 16 % on resonance. Advances in this area are limited by the combination of currently available cavity optics and the necessity of using long cavities, and thus large mm-scale beams, to achieve the required storage times [59].

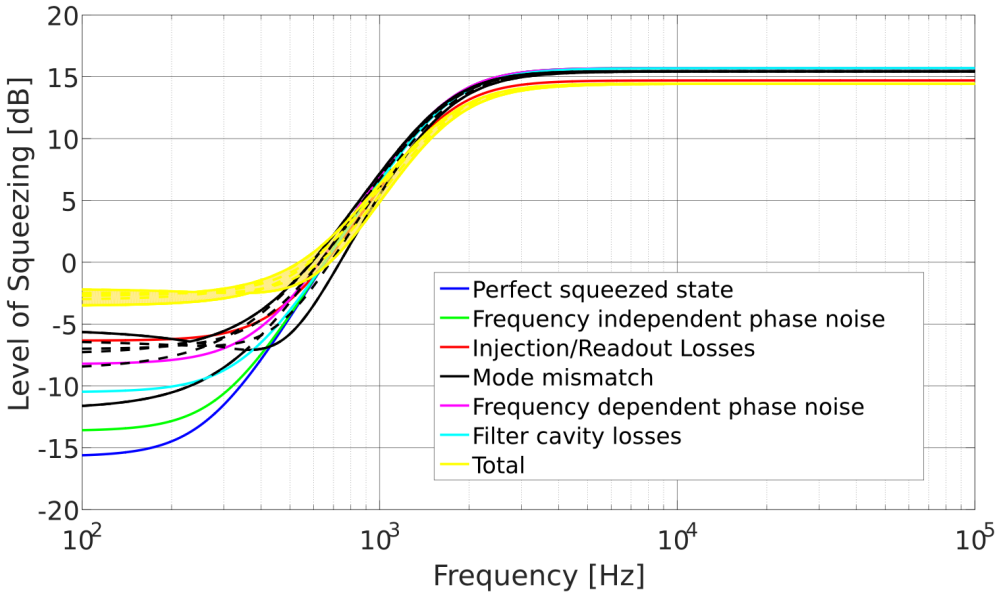

Figure 6-10: The model prediction for the amplitude quadrature. Given the large contributions from mode mismatch and frequency-dependent phase noise, it appears that we were using too high of a non-linear gain to achieve optimal low frequency performance.

The mode coupling between the squeezed field and the filter cavity must also be considered. As descussed in Chapter 5, this effect is more subtle than a simple loss since that portion of the squeezed vacuum not matched to the filter cavity is not rotated in the desired manner and yet still arrives at the homodyne detector. This "dephasing" effect corrupts the squeezed quadrature with noise from its orthogonal counterpart in a frequency-dependent manner [65].

Cavity birefringence [7, 12] was investigated as a possible source of frequency-dependent loss. However, studies verified that the elliptical birefringence in the system, which unlike linear birefringence cannot easily be countered, was negligible. This effect should be revisited in the context of any future systems.

Mitigating the above-mentioned technical noise effects, rather than concentrating on generating stronger squeezing at the source, is currently the most profitable route toward improved performance.

Figures 6-10 and 6-11 give a more detailed accounting of the impact of loss and technical noise on the amplitude ($\phi = 0$ in figure 6-8) and phase quadrature ($\phi = 90$)

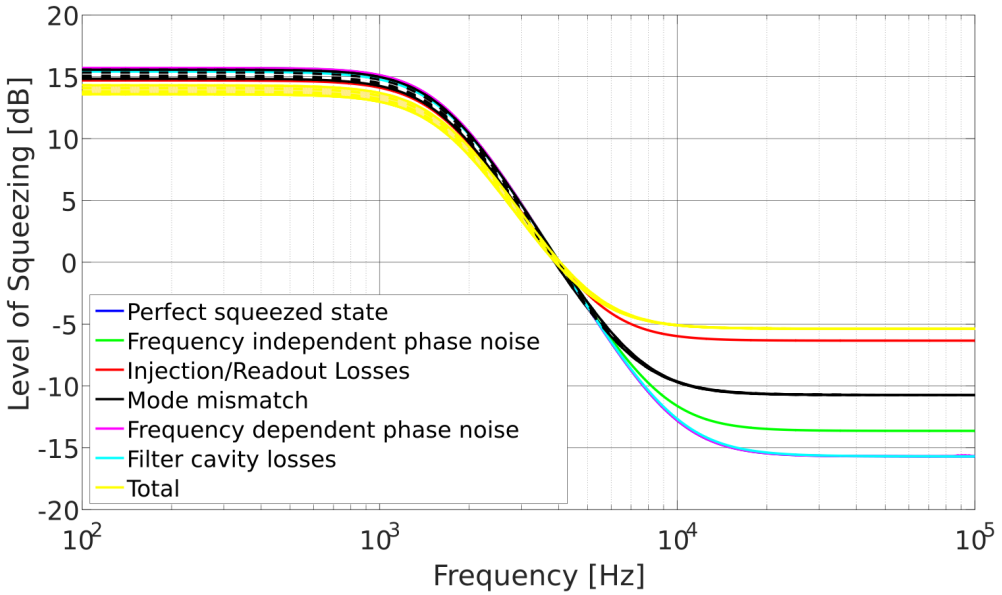

Figure 6-11: The model prediction for the phase quadrature. The squeezing level at high frequencies is primarily limited by propagation losses and mode mismatch at the homodyne readout.

respectively. Note that, in these figures, the 29% detection loss is broken up into two terms: Injection/Readout losses and mode mismatch. We see that the level of high frequency squeezing is completely dominated by detection losses. the low frequency squeezing, on the other hand, appears to be mostly limited by readout/injection losses, mode mismatch, and frequency-dependent phase noise. As discussed in Section 5.3, both frequency-dependent phase noise and mode mismatch result in the measurement quadrature being contaminated with a projection from the antisqueezed quadrature. Therefore, Figure 6-10 suggests that we were using too high of a nonlinear gain to achieve optimal performance at low frequencies.

6.2.2 Detuning drift

When applying this technique for quantum noise reduction in Advanced LIGO, maintaining the correct filter cavity detuning is critical for achieving the optimal sensitivity improvement. One major limitation of the 2 meter prototype was that the detuning was not stable as a function of time. As shown in Figure 6-12, the filter cavity

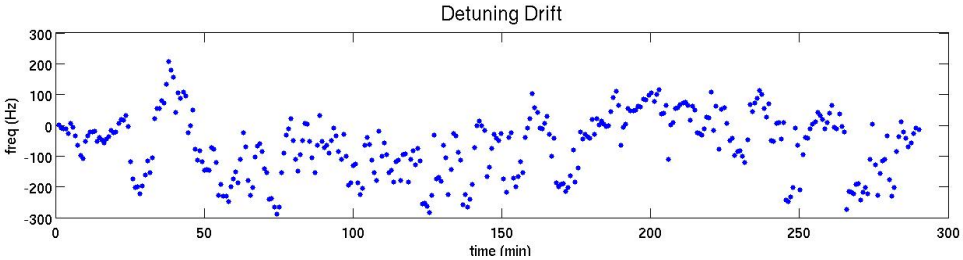

Figure 6-12: Drift in the filter cavity detuning as a function of time. Variations as large as ± 300 Hz are common.

detuning can drift by several hundred hertz over a relatively short time interval.

This was observed in the spectra presented in Figure 6-8. In Figure 6-13 we've altered the curve fitting code to hold the detuning fixed at the optimal value rather than allowing it to vary to optimize the overlap with the model prediction. Though most of the curves still look OK, we see that one of the quadratures differs significantly from the model. This is due to a drift in the detuning between measurements.

This issue was never thoroughly investigated, though there are two likely causes which are both rooted in the fact that we stabilize the detuning using the cavity response at the second harmonic wavelength. During typical operation, the 532 nm and 1064 nm cavities were rarely aligned to be perfectly co-linear. This makes it possible for there to be some alignment-to-length coupling which could cause the 1064 nm resonance to drift with respect to the 532 nm resonance. Also, because of the enormous gap between the 1064 nm finesse ($\tilde{3}0000$) and the 532 nm finesse ($\tilde{1}50$) a small offset in the green servo lock point can have a significant impact on the 1064 nm detuning. For this reason, we plan to increase the 532 nm finesse to ≈ 2000 for the Advanced LIGO filter cavity.

6.2.3 Scaling for gravitational wave detectors

While this demonstration of frequency-dependent squeezing has brought the squeezed quadrature rotation frequency 4 orders of magnitude closer to that required by gravitational-wave detectors, it is still a factor of $\sim$20 away from the 50 Hz target of Advanced LIGO. It is foreseen, however, that the initial implementation of frequency depen-

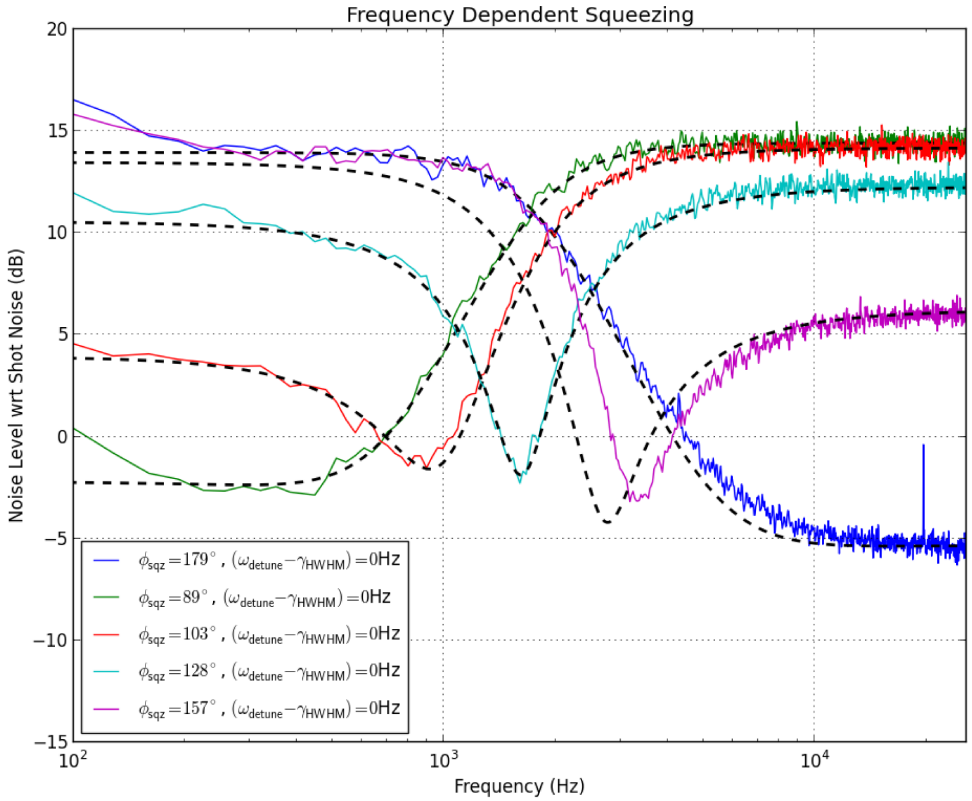

Figure 6-13: Fit for data from Figure 6-8. Here, we do not allow the fit code to account for detuning drift by allowing the detuning for each spectrum to vary as a free parameter. The poor agreement between the fit and spectrum for $\phi_{sqz} = 157$ indicates that the detuning had drifted from the optimal value.

dent squeezing in Advanced LIGO will involve a filter cavity 16 m in length, or a factor of 8 longer than the cavity used in this demonstration [42]. Furthermore, detailed measurements of losses in long-storage time cavities [59], and calculations of the impact of these losses on the performance of frequency-dependent squeezing [65], indicate that a 16 m cavity with finesse roughly 3 times that of the one used in the present work will be sufficient for Advanced LIGO. Such a filter cavity would have a storage time of 2.5 ms, and $\tau_{\rm decoherence} \simeq 0.7$ ms, which is sufficient to maintain a modest level of squeezing below the rotation frequency [42, 65].

Based on the results presented here, previous experimental work [35, 59, 102] and extensive theoretical studies [42, 65, 82], the authors and other members of the LIGO

Laboratory have begun the process of designing and building a full-scale prototype frequency-dependent squeezed light source for Advanced LIGO.

6.3 Conclusions

The principal goal of this endeavor was to demonstrate frequency-dependent quadrature rotation in a band relevant to gravitational-wave detectors, informing the design of all future squeezed light sources in the field. A frequency-independent squeezed vacuum source is only able to reduce noise in the band in which its (fixed) low-noise quadrature is well-aligned to the interferometer signal field. In this case, the observed noise reduction would be approximated by a single one of the curves shown in Fig. 6-8. For example, squeezing the quadrature phase, as previously demonstrated in LIGO and GEO600, would reduce noise at high frequency and increase noise at low frequency, as described by the blue, $\phi = 90°$, curve. The equivalent frequency-dependent source offers equal performance at high frequency but a relative improvement of nearly a factor of 10 in strain amplitude at low frequency.

Applied to a gravitational-wave detector whose optomechanical response conforms with the filter cavity rotation, and assuming the same $\sim$30 % total losses, the overall noise reduction available from this frequency-dependent squeezed vacuum source is given by the solid black curve in Fig. 6-8. This trace represents the lower envelope of the recorded data and the infinite family of curves at intermediate quadratures.

All present ideas for extending the reach of ground-based gravitational-wave observation rely on audio-band frequency-dependent squeezing [3, 39, 86]. We have demonstrated quadrature rotation of squeezed vacuum at audio frequencies, bringing frequency-dependent squeezing 4 orders of magnitude closer to the required frequency regime. Moreover, the measurement uses a relatively short filter cavity and thus leaves a clear path toward scaling to longer storage times.

Extrapolating the results to the case of Advanced LIGO, assuming parameters within reach of current technology, we find that the reduction of quantum noise with frequency-dependent squeezing increases the volume of the detectable universe by

about a factor of two [75]. Larger gains, up to nearly a factor of 10 in volume, are achievable when frequency-dependent squeezing is combined with other improvements [75].

Chapter 7

Implications for Advanced LIGO

The analysis presented in Chapter 3 outlining the design requirements for the Advanced LIGO squeezed light source was based on our understanding at the time of the technical requirements and experimental challenges of implementing frequency-dependent squeezed light injection with Advanced LIGO [42,82]. In subsequent years, our community has gained a great deal of knowledge on frequency-dependent squeezing [65, 83], in-vacuum squeezer design and operation [84, 112, 113], low phase noise squeezed light source design [84], and the impact of squeezing on the astrophysical reach of gravitational wave detectors [39, 69, 75]. The results from the first Advanced LIGO observation run [2, 29] suggest that binary black hole systems are far more prevalent than previously expected. Also, commissioning work to date suggests that reaching the desired operating power will be a significant challenge. Now that the addition of squeezing to Advanced LIGO appears to be on the horizon, it is worth re-visiting our original proposal in light of these more recent developments.

In this chapter, we will reflect on the past several years of research and discuss the implications for the design and performance of the Advanced LIGO squeezed light source. We will also discuss some potential changes for the control scheme and optical design to incorporate lessons learned from the two meter filter cavity prototype and the development of our in-vacuum squeezed light source. Finally, we will highlight some barriers to implementing squeezing in Advanced LIGO that were not addressed in Chapter 3 and discuss potential remedies as well as lingering questions which

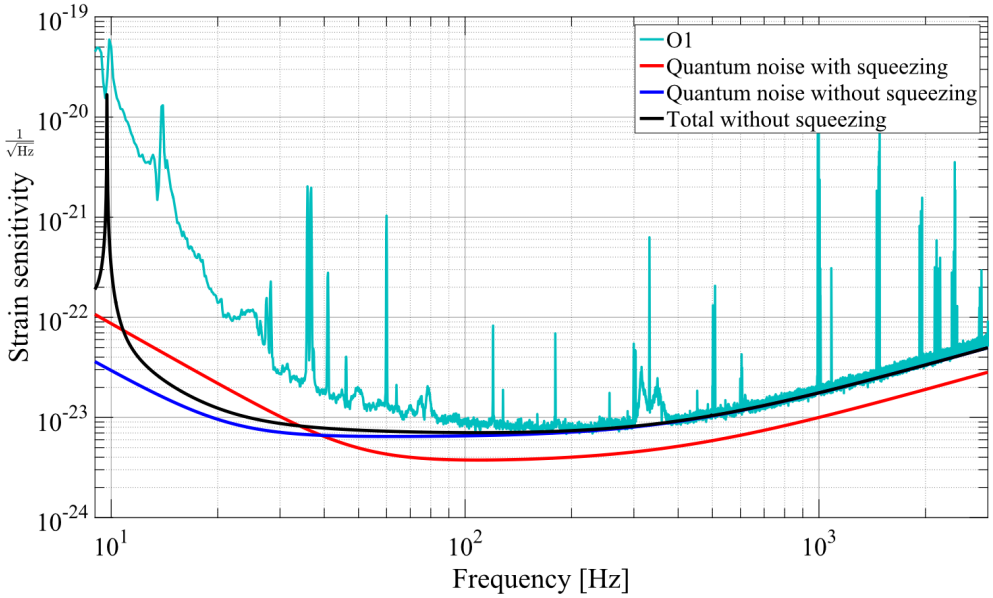

Figure 7-1: Sensitivity of the LIGO Hanford Observatory during the first observation run of Advanced LIGO. The black trace shows the total noise level predicted using the GWINC simulation tool. Note that there is a substantial amount of additional technical noise below 100 Hz. Given the current injection power (20 W) and technical noise, we are not close to being radiation pressure noise limited. This suggests that we would still benefit from injecting frequency-*independent* squeezed vacuum. The red trace shows the quantum noise level assuming 10 dB of injected squeezing, 10 mrad of phase noise, and 25% total loss.

require further study.

7.1 Prospects for improving the sensitivity of Advanced LIGO using squeezed light

In light of recent analysis of benefit from squeezed vacuum injection [69, 75], the impact of filter cavity technical noise [65], and the results presented in Chapters 4 and 6 we may now make projections for the sensitivity improvement we expect with squeezing for Advanced LIGO and various future upgrades.

7.1.1 Frequency-independent squeezing as an early upgrade

We begin by considering the current state of Advanced LIGO. Though Advanced LIGO did meet its target sensitivity for its first observing run, it did not attain the design sensitivity presented in Figure 1-2. In fact, it is unlikely that we will reach this sensitivity level before installing a squeezed vacuum source in at least one of the two observatories during the commissioning period between the second and third observing runs.

Significant technical issues need to be addressed before Advanced LIGO can meet its design sensitivity. Much of the excess technical noise between 20 Hz and 100 Hz is not well understood and may take significant time and effort to overcome. Also, operating at full sensitivity will require increasing the injected power from 20 W to 150 W. Operating the interferometer at such high power can cause several technical issues such as thermal lensing and the excitation of parametric instabilities [**?**].

It is also likely that the in-vacuum squeezed light source will be ready for installation before the filter cavity. Given these realities it is worth considering installing a frequency independent squeezer as soon as possible. As shown in Figure 7-1, this would allow us to increase our sensitivity above 100 Hz without causing significant degradation at lower frequencies due to the increase in radiation pressure noise.

Its also worth noting that, in the limit of zero loss, the impact of frequency independent squeezing on our quantum noise level is completely equivalent to increasing the laser power. In this sense, frequency independent squeezing provides us with a viable alternative to turning up the laser power in the event that operating at full power proves to be impractical.

7.1.2 The impact of technical noise from a realistic filter cavity

As discussed in Section 5.3, technical imperfections of the filter cavity will allow a portion of our anti-squeezing to contaminate the measurement quadrature and degrade the low frequency sensitivity of the interferometer. Recent analysis of the impact of squeezed light injection on the astrophyscial reach of Advanced LIGO suggest that

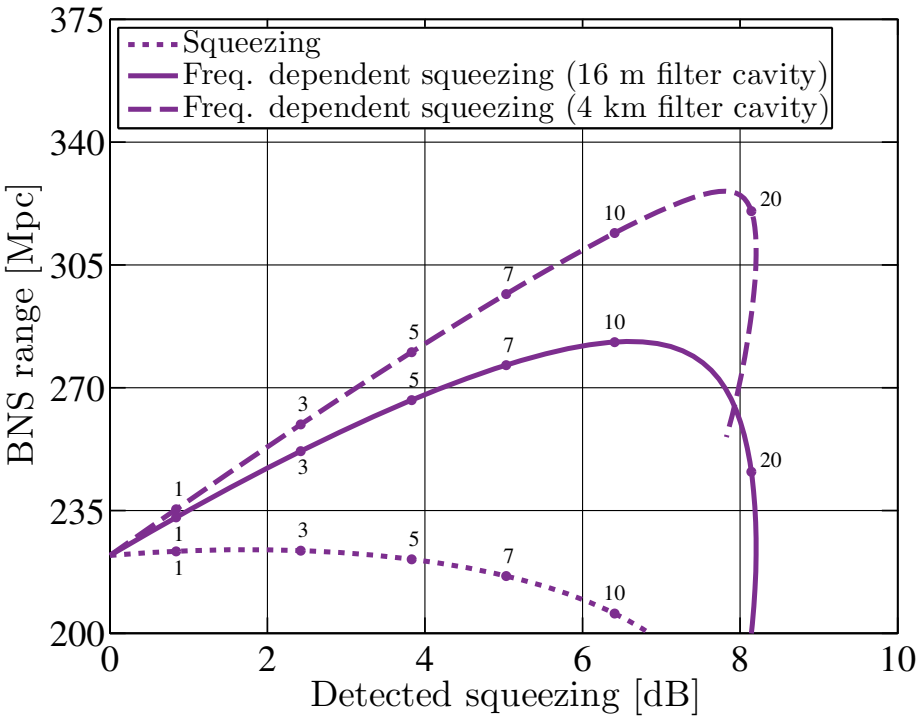

Figure 7-2: The detection range for binary neutron star inspiral events as a function of the level of injected squeezing (adapted from Reference [75]). Due to technical imperfections of the filter cavity, very high levels of injected squeezing can reduce the improvement in sensitivity. These effects are less of a limitation for longer filter cavities.

operating with the optimal low frequency sensitivity is critical for the detection and analysis of gravitational waves from compact binary inspirals [69, 75]. To date, we have only detected gravitational waves from binary black hole systems which merge at frequencies in the lower end to the Advanced LIGO sensitivity band [2, 29]

As a result, we will most likely choose to operate the squeezer with a relatively low level of injected squeezing when the interferometer is taking data. Figure 7-2 shows that, with a 16 m filter cavity, 10 dB of injected squeezing is optimal for detecting gravitational waves from binary neutron star (BNS) systems.

In Chapter 3, we calculated that 20-25% total optical loss allows one to achieve $\geq$ 6 dB of squeezing enhancement provided that we limit our total phase noise to $\leq$ 10 mrad. This number assumes that we are free to increase the level of injected squeezing in order to maximize the level of measured squeezing at frequencies where we are shot noise limited.

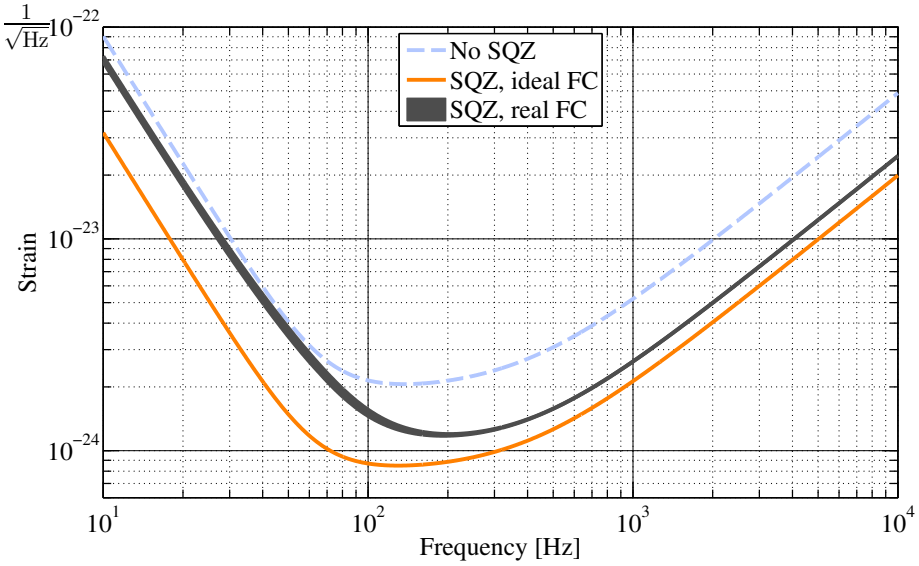

Figure 7-3: Expected quantum noise level in Advanced LIGO. Three cases are shown. The blue dashed trace represents the expected quantum noise performance of Advanced LIGO at full design sensitivity. The orange curve shows the quantum noise performance of Advanced LIGO with an ideal filter cavity and 15% optical loss. The black curve shows the quantum noise performance with the proposed Advanced LIGO filter cavity described in Section 5.4. With a realistic filter cavity, the squeezer must be operated with a lower nonlinear gain. This optimizes the performance at low measurement frequencies but reduces the level of squeezing at frequencies where the interferometer is shot noise limited.

From Figure 5-7, we see that when limited to 10 dB of injected squeezing (nonlinear gain of g$\leq$ 5) limiting our optical loss to 25% will only allow us to reduce our shot noise level by 5 dB. Attaining a 6 dB sensitivity improvement will require reducing the total optical loss to 15% as shown in Figure 7-3.

Also figure 5-7 shows that, with only 10 dB of injected squeezing, the impact of phase noise is negligible with 25% total loss. It also shows that our long term goal of a 10 dB improvement in sensitivity would require reducing our total optical loss to less than 2%. To date, not even table-top squeezing experiments have achieved such a low level of loss.

In order to take full advantage of the reduction in optical loss and phase noise we expect for Advanced LIGO, we would need to circumvent the limitations imposed on us by the filter cavity. Given the level of loss in conventional optical coatings, our only viable strategy at the moment its to make the filter cavity substantially longer.

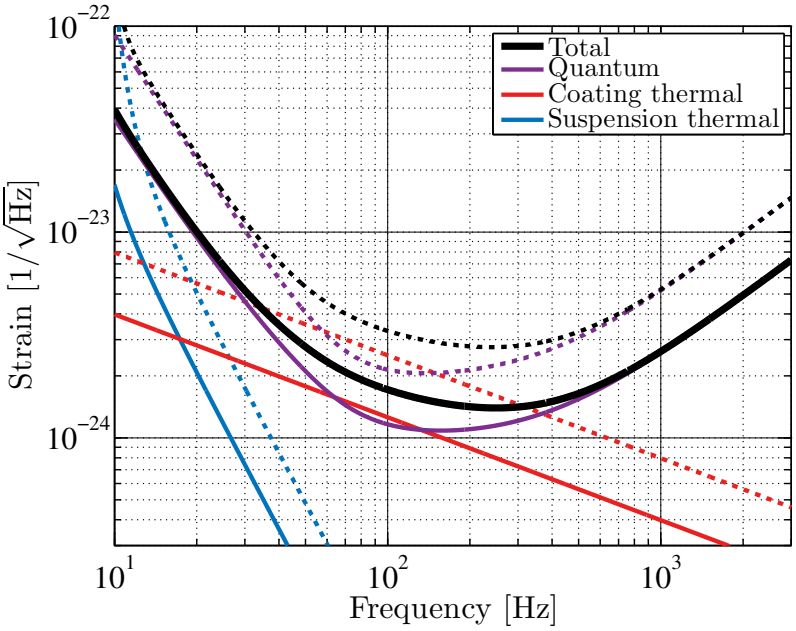

Figure 7-4: Strain sensitivity of a possible upgrade to Advanced LIGO (adapted from Reference [75]). The dashed lines represent the noise levels for coating thermal noise, quantum noise, suspension thermal noise for Advanced LIGO. The solid curves show how these noise terms would scale if this upgrade were implemented.

As shown in Figure 7-2, with a kilometer-scale filter cavity the constraints imposed on the level of injected squeezing are relaxed considerably. Unfortunately, this upgrade is unlikely due to the substantial cost of building such a cavity.

7.1.3 Doubling the range of Advanced LIGO

Frequency dependant squeezing is one of several upgrades that have been proposed for Advanced LIGO. Below 100 Hz, Advanced LIGO is limited by both quantum noise and thermal noise. In order to maximize the sensitivity improvement from squeezed vacuum injection, it is necessary to reduce thermal noise as well. Reference [75] discusses several potential modifications to Advanced LIGO which address both quantum noise and thermal noise limitations:

- **Larger beam spot size:** Increasing the size of the beam spot reduces brownian coating thermal noise in proportion to the beam diameter by averaging over a larger coating area.

- **Double the test mirror mass:** This would reduce radiation pressure noise by a factor of two. A larger surface area would also accommodate a larger beam spot size.

- **Longer suspension fibers:** Suspension thermal noise scales as 1/L where L is the length of the suspension fiber.

- **frequency-dependent squeezing:** Add a squeezer and a filter cavity to achieve a broadband reduction in quantum noise.

A plot of the expected improvement in sensitivity is shown in Figure 7-4. If implemented in full, these upgrades would double the detection range of Advanced LIGO for binary neutron star and binary black hole inspirals [75].

7.1.4 Beyond Advanced LIGO

As of now, plans for third generation gravitational wave detectors are still tentative. The most established proposals call for adding cryogenics to reduce thermal noise [3], increasing the interferometer arm length to reduce the impact of displacement noise terms (which scale as 1/L where L is the arm length) [39], or both [86].

One common element to all future designs is the injection of frequency-dependent squeezing to achieve a broadband reduction in quantum noise. Many designs call for 10 dB of squeezing. In light of the discussion in Section 7.1.2, this will most likely necessitate a kilometer-scale filter cavity to reduce the impact of filter cavity technical imperfections. As discussed in Chapter 3, this will also require that the total frequency independent loss be limited to $\leq 10\%$. Using a low phase noise squeezed vacuum source like the one presented in Chapter 4 will be necessary to relax the loss requirements as much as possible.

Despite these daunting requirements, it is clear that squeezed vacuum injection is a technique which will be vital to the field of gravitational wave astronomy for the foreseeable future.

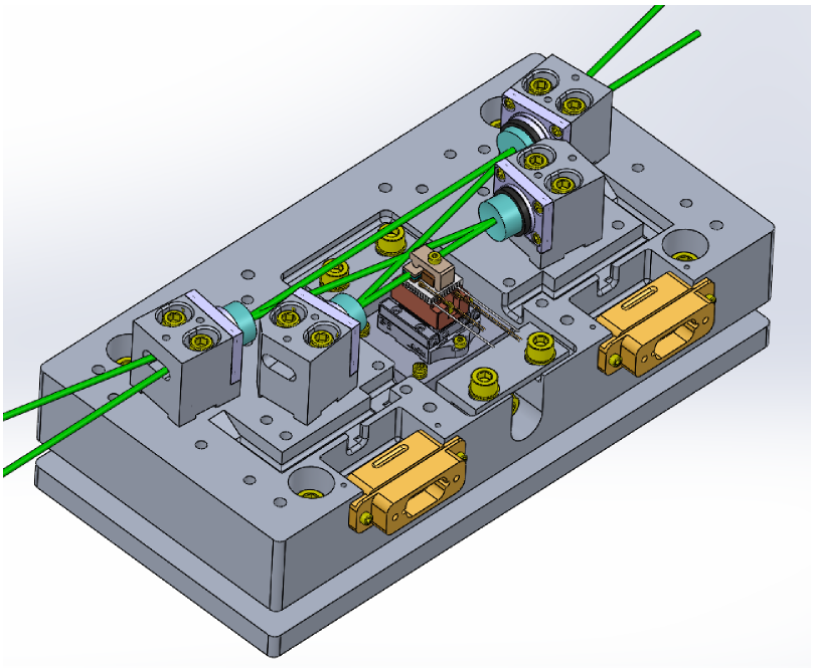

Figure 7-5: A Solidworks model of our new metal based VOPO design. Most of the components are screwed together which will allow for rapid assembly, alignment, and (if necessary) replacement of all major components.

7.2 Proposed changes for Advanced LIGO squeezer

We now discuss some changes to the Advanced LIGO squeezer design proposed in Chapter 3. These will be based on lessons learned from the two prototype experiments conducted at MIT over the last several years which were discussed previously in Chapter 4 and Chapter 6.

7.2.1 Modification of the VOPO Design

The in-air OPO design used during the H1 squeezing experiment suffered from a very high level of length noise which added more than 20 mrad of additional phase noise [37]. In Chapter 3 we proposed using a monolithic design for the Advanced LIGO OPO, similar to the design used for the Advanced LIGO Output Mode Cleaner cavity. Such a design would be UHV compatible and have a negligible phase noise contribution from OPO cavity length noise

We were aware at the time that this design was overkill in terms of the cavity

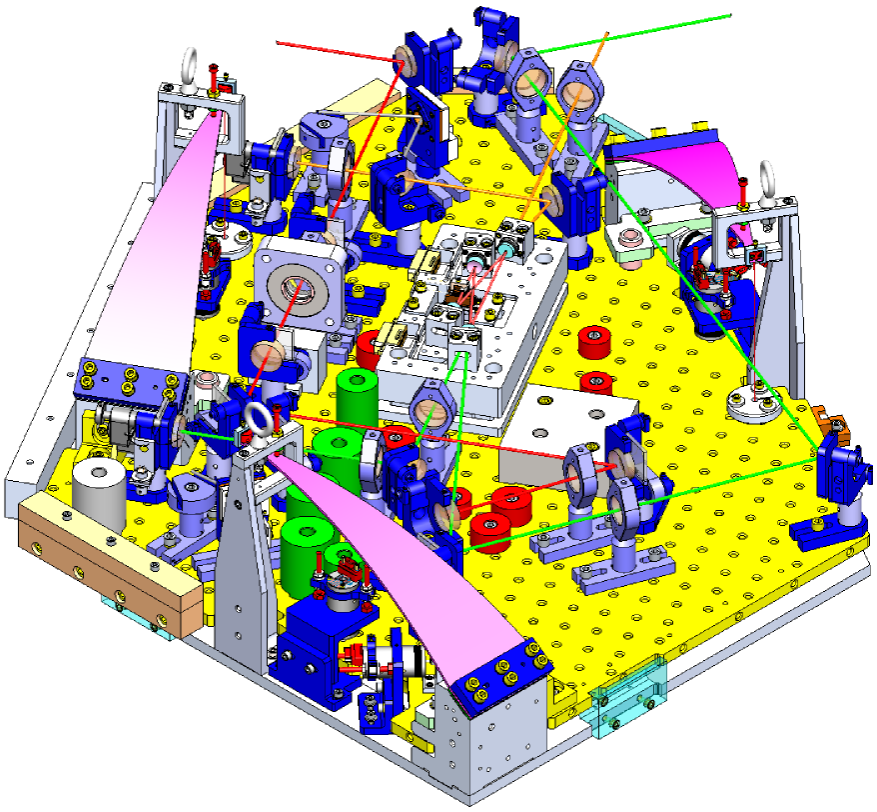

Figure 7-6: A Solidworks model of the suspended platform for our VOPO cavity. This platform will also house the fiber couplers and injection optics for the pump and CLF fields and an additional Faraday isolator used for injecting the squeezed field into the filter cavity.

length noise requirements, but we figured that it made sense to just copy an existing cavity construction method. Unfortunately, the monolithic design proved to be quite difficult to assemble. Our cavity layout resulted in the higher order mode spacing and cavity alignment being extremely sensitive to the position and orientation of the two curved mirrors.

As a result, we decided to switch back to a metal based design for easier assembly [74]. Based on the in-air phase noise and OPO length noise measurements presented in Chapter 4, we believe that we have roughly a factor of 10 of headroom for additional length noise. Once the VOPO is suspended in vacuum (see the suspension in Figure 7-6), we expect to meet the length noise requirement easily.

We are also planning on doubling the finesse of our cavity for 532 nm in order to decrease the amount of pump power that needs to be fiber-coupled into vacuum to

operate the VOPO. Besides a slight increase in our susceptibility to added phase noise from VOPO length noise (see Equation 3.4), we don't see any significant downsides to this design change.

7.2.2 Mitigation of filter cavity detuning drift

In order to obtain the optimal sensitivity improvement from frequency-dependent squeezing, it is necessary that the filter cavity detuning be held near its optimal value given in Table 5.1. As shown in Figure 6-12, our 2 m prototype filter cavity suffered from a significant level of drift in the filter cavity detuning. We suspect that this was due to the large gap in finesse between the 1064 nm cavity resonance (≈ 30000) and the 532 nm resonance (≈ 150) used for our cavity length servo. Small offsets in the length servo result in a larger shift in the 1064 nm detuning relative to the narrow 1064 nm resonance. Detuning fluctuations as large as ± 300 Hz were observed. We plan to address this by increasing the 532 nm cavity finesse to ≈ 2000. The detuning drift will scale as:

$$\Delta_{16m} = \frac{2\,m}{16\,m} \times \frac{150}{2000} \Delta_{2m} \tag{7.1}$$

where Δ_{16m} and Δ_{2m} denote the detuning drift in Hz for our 16 m and 2 m filter cavity respectively. Provided that this is the dominant source of detuning drift, this rescaling should reduce the drift down to ± 2.8 Hz.

7.2.3 Simplified control scheme

One of the most significant limitations of the 2 m filter cavity setup was the complexity of the control scheme. Producing frequency-dependent squeezing with that setup required three lasers and eight servos [1]. As a result it was difficult to run that apparatus with the high duty cycle required for use with Advanced LIGO. In this section I'll propose a simplified control scheme which should lead to a considerable

[1] Employing the same control scheme for Advanced LIGO would require a 9th servo to phase lock the filter cavity laser to the PSL

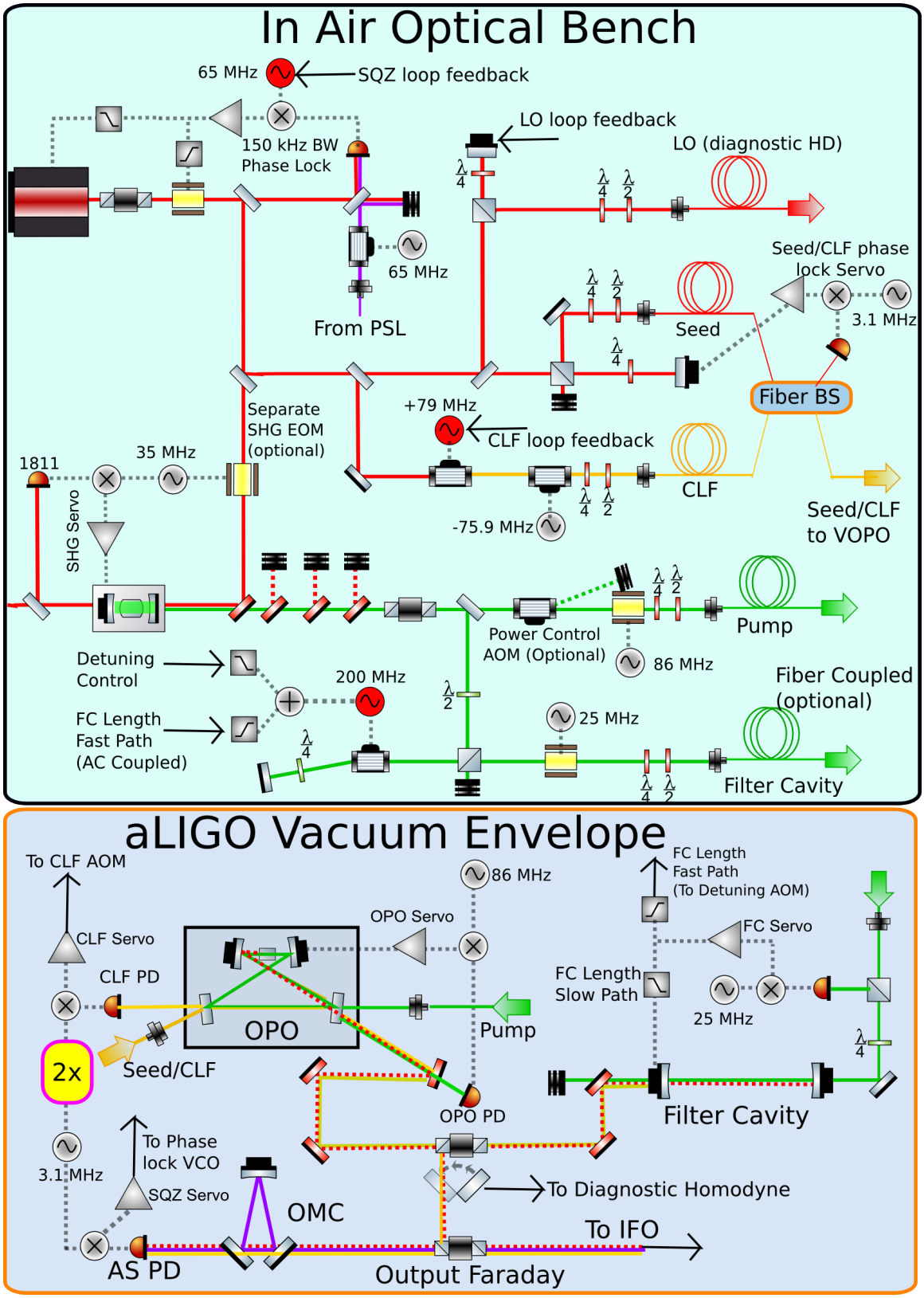

Figure 7-7: Schematic of proposed control scheme for the Advanced LIGO squeezed light source. The control scheme is described in detail in the main text.

improvement in ease of use. A schematic of my proposed design is shown in Figure 7-7.

No auxiliary lasers: One can achieve a significant reduction in complexity by using only one laser source to operate the Advanced LIGO squeezer. As discussed in Section 4.1.2, one can replace the auxiliary laser used to generate the CLF with our 2 m Filter cavity setup with two AOMs without adding a significant level technical noise due to seed field contamination. We may lock the CLF servo (2Ω quadrature control loop) by feeding back to a VCO driving one of the AOMs as was done with our in-vacuum squeezer presented in Chapter 4.

One may also eliminate the need for a separate filter cavity laser and SHG by obtaining the 532 nm field required for locking the filter cavity by picking off a small fraction of the pump field. This field is then double-passed through an AOM and used to lock the filter cavity length to the pump laser frequency. The detuning of the squeezed field relative to the filter cavity can be controlled by varying the frequency of the RF source driving this AOM. If desired, additional bandwidth for the filter cavity length servo can be obtained by also feeding back to the drive frequency of the detuning AOM at higher frequencies. However, one must carefully AC couple this feedback path as any DC feedback would result in an offset from the desired filter cavity detuning.

ISS and seed servo: DC Intensity stabilization of the pump field can greatly reduce drift in the level of squeezing produced by an OPO [43, 108]. For this reason a Mach-Zehnder interferometer was used with the H1 squeezer [43] and the GEO 600 Squeezer [108] to stabilize the level of pump power. For the VOPO, we require an actuator which does not couple to the alignment to avoid misaligning our optical fiber. Here, I suggest using an AOM, whose drive power may be varied to adjust the level of pump power being shunted into the first order beam. As a possible alternative, we are working on a new control scheme for the SHG cavity where we lock side-of-fringe to stabilize the level of generated pump power.

The seed servo loop shown in Figure 6-6 used for generating a bright diagnostic field for aligning our 2 m filter cavity required the use of a pick-off beam. This setup is not ideal for an in-vacuum squeezer, as it would require an in-vacuum motorized

flipper mount or waveplate. Such components require a vent of HAM 6 in order to install a replacement if they break. As an alternative, one may stabilize the nonlinear gain of the seed field using either a dither servo in reflection off the OPO cavity or by phase locking the seed field to the CLF field, as shown in Figure 7-7. Unlike the servo used for the 2 m filter cavity experiment, neither of these error signals directly depend on the level of transmitted seed power. The transmitted seed power will still drift if the incident seed power changes even after one stabilizes the non-linear gain.

OPO, SHG, FSS, and SQZ servos: As of now, I propose keeping the remaining servo loops more or less the same as they were for the H1 squeezing experiment. The only major change I propose is obtaining the SQZ loop error signal (1Ω quadrature control error signal) in transmission through the Output Mode Cleaner (OMC). As discussed in Chapter 3, this will greatly reduce the lock point errors generated by alignment jitter: the principle source of phase noise in the H1 Squeezing experiment.

One remaining question is whether we want to "invert" the control scheme for the OPO loop by feeding back to the pump laser frequency path. With this control topology, the SQZ loop error signal would be fed back to the piezo on the OPO cavity. This would allow us to substantially increase the bandwidth of the OPO loop but would most likely limit the bandwidth of the SQZ loop to a few kHz [2]. The idea here is to use the OPO as a reference cavity as its length noise should be modest once it is moved into vacuum.

Though we need to make a full noise budget to know for sure, I suspect that this control scheme inversion is likely to do more harm than good. Even with low length noise, the VOPO is still a poor candidate for a reference cavity. Due to its short length and low finesse, the PDH error signal is typically buried in shot noise. For the VOPO prototype discussed in Chapter 4, the shot noise level was around $10\text{Hz}/\sqrt{\text{Hz}}$ and our free-running error signal spectrum was completely shot noise limited above a few kHz[3]. The modulation depth of the PDH sidebands in that experiment was kept modest (≈ 0.01) to minimize the phase noise contribution from the control sidebands.

[2]The SQZ bandwidth will still be limited to ≈ 10 kHz due to the LIGO arm cavity FSR (37.5 kHz) with my proposed control scheme.

[3]In principle, this can be a significant source of filter cavity detuning noise [81]

I believe that the additional filtering of RF phase noise provided by the OMC should allow us to increase the modulation depth substantially. Even if we optimize the control sideband modulation depth (which will significantly increase the amount of pump power we need to fiber couple into vacuum), the shot noise level will still be above $0.1\text{Hz}/\sqrt{\text{Hz}}$.

The SQZ loop error signal, by comparison, is an outstanding reference for phase noise suppression provided that lock-point errors in our quadrature control loops are not a significant issue. This suggests that we may be better off using the frequency path for the SQZ loop in order to keep its bandwidth as high as possible.

7.3 An unresolved issue: technical noise from backscattered light

As discussed in Chapter 3, one potential pitfall of implementing squeezed light injection in Advanced LIGO is the degradation of the interferometer's low frequency sensitivity due to technical noise from the light backscattered by the squeezer [27,82]. Since we anticipate that Advanced LIGO will be quantum noise limited down to 10 Hz, we require that this noise be well below the quantum noise level of the interferometer. Our current design assumes that the only source of technical noise on the backscattered field is due to path length fluctuations along the squeezing injection path. Therefore, one can mitigate the noise by moving the OPO and all injection optics into vacuum and seismically isolating them.

Subsequent analysis has revealed that there are two additional sources of technical noise that can contribute significantly for the level of backscattered power assumed in Figure 3-2: Intensity and frequency noise on the pump field which is down-converted onto the backscattered field via the nonlinear interaction in the OPO, and length noise on the filter cavity which can impose both phase and intensity noise on the portion of the backscattered field which resonates in the filter cavity. We discuss each in turn in the next two subsections, and then conclude by discussing the implications

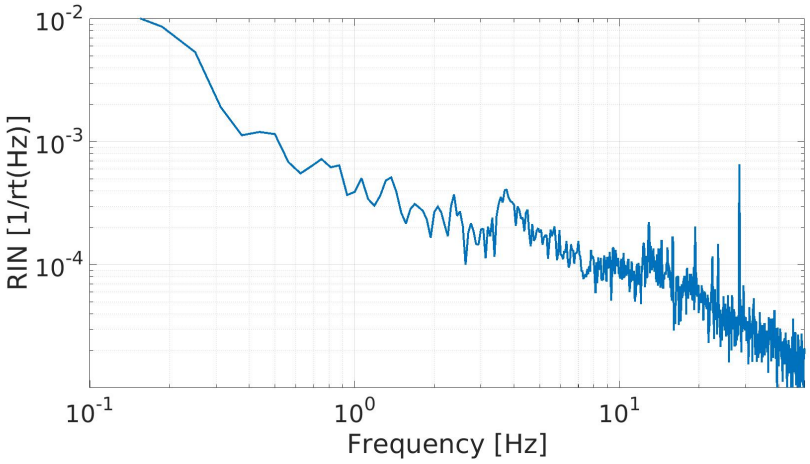

Figure 7-8: A spectrum of the relative intensity noise (RIN) on the pump field for the squeezer presented in Chapter 4. This level is elevated due to polarization fluctuations added by the optical fibers that are converted into intensity noise by the polarizer after the fiber.

of these technical noise sources for our squeezer design.

7.3.1 Down-conversion of noise on the pump field

The down-conversion of pump intensity and phase noise discussed previously in Section 4.2.3 will add technical noise to any portion of the backscattered field which seeds the OPO cavity. This level of noise can be significant if the backscattered power level is large enough. For the red curve in Figure 3-2, we assumed that there was no additional Faraday installed between the OPO and interferometer and that we only get 23 dB of isolation from the Output Faraday isolator. With these assumptions, the level of backscattered light seeding the OPO is equivalent to roughly 5 nW of seed power incident on the OPO input coupler[4]. This would require that the noise on our pump field be limited to a RIN of $\leq 1.5 \times 10^{-7}$ and a phase noise of $\leq 3 \times 10^{-7}\mathrm{rad}/\sqrt{\mathrm{Hz}}$. The setup for Advanced LIGO will include an additional Faraday isolator for the filter cavity, and we now expect roughly 30 dB of isolation from the output Faraday isolator. Assuming 60 dB of attenuation from the Faraday isolators, this will relax our requirements for the pump field somewhat: RIN $\leq 1 \times 10^{-5}$, phase noise

[4]This leads to a circulating seed power that is roughly 7 orders of magnitude larger than what we get from the 0.38 fW of seed contamination on our CLF field when generated using the double AOM setup described in Chapter 4.

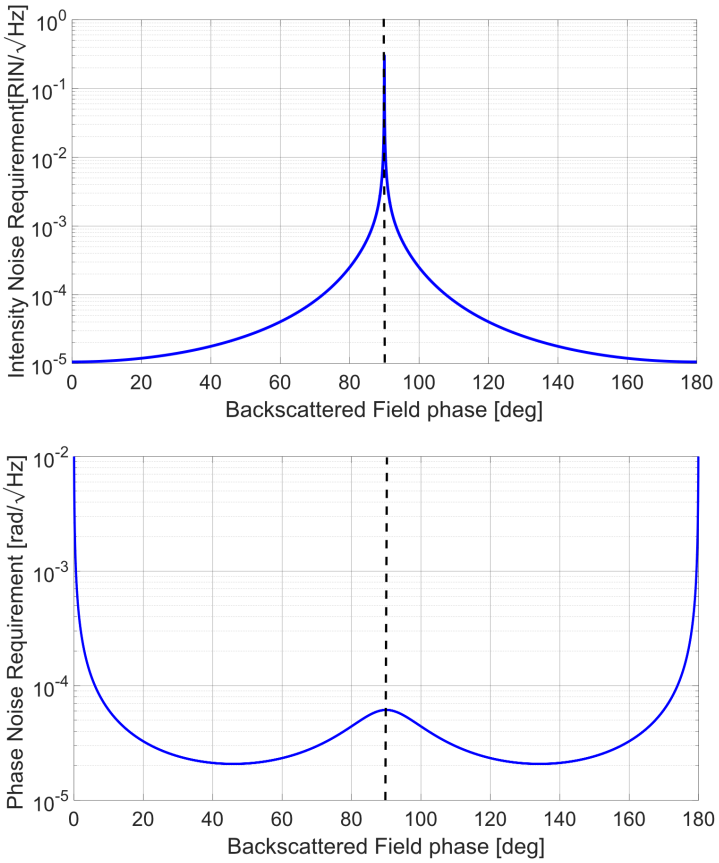

Figure 7-9: Requirements for the noise on the pump field assuming 60 dB of attenuation (from the output Faraday isolator and one additional Faraday isolator) of the backscattered field prior to reaching the OPO. Further attenuation due to the OPO, quantified by R_{OPO} depends on the phase of the backscattered field (see Equation 3.9). The dashed line corresponds to the anticipated mean phase of the backscattered field (See Sections 1.2.4 and 2.5.3 for discussion of interferometer field phase convention).

$\leq 2 \times 10^{-5}\,\mathrm{rad}/\sqrt{\mathrm{Hz}}$.

Given this level of backscattered power, this phase noise requirement is still quite stringent: It corresponds to a relative frequency noise between the backscattered and pump fields of $\leq 2\times10^{-4}\,\mathrm{Hz}/\sqrt{\mathrm{Hz}}$ at 10 Hz. A full noise budget of the Advanced LIGO squeezer is required to determine what level of phase noise suppression is realistic. The RIN requirement is less intimidating. However, the intensity noise level on the pump field for the in-vacuum squeezer described in Chapter 4 was actually quite high due to polarization fluctuations imposed on our pump field by our optical fibers. A measured RIN spectrum is shown in Figure 7-8.

As we can see in Figure 7-9, these values represent worse-case estimates assuming

that the phase of the backscattered light is completely unconstrained. During the Initial LIGO squeezing experiment, the phase of the backscattered field was reasonably well aligned with the squeezed quadrature angle (90 deg in Figure 7-9) [27]. If this is indeed the case for Advanced LIGO, this will relax our requirements on the pump field RIN considerably.

7.3.2 Technical noise from filter cavity length fluctuations

Due to the high finesse of the filter cavity (≈ 75000), modest length fluctuations will impose a significant amount of technical noise on the backscattered field. Since the filter cavity is detuned, this will add noise in both the amplitude and phase quadrature. Transfer functions from the cavity length noise to both quadratures are shown in Figure 7-10. From these transfer functions, we may compute our requirements for the filter cavity length noise. Again we will assume that the phase of the backscattered field is unconstrained implying that our technical noise could come from either quadrature. We now write the requirements in terms of backscattered field RIN and phase noise and assume that we must always satisfy both requirements simultaneously. In the phase quadrature, this may be computed in analogy with Equation 3.10:

$$\frac{RIN_{sc}}{RIN_{qn}}(f) = \lambda \frac{d\phi_{sc}}{dL_{fc}}(f)\delta L_{fc}(f)\sqrt{\frac{\eta_{PD}P_{sc}}{\lambda hc}} \leq \frac{10^{s/20}}{10}\,. \tag{7.2}$$

where $\delta L_{fc}(f)$ is the filter cavity length fluctuations in $\mathrm{m}/\sqrt{\mathrm{Hz}}$, $\frac{d\phi_{sc}}{dL_{fc}}(f)$ is the transfer function from filter cavity length noise to backscattered field phase noise plotted in Figure 7-10, and all other variables are defined as in Equation 3.10. Likewise, we may compute the requirement in the amplitude quadrature as

$$\frac{RIN_{sc}}{RIN_{qn}}(f) = \frac{dRIN_{sc}}{dL_{fc}}(f)\delta L_{fc}(f)\sqrt{\frac{\lambda\eta_{PD}P_{sc}}{2hc}} \leq \frac{10^{s/20}}{10}\,. \tag{7.3}$$

where $\frac{dRIN_{sc}}{dL_{fc}}(f)$ is the transfer function from cavity length noise to backscattered field RIN plotted in Figure 7-10. Assuming 10 dB of broadband squeezing (s=-10) and a level of backscatter isolation identical to that assumed in Figure 3-2 (73 dB),

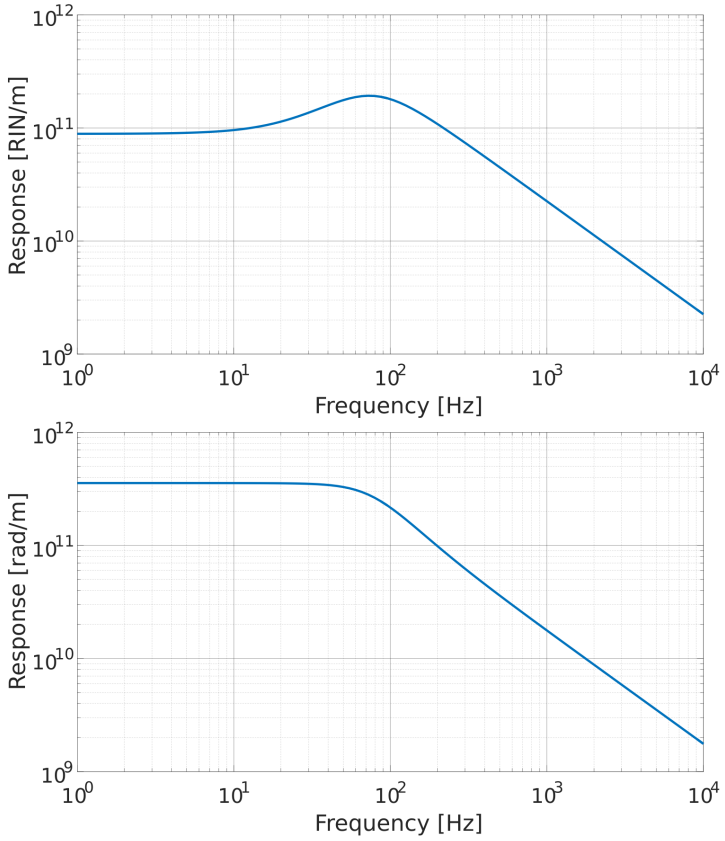

Figure 7-10: Transfer functions from filter cavity length noise to technical noise on the backscattered field assuming the cavity parameters given in Table 5.1. The top panel shows the transfer function from length noise to backscatter field relative intensity noise (RIN). The bottom panel shows the transfer function from length noise to backscattered field phase noise.

we would require that the filter cavity length noise be limited to $\leq 5 \times 10^{-19}\mathrm{m}/\sqrt{\mathrm{Hz}}$ at 10 Hz.

Clearly, the single stage tip-tilt suspensions [97] we'd hoped to use for our filter cavity will not be suitable without significantly attenuating the level of backscattered power which would add additional optical loss. The only suspended optics used in LIGO that can achieve anything close to this level of length noise performance at 10 Hz are the test mass suspensions mounted to a BSC-ISI. Using such optics for our filter cavity is impractical in terms of both cost and complexity.

A better strategy would be to choose an intermediate suspension design with reasonably good performance at 10 Hz, such as the Advanced LIGO HAM Small

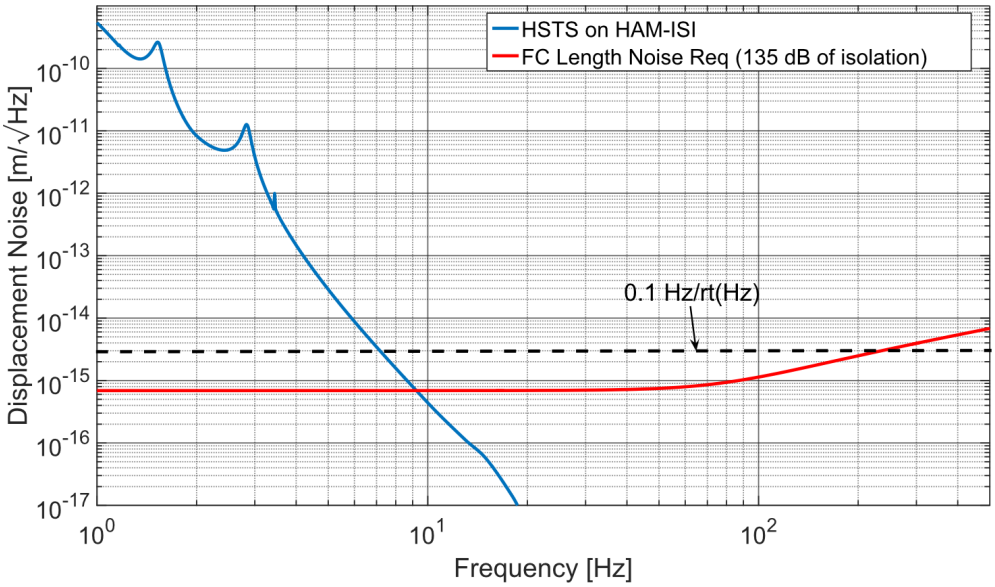

Figure 7-11: Length noise requirement for the filter cavity assuming the cavity parameters given in Table 5.1 and 135 dB of backscatter attenuation. In this case, the free-running length noise of a filter cavity constructed using two HAM Small Triple Suspension (HSTS) would meet our requirements. We note that a significant suppression of the HSTS length noise above 10 Hz would require that the filter cavity be locked to a well-stabilized laser source (frequency noise $\ll 1 \times 10^{-2}\,\mathrm{Hz}/\sqrt{\mathrm{Hz}}$ at 10 Hz). A dashed line indicating a frequency noise level of $0.1\,\mathrm{Hz}/\sqrt{\mathrm{Hz}}$ expressed in terms of cavity displacement noise is plotted for reference.

Triple Suspension (HSTS) [90], and bridge the remaining gap by adding additional backscatter attenuation. Figure 7-11 shows how we may achieve suitable performance with a triple suspension if we attain a total isolation from backscatter of ≈ 135 dB. In principle, one could suppress the length noise of the filter cavity above 10 Hz by locking its length to a stable laser source to relax our backscatter attenuation requirements[5]. However, this would require that our reference field have a frequency noise level well below $1 \times 10^{-2}\,\mathrm{Hz}/\sqrt{\mathrm{Hz}}$ at 10 Hz which may not be possible with the control scheme depicted in Figure 7-7. In particular, the control scheme as currently conceived does not suppress phase noise added to the 532 nm field due to path length fluctuations as it propagates from the SHG output to the filter cavity. We can estimate the level of degradation at 10 Hz along this path using accelerometer data from the H1 squeezer table (see Figure 7-1 in Reference [36]):

[5]It appears that the HSTS actuators do have sufficient bandwidth [64]

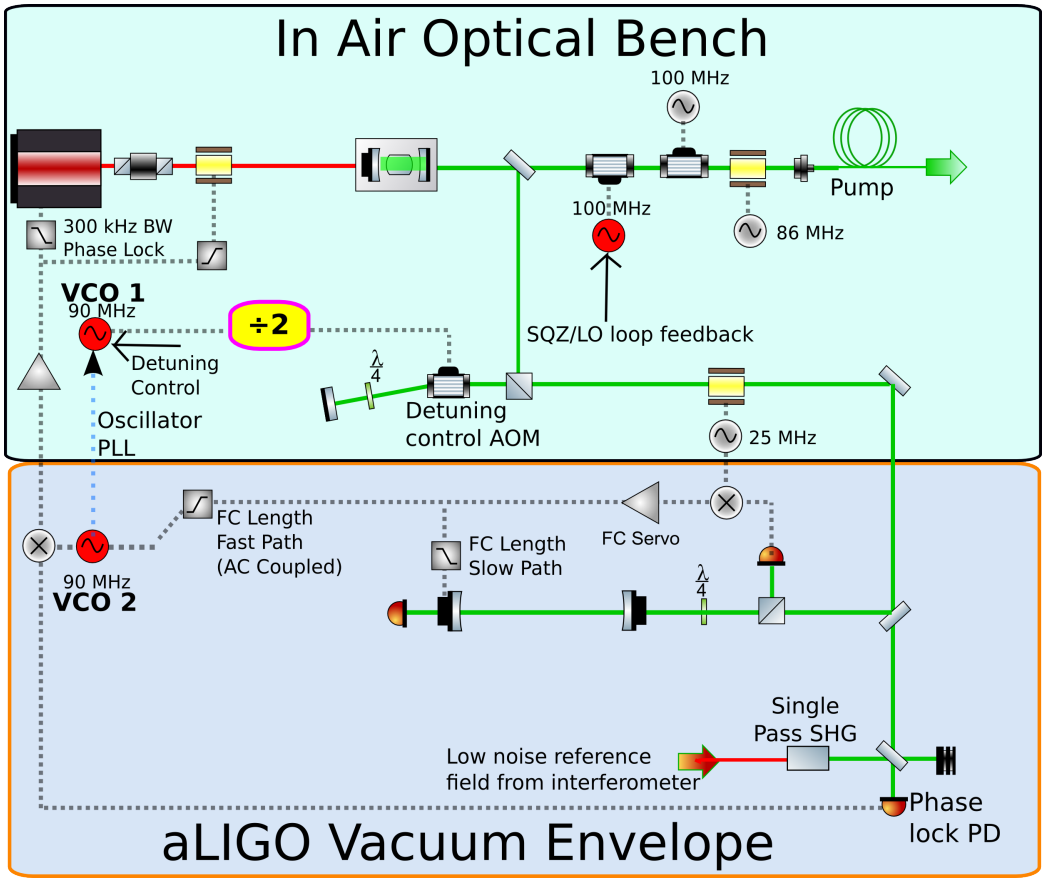

Figure 7-12: A modified version of the control scheme depicted in Figure 7-7 designed to maximize suppression of filter cavity length fluctuations. For simplicity, only the servo loops which require modification are shown. Significant suppression of the filter cavity length noise requires that it be stabilized to a field with frequency noise $\ll 1 \times 10^{-2}\,\mathrm{Hz}/\sqrt{\mathrm{Hz}}$. The frequency noise of the 532 nm field incident on the filter cavity may be stabilized by phase locking it to a low noise reference field from the interferometer that is single passed through an SHG crystal. This servo would replace the phase lock between the pump and PSL fields shown in Figure 7-7. Modifying the phase lock servo as shown here would deprive us of the required frequency path actuator for the SQZ loop. An additional actuator may be obtained by passing the pump field through a pair of AOMs and feeding back to a voltage-controlled oscillator (VCO) driving one of the modulators. It may be desirable to place the AOM pair after the pick-off for the filter cavity field to avoid imposing the control signal for the SQZ loop on the filter cavity field. In principle, this control signal can add noise to the filter cavity field since the SQZ servo is compensating for phase fluctuations added after the pick-off (e.g. phase noise from the pump fiber and OPO cavity length noise). Here, the filter cavity detuning is determined by the drive frequencies of two VCOs labelled VCO 1 and VCO 2. The frequency of VCO 1 is set to $2n \times \mathrm{FSR} + 2\Delta\omega_{fc}$ where n is an integer, FSR denotes the cavity free spectral range and $\Delta\omega_{fc}$ is the desired squeezed field detuning. The filter cavity is then locked on resonance to the frequency shifted 532 nm field. VCO 2, which is used to demodulate the error signal for the phase lock, is itself phase locked to VCO 1. Its drive frequency is given by $2n \times \mathrm{FSR} + 2\Delta\omega_{fc} + \delta_{fc}(t)$ where $\delta_{fc}(t)$ is the control signal from the filter cavity length servo that is applied to VCO 2. Provided that this control signal is properly AC coupled, the detuning of the squeezed field will be given by $\Delta\omega_{fc}$.

$$\delta\omega_g = \frac{2\pi}{\lambda_g}\delta x(f) \times f \approx \frac{2\pi}{532\,\mathrm{nm}} 3 \times 10^{-10}\,\mathrm{m}/\sqrt{\mathrm{Hz}} \times 10\,\mathrm{Hz} \approx 2\pi \times 10^{-2}\,\mathrm{Hz}/\sqrt{\mathrm{Hz}} \quad (7.4)$$

This suggests that we may have difficulty suppressing the length noise of the filter cavity with the current control scheme, though a full noise budget will be required before any final decisions are made.[6]

One could modify the control scheme to minimize the frequency noise of the 532 nm field used to stabilize the filter cavity length by deriving the error signal for the phase lock servo right before the filter cavity. Ideally, one would use a low noise reference field from the interferometer itself (which has a frequency noise level of order $10^{-7}\,\mathrm{Hz}/\sqrt{\mathrm{Hz}}$ at 10 Hz) rather than a field which is fiber coupled from the PSL. This phase lock PD may need to be placed in vacuum to avoid degradation due to path length fluctuations between the phase lock pick-off and the filter cavity. Figure 7-12 depicts these modifications in detail.

Provided that the frequency noise on the filter cavity field has been well suppressed, it should be possible to reduce the backscatter attenuation requirement to 90-100 dB. Figure 7-13 shows the expected length noise performance of the filter cavity after suppressing cavity length fluctuations with a modest 100 Hz bandwidth servo. With this length noise performance, a backscatter attenuation of 100 dB is now sufficient.

7.3.3 Reduction of the backscattered field

So far, we have implicitly assumed a relatively simple model for the attenuation of backscattered light. We assumed that all light is attenuated by 30 dB by each Faraday isolator regardless of polarization content. In general, this will not be true, particularly for the Faraday used to inject the squeezed field into the filter cavity. Also, we've assumed that the backscattered field is perfectly mode matched and

[6]Picking off the 532 nm field for stabilizing the filter cavity length *after* the pump field is fiber coupled into vacuum may be an option, provided that the frequency noise of the pump field at this point is sufficiently low. This might require an in-vacuum AOM to control the filter cavity detuning.

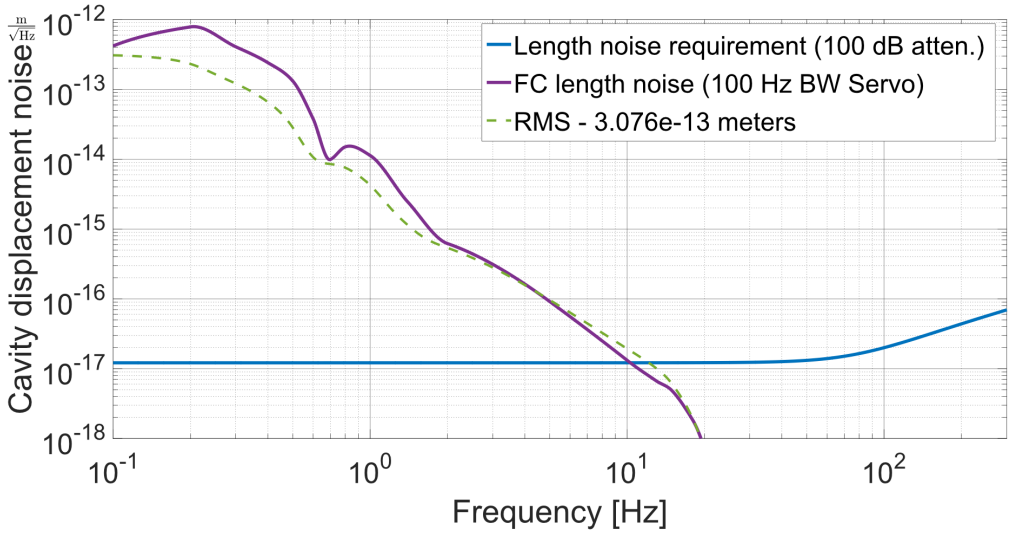

Figure 7-13: Filter cavity length noise requirement with 100 dB of backscatter attenuation (figure courtesy of John Miller). The filter cavity should meet this requirement above 10 Hz when it is stabilized to a low noise reference field with a modest 100 Hz bandwidth. Further relaxation of the backscatter attenuation requirement may be possible by optimizing the length servo.

polarization matched into both the filter cavity and the OPO. In practice, the filter cavity will be birefringent and only one eigen-polarization will resonate. Also, only one polarization component of the backscattered field will actually be directed towards the OPO cavity. The other polarization is sent back to the interferometer. This polarization does not get attenuated by the intrinsic backscatter isolation provided by the traveling wave geometry of our OPO cavity (which is quantified by the cavity reflection coefficient R_{OPO} defined in Equation 3.9). Clearly, we need to make a more realistic model of this system in order to determine what changes are needed to achieve the required attenuation of the backscattered field.

It is also worth noting that a significant reduction in the required backscatter attenuation could be achieved by implementing balanced homodyne readout with Advanced LIGO, as this would allow LIGO to operate on a dark fringe with significantly less power at the AS Port. This idea has been gaining some traction within the LIGO community [47].

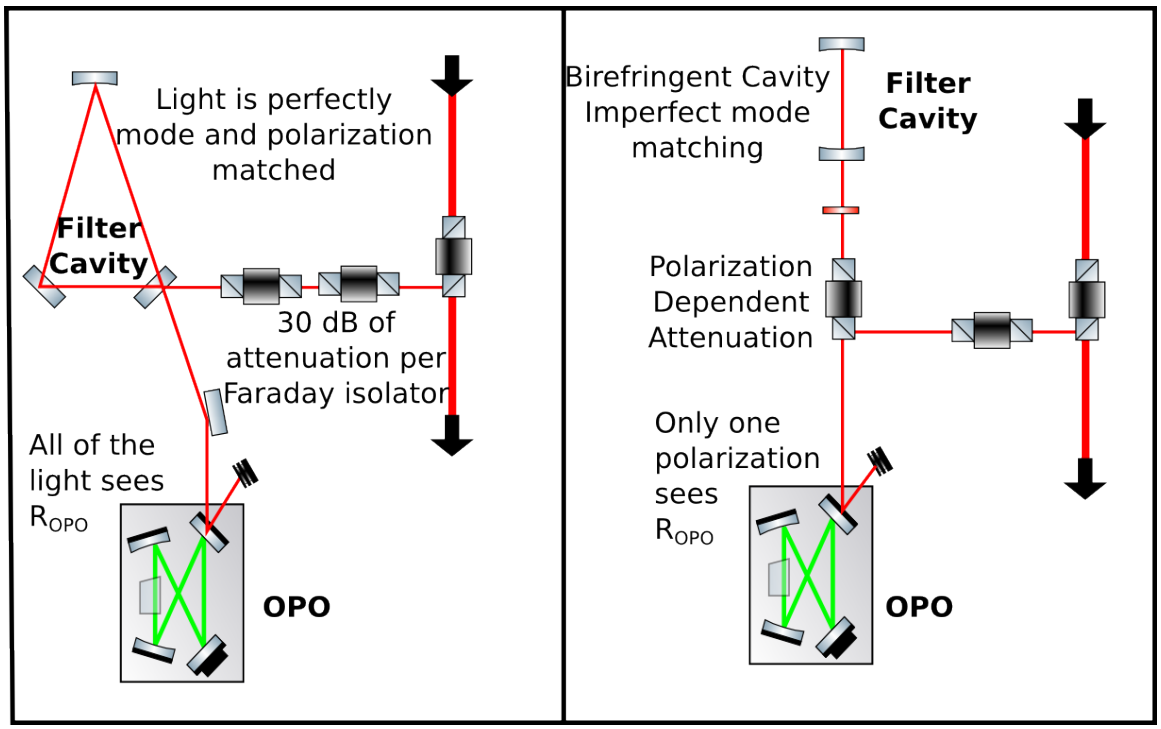

Figure 7-14: **Left Panel**: Idealized model of backscatter attenuation assuming 30 dB of attenuation per Faraday isolator, no polarization dependent effects, and that all of our backscatter field benefits from the intrinsic isolation of our travelling wave OPO cavity. **Right Panel**: A more realistic model of backscatter attenuation which assumes that the attenuation will be polarization dependent, that the filter cavity is birefringent, and that one polarization reflecting off of the filter cavity is sent directly back to the interferometer without reflecting off of the OPO.

7.4 Summary

The principle goal of this thesis was to develop a design for the Advanced LIGO squeezed vacuum source and to demonstrate viability of the various design elements through proof-of-principle tabletop experiments.

In Chapter 3 I proposed a design which addressed two of the technical limitations observed during the Enhanced LIGO squeezing experiment by moving the OPO cavity into vacuum: squeezed quadrature fluctuations and technical noise from path length fluctuations along the squeezing injection path. The proposed design also called for adding a quantum filter cavity to allow for simultaneous suppression of both radiation pressure noise and shot noise.

The remainder of the thesis covered two proof-of-princple experiments during

which most of the key techniques and technologies required for the Advanced LIGO squeezer were developed. In Chapter 4 an in-vacuum squeezed light source with ultra-low phase noise was presented and in Chapter 6 an experimental demonstration of the generation of frequency-dependent squeezed vacuum in the audio band was described in detail.

Though I proposed a few minor changes to the optical design and control scheme in this chapter, the design presented in Chapter 3 still appears to meet our needs. The most significant issue with our current design is the technical noise added to the backscattered field by filter cavity length fluctuations. However, this limitation is not fundamental and can be addressed by using an improved suspension design, suppressing cavity length fluctuations by locking it to a quiet laser source, reducing the required cavity finesse by increasing the cavity length, or by attenuating the backscattered field.

In light of all of these developments, it appears that the addition of squeezed vacuum injection is a viable early upgrade for Advanced LIGO.

Appendix A

Quadrature Control and Phase Noise

In this Appendix I will build on some of the previous work from Sheila Dwyer's thesis. She computed closed-form expressions for several key sources of phase noise which were very important for understanding the phase noise present during the initial LIGO squeezing experiment [37].

Here I will present a generalized summary of Sheila's phase noise calculations. I will also derive the response of the coherent control scheme to various sources of technical noise which, to my knowledge, has not been computed in detail previously. Finally I will present an updated calculation of the impact of alignment fluctuations on our phase noise.

A.1 Squeezed Quadrature fluctuations

In Section2.4.3, we computed the quantum noise variance of the squeezed vacuum field exiting our OPO assuming that the OPO cavity is co-resonant and we have perfect phase matching. Now we compute the quadrature variance of our squeezed field in full generality. In order to do this, we must recompute our quadrature variance using the general form of our OPO matrix $\mathbf{M}$ given in Equation 2.18 rather than the simplified version given in Equation 2.23 which we used to compute our expressions for the quadrature variance given in Equation 2.26. From Equation 2.21, we may then compute the quadrature variance as follows:

$$\begin{aligned}\mathbf{V}^f_{out}(\omega) = &\left(2\gamma^f_r(i\omega\mathbf{I} - \gamma^{tot}_r\Gamma\mathbf{M}\Gamma^{-1})^{-1} - \mathbf{I}\right) \circ \left(2\gamma^f_r(i\Omega\mathbf{I} - \gamma^{tot}_r\Gamma\mathbf{M}\Gamma^{-1})^{-1} - \mathbf{I}\right)^* \mathbf{V}^f_{in}(\Omega) \\ &+ 4\gamma^f_r\gamma^{CLF}_r(i\omega\mathbf{I} - \gamma^{tot}_r\Gamma\mathbf{M}\Gamma^{-1})^{-1} \circ [(i\Omega\mathbf{I} - \gamma^{tot}_r\Gamma\mathbf{M}\Gamma^{-1})^{-1}]^*\mathbf{V}^{CLF}_{in}(\Omega) \\ &+ 4\gamma^f_r\gamma^l_r(i\omega\mathbf{I} - \gamma^{tot}_r\Gamma\mathbf{M}\Gamma^{-1})^{-1} \circ [(i\Omega\mathbf{I} - \gamma^{tot}_r\Gamma\mathbf{M}\Gamma^{-1})^{-1}]^*\mathbf{V}^l_{in}(\Omega)\end{aligned} \tag{A.1}$$

where $\circ$ denotes the element-wise matrix product and * denotes complex conjugate and all relevant matrices were defined previously in Sections 2.4.2 and 2.4.3. As before, we may set all variances on the left hand side of Equation A.1 equal to 1 since they represent un-squeezed vacuum fluctuations entering the OPO. Our measured variance is then given by the following inner product

$$V = \begin{pmatrix}\cos^2\theta_{LO} & \sin^2\theta_{LO}\end{pmatrix}\mathbf{V}^f_{out} \tag{A.2}$$

In general the orientation of the squeezing ellipse may differ from $\theta_B/2$ when the cavity length, crystal position, or crystal temperature are offset from their ideal values. We must, therefore, generalize our definition of the squeezing angle given in Equation 2.42 by adding an offset term $\delta\theta_{sqz}$:

$$\theta_{sqz} = \theta_B/2 - \theta_{LO} + \delta\theta_{SQZ}(L, T, y) \tag{A.3}$$

Assuming that our offsets from the ideal operating point are small, our quadrature variance will be first order insensitive to fluctuations in length, temperature, and pump field phase. As discussed in Ref. [37], one may approximate the second order change in the quadrature variance as a first order shift in the squeezing angle θ_{sqz}.

We may compute the response of our squeezing angle to a fluctuation in some variable Y about its mean value $\bar{Y}$ by considering the impact of a static offset in Y ($\bar{Y} \rightarrow \bar{Y} + \Delta Y$) on our quadrature variance evaluated in a quadrature where the variance depends linearly on the squeezing angle ($\theta_{sqz} = \pi/4$).

$$\frac{d\theta_{sqz}}{dY} = \frac{\frac{dV}{dY}\big|_{\theta_{sqz}=\pi/4, Y=\bar{Y}}}{\frac{dV}{d\theta_{sqz}}\big|_{\theta_{sqz}=\pi/4, Y=\bar{Y}}} \tag{A.4}$$

Several closed-form expressions for the response of the squeezing angle to fluctuations in temperature, length, and pump phase can be found in Ref. [37] and in Chapter 5 of [36].

A.2 Technical Noise Coupling in Coherent Control

Note to the reader: *This section details a calculation which may be useful for making a noise model of the Advanced LIGO Squeezer. This was basically the last thing I did before graduating and I'm not 100% confident that everything here is correct. I didn't get a chance to plug in numbers and check things rigorously. Therefore, it represents incomplete work. The description here is fairly terse. I'd recommend reading Chapter 5 in Kirk McKenzie's thesis first [70]. It discusses a similar but much simpler calculation in great detail. This calculation uses the same formalism.*

In order to look at noise couplings for coherent control, we need to modify the formalism used in Section 4.2.3 and 2.4.2 to include both our upper and lower coherent control fields along with their noise sidebands. The Heisenberg-Langevin Equations of motion [31, 49] for this three-field system are given by[1]

$$\begin{aligned}
\dot{a}_s &= -\left(\gamma_r^{tot} + i\Omega_{CLF} - i\Delta_r\right) a_s + \epsilon a_i^\dagger b + \sqrt{2\gamma_r^{CLF}} A_s \\
\dot{a}_i &= -\left(\gamma_r^{tot} - i\Omega_{CLF} - i\Delta_r\right) a_i + \epsilon a_s^\dagger b \\
\dot{b} &= -\left(\gamma_g^{tot} - i\Delta_g\right) b - \frac{\epsilon^*}{2} a_s a_i + \sqrt{2\gamma_g^f} B_{in}
\end{aligned} \tag{A.5}$$

where we've omitted input fields with no coherent amplitude (ie vacuum fluctuations) since we are only concerned with classical noise at the moment. These equations of motion are fully general, allowing for non-zero detunings due to a change in cavity

[1] Here, we are working in a rotating frame where our fields are defined as follows $a_s(t) = a_{s,0}\mathrm{e}^{i\omega t}$ and $a_i(t) = a_{i,0}\mathrm{e}^{-i\omega t}$

length or crystal temperature and phase mismatch. As usual, we Fourier transform these equations and write all fields in terms of DC and fluctuating components

$$a_s \to \bar{a}_s + \delta a_s,\ a_i \to \bar{a}_i + \delta a_i,\ b \to \bar{b} + \delta b \tag{A.6}$$

Likewise I will also choose to express our detunings Δ_g and Δ_r and our nonlinear interaction strength ϵ in terms of DC and fluctuating components

$$\Delta_g \to \bar{\Delta}_g + \delta\Delta_g,\ \Delta_r \to \bar{\Delta}_r + \delta\Delta_r,\ \epsilon \to \bar{\epsilon} + \delta\epsilon \tag{A.7}$$

These expressions, in turn, may be expressed in terms of changes in the cavity length and crystal temperature:

$$L \to \bar{L} + \delta L,\ \ \Delta T \to \Delta T + \delta T \tag{A.8}$$

where we have defined $\bar{L}$ as the cavity length on resonance and $\Delta T = T - T_0$ as the temperature offset from the phase matching temperature T_0. As usual, we will assume that our OPO servo drives $\bar{\Delta_g} \to 0$. Also, we will ignore the fluctuations in the nonlinear interaction strength ($\delta\epsilon = 0$) since our temperature fluctuations $\delta\Delta T$ will be small compared to FWHM of our phase matching distribution. The terms in Equations A.7 can then be written as

$$\bar{\Delta_g} = 0 \tag{A.9}$$

$$\bar{\Delta_r} = \frac{\Delta\phi_r(\Delta T, \Delta y)}{\tau} + \frac{\omega_0}{\bar{L}}\delta L \tag{A.10}$$

$$\bar{\epsilon} = \epsilon_0 \mathrm{e}^{iL_c\Delta k(T)/2}\mathrm{sinc}(L_c\Delta k(T)/2) \tag{A.11}$$

$$\delta\Delta_g = \frac{2\omega_0 L_{c,tot}}{\bar{L}}\left(\frac{dn(\omega_g)}{dT} + n(\omega_g)\alpha_{KTP}\right)\delta T + \frac{2\omega_0}{\bar{L}}\delta L \tag{A.12}$$

$$\delta\Delta_r = \frac{\omega_0 L_{c,tot}}{\bar{L}}\left(\frac{dn(\omega_r)}{dT} + n(\omega_r)\alpha_{KTP}\right)\delta T + \frac{\omega_0}{\bar{L}}\delta L \tag{A.13}$$

$$\delta\epsilon = 0 \tag{A.14}$$

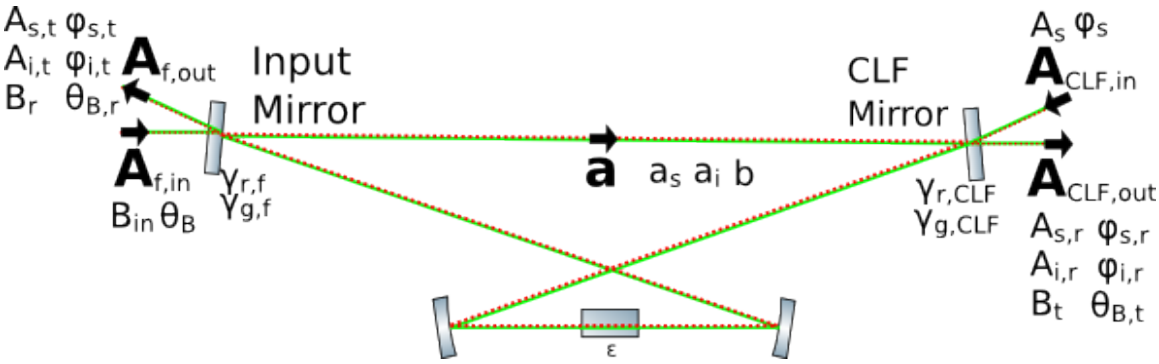

Figure A-1: Naming convention for our fields. Field vector names are shown in bold text while the individual signal, idler, and pump field amplitudes and phases are shown in ordinary text.

where $\Delta\phi_r(T, y)$ represents our deviation from co-resonance and is given by Equation 4.17, τ is our cavity round trip time, and $\Delta k(T)$ represents our phase mismatch and is given by Equation 4.13.

We will break our calculation into two parts. First in Section A.2.1 we will compute the DC field amplitudes and phases as well as their corresponding quadrature control error signals. Then, in Section A.2.2 we'll compute the impact of fluctuations on the Pump field, Control field, and cavity length on our quadrature control error signals.

A.2.1 DC Fields

In Section 2.7, we dealt with a simplified picture of coherent control in which we neglected the detuning of the coherent control sidebands, phase mismatch, and deviation from co-resonance. This was done for pedagogical reasons. Now we will quickly rederive these results in full generality. In order to determine the DC field amplitudes, we gather the non-fluctuating terms in equation A.5 after making the substitutions described in Equation A.6. We will neglect the $\bar{a}_s\bar{a}_i$ term in the equation for $\bar{b}$, assuming that the circulating pump field is undepleated. We can then solve for the pump field immediately

$$\bar{b} = \frac{\sqrt{2\gamma_g^{in}}B_{in}}{\gamma_g^{tot}} \tag{A.15}$$

We then plug $\bar{b}$ into our system of equations for $\bar{a}_s, i$ which we now write in matrix

form

$$\bar{\mathbf{a}} = \sqrt{2\gamma_r^{CLF}} \left(i\Omega_{CLF}\mathbf{I} - \gamma_r^{tot}\bar{\mathbf{M}} \right)^{-1} \bar{\mathbf{A}}_{CLF,in} \tag{A.16}$$

where we have defined

$$\bar{\mathbf{a}} = \begin{pmatrix} \bar{a}_s \\ \bar{a}_i^* \end{pmatrix}, \; \bar{\mathbf{A}}_{CLF,in} = \begin{pmatrix} A_s \mathrm{e}^{i\phi_s} \\ 0 \end{pmatrix}, \; \bar{\mathbf{M}} = \begin{pmatrix} -1 + \frac{i\bar{\Delta}_r}{\gamma_r^{tot}} & \frac{\bar{\epsilon}\bar{b}}{\gamma_r^{tot}} \\ \frac{\bar{\epsilon}^*\bar{b}^*}{\gamma_r^{tot}} & -1 - \frac{i\bar{\Delta}_r}{\gamma_r^{tot}} \end{pmatrix} \tag{A.17}$$

We can then compute the fields in reflection and transmission using our Input-Output relations

$$\bar{\mathbf{A}}_{CLF,out} = \begin{pmatrix} A_{s,r}\mathrm{e}^{i\phi_{s,r}} \\ A_{i,r}\mathrm{e}^{-i\phi_{i,r}} \end{pmatrix} = \sqrt{2\gamma_r^{CLF}}\bar{\mathbf{a}} - \bar{\mathbf{A}}_{CLF,in}, \quad \bar{\mathbf{A}}_{f,out} = \begin{pmatrix} A_{s,t}\mathrm{e}^{i\phi_{s,t}} \\ A_{i,t}\mathrm{e}^{-i\phi_{i,t}} \end{pmatrix} = \sqrt{2\gamma_r^{f}}\bar{\mathbf{a}} \tag{A.18}$$

where we have introduced the appropriate variables to represent the amplitude and phase of our output fields. Using our output fields, we may compute our quadrature control error signal in reflection:

$$E_{2\Omega} = 2A_{s,r}A_{i,r}\sin\left(\phi_{s,r} - \phi_{i,r} - \psi_{2\Omega}\right) \tag{A.19}$$

We see that the $2\Omega_{CLF}$ loop stabilizes the relative phase between the upper and lower sideband. In general, the nonlinear interaction will enforce a strict phase relationship between the signal and idler control sideband phases which will depend on pump phase via the relation $\phi_{i,r} = \theta_B - \phi_{s,r} + \zeta$, where ζ is an offset value which depends on the sideband detuning, phase mismatch, and the level of deviation from co-resonance[2]. Therefore this servo will also serve to stabilize the signal sideband phase relative to the pump phase.The error signal in transmission

[2]The relation given in Section 2.7, $\phi_{i,r} = \theta_B - \phi_{s,r}$, only holds when the detuning of the control sidebands is negligible. In Sheila Dwyer's Thesis [36] and a related technical note [38], this relation was incorrectly (I think) assumed to hold for arbitrary control sideband detuning.

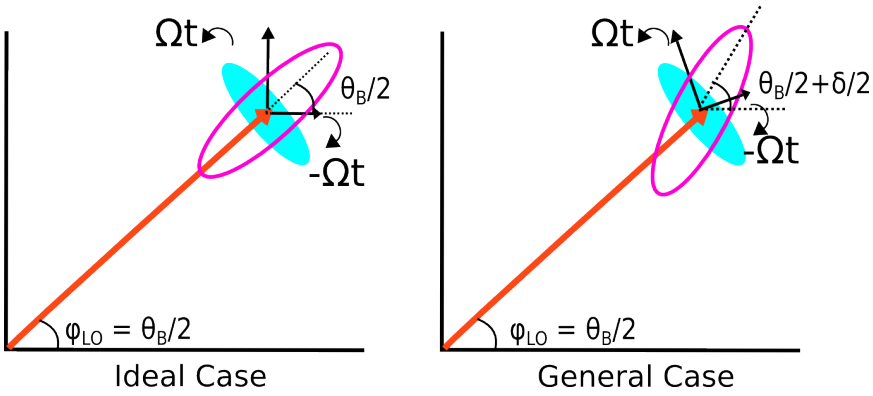

Figure A-2: These two plots show the relative orientation of the local oscillator field (red arrow), squeezing ellipse (Blue ellipse), and our coherent control sidebands. Here, we are measuring the squeezed quadrature by choosing $\psi_{1\Omega}$ such that $\phi_{LO} = \theta_B/2$ when our $1\Omega_{CLF}$ servo is locked. Because the two sidebands are unbalanced, their sum over time traces out the plotted pink ellipse. Since the $2\Omega_{CLF}$ servo is locked, this ellipse will have a fixed orientation relative to that of the squeezing ellipse. In the ideal case where we're phase matched, co-resonant, and the sidebands have negligible detuning, the semi-major axis of our modulation sideband ellipse lines up with the squeezed quadrature. In general this is not always the case.

$$E_{1\Omega} = 2A_{LO}\Big[A_{s,t}\cos\left(\frac{\phi_{s,t}+\phi_{i,t}}{2} - \phi_{LO} + \psi_{1\Omega}\right) + A_{i,t}\cos\left(\frac{\phi_{s,t}+\phi_{i,t}}{2} - \phi_{LO} - \psi_{1\Omega}\right)\Big] \quad \text{(A.20)}$$

When the $2\Omega_{CLF}$ servo is locked, the following relation will hold

$$\frac{\phi_{s,t}+\phi_{i,t}}{2} = \frac{\theta_B}{2} + \frac{\zeta}{2} \quad \text{(A.21)}$$

For the ideal case when our cavity is phase-matched, co-resonant, and the detuning of the CLF sidebands is negligible, $\zeta = 0$. In order to measure the squeezed quadrature, we must set $\phi_{1\Omega}$ in Equation A.20 such that ϕ_{LO} lines up with the orientation of the squeezing ellipse[3]

$$\phi_{LO} = \theta_B/2 + \delta\theta_{SQZ} \quad \text{(A.22)}$$

[3]I will make no attempt to derive general expressions for ζ and $\delta\theta_{SQZ}$ in closed-form. These are place-holders whose exact expression must be derived for the system parameters of interest.

When we are co-resonant and phase matched, the orientation of the squeezing ellipse is completely determined by the phase of the pump field and $\delta\theta_{SQZ} = 0$. If the cavity length or temperature shift, this will no longer be the case, as discussed in Section A.1. We can solve for the correct demodulation phase for measuring squeezing by substituting Equations A.21 and A.22 into Equation A.20, setting Equation A.20 equal to zero, and solving for the desired demodulation phase

$$\tan(\psi_{1\Omega}) = \frac{A_{s,t} + A_{i,t}}{A_{s,t} - A_{i,t}} \cot\left(\frac{\zeta}{2} - \delta\theta_{SQZ}\right) \tag{A.23}$$

For the ideal case $\psi_{1\Omega} = \pi/2$ and the semi-major axis of our error signal ellipse is aligned with the squeezed quadrature as shown in Figure A-2. Our error signal simplifies to the form given in Equation 2.61 which we rewrite in terms of our new notation

$$E_{1\Omega} = 2A_{LO}(A_{s,t} + A_{i,t}) \sin(\theta_B/2 - \phi_{LO}) \tag{A.24}$$

To conclude this section, we will write out the above relations for our typical operating conditions: co-resonant with perfect phase matching but non-negligible control sideband detuning. In this case $\delta\theta_{SQZ} = 0$ Our circulating field is given by

$$\begin{pmatrix} \bar{a}_s \\ \bar{a}_i^* \end{pmatrix} = \frac{\sqrt{2\gamma_r^{clf}} A_s}{\gamma_r^{tot} \sqrt{\left[1 - x^2 - \left(\frac{\Omega_{CLF}}{\gamma_r^{tot}}\right)^2\right]^2 + \left(\frac{2\Omega_{CLF}}{\gamma_r^{tot}}\right)^2}} \begin{pmatrix} \sqrt{1 + \left(\frac{\Omega_{CLF}}{\gamma_r^{tot}}\right)^2} e^{i(\nu + \phi_s + \mu)} \\ x e^{-i(\theta_B - \phi_s - \mu)} \end{pmatrix} \tag{A.25}$$

where we've defined

$$\nu = \arctan\left(\frac{\Omega_{CLF}}{\gamma_r^{tot}}\right), \quad \mu = \arctan\left(\frac{2\Omega_{CLF}}{\gamma_r^{tot}\left[1 - x^2 - (\frac{\Omega_{CLF}}{\gamma_r^{tot}})^2\right]}\right) \tag{A.26}$$

We see that, in this case, $\zeta = \nu$. our quadrature control error signals are given by[4]

[4]For typical values of γ_r^{CLF}, the second term in the 2Ω error signal is several orders of magnitude smaller than the first term.

$$\mathrm{E}_{2\Omega_{CLF}} = \frac{4\bar{A}_s^2 x \gamma_r^{CLF}}{\gamma_r^{tot}\sqrt{\left[1-x^2-\left(\frac{\Omega_{CLF}}{\gamma_r^{tot}}\right)^2\right]^2+\left(\frac{2\Omega_{CLF}}{\gamma_r^{tot}}\right)^2}}\Big[\cos(\theta_B-2\phi_s-\mu-\psi_{2\Omega})+ \frac{2\gamma_r^{CLF}\sqrt{1+\left(\frac{\Omega_{CLF}}{\gamma_r^{tot}}\right)^2}}{\sqrt{\left[1-x^2-\left(\frac{\Omega_{CLF}}{\gamma_r^{tot}}\right)^2\right]^2+\left(\frac{2\Omega_{CLF}}{\gamma_r^{tot}}\right)^2}}\cos(\theta_B-2\phi_s-2\mu-\nu-\psi_{2\Omega})\Big] \quad \text{(A.27)}$$

and

$$\mathrm{E}_{1\Omega_{CLF}} = \frac{4A_s A_{lo}\sqrt{\gamma_r^{CLF}\gamma_r^f}}{\gamma_r^{tot}\sqrt{\left[1-x^2-\left(\frac{\Omega_{CLF}}{\gamma_r^{tot}}\right)^2\right]^2+\left(\frac{2\Omega}{\gamma_r^{tot}}\right)^2}}[x\cos(\theta_B-\phi_s-\mu-\phi_{lo}-\psi_{1\Omega}) + \sqrt{1+\left(\frac{\Omega_{CLF}}{\gamma_r^{tot}}\right)^2}\cos(\nu+\mu+\phi_s-\phi_{lo}+\psi_{1\Omega})] \quad \text{(A.28)}$$

A.2.2 The impact of technical noise

Now that we've computed our DC fields and lock points, we will examine the impact of technical noise on our quadrature control error signals. We will compute noise couplings to first-order only, dropping non-linear terms like $\delta a_s^* \delta b$. We may then compute the intra-cavity AC fields for the pump and two control field sidebands by writing the fluctuating terms in our Equations of motion (A.5) in matrix form in analogy with Equation A.16

$$\delta\mathbf{a}(\omega) = (i\mathbf{M}_\Omega - \mathbf{M})^{-1}\left[\mathbf{M}_{CLF}\delta\mathbf{A}_{CLF,in}(\omega) + \mathbf{M}_f\delta\mathbf{A}_{f,in}(\omega) + \mathbf{A}_L + \mathbf{A}_T\right] \quad \text{(A.29)}$$

where we are using ω to denote our audio sideband frequency. Above, we have generalized our definition of $\mathbf{M}$

$$\mathbf{M} = \begin{pmatrix} -\gamma_r^{tot} + i\bar{\Delta}_r & 0 & 0 & \bar{\epsilon}\bar{b} & \bar{\epsilon}\bar{a}_i^* & 0 \\ 0 & -\gamma_r^{tot} - i\bar{\Delta}_r & \bar{\epsilon}^*\bar{b}^* & 0 & 0 & \bar{\epsilon}^*\bar{a}_i \\ 0 & \bar{\epsilon}\bar{b} & -\gamma_r^{tot} + i\bar{\Delta}_r & 0 & \bar{\epsilon}\bar{a}_s^* & 0 \\ \bar{\epsilon}^*\bar{b}^* & 0 & 0 & -\gamma_r^{tot} - i\bar{\Delta}_r & 0 & \bar{\epsilon}^*\bar{a}_s \\ -\frac{\bar{\epsilon}^*\bar{a}_i}{2} & 0 & -\frac{\bar{\epsilon}^*\bar{a}_s}{2} & 0 & -\gamma_g^{tot} + i\bar{\Delta}_g & 0 \\ 0 & -\frac{\bar{\epsilon}\bar{a}_i^*}{2} & 0 & -\frac{\bar{\epsilon}\bar{a}_s^*}{2} & 0 & -\gamma_g^{tot} - i\bar{\Delta}_g \end{pmatrix} \tag{A.30}$$

as well as our definitions for our field vectors

$$\delta\mathbf{a}(\omega) = \begin{pmatrix} \delta a_s(\Omega_{CLF} + \omega) \\ \delta a_s^*(\Omega_{CLF} - \omega) \\ \delta a_i(-\Omega_{CLF} + \omega) \\ \delta a_i^*(-\Omega_{CLF} - \omega) \\ \delta b(\omega) \\ \delta b^*(-\omega) \end{pmatrix}, \ \delta\mathbf{A}_{clf,in} = \begin{pmatrix} \delta A_s(\Omega_{CLF} + \omega) \\ \delta A_s^*(\Omega_{CLF} - \omega) \\ 0 \\ 0 \\ 0 \\ 0 \end{pmatrix}, \ \delta\mathbf{A}_{f,in} = \begin{pmatrix} 0 \\ 0 \\ 0 \\ 0 \\ \delta B_{in}(\omega) \\ \delta B_{in}^*(-\omega) \end{pmatrix} \tag{A.31}$$

and we have defined

$$\mathbf{M}_i = \begin{pmatrix} \sqrt{2\gamma_r^i} & 0 & 0 & 0 & 0 & 0 \\ 0 & \sqrt{2\gamma_r^i} & 0 & 0 & 0 & 0 \\ 0 & 0 & \sqrt{2\gamma_r^i} & 0 & 0 & 0 \\ 0 & 0 & 0 & \sqrt{2\gamma_r^i} & 0 & 0 \\ 0 & 0 & 0 & 0 & \sqrt{2\gamma_g^i} & 0 \\ 0 & 0 & 0 & 0 & 0 & \sqrt{2\gamma_g^i} \end{pmatrix} \tag{A.32}$$

and

$$\mathbf{M}_\Omega = \begin{pmatrix} -\Omega+\omega & 0 & 0 & 0 & 0 & 0 \\ 0 & \Omega+\omega & 0 & 0 & 0 & 0 \\ 0 & 0 & \Omega+\omega & 0 & 0 & 0 \\ 0 & 0 & 0 & -\Omega+\omega & 0 & 0 \\ 0 & 0 & 0 & 0 & \omega & 0 \\ 0 & 0 & 0 & 0 & 0 & \omega \end{pmatrix} \approx \begin{pmatrix} \Omega & 0 & 0 & 0 & 0 & 0 \\ 0 & -\Omega & 0 & 0 & 0 & 0 \\ 0 & 0 & -\Omega & 0 & 0 & 0 \\ 0 & 0 & 0 & \Omega & 0 & 0 \\ 0 & 0 & 0 & 0 & 0 & 0 \\ 0 & 0 & 0 & 0 & 0 & 0 \end{pmatrix} \tag{A.33}$$

where we've pointed out that the audio sideband frequency ω may be neglected since $\omega << \gamma_r^{tot}, \gamma_g^{tot}, \Omega_{CLF}$. However, a fully frequency dependent calculation may be done if desired using the formalism presented in this section. We also have additional terms which account for our length and temperature fluctuations:

$$\delta\mathbf{A}_L = \begin{pmatrix} i\bar{a}_s \frac{\omega_0}{L}\delta L \\ -i\bar{a}_s^* \frac{\omega_0}{L}\delta L^* \\ i\bar{a}_i \frac{\omega_0}{L}\delta L \\ -i\bar{a}_i^* \frac{\omega_0}{L}\delta L^* \\ i\bar{b} \frac{2\omega_0}{L}\delta L \\ -i\bar{b}^* \frac{2\omega_0}{L}\delta L^* \end{pmatrix}, \quad \delta\mathbf{A}_T = \begin{pmatrix} i\bar{a}_s \frac{\omega_0 L_{c,tot}}{L}\left[\frac{dn(\omega_0)}{dT} + n(\omega_0)\alpha_{KTP}\right]\delta T \\ -i\bar{a}_s^* \frac{\omega_0 L_{c,tot}}{L}\left[\frac{dn(\omega_0)}{dT} + n(\omega_0)\alpha_{KTP}\right]\delta T^* \\ i\bar{a}_i \frac{\omega_0 L_{c,tot}}{L}\left[\frac{dn(\omega_0)}{dT} + n(\omega_0)\alpha_{KTP}\right]\delta T \\ -i\bar{a}_i^* \frac{\omega_0 L_{c,tot}}{L}\left[\frac{dn(\omega_0)}{dT} + n(\omega_0)\alpha_{KTP}\right]\delta T^* \\ i\bar{b} \frac{2\omega_0 L_{c,tot}}{L}\left[\frac{dn(2\omega_0)}{dT} + n(2\omega_0)\alpha_{KTP}\right]\delta T \\ -i\bar{b}^* \frac{2\omega_0 L_{c,tot}}{L}\left[\frac{dn(2\omega_0)}{dT} + n(2\omega_0)\alpha_{KTP}\right]\delta T^* \end{pmatrix} \tag{A.34}$$

We then compute the output fluctuations using the input-output relations defined in Equation 2.12. We will also express these fields in the quadrature picture using our 1-photon to 2-photon transition matrix:

$$\Gamma = \begin{pmatrix} 1 & 1 & 0 & 0 & 0 & 0 \\ i & -i & 0 & 0 & 0 & 0 \\ 0 & 0 & 1 & 1 & 0 & 0 \\ 0 & 0 & i & -i & 0 & 0 \\ 0 & 0 & 0 & 0 & 1 & 1 \\ 0 & 0 & 0 & 0 & i & -i \end{pmatrix} \tag{A.35}$$

We now compute the output field quadrature fluctuations in terms of the fluctuations on the input fields and the appropriate transfer functions

$$\begin{aligned} \delta\mathbf{X}_{CLF,out} &= \Theta_{[CLF,CLF]}\delta\mathbf{X}_{CLF,in} + \Theta_{[f,CLF]}\delta\mathbf{X}_{f,in} + \Theta_{[\Delta,CLF]}(\mathbf{A}_L + \mathbf{A}_T) \\ \delta\mathbf{X}_{f,out} &= \Theta_{[CLF,f]}\delta\mathbf{X}_{CLF,in} + \Theta_{[f,f]}\delta\mathbf{X}_{f,in} + \Theta_{[\Delta,f]}(\mathbf{A}_L + \mathbf{A}_T) \end{aligned} \tag{A.36}$$

where $\delta\mathbf{X} = \Gamma\delta\mathbf{A}$ represent our quadrature fluctuations and our transfer function matrices are given by

$$\Theta_{[CLF,CLF]} = \Gamma\left[\mathbf{M}_{CLF}(i\mathbf{M}_\Omega - \mathbf{M})^{-1}\mathbf{M}_{CLF} - \mathbf{I}\right]\Gamma^{-1} \tag{A.37}$$

$$\Theta_{[f,CLF]} = \Gamma\mathbf{M}_{CLF}(i\mathbf{M}_\Omega - \mathbf{M})^{-1}\mathbf{M}_f\Gamma^{-1} \tag{A.38}$$

$$\Theta_{[\Delta,CLF]} = \Gamma\mathbf{M}_{CLF}(i\mathbf{M}_\Omega - \mathbf{M})^{-1} \tag{A.39}$$

$$\Theta_{[CLF,f]} = \Gamma\mathbf{M}_f(i\mathbf{M}_\Omega - \mathbf{M})^{-1}\mathbf{M}_{CLF}\Gamma^{-1} \tag{A.40}$$

$$\Theta_{[f,f]} = \Gamma\left[\mathbf{M}_f(i\mathbf{M}_\Omega - \mathbf{M})^{-1}\mathbf{M}_f - \mathbf{I}\right]\Gamma^{-1} \tag{A.41}$$

$$\Theta_{[\Delta,f]} = \Gamma\mathbf{M}_f(i\mathbf{M}_\Omega - \mathbf{M})^{-1} \tag{A.42}$$

When computing our noise couplings, it will be convenient to express our fluctuations in terms of intensity noise in units of $\mathrm{W}/\sqrt{\mathrm{Hz}}$ and phase noise in units of $\mathrm{radians}/\sqrt{\mathrm{Hz}}$ for our amplitude quadrature and phase quadrature respectively. We introduce the following vector notation for our fluctuations on the signal, idler and pump fields expressed in these units:

$$\delta\mathbf{N} = \begin{pmatrix} \delta P_s \\ \delta\phi_s \\ \delta P_i \\ \delta\phi_i \\ \delta P_B \\ \delta\theta_B \end{pmatrix} \tag{A.43}$$

Using this notation, we can rewrite our fluctuation in terms of the desired quantities by making the following substitutions [5]:

$$\begin{aligned} \mathbf{Q}_{CLF,out}\delta\mathbf{N}_{CLF,out} = \delta\mathbf{X}_{CLF,out},\ \mathbf{Q}_{f,out}\delta\mathbf{N}_{f,out} = \delta\mathbf{X}_{f,out}, \\ \mathbf{Q}_{CLF,in}\delta\mathbf{N}_{CLF,in} = \delta\mathbf{X}_{CLF,in},\ \mathbf{Q}_{f,in}\delta\mathbf{N}_{f,in} = \delta\mathbf{X}_{f,in} \end{aligned} \tag{A.44}$$

where we have defined the matrices:

$$\mathbf{Q}_{CLF,out} = \frac{1}{\sqrt{\hbar\omega_0}} \begin{pmatrix} \sqrt{\frac{1}{P_{s,r}}} & 0 & 0 & 0 & 0 & 0 \\ 0 & \sqrt{P_{s,r}} & 0 & 0 & 0 & 0 \\ 0 & 0 & \sqrt{\frac{1}{P_{i,r}}} & 0 & 0 & 0 \\ 0 & 0 & 0 & \sqrt{P_{i,r}} & 0 & 0 \\ 0 & 0 & 0 & 0 & \sqrt{\frac{1}{2P_{B,t}}} & 0 \\ 0 & 0 & 0 & 0 & 0 & \sqrt{\frac{P_{B,t}}{2}} \end{pmatrix} \tag{A.45}$$

[5] These expressions are analogous to Equation A12 from the DnD paper [65] rewritten in terms of the desired units. I drop a factor of $\sqrt{2}$ since I'm using a different normalization for my quadrature operators (differ by a factor of $\sqrt{2}$ from equation A9 in the DnD paper).

$$\mathbf{Q}_{f,out} = \frac{1}{\sqrt{\hbar\omega_0}} \begin{pmatrix} \sqrt{\frac{1}{P_{s,t}}} & 0 & 0 & 0 & 0 & 0 \\ 0 & \sqrt{P_{s,t}} & 0 & 0 & 0 & 0 \\ 0 & 0 & \sqrt{\frac{1}{P_{i,t}}} & 0 & 0 & 0 \\ 0 & 0 & 0 & \sqrt{P_{i,t}} & 0 & 0 \\ 0 & 0 & 0 & 0 & \sqrt{\frac{1}{2P_{B,r}}} & 0 \\ 0 & 0 & 0 & 0 & 0 & \sqrt{\frac{P_{B,r}}{2}} \end{pmatrix} \tag{A.46}$$

$$\mathbf{Q}_{CLF,in} = \frac{1}{\sqrt{\hbar\omega_0}} \begin{pmatrix} \sqrt{\frac{1}{P_s}} & 0 & 0 & 0 & 0 & 0 \\ 0 & \sqrt{P_s} & 0 & 0 & 0 & 0 \\ 0 & 0 & 0 & 0 & 0 & 0 \\ 0 & 0 & 0 & 0 & 0 & 0 \\ 0 & 0 & 0 & 0 & 0 & 0 \\ 0 & 0 & 0 & 0 & 0 & 0 \end{pmatrix} \tag{A.47}$$

$$\mathbf{Q}_{f,in} = \frac{1}{\sqrt{\hbar\omega_0}} \begin{pmatrix} 0 & 0 & 0 & 0 & 0 & 0 \\ 0 & 0 & 0 & 0 & 0 & 0 \\ 0 & 0 & 0 & 0 & 0 & 0 \\ 0 & 0 & 0 & 0 & 0 & 0 \\ 0 & 0 & 0 & 0 & \frac{1}{\sqrt{2P_{B,in}}} & 0 \\ 0 & 0 & 0 & 0 & 0 & \sqrt{\frac{P_{B,in}}{2}} \end{pmatrix} \tag{A.48}$$

Equation A.36 can then be rewriten as:

$$\begin{aligned} \delta\mathbf{N}_{CLF,out} &= \mathbf{W}_{[CLF,CLF]}\delta\mathbf{N}_{CLF,in} + \mathbf{W}_{[f,CLF]}\delta\mathbf{N}_{f,in} + \mathbf{W}_{[\Delta,CLF]}(\mathbf{A}_L + \mathbf{A}_T) \\ \delta\mathbf{N}_{f,out} &= \mathbf{W}_{[CLF,f]}\delta\mathbf{N}_{CLF,in} + \mathbf{W}_{[f,f]}\delta\mathbf{N}_{f,in} + \mathbf{W}_{[\Delta,f]}(\mathbf{A}_L + \mathbf{A}_T) \end{aligned} \tag{A.49}$$

where we have defined the following transfer function matrices

$$\mathbf{W}_{[CLF,CLF]} = \mathbf{Q}_{CLF,out}^{-1}\Gamma\left[\mathbf{M}_{CLF}(i\mathbf{M}_{\Omega}-\mathbf{M})^{-1}\mathbf{M}_{CLF}-\mathbf{I}\right]\Gamma^{-1}\mathbf{Q}_{CLF,in} \tag{A.50}$$

$$\mathbf{W}_{[f,CLF]} = \mathbf{Q}_{CLF,out}^{-1}\Gamma\mathbf{M}_{CLF}(i\mathbf{M}_{\Omega}-\mathbf{M})^{-1}\mathbf{M}_{f}\Gamma^{-1}\mathbf{Q}_{f,in} \tag{A.51}$$

$$\mathbf{W}_{[\Delta,CLF]} = \mathbf{Q}_{CLF,out}^{-1}\Gamma\mathbf{M}_{CLF}(i\mathbf{M}_{\Omega}-\mathbf{M})^{-1} \tag{A.52}$$

$$\mathbf{W}_{[CLF,f]} = \mathbf{Q}_{f,out}^{-1}\Gamma\mathbf{M}_{f}(i\mathbf{M}_{\Omega}-\mathbf{M})^{-1}\mathbf{M}_{CLF}\Gamma^{-1}\mathbf{Q}_{CLF,in} \tag{A.53}$$

$$\mathbf{W}_{[f,f]} = \mathbf{Q}_{f,out}^{-1}\Gamma\left[\mathbf{M}_{f}(i\mathbf{M}_{\Omega}-\mathbf{M})^{-1}\mathbf{M}_{f}-\mathbf{I}\right]\Gamma^{-1}\mathbf{Q}_{f,in} \tag{A.54}$$

$$\mathbf{W}_{[\Delta,f]} = \mathbf{Q}_{f,out}^{-1}\Gamma\mathbf{M}_{f}(i\mathbf{M}_{\Omega}-\mathbf{M})^{-1} \tag{A.55}$$

Now that we've computed our output fields, we need to determine how our output fluctuations couple to our two error signals. We begin with our $2\Omega_{CLF}$ error signal, $E_{2\Omega}$, given in Equation A.19. We must re-express this error signal in Watts by making the following substitutions

$$B_t \rightarrow \sqrt{P_{B,t}},\;\; A_{s,r} \rightarrow \sqrt{P_{s,r}},\;\; A_{i,r} \rightarrow \sqrt{P_{s,r}} \tag{A.56}$$

Now, we compute a vector of partial derivatives which show how our error signal phase noise spectrum depends on our output field fluctuations:

$$\Delta_{2\Omega} = \begin{pmatrix} \frac{\partial\delta\phi_{2\Omega}}{\partial P_{s,r}} \\ \frac{\partial\delta\phi_{2\Omega}}{\partial \phi_{s,r}} \\ \frac{\partial\delta\phi_{2\Omega}}{\partial P_{i,r}} \\ \frac{\partial\delta\phi_{2\Omega}}{\partial \phi_{i,r}} \\ \frac{\partial\delta\phi_{2\Omega}}{\partial P_{B,t}} \\ \frac{\partial\delta\phi_{2\Omega}}{\partial \theta_{B,t}} \end{pmatrix} = \frac{1}{2A_{s,r}A_{i,r}} \begin{pmatrix} \frac{\partial E_{1\Omega}}{\partial P_{s,r}} \\ \frac{\partial E_{1\Omega}}{\partial \phi_{s,r}} \\ \frac{\partial E_{1\Omega}}{\partial P_{i,r}} \\ \frac{\partial E_{1\Omega}}{\partial \phi_{i,r}} \\ \frac{\partial E_{1\Omega}}{\partial P_{B,t}} \\ \frac{\partial E_{1\Omega}}{\partial \theta_{B,t}} \end{pmatrix} = \begin{pmatrix} 0 \\ 1 \\ 0 \\ -1 \\ 0 \\ 0 \end{pmatrix} \tag{A.57}$$

where we've defined our error signal phase as $\phi_{2\Omega} = \phi_{s,r} - \phi_{i,r}$. Finally, we may compute the total fluctuations sensed by our error signal, $\delta\phi_{2\Omega}$, by multiplying these partial derivatives by the output field fluctuations. This is obtained by computing the following inner product

$$\begin{aligned}\delta\phi_{2\Omega} &= (\Delta_{2\Omega})^t \ \delta\mathbf{N}_{CLF,out} \\ &= (\Delta_{2\Omega})^t \left[\mathbf{W}_{[CLF,CLF]}\delta\mathbf{N}_{CLF,in} + \mathbf{W}_{[f,CLF]}\delta\mathbf{N}_{f,in} + \mathbf{W}_{[\Delta,CLF]}(\mathbf{A}_L + \mathbf{A}_T)\right]\end{aligned} \tag{A.58}$$

We can compute our expected amplitude spectral density by calculating the quantity

$$s_{2\Omega} = \sqrt{\langle|\delta\phi_{2\Omega}|^2\rangle} \tag{A.59}$$

We will now perform a similar analysis for the 1Ω loop. In order to define our error signal phase $\phi_{1\Omega}$ it is useful to rewrite Equation A.20 in terms of a single sinusoid [1]

$$\begin{aligned}E_{1\Omega} = 2A_{LO}\sqrt{(A_{s,t}+A_{i,t})^2\cos^2\psi_{1\Omega} + (A_{s,t}-A_{i,t})^2\sin^2\psi_{1\Omega}}\cos\Big[\frac{\phi_{s,t}+\phi_{i,t}}{2} - \phi_{LO} \\ + \tan^{-1}\left(\frac{A_{s,t}-A_{i,t}}{A_{s,t}+A_{i,t}}\tan\psi_{1\Omega}\right)\Big]\end{aligned} \tag{A.60}$$

where our demodulation phase $\psi_{1\Omega}$ is chosen according to Equation A.23. Our error signal phase now depends on our sideband *amplitudes* as well as their phase

$$\phi_{1\Omega} = \frac{\phi_{s,t}+\phi_{i,t}}{2} - \phi_{LO} + \tan^{-1}\left(\frac{A_{s,t}-A_{i,t}}{A_{s,t}+A_{i,t}}\tan\psi_{1\Omega}\right) \tag{A.61}$$

Therefore, in general, intensity noise on the signal and idler sidebands will couple parasitically to our 1Ω error signal. However, in the ideal case (co-resonant, no sideband detuning, phase matched) when $E_{1\Omega}$ is described by Equation A.24, this error signal is first order insensitive to intensity noise. Again, before taking partial derivatives it is useful to rewrite Equation A.20 in terms of Watts by making the following substitutions.

$$B_r \to \sqrt{P_{B,r}},\ \ A_{s,t} \to \sqrt{P_{s,t}},\ \ A_{i,t} \to \sqrt{P_{s,t}},\ \ A_{LO} \to P_{LO} \tag{A.62}$$

The coupling of our fluctuations to the error signal phase are then given by:

$$\Delta_{1\Omega} = \begin{pmatrix} \frac{\partial \phi_{1\Omega}}{\partial P_{s,t}} \\ \frac{\partial \phi_{1\Omega}}{\partial \phi_{s,t}} \\ \frac{\partial \phi_{1\Omega}}{\partial P_{i,t}} \\ \frac{\partial \phi_{1\Omega}}{\partial \phi_{i,t}} \\ \frac{\partial \phi_{1\Omega}}{\partial P_{B,r}} \\ \frac{\partial \phi_{1\Omega}}{\partial \theta_{B,r}} \end{pmatrix} = \begin{pmatrix} \frac{\partial E_{1\Omega}}{\partial P_{s,t}} \frac{\partial \phi_{1\Omega}}{\partial E_{1\Omega}} \\ \frac{1}{2} \\ \frac{\partial E_{1\Omega}}{\partial P_{i,t}} \frac{\partial \phi_{1\Omega}}{\partial E_{1\Omega}} \\ \frac{1}{2} \\ 0 \\ 0 \end{pmatrix} \tag{A.63}$$

where the relevant partial derivatives are given by

$$\frac{\partial \phi_{1\Omega}}{\partial E_{1\Omega}} = \left(\frac{\partial E_{1\Omega}}{\partial \phi_{1\Omega}} \right)^{-1} = \frac{1}{2A_{LO}\sqrt{(A_{s,t} + A_{i,t})^2 \cos^2 \psi_{1\Omega} + (A_{s,t} - A_{i,t})^2 \sin^2 \psi_{1\Omega}}} \tag{A.64}$$

$$\frac{\partial E_{1\Omega}}{\partial P_{s,t}} = \sqrt{\frac{P_{LO}}{P_{s,t}}} \cos\left(\frac{\zeta}{2} - \delta\theta_{SQZ} + \psi_{1\Omega} \right) \tag{A.65}$$

$$\frac{\partial E_{1\Omega}}{\partial P_{i,t}} = \sqrt{\frac{P_{LO}}{P_{i,t}}} \cos\left(\frac{\zeta}{2} - \delta\theta_{SQZ} - \psi_{1\Omega} \right) \tag{A.66}$$

where we have evaluated all partial derivatives at the lock point. We may then write our total fluctuations on $\phi_{1\Omega}$ as

$$\delta\phi_{1\Omega} = (\Delta_{1\Omega})^t \delta\mathbf{N}_{out,f} - \delta\phi_{LO} \tag{A.67}$$

where we've added the additional phase fluctuations on the LO field, $\delta\phi_{LO}$, which couple directly to our error signal phase.

A.3 Calculation of squeezed quadrature lock point errors due to misalignment

Note to the reader: *This section is a calculation from one of my papers [82]. It does not account the rotation of the error signal ellipse in the presence of non-negligible control sideband detuning as depicted in Figure A-2. Unfortunately, I didn't have*

time to update this calculation. I expect the exact numbers to change, but qualitatively everything should still hold. We should still find that we get a dramatic reduction in lock point errors by measuring the error signal in transmission through the Output mode cleaner. This section builds on a previous calculation in section 5.4 of Sheila Dwyer's thesis [36].

As described in Chapter 3, the coherent control scheme used in all squeezed vacuum sources deployed at gravitational wave detectors to date is used to stabilize two phases. An error signal derived in reflection from the OPO is used to stabilize the phase difference between the two control sidebands $\psi = \phi^+ - \phi^-$. Setting ϕ^+ equal to zero for simplicity, the phase of the second control sideband generated in the OPO, ϕ^-, is equal to the phase of the pump field θ_B. At the interferometer output, a second error signal is derived to stabilize the phase between the control and interferometer fields $\phi = \phi^+ - \phi^{ifo}$. Stabilizing these two phases locks the relative phase between the squeezed field and the interferometer beam, or *squeezing angle*:

$$\theta_{sqz} = \theta_B/2 - \phi^{ifo} = \phi - \psi/2 \tag{A.68}$$

In general, the interferometer and control fields at the detector output can both be misaligned and contain some higher order mode content. For the remainder of this analysis, I will expand both fields in terms of the TEM_{ij} eigenmodes of the interferometer OMC cavity. In the presence of higer order modes, the error signal used to lock ϕ, after demodulation at the control frequency Ω and low pass filtering, can be expressed as [37]:

$$\begin{aligned} I_{err} &\propto a_{00}^{ifo} a_{00}^{+} \cos(-\phi + \theta_{dm}) + a_{00}^{ifo} a_{00}^{-} \cos(\phi - \psi + \theta_{dm}) \\ &+ \sum_{ij} a_{ij}^{ifo} \left[a_{ij}^{+} \cos\left(-\phi + \phi_{ij}^{ifo} - \phi_{ij}^{+} + \theta_{dm}\right) + a_{ij}^{-} \cos\left(\phi - \psi + \phi_{ij}^{-} - \phi_{ij}^{ifo} + \theta_{dm}\right) \right] \end{aligned} \tag{A.69}$$

Above, a_{ij}^{ifo}, a_{ij}^{+}, and a_{ij}^{-} represent the norm of the electric field amplitude for the

TEM_{ij} component of the interferometer and control fields respectively and θ_{dm} is the demodulation phase. Here, ϕ_{ij}^{ifo}, ϕ_{ij}^{+}, and ϕ_{ij}^{-} are the phase shifts between the TEM_{00} and TEM_{ij} modes for the interferometer and control fields. When we derive the error signal from the fields incident on the OMC, we can make a few simplifications to eq. A.69.

$$\begin{aligned} I_{err} &\propto \cos(-\phi + \theta_{dm}) + \alpha \cos(\phi - \psi + \theta_{dm}) \\ &+ \sum_{ij} \rho_{ij}^{ifo} \rho_{ij}^{clf} \left[\cos(-\phi + \phi_{ij} + \theta_{dm}) + \alpha \cos(\phi - \psi - \phi_{ij} + \theta_{dm})\right] \end{aligned} \tag{A.70}$$

In this case the phases ϕ_{ij}^{+} and ϕ_{ij}^{-} are equal and we will express both as ϕ_{ij}^{clf} as was done in section 4.2. The factors ρ_{ij}^{ifo}, ρ_{ij}^{clf}, and ϕ_{ij}, are identical to those in section 3 as well:

$$\rho_{ij}^{ifo} = \frac{a_{ij}^{ifo}}{a_{00}^{ifo}} \qquad \rho_{ij}^{clf} = \frac{a_{ij}^{+}}{a_{00}^{+}} \qquad \phi_{ij} = \phi_{ij}^{ifo} - \phi_{ij}^{clf} \tag{A.71}$$

In A.69, we have pulled out a common factor of $a_{00}^{ifo} a_{00}^{+}$ from all terms. We have also used the fact that the ratio of the amplitudes of the two control sidebands is the same in all spacial modes to make the following substitution:

$$\alpha = \frac{a_{00}^{+}}{a_{00}^{-}} = \frac{a_{ij}^{-}}{a_{ij}^{+}} \tag{A.72}$$

Note that the expression on the first line of equations A.69 and A.70 is the error signal in the absence of higher order mode content. We tune θ_{dm} so that the first line is zero when ϕ and ψ correspond to the desired squeezing angle. For interferometers using DC readout, [46] we desire amplitude squeezing at the output and set $\theta_{dm} = \psi/2 - \pi/2$ so that the error signal is zero when $\phi = \pi/2 + \theta_{dm}$ and $\theta_{sqz} = 0$. Now we include a small misalignment such that $a_{ij} \ll a_{00}$ for all fields. When we lock and $I_{err} = 0$, then $\phi \approx \pi/2 + \theta_{dm} + \Delta\phi$ where $\Delta\phi$ is a small angle. Plugging these phases into equation A.70, we obtain:

$$I_{err} \propto -(1-\alpha)\left[\sin(\Delta\phi) + \sum_{ij} \rho_{ij}^{ifo}\rho_{ij}^{clf}\sin(\Delta\phi - \phi_{ij})\right] \tag{A.73}$$

We can then solve for the lock point error $\Delta\phi$ by setting I = 0 and using the small angle approximation to first order. This gives us equation 3.5, which we have restated below for clarity:

$$\Delta\phi = \frac{\sum_{ij}\rho_{ij}^{clf}\rho_{ij}^{ifo}sin\phi_{ij}}{1+\sum_{ij}\rho_{ij}^{clf}\rho_{ij}^{ifo}cos\phi_{ij}} \approx \sum_{ij}\rho_{ij}^{clf}\rho_{ij}^{ifo}sin\phi_{ij} \tag{A.74}$$

Since it is the presence of higher order modes which leads to lock point errors, it is desirable to derive the error signal in transmission through the OMC in order to filter out higher order mode content. We proceed to calculate the lock point errors in this case by returning to A.69 and including the effect of the cavity on all phases and field amplitudes. Note that many of the assumptions made in deriving equation A.70 are no longer valid once the fields pass through the OMC. The field amplitudes are modified as follows:

$$\begin{aligned}
a_{00,\,tr}^{ifo} &= T(0)\; a_{00}^{ifo} & a_{ij,\,tr}^{ifo} &= T(\Delta\omega(i,j))\; a_{ij}^{ifo} \\
a_{00,\,tr}^{+} &= T(\Omega)\; a_{00}^{+} & a_{ij,\,tr}^{+} &= T(\Omega+\Delta\omega(i,j))\; a_{ij}^{+} \\
a_{00,\,tr}^{-} &= T(-\Omega)\; a_{00}^{-} & a_{ij,\,tr}^{-} &= T(-\Omega+\Delta\omega(i,j))\, a_{ij}^{-}
\end{aligned} \tag{A.75}$$

Here, T(ω) is the cavity amplitude transmission for a field with detuning ω and $\Delta\omega(i,j)$ is the frequency shift of the cavity resonance for the TEM$_{ij}$ mode. In order to simplify our expressions for the phases, we will treat the case where the OMC cavity is linear and note that generalizing to the case of a travelling wave cavity is straightforward. Assuming that the control side-bands are well outside of the cavity linewidth, the phase shifts in transmission are:

$$\begin{aligned} \phi_{tr}^{ifo} &= \phi^{ifo} \quad \phi_{tr}^{+} = \phi^{+} - \pi/2 \quad \phi_{tr}^{-} = \phi^{-} + \pi/2 \\ \psi_{tr} &= \psi - \pi \quad \phi_{tr} = \phi - \pi/2 \quad \theta_{sqz,tr} = \theta_{sqz} \end{aligned} \tag{A.76}$$

We also assume that the first several higher order modes are well outside of the cavity linewidth and lie above the cavity resonance:

$$\phi_{ij,tr}^{ifo} = \phi_{ij}^{ifo} - \pi/2 \quad \phi_{ij,tr}^{+} = \phi_{ij}^{+} - \pi/2 \quad \phi_{ij,tr}^{-} = \phi_{ij}^{-} - \pi/2 \tag{A.77}$$

Plugging equations A.75 and A.76 into equation A.69 and simplifying yields:

$$\begin{aligned} I_{err} \propto \cos(-\phi_{tr} + \theta_{dm}) + \alpha \cos(\phi_{tr} - \psi_{tr} + \theta_{dm}) + \sum_{ij} \frac{T(\Delta\omega(i,j))}{T(\Omega)} \rho_{ij}^{ifo} \rho_{ij}^{clf} \\ \times [\cos(-\phi_{tr} + \phi_{ij} + \theta_{dm}) T(\Omega + \Delta\omega(i,j)) + \alpha \cos(\phi_{tr} - \psi_{tr} - \phi_{ij} + \theta_{dm}) T(-\Omega + \Delta\omega(i,j))] \end{aligned} \tag{A.78}$$

We proceed as before and set $\theta_{dm} = \psi_{tr}/2 - \pi/2$ and $\phi_{tr} \approx \pi/2 + \theta_{dm} + \Delta\phi$. Again we set I = 0 and make the small angle approximation to first order and solve for $\Delta\phi$ to obtain:

$$\begin{aligned} \Delta\phi &\approx \sum_{ij} A_{ij} \rho_{ij}^{ifo} \rho_{ij}^{clf} \sin(\phi_{ij}) \\ A_{ij} &= \frac{T(\Delta\omega(i,j))}{(1-\alpha)T(\Omega)} \left[T(\Omega + \Delta\omega(i,j)) - \alpha T(-\Omega + \Delta\omega(i,j)) \right] \end{aligned} \tag{A.79}$$

Table A.1 shows the values of A_{ij} for the first 10 sets of higher order modes using the parameters for the advanced LIGO OMC. We see that the reduction in the coupling of alignment jitter to quadrature fluctuations typically exceeds two orders of magnitude.

For a higher order modes with large values of i and j $\Delta\omega(i,j)$ will eventually be comparable to the OMC cavity free spectral range. If all fields are still well outside

mode order	1	2	3	4	5
$\mathbf{A}_{ij}$	0.0012	0.00071	0.0011	0.0086	0.0080

mode order	6	7	8	9	10
$\mathbf{A}_{ij}$	0.00086	0.00075	0.0020	0.11	0.0014

Table A.1: Coupling coefficients A_{ij} calculated using the parameters for the advanced LIGO OMC. This cavity has a finesse of 390, higher order mode spacing of 58 MHz, and a free spectral range of 264.8 MHz. The detuning of the control sidebands, Ω, is 15 MHz. A mode order of n corresponds to any mode TEM_{ij} with $i + j = n$.

of the cavity linewidth but the two control side-bands lie on opposite sides of a cavity resonance, one of the two ϕ_{ij}'s in equation A.78 will pick up a factor of π resulting in the corresponding term in A_{ij} picking up a minus sign. If one of the fields becomes close to the cavity resonance, the approximations in equations A.76 and A.77 may break down. However, it typically is possible to design the OMC and pick Ω such that this will not happen until the mode order is quite large. It is then a reasonable approximation to terminate the sum in equation A.79 before this becomes a problem and the result derived above remains valid.

Appendix B

Symbol definitions

Latin Symbols	Description	Expression
$a(t)$, $a(\Omega)$	Annihilation operator for fundamental cavity field (Except in Chapter 1)	
$\bar{a} + \delta a(t)$	DC plus fluctuating field	$a(t)$
a_+ (a_-)	Annihilation operator for upper (lower) sideband	$a(\Omega)$ ($a(-\Omega)$)
$a_1(\Omega)$	Amplitude quadrature operator	$\frac{a_+ + a_-^\dagger}{\sqrt{2}}$
$a_2(\Omega)$	Phase quadrature operator	$\frac{a_+ - a_-^\dagger}{i\sqrt{2}}$
$A_{f,in}$ ($B_{f,in}$)	Annihilation operator for field incident on OPO input mirror at fundamental (pump) frequency	
$A_{f,out}$ ($B_{f,out}$)	Annihilation operator for field reflected from OPO input mirror at fundamental (pump) frequency	
$A_{CLF,in}$ ($B_{CLF,in}$)	Annihilation operator for field incident on OPO CLF mirror at fundamental (pump) frequency	
$A_{CLF,out}$ ($B_{CLF,out}$)	Annihilation operator for field reflected from OPO CLF mirror at fundamental (pump) frequency	
$A_{l,in}$ ($B_{l,in}$)	Annihilation operator for field arising from OPO intra-cavity losses at fundamental (pump) frequency	
$b(t)$, $b(\Omega)$	Annihilation operator for pump intra-cavity field (Except in Chapter 1)	
c	Speed of light	
$D(\alpha)$	Displacement operator	
e	electron charge	
$E(t)$	Electric field	
G	Parametric amplification (de-amplification)	
g	Nonlinear gain	$\frac{1}{(1-x)^2}$
H	Hamiltonian operator	
$h_{qn}(\Omega)$	quantum noise strain spectral density	

$h_{SQL}(\Omega)$	The standard quantum limit	$\sqrt{\frac{8\hbar}{M\Omega^2 L_{arm}^2}}$
I	Photocurrent	
$\mathbf{I}$	Identity matrix	
$k_r(k_g)$	Wavenumber for the fundamental (pump) field	$\frac{2\pi}{\lambda_r}$
L_c	Interaction Length of PPKTP crystal	
$L_{c,tot}$	Total Length of PPKTP crystal	
M	Mirror mass	
$\mathbf{M}$	Matrix operator for OPO	
P	Laser power	
P_{thresh}	Incident pump power at threshold	
P_{circ}	Power circulating in interferometer arms	
P_{sc}	Backscattered power	
R_i	Mirror i power reflectivity	
R_{OPO}	OPO reflection coefficient	
$S(r)$	Squeezing operator (r =squeezing factor)	
T_i	Mirror i power transmission	
T	Temperature	
$\mathbf{T}$	transmission matrix	
T_0	Phase matching temperature	
V_1	Amplitude quadrature variance	
V_2	Phase quadrature variance	
V_-	Squeezed quadrature variance	
V_+	Anti-squeezed quadrature variance	
$V(\theta_s qz)$	Variance at quadrature angle θ_{sqz}	
V_{meas}	Measured quadrature variance	
	$V_- \cos^2(\theta_B/2 - \theta_{LO} + V_+ \sin^2(\theta_B/2 - \theta_{LO})$	
x	Normalized nonlinear interaction strength	$\sqrt{\frac{P}{P_{thresh}}}$ $= 1 - 1/\sqrt{g}$
X_1	Alternate form of amplitude quadrature operator	$A_+ + A_-^\dagger$
X_2	Alternate form of phase quadrature operator	$-i(A_+ - A_-^\dagger)$

Greek Symbols	Description	Expression
α	coherent state eigenvalue	
α_{KTP}	thermal expansion coefficient for KTP	
$\alpha_p(\Omega)$	quadrature rotation at frequency Ω	
Γ	one-photon to two-photon matrix	
$\gamma^i_{r,g}$	Loss rate for fundamental (r) or pump (g) field at coupler j	$(1-\sqrt{R_i})/\tau$
$\gamma^{tot}_{r,g}$	total cavity field decay rate for fundamental (r) or pump (g) field.	
γ_{fc}	Filter cavity half bandwidth	
Δ_r	cavity detuning at fundamental frequency	
Δ_g	cavity detuning at pump frequency	
Δk	phase mismatch parameter	
$\Delta\phi_{rt}$	cavity dispersion mismatch	
$\Delta\omega_{fc}$	Filter cavity detuning	
δa	fluctuating component of field a	
ϵ	nonlinear coupling parameter	
η_{esc}	OPO Escape efficiency	$\gamma^f_r/\gamma^{tot}_r$
η_{PD}	Photodiode quantum efficiency	
η_{prop}	Propagation efficiency	
$\mathcal{K}(\Omega)$	Radiation pressure coupling coefficient	
θ_{SQZ}	Squeezing angle	
θ_{rms}	RMS Level of phase noise	
θ_b	pump field phase	
θ_w	PPKTP crystal wedge angle	
λ	Poling period of PPKTP crystal	
$\lambda_{r,g}$	wavelength of fundamental (r) and pump (g) fields	
τ	OPO cavity round trip time	L/c
ω_0	Fundamental carrier frequency on resonance	
ω_r	Frequency of fundamental field	
ω_g	Frequency of pump field	
Ω	Sideband frequency, measurement frequency	
Ω_{CLF}	CLF detuning	
Ω_{SQL}	SQL frequency	

Bibliography

[1] Formula for addition of two arbitrary sinusoids. `http://dspguru.com/sites/dspguru/files/Sum_of_Two_Sinusoids.pdf`. Accessed: 2016-06-17.

[2] Abbott, B. P., et al. Gw151226: Observation of gravitational waves from a 22-solar-mass binary black hole coalescence. *Phys. Rev. Lett. 116* (Jun 2016), 241103.

[3] Adhikari, R. X. Gravitational radiation detection with laser interferometry. *Rev. Mod. Phys. 86* (Feb 2014), 121–151.

[4] Anderson, D. Z. Alignment of resonant optical cavities. *Appl. Opt. 23*, 17 (Sep 1984), 2944–2949.

[5] Aoki, T., Takahashi, G., and Furusawa, A. Squeezing at 946nm with periodically poled $KTiOPO_4$. *Optics Express 14* (July 2006), 6930–6935.

[6] Arai, K., Barnum, S., Fritschel, P., Lewis, J., and Waldman, S. Output mode cleaner design. *LIGO Technical Note T1000276-v5* (2013).

[7] Asenbaum, P., and Arndt, M. Cavity stabilization using the weak intrinsic birefringence of dielectric mirrors. *Opt. Lett. 36*, 19 (Oct 2011), 3720–3722.

[8] Aso, Y., Michimura, Y., Somiya, K., Ando, M., Miyakawa, O., Sekiguchi, T., Tatsumi, D., and Yamamoto, H. Interferometer design of the kagra gravitational wave detector. *Phys. Rev. D 88* (Aug 2013), 043007.

[9] Aspelmeyer, M., Kippenberg, T. J., and Marquardt, F. Cavity optomechanics. *Rev. Mod. Phys. 86* (Dec 2014), 1391–1452.

[10] Barsotti, L. Low loss faraday isolators for squeezed light injection. *LIGO Technical Note T1400274-v3* (2015).

[11] Barsotti, L. Low loss faraday isolators for squeezed light injection. *LIGO Technical Note T1400715-v3* (2015).

[12] Boon-Engering, J., van der Veer, W., Bente, E., and Hogervorst, W. Stabilization of an optical cavity containing a birefringent element. *Optics Communications 140*, 4âĂŞ6 (1997), 285 – 288.

[13] Boyd, R. W. *Nonlinear Optics*. Elsevier, Academic Press, Burlington, MA, 2008.

[14] Brooks, A., Adhikari, R., Ballmer, S., Barsotti, L., Fulda, P., Perrecea, A., and Ottaway, D. Active wavefront control in and beyond advanced ligo. *LIGO Technical Note T1400274-v3* (2015).

[15] Brooks, D. W. C., Botter, T., Brahms, N., Purdy, T. P., Schreppler, S., and Stamper-Kurn, D. M. Ponderomotive light squeezing with atomic cavity optomechanics. *Nature 488* (Aug. 2012), 476–480.

[16] Buchler, B. *Electro-Optic Control of Quantum Measurements*. PhD thesis, Australian National University, 2001.

[17] Buonanno, A., and Chen, Y. Optical noise correlations and beating the standard quantum limit in advanced gravitational-wave detectors. *Classical and Quantum Gravity 18*, 15 (2001), L95.

[18] Buonanno, A., and Chen, Y. Quantum noise in second generation, signal-recycled laser interferometric gravitational-wave detectors. *Phys. Rev. D 64*, 4 (Aug. 2001), 042006.

[19] Buonanno, A., and Chen, Y. Signal recycled laser-interferometer gravitational-wave detectors as optical springs. *Phys. Rev. D 65* (Jan 2002), 042001.

[20] Buonanno, A., and Chen, Y. Scaling law in signal recycled laser-interferometer gravitational-wave detectors. *Phys. Rev. D 67* (Mar 2003), 062002.

[21] Caves, C. M. Quantum-Mechanical Radiation-Pressure Fluctuations in an Interferometer. *Physical Review Letters 45* (July 1980), 75–79.

[22] Caves, C. M. Quantum-mechanical noise in an interferometer. *Phys. Rev. D 23* (Apr. 1981), 1693–1708.

[23] Caves, C. M., and Schumaker, B. L. New formalism for two-photon quantum optics. I - Quadrature phases and squeezed states. II - Mathematical foundation and compact notation. *Phys. Rev. A 31* (May 1985), 3068–3111.

[24] Chelkowski, S., Vahlbruch, H., Danzmann, K., and Schnabel, R. Coherent control of broadband vacuum squeezing. *Phys. Rev. A 75* (Apr 2007), 043814.

[25] Chelkowski, S., Vahlbruch, H., Hage, B., Franzen, A., Lastzka, N., Danzmann, K., and Schnabel, R. Experimental characterization of frequency-dependent squeezed light. *Physical Review A 71*, 1 (Jan. 2005).

[26] Chua, S. S. Y. *Quantum enhancement of a 4km laser interferometer gravitational-wave detector*. PhD thesis, The Australian National University, 2013.

[27] Chua, S. S. Y., Dwyer, S., Barsotti, L., Sigg, D., Schofield, R. M. S., Frolov, V. V., Kawabe, K., Evans, M., Meadors, G. D., Factourovich, M., Gustafson, R., Smith-Lefebvre, N., Vorvick, C., Landry, M., Khalaidovski, A., Stefszky, M. S., Mow-Lowry, C. M., Buchler, B. C., Shaddock, D. A., Lam, P. K., Schnabel, R., Mavalvala, N., and McClelland, D. E. Impact of backscattered light in a squeezing-enhanced interferometric gravitational-wave detector. *Classical and Quantum Gravity 31*, 3 (2014), 035017.

[28] Chua, S. S. Y., Stefszky, M. S., Mow-Lowry, C. M., Buchler, B. C., Dwyer, S., Shaddock, D. A., Lam, P. K., and McClelland, D. E. Backscatter tolerant squeezed light source for advanced gravitational-wave detectors. *Opt. Lett. 36*, 23 (Dec 2011), 4680–4682.

[29] Collaboration, L. S., and Collaboration, V. Observation of gravitational waves from a binary black hole merger. *Phys. Rev. Lett. 116* (Feb 2016), 061102.

[30] Collaboration, T. L. S., and Collaboration, V. Predictions for the rates of compact binary coalescences observable by ground-based gravitational-wave detectors. *Classical and Quantum Gravity 27*, 17 (2010), 173001.

[31] Collett, M. J., and Gardiner, C. W. Squeezing of intracavity and traveling-wave light fields produced in parametric amplification. *Phys. Rev. A 30* (Sep 1984), 1386–1391.

[32] Corbitt, T. *Quantum Noise and Radiation Pressure Effects in High Power Optical Interferometers*. PhD thesis, Massachusetts Institute of Technology, 2008.

[33] Corzo, N. V., Glorieux, Q., Marino, A. M., Clark, J. B., Glasser, R. T., and Lett, P. D. Rotation of the noise ellipse for squeezed vacuum light generated via four-wave mixing. *Phys. Rev. A 88* (Oct 2013), 043836.

[34] Degallaix, J., et al. Advanced Virgo status. *9th LISA Symposium, Astronomical Society of the Pacific Conference Series 467* (2012), 151.

[35] Dooley, K. L., Schreiber, E., Vahlbruch, H., Affeldt, C., Leong, J. R., Wittel, H., and Grote, H. Phase control of squeezed vacuum states of light in gravitational wave detectors. *Opt. Express 23*, 7 (Apr 2015), 8235–8245.

[36] Dwyer, S. *Quantum noise reduction using squeezed states in LIGO*. PhD thesis, Massachusetts Institute of Technology, 2013.

[37] Dwyer, S., Barsotti, L., Chua, S. S. Y., Evans, M., Factourovich, M., Gustafson, D., Isogai, T., Kawabe, K., Khalaidovski, A., Lam, P. K., Landry, M., Mavalvala, N., McClelland, D. E., Meadors, G. D., Mow-Lowry, C. M., Schnabel, R., Schofield, R. M. S., Smith-Lefebvre, N., Stefszky, M., Vorvick, C., and Sigg, D. Squeezed quadrature fluctuations in a gravitational wave detector using squeezed light. *Opt. Express 21*, 16 (Aug 2013), 19047–19060.

[38] Dwyer, S., Chua, S., Stefszky, M., Sigg, D., and Mavalvala, N. H1 squeezer noise model. *LIGO Technical Note T0900325-v1* (2009).

[39] Dwyer, S., Sigg, D., Ballmer, S. W., Barsotti, L., Mavalvala, N., and Evans, M. Gravitational wave detector with cosmological reach. *Phys. Rev. D 91* (Apr 2015), 082001.

[40] Eberle, T., Steinlechner, S., Bauchrowitz, J., Händchen, V., Vahlbruch, H., Mehmet, M., Müller-Ebhardt, H., and Schnabel, R. Quantum Enhancement of the Zero-Area Sagnac Interferometer Topology for Gravitational Wave Detection. *Physical Review Letters 104*, 25 (June 2010), 251102.

[41] Emanueli, S., and Arie, A. Temperature-dependent dispersion equations for ktiopo4 and ktioaso4. *Appl. Opt. 42*, 33 (Nov 2003), 6661–6665.

[42] Evans, M., Barsotti, L., Kwee, P., Harms, J., and Miao, H. Realistic filter cavities for advanced gravitational wave detectors. *Phys. Rev. D 88*, 2 (July 2013), 022002.

[43] Factourovich, M. *Classical and Quantum Aspects of the Detection of Gravitational waves*. PhD thesis, Collumbia, 2015.

[44] Fejer, M. M., Magel, G. A., Jundt, D. H., and Byer, R. L. Quasi-phase-matched second harmonic generation: tuning and tolerances. *IEEE Journal of Quantum Electronics 28*, 11 (Nov 1992), 2631–2654.

[45] Fox, A. M., Baumberg, J. J., Dabbicco, M., Huttner, B., and Ryan, J. F. Squeezed light generation in semiconductors. *Phys. Rev. Lett. 74* (Mar 1995), 1728–1731.

[46] Fricke, T. T., Smith-Lefebvre, N., Abbott, R., Adhikari, R., Dooley, K. L., Evans, M., Fritschel, P., Frolov, V. V., Kawabe, K., Kissel, J. S., Slagmolen, B. J. J., and Waldman, S. J. Dc readout experiment in enhanced ligo. *Classical and Quantum Gravity 29*, 6 (2012), 065005.

[47] Fritschel, P., Evans, M., and Frolov, V. Balanced homodyne readout for quantum limited gravitational wave detectors. *Opt. Express 22*, 4 (Feb 2014), 4224–4234.

[48] Fürst, J. U., Strekalov, D. V., Elser, D., Aiello, A., Andersen, U. L., Marquardt, C., and Leuchs, G. Quantum light from a whispering-gallery-mode disk resonator. *Phys. Rev. Lett. 106* (Mar 2011), 113901.

[49] Gardiner, C. W., and Collett, M. J. Input and output in damped quantum systems: Quantum stochastic differential equations and the master equation. *Phys. Rev. A 31* (Jun 1985), 3761–3774.

[50] Goda, K. *Development of techniques for Quantum-enhanced laser-interferometer gravitational-wave detectors.* PhD thesis, Massachusetts Institute of Technology, 2007.

[51] Goda, K., McKenzie, K., Mikhailov, E. E., Lam, P. K., McClelland, D. E., and Mavalvala, N. Photothermal fluctuations as a fundamental limit to low-frequency squeezing in a degenerate optical parametric oscillator. *Phys. Rev. A 72* (Oct 2005), 043819.

[52] Grote, H., Danzmann, K., Dooley, K. L., Schnabel, R., Slutsky, J., and Vahlbruch, H. First long-term application of squeezed states of light in a gravitational-wave observatory. *Phys. Rev. Lett. 110* (May 2013), 181101.

[53] Harms, J., Chen, Y., Chelkowski, S., Franzen, A., Vahlbruch, H., Danzmann, K., and Schnabel, R. Squeezed-input, optical-spring, signal-recycled gravitational-wave detectors. *Phys. Rev. D 68* (Aug 2003), 042001.

[54] Harms, J., Chen, Y., Chelkowski, S., Franzen, A., Vahlbruch, H., Danzmann, K., and Schnabel, R. Squeezed-input, optical-spring, signal-recycled gravitational-wave detectors. *Phys. Rev. D 68* (Aug 2003), 042001.

[55] Horrom, T., Romanov, G., Novikova, I., and Mikhailov, E. E. All-atomic generation and noise-quadrature filtering of squeezed vacuum in hot rb vapor. *Journal of Modern Optics 60*, 1 (2013), 43–49.

[56] Isogai, T. Homodyne detector. *LIGO Electronics Schematic D1300671-v5* (2015).

[57] Isogai, T. Homodyne photodetector design. *LIGO Technical Note T1500040-v1* (2015).

[58] Isogai, T. *Applications of Long Storage Time Optical Cavities.* PhD thesis, Massachusetts Institute of Technology, 2016.

[59] Isogai, T., Miller, J., Kwee, P., Barsotti, L., and Evans, M. Loss in long-storage-time optical cavities. *Opt. Express 21*, 24 (Dec 2013), 30114–30125.

[60] Kasprzack, M., Canuel, B., Cavalier, F., Day, R., Genin, E., Marque, J., Sentenac, D., and Vajente, G. Performance of a thermally deformable mirror for correction of low-order aberrations in laser beams. *Appl. Opt. 52*, 12 (Apr 2013), 2909–2916.

[61] Khalaidovski, A. *Beyond the quantum limit: a squeezed-light laser in GEO600*. PhD thesis, University of Hanover, 2012.

[62] Khalili, F. Y. Quantum variational measurement in the next generation gravitational-wave detectors. *Phys. Rev. D 76* (Nov 2007), 102002.

[63] Kimble, H. J., Levin, Y., Matsko, A. B., Thorne, K. S., and Vyatchanin, S. P. Conversion of conventional gravitational-wave interferometers into quantum nondemolition interferometers by modifying their input and/or output optics. *Phys. Rev. D 65* (Dec 2001), 022002.

[64] Kissel, J. Ham small triple suspension actuation ranges. *LIGO Technical Note T1300079-v2* (2014).

[65] Kwee, P., Miller, J., Isogai, T., Barsotti, L., and Evans, M. Decoherence and degradation of squeezed states in quantum filter cavities. *Phys. Rev. D 90* (Sep 2014), 062006.

[66] Lambrecht, A., Coudreau, T., Steinberg, A. M., and Giacobino, E. Squeezing with cold atoms. *EPL (Europhysics Letters) 36*, 2 (1996), 93.

[67] Lisa Barsotti and Jan Harms and Roman Schnabel. Squeezed vacuum states of light for gravitational wave detectors. *LIGO-P1600121* (2016).

[68] Liu, Z., Fulda, P., Arain, M. A., Williams, L., Mueller, G., Tanner, D. B., and Reitze, D. H. Feedback control of optical beam spatial profiles using thermal lensing. *Appl. Opt. 52*, 26 (Sep 2013), 6452–6457.

[69] Lynch, R., Vitale, S., Barsotti, L., Evans, M., and Dwyer, S. Effect of squeezing on parameter estimation of gravitational waves emitted by compact binary systems. *Phys. Rev. D, in press* (Jan. 2015).

[70] McKenzie, K. *Squeezing in the Audio Gravitational Wave Detection Band*. PhD thesis, The Australian National University, 2008.

[71] McKenzie, K., Grosse, N., Bowen, W. P., Whitcomb, S. E., Gray, M. B., McClelland, D. E., and Lam, P. K. Squeezing in the audio gravitational-wave detection band. *Phys. Rev. Lett. 93* (Oct 2004), 161105.

[72] Meers, B. J. Recycling in laser-interferometric gravitational-wave detectors. *Phys. Rev. D 38* (Oct 1988), 2317–2326.

[73] Mehmet, M., Ast, S., Eberle, T., Steinlechner, S., Vahlbruch, H., and Schnabel, R. Squeezed light at 1550 nm with a quantum noise reduction of 12.3 db. *Opt. Express 19*, 25 (Dec 2011), 25763–25772.

[74] Miller, J. Vopo-preliminary optical design. *LIGO Technical Note T1500468-v1* (2016).

[75] Miller, J., Barsotti, L., Vitale, S., Fritschel, P., Evans, M., and Sigg, D. Prospects for doubling the range of Advanced LIGO. *Phys. Rev. D 91* (Mar 2015), 062005.

[76] Mueller, G., Shu, Q.-Z., Adhikari, R., Tanner, D. B., Reitze, D., Sigg, D., Mavalvala, N., and Camp, J. Determination and optimization of mode matching into optical cavities by heterodyne detection. *Optics Letters 25* (Feb. 2000), 266–268.

[77] na Sandoval, F. M., Adhikari, R. X., Frolov, V., Harms, J., Lee, J., Sankar, S., Saulson, P. R., and Smith, J. R. Large-angle scattered light measurements for quantum-noise filter cavity design studies. *J. Opt. Soc. Am. A 29*, 8 (Aug 2012), 1722–1727.

[78] na Sandoval, F. M., Adhikari, R. X., Frolov, V., Harms, J., Lee, J., Sankar, S., Saulson, P. R., and Smith, J. R. Large-angle scattered light measurements for quantum-noise filter cavity design studies. *J. Opt. Soc. Am. A 29*, 8 (Aug 2012), 1722–1727.

[79] Nishizawa, N., Kume, S., Mori, M., Goto, T., and Miyauchi, A. Squeezed light generation with 1.064 Âţ m nd:yag laser and 0.85 Âţ m single-mode fiber. *Japanese Journal of Applied Physics 33*, 1R (1994), 138.

[80] Notcutt, M., Ma, L.-S., Ludlow, A. D., Foreman, S. M., Ye, J., and Hall, J. L. Contribution of thermal noise to frequency stability of rigid optical cavity via hertz-linewidth lasers. *Phys. Rev. A 73* (Mar 2006), 031804.

[81] Oelker, E. LASTI iLOG entry 5/30/2016.

[82] Oelker, E., Barsotti, L., Dwyer, S., Sigg, D., and Mavalvala, N. Squeezed light for advanced gravitational wave detectors and beyond. *Opt. Express 22*, 17 (Aug. 2014), 21106–21121.

[83] Oelker, E., Isogai, T., Miller, J., Tse, M., Barsotti, L., Mavalvala, N., and Evans, M. Audio-band frequency-dependent squeezing for gravitational wave detectors. *Phys. Rev. Lett 116* (2016), 041102.

[84] Oelker, E., Mansell, G., Tse, M., Miller, J., Matichard, F., Barsotti, L., Fritschel, P., McClelland, D. E., Evans, M., and Mavalvala., N. Ultra-low phase noise squeezed vacuum source for gravitational wave detectors. *Optica 3* (2016).

[85] Ourjoumtsev, A., Kubanek, A., Koch, M., Sames, C., Pinkse, P. W. H., Rempe, G., and Murr, K. Observation of squeezed light from one atom excited with two photons. *Nature 474* (June 2011), 623–626.

[86] Punturo, M., et al. The einstein telescope: a third-generation gravitational wave observatory. *Class. Quantum Grav. 27*, 19 (2010), 194002.

[87] Purdue, P., and Chen, Y. Practical speed meter designs for quantum nondemolition gravitational-wave interferometers. *Phys. Rev. D 66* (Dec 2002), 122004.

[88] Purdy, T. P., Yu, P.-L., Peterson, R. W., Kampel, N. S., and Regal, C. A. Strong optomechanical squeezing of light. *Phys. Rev. X 3* (Sep 2013), 031012.

[89] Qin, J., Zhao, C., Ma, Y., Chen, X., Ju, L., and Blair, D. G. Classical demonstration of frequency-dependent noise ellipse rotation using optomechanically induced transparency. *Phys. Rev. A 89* (Apr 2014), 041802.

[90] Robertson, N., Barton, M., Mayer, M., Romie, J., Torrie, C., and Kissel, J. Ham small triple suspension final design document. *LIGO Technical Note T09004356-v9* (2013).

[91] Safavi-Naeini, A. H., Groeblacher, S., Hill, J. T., Chan, J., Aspelmeyer, M., and Painter, O. Squeezing of light via reflection from a silicon micromechanical resonator. *Nature 500* (Aug. 2013), 185–189.

[92] Schreiber, E., Dooley, K. L., Vahlbruch, H., Affeldt, C., Bisht, A., Leong, J. R., Lough, J., Prijatelj, M., Slutsky, J., Was, M., Wittel, H., Danzmann, K., and Grote, H. Alignment sensing and control for squeezed vacuum states of light. *Opt. Express 24*, 1 (Jan 2016), 146–152.

[93] Scully, M. O., and Zubairy, M. S. *Quantum Optics*. Cambridge University Press, Cambridge, UK, 1997.

[94] Shelby, R. M., Levenson, M. D., Perlmutter, S. H., DeVoe, R. G., and Walls, D. F. Broad-band parametric deamplification of quantum noise in an optical fiber. *Phys. Rev. Lett. 57* (Aug 1986), 691–694.

[95] Siegman, A. *Lasers*. University Science Books, 1986.

[96] Skeldon, K. D., Clubley, D. A., Newton, G. P., Thieux, S., Gradowski, M. V., and Barr, B. W. Measurements of an ultra-low loss polarizer for Îż = 1064 nm using a high finesse optical cavity. *Journal of Modern Optics 48*, 4 (2001), 695–702.

[97] Slagmolen, B., Mullavey, A., Miller, J., and McClelland, D. aligo isc beam steering:tip-tilt suspension design. *LIGO Technical Note T1000042-v3* (2014).

[98] Stefszky, M. *Generation and detection of Low-frequency squeezing for gravitational-wave detection*. PhD thesis, Australia National University, 2012.

[99] Stefszky, M. S., Mow-Lowry, C. M., Chua, S. S. Y., Shaddock, D. A., Buchler, B. C., Vahlbruch, H., Khalaidovski, A., Schnabel, R., Lam, P. K., and McClelland, D. E. Balanced homodyne detection of

optical quantum states at audio-band frequencies and below. *Classical and Quantum Gravity 29*, 14 (2012), 145015.

[100] Teich, M. C., and Saleh, B. E. A. Squeezed state of light. *Quantum Optics: Journal of the European Optical Society Part B 1*, 2 (1989), 153.

[101] The LIGO Scientific Collaboration. A gravitational wave observatory operating beyond the quantum shot-noise limit. *Nature Physics 7* (Dec. 2011), 962–965.

[102] The LIGO Scientific Collaboration. Enhanced sensitivity of the LIGO gravitational wave detector by using squeezed states of light. *Nature Photonics 7* (Aug. 2013), 613–619.

[103] The LIGO Scientific Collaboration. Advanced ligo. *Classical and Quantum Gravity 32*, 7 (2015), 074001.

[104] Tse, M. LASTI iLOG entry 11/06/2015.

[105] Tse, M. LASTI iLOG entry 11/16/2015.

[106] Vahlbruch, H., Chelkowski, S., Danzmann, K., and Schnabel, R. Quantum engineering of squeezed states for quantum communication and metrology. *New j. Phys. 9* (Oct 2007).

[107] Vahlbruch, H., Chelkowski, S., Hage, B., Franzen, A., Danzmann, K., and Schnabel, R. Coherent control of vacuum squeezing in the gravitational-wave detection band. *Phys. Rev. Lett. 97* (Jul 2006), 011101.

[108] Vahlbruch, H., Khalaidovski, A., Lastzka, N., Gräf, C., Danzmann, K., and Schnabel, R. The GEO 600 squeezed light source. *Classical and Quantum Gravity 27*, 8 (Apr. 2010), 084027.

[109] Vahlbruch, H., Mehmet, M., Chelkowski, S., Hage, B., Franzen, A., Lastzka, N., Gossler, S., Danzmann, K., and Schnabel, R. Observation of squeezed light with 10-db quantum-noise reduction. *Phys. Rev. Lett. 100* (Jan 2008), 033602.

[110] Valle, F. D., Milotti, E., Ejlli, A., Gastaldi, U., Messineo, G., Piemontese, L., Zavattini, G., Pengo, R., and Ruoso, G. Extremely long decay time optical cavity. *Opt. Express 22*, 10 (May 2014), 11570–11577.

[111] Vander-Hyde, D., Amra, C., Lequime, M., MagaÃśa-Sandoval, F., Smith, J. R., and Zerrad, M. Optical scatter of quantum noise filter cavity optics. *Classical and Quantum Gravity 32*, 13 (2015), 135019.

[112] Wade, A., Mansell, G., Chua, S. S. Y., Ward, R., Slagmolen, B., Shaddock, D., and Mclelland, D. A squeezed light source operated under high vacuum. *Nat. Sci. Rep. 4* (Dec 2015), 18052.

[113] Wade, A., Mansell, G., McRae, T., Chua, S., Yap, M., Ward, R., Slagmolen, B., Shaddock, D., and McClelland, D. E. Optomechanical design and construction of a vacuum-compatible optical parametric oscillator for generation of squeezed light. *In Preparation* (2016).

[114] Zhang, T. C., Goh, K. W., Chou, C. W., Lodahl, P., and Kimble, H. J. Quantum teleportation of light beams. *Phys. Rev. A 67* (Mar 2003), 033802.